Multifunctional Nanomaterials for Textile Finishing: Synthesis, Characterization and Application

July 2023

Multifunctional Nanomaterials for Textile Finishing: Synthesis, Characterization and Application

A Dissertation Submitted to the Department of Chemistry, University of Dhaka for the Partial Fulfillment of the Requirements of the Degree of Doctor of Philosophy in Physical Chemistry

Submitted by

Registration No. 11

Session: 2017-2018

Examination Roll No. 2

DEPARTMENT OF CHEMISTRY

PHYSICAL CHEMISTRY RESEARCH LABORATORY

University of Dhaka

Dhaka-1000, Bangladesh

July 2023

Dedicated

to

My Parents, My Childrens,

My Husband,

and

My Supervisors

Acknowledgements

I would like to express my deepest appreciation to alumni of MCRL group Department of Chemistry, University of Dhaka. Specially **Professor Dr. Gulshan Ara**, Department of Chemistry, Jagannath University, Dhaka and **Assistant Professor Dr. Ferdousi Begum,** Department of Chemistry, BSMR Maritime University, Dhaka for valuable and advice and kind assistance for solving various problems related to research experiments.

I wish to express my heartfelt thanks to all the teachers and students of Physical Chemistry section of the Department for their cooperation.

I am thankful to my husband **Saiful Islam Khan** and children **Zarif Islam Khan** and **Zunairah Islam Khan** for their incessant ethical support. I am grateful to my parents and my keen gratitude is also for all the other members of my family and well-wishers for their encouragement.

(Kawser Parveen Chowdhury)

Declaration

The research work described in this thesis was carried out by the author of this thesis in the Department of Chemistry, University of Dhaka, Dhaka-1000, Bangladesh. This work has not been presented and will not be presented for any other degree.
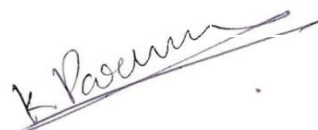
Dr. Md. Abu Bin Hasan Susan
Professor

Department of Chemistry

University of Dhaka

Dhaka-1000

Bangladesh

Ph.D. Supervisor

Prof. Dr. Md. Zulhash Uddin

Chairman,

Department of Wet Process Engineering

Bangladesh University of Textiles

Ph.D. Supervisor

Kawser Parveen Chowdhury

Department of Chemistry

University of Dhaka

Dhaka-1000

Bangladesh

Author (Ph.D. Student)

Abstract

The application of nanoparticles (NPs) to textile finishing processes has opened up various opportunities for improving performance and functionality of textiles. The primary aim of the study has been to create and produce finishes using TiO_2, ZnO, and Ag and their core@shell nanomaterials that provide favorable characteristics to textiles, including but not limited to antimicrobial, UV protection, and self-cleaning properties. The research encompasses sol-gel, hydrothermal, and wet chemical methodologies for synthesizing nanomaterials for textile applications. A range of characterization methodologies, such as the particle size and the microstructure, was obtained by dynamic light scattering (DLS), Fourier transform infrared (FTIR) spectroscopy, UV-vis spectroscopy, X-ray diffraction (XRD), transmission electron microscopy (TEM). The morphology and thermal properties of the nanomaterial-coated cotton fabric were obtained with scanning electron microscopy (SEM) and thermogravimetric analysis (TGA), respectively. The study also focuses on unravelling the mechanisms that underlie the interaction between nanoparticles and textile substrates, clarifying the variables affecting the performance of nanomaterial-based finishes on antimicrobial efficacy, UV protection, and self-cleaning properties. The investigation of the photocatalytic efficacy of TiO_2 NPs coated fabric was conducted through the degradation of methylene blue utilizing UV radiation. The results indicate that the fabric coated with TiO_2 NPs has the potential to be utilized in the development of self-cleaning clothing, as evidenced by the degradation of 75% of the dye within a five hours timeframe. The self-cleaning properties were examined using coffee and curry strains as model dirt. After 20 h of xenon UV light exposure, it was observed that TiO_2 NPs coated cotton textiles were able to effectively remove 58% of coffee stains and 76% of curry

stains. The photocatalytic activity of the ZnO NPs coated fabric was examined by degrading methylene blue using UV radiation. 83% of the dye was degraded in 3h, suggesting that ZnO NPs coated fabric can be used in self-cleaning clothing. ZnO NP-coated cotton textiles are observed to clean 67% coffee strain and 82% curry strain after 20h of xenon UV light exposure. The antibacterial effectiveness of Ag NPs was evaluated and the results indicated a reduction of over 98% for *Staphylococcus aureus* and around 99.9% for *Escherichia coli* bacteria. The coated fabric demonstrated a favorable ultraviolet protection factor (UPF) 26.01. The coated fabric effectively removed curry stains following a 20-hour exposure to xenon UV light. $TiO_2@ZnO$ NPs-coated cotton textiles are observed to clean 80% coffee stain and 90% curry stain after 20h of xenon UV light exposure. Fifthly, the antibacterial effectiveness of $TiO_2@Ag$ NPs was evaluated, and the results indicated a reduction of over 99.9% for *Staphylococcus aureus* and around 99.9% for *Escherichia coli* bacteria. The coated fabric demonstrated a favorable ultraviolet protection factor (UPF) 28.4. The coated fabric effectively removed curry stains following a 20-hour exposure to xenon UV light. Sixthly, the antibacterial effectiveness of ZnO@Ag NPs was evaluated, and the results indicated a reduction of over 99.9% for *Staphylococcus aureus* and around 99.9% for *Escherichia coli* bacteria. The coated fabric demonstrated a favorable ultraviolet protection factor (UPF) 26.14. The coated fabric effectively removed curry stains following a 20-hexposure to xenon UV light. This work explores the potential offered by multifunctional NPs in textile finishing, combining scientific investigation with practical applications to advance the field of textile engineering. Through the exploration of synthesis, characterization, and application, this study makes a valuable contribution to

advancing functional textiles. Ultimately, this research opens the door for novel and

sustainable textile finishing techniques that will benefit academia and industry

Title of the thesis:

Multifunctional Nanomaterials for Textile Finishing: Synthesis, Characterization and Application

Submitted by:

Kawser Parveen Chowdhury, Ph.D. Student, Department of Chemistry, University of Dhaka

The general description and outline of this thesis are given below:

Chapter 1: General Introduction

Chapter 1 gives a general introduction and describes the necessity and objective of the present research.

Chapter 2: Functional Photocatalytic and Self-cleaning Finish Fabric with TiO_2 Nanoparticles

Chapter 2 discusses synthesis of TiO_2 nanoparticles and their characterization. TiO_2 nanoparticles were synthesized by using sol-gel process. Various techniques such as dynamic light scattering (DLS), Fourier transform infrared (FTIR) and UV-vis spectroscopy, X-ray diffraction (XRD), and transmission electron microscopy (TEM) were carried out for characterization of the synthesized TiO_2 nanoparticles. Scanning electron microscopy (SEM) has been used for analyzing surface morphology of the textile materials (cotton fabrics) coated with the TiO_2 nanoparticles. Pad-dry-cure technique was used to make a transparent and thin adhesive surface of TiO_2 nanoparticles on the fabric materials. The photocatalytic performance and self-washing properties of TiO_2 nanoparticles coated fabrics have been investigated with the decolorization of methylene blue, coffee and curry marks under UV light. The experimental results showed the removal of 75% methylene blue after 5 hours, 58% coffee stain and 76% curry marks after 20 hours.

Chapter 3: Synthesis and characterization of ZnO Naoparticles for Application in Self-cleaning Textiles

Chapter 3 presents the preparation ZnO nanoparticles and their characterization. Hydrothermal method has been used for synthesize ZnO nanoparticles. A thin and transparent adhesive film of the ZnO nanoparticles on the surface of fabric materials has been produced with pad-dry-cure technique. The surface morphology of the formulated textile with ZnO nanoparticles has been investigated with DLS, FTIR and UV-vis spectroscopy, XRD, and TEM, SEM and thermogravimetric analysis (TGA). To study the photocatalytic performance of the ZnO nanoparticles for understanding the self-washing behavior of the fabric materials coated with the nanomaterials methylene blue as dye, coffee spot and curry marks were used as typical model dirt. It has been shown that 83% methylene blue in 3 hours, 67% coffee stain, and 82% curry spot after 20 hours was removed under UV light irradiation.

Chapter 4: Silver Nanoparticles Coated Cotton Fabric for UV Protection, Self-cleaning and Antibacterial Textiles

In Chapter 4 synthesis and characterization of Ag nanoparticles have been described. Wet chemical method was used to synthesize Ag nanoparticles. Various technique like DLS, FTIR, UV-vis spectroscopy, XRD, TEM were used to characterize the synthesized Ag nanoparticles. The surface morphology of the fabric materials with the Ag nanoparticles coating was investigated using SEM. Antibacterial properties along with UV protection behavior and self-washing performances of the developed textile materials with nanoparticles were examined. The result showed removal of 98% a gram-positive bacterium (*Staphylococcus aureus*) and approximately 99.9% a gram-negative bacterium (*Escherichia coli*) by the fabric coated with Ag nanoparticles.

Chapter 5: Multifunctional Finishing of Cotton Fabric by TiO$_2$@Ag Nanoparticles

Chapter 5 describes synthesis of titanium dioxide@silver nanoparticles (TiO$_2$@Ag NPs) by wet chemical method and characterization using DLS, FTIR, XRD, TEM and UV-vis spectroscopy. The surface morphology of the cotton fabric coated with TiO$_2$@Ag NPs was

carried out by SEM. UV protection behavior, self-cleaning action, and antibacterial properties for both gram-positive and gram-negative bacterium of the modified fabric with TiO$_2$@Ag NPs have been examined. The experimental results showed removal of 99.9% bacteria. The study also demonstrated a favorable UPF of 26.14.

Chapter 6: Multifunctional ZnO@Ag Nanoparticles on Cotton Fabric for UV Protection, Self-cleaning and Antibacterial Activity

In chapter 6 synthesis of ZnO@Ag nanoparticles by wet chemical method and their characterization using DLS, FTIR, UV-vis spectroscopy, XRD, and TEM have been described. Cotton fabrics have been developed with ZnO@Ag nanoparticles for multifunctional performance like UV protection, self-washing ability, and antibacterial activity. The experimental results showed extraordinary performance for the developed fabrics with ZnO@Ag nanoparticles such as more than 99.9% destroying of bacteria, good UPF of 26.14, and remarkable self-cleaning for curry stains.

Chapter 7: Synthesis and Application of TiO$_2$@ZnO Nanoparticles for Self-cleaning Cotton Fabrics

Chapter 7 explains synthesis and characterization of TiO$_2$@ZnO nanoparticles by DLS, FTIR, XRD, TEM, and UV-vis spectroscopy. The developed fabrics with TiO$_2$@ZnO NPs has been investigated for self-cleaning activity. The result showed outstanding self-cleaning property for coffee stain (80%) and curry stain (90%) under UV light.

Chapter 8: General Conclusions and Prospect

Chapter 8 summarizes the results for a general conclusion and discussed the future prospect of metal and metal oxide nanoparticles for developing textile materials with promising multifunction such as UV protection behavior, self-cleaning property, antibacterial activity without damaging the fiber of the fabrics.

Contents

Table of Figures

List of Tables

1. General Introduction

1.1   Introduction

The swift progressions in nanotechnology have facilitated pioneering breakthroughs in diverse scientific domains. The field of textile engineering has experienced significant advancements, particularly with the incorporation of nanomaterials, which has transformed conventional textile finishing techniques.[1]   The application of multifunctional nanomaterials in textile finishing has expanded the possibilities, resulting in improved functionalities and superior performance of textiles.[2]

The present PhD dissertation, entitled "Multifunctional Nanomaterials for Textile Finishing: Synthesis, Characterization, and Application," explores the domain of nanotechnology and its utilization in creating functional textile finishes. Due to the rising demand for such textiles, integrating nanomaterials has become essential in meeting the desired functionality in textiles across various industries, including healthcare, sportswear, automotive, and aerospace.[3]

The main objective of this study has been to investigate the synthesis, characterization, and application of multifunctional nanomaterials in textile finishing processes for the creation and implementation of multifunctional nanomaterials coatings that confer advantageous characteristics, such as antimicrobial efficacy, UV protection, and self-cleaning properties, onto textile substrates.

To sum up, this work investigates the potential of multifunctional nanomaterials in textile finishing. This research has numerous practical implications. This study aims at enhancing the domain of textile engineering and promoting the creation of practical textiles that can substantially influence diverse industries by examining their synthesis, characterization, and application. This study also focuses on the facilitation of the development of sustainable and innovative solutions in textile finishing by integrating scientific exploration and practical applications. The ultimate goal has been to advance academic research and industrial progress.

1.2 Objective of the study

The objective of the work has been to produce a self-cleaning, UV-protective, and antimicrobial multifunctional textile for combat clothing and healthcare and hygiene fabric.

1.3 Multifunctional textiles

Recently, there has been a significant transformation in the textile industry due to customer demand for high-performance, value-added textiles.[4] Multifunctional textiles is a category of sophisticated textile materials that provide aesthetic and decorative functions and furnish numerous functional features like UV protection, self-cleaning, hydrophobicity, antimicrobial, air permeability, tensile and tear strength, pilling and abrasion resistance, thermoregulation, electrical conductance and washing fastness.[5] Multifunctional textiles have the potential to provide various applications and advantages across diverse industries by integrating various functionalities into a single textile material.[6] These textiles have been designed to demonstrate a blend of advantageous attributes, including heightened efficacy, superior utility, and increased worth, by integrating specialized substances, coatings, or procedures.[7] Moreover, these textiles were made possible by nanotechnology, opening up new possibilities for use in industries including healthcare, sports, fashion, the automobile industry, protection, etc.[8,9] Numerous functional nanomaterials, including nanoparticles, nanotubes, and nanocomposites, have been introduced into textiles at several phases of the manufacturing process, including the spinning process for fibers and yarn, and finishing process for fabrics.[10]

This research focuses on synthesizing TiO_2, ZnO and Ag nanomaterials and their core@shells. These nanomaterials have been incorporated into cotton fabric by finishing process to impart multifunctionality in textiles, such as antimicrobial, self-cleaning, and UV-protection.

1.4 Nanomaterials

According to ISO (2015), a nanomaterial is a substance with at least one external dimension ranging from approximately 1 to 100 nanometers or a surface or internal structure that

exhibits nanoscale dimensions.[11] Nanomaterials possess significant potential for integrating various functional properties within textiles. Varied classifications of nanomaterials utilized in diverse textile application fields include carbon-based nanomaterials, inorganic nanoparticles, hybrid nanomaterials, polymeric nanomaterials, composite nanoparticles, core@shell nanoparticles, etc.

Here, three inorganic nanoparticles are used for synthesis, characterization and application on cotton knit fabric. TiO_2, ZnO, Ag nanoparticles. TiO_2 and ZnO are metal oxide-based, and Ag is metal-based nanoparticles. Moreover, TiO_2@ZnO, TiO_2@Ag, and ZnO@Ag core@shell nanoparticles are also used for synthesis, characterization and application on cotton knit fabric.

1.5   Synthesis

1.5.1   Sol-gel process

The sol-gel technique is a wet-chemical method widely utilized to synthesize nanomaterials. This approach is employed in the fabrication of diverse types of metal-oxide nanomaterials. This approach involves the conversion of a liquid precursor into a sol during the synthesis process, which is then transformed into a network structure known as a gel.[12] During the initial stage, the metal oxide undergoes hydrolysis in water or alcohol, forming a sol. Subsequently, condensation ensues, leading to a rise in the viscosity of the solvent and the formation of porous structures during an aging period.[13] Polycondensation persists throughout the aging process, leading to structural, physical, and porous alterations. As the material undergoes the aging process, there is a reduction in porosity and an increase in the inter-particle spacing of the colloidal constituents. After aging, desiccation occurs, whereby the gel removes water and organic solvents. Finally, calcination is carried out to obtain nanoparticles.[14] The sol-gel method is influenced by various factors, including the type of precursor used, the hydrolysis rate, the aging duration, the pH level, and the molar ratio between the precursor and H_2O.[15] The sol-gel technique is a cost-effective approach that offers several benefits, including the homogeneity of the resulting material, low processing temperatures, and ease of producing composites and intricate nanostructures.[16]

1.5.2 Hydrothermal process

Hydrothermal material processing is commonly referred to as superheated aqueous solution processing.[17] Hydrothermal technology encompasses the domain of supercritical water and supercritical fluid technology. Supercritical water technology employs water as the solvent within the system. In contrast, supercritical fluid technology broadly encompasses solvents such as CO_2 and various other organic solvents. Utilizing these solvents, which possess lower critical temperature and pressure than water, facilitates the processing of materials under significantly reduced temperature and pressure conditions. Supercritical water (SCW) and supercritical fluids (SCFs) are highly effective reaction media for the hydrothermal processing of nanoparticles.[18] This is due to their ability to modulate the reaction rate and equilibrium by manipulating the dielectric constant and solvent density through changes in pressure and temperature. As a result, these conditions facilitate higher reaction rates and the production of smaller particles. The stability of the reaction products in SCF conditions results in the formation of fine particles. [19] The hydrothermal method is a suitable approach for the manipulation of exceedingly fine powders that exhibit elevated levels of purity, regulated stoichiometry, superior quality, a limited range of particle sizes, controlled morphology, uniformity, minimal defects, compact particles, heightened crystallinity, exceptional reproducibility, regulated microstructure, high reactivity, and ease of sintering, among other desirable characteristics.[20] Moreover, the methodology above enables various benefits such as conservation of energy, utilization of equipment with larger volume, enhanced nucleation regulation, pollution prevention, increased dispersion, accelerated reaction rates, improved control over shape, and reduced temperature operations while the solvent is present. The hydrothermal technique is advantageous in nanotechnology due to its suitability for producing customized particulate matter, giving it an edge over other materials processing methods. The phrase "designer articulates" pertains to particles that exhibit exceptional levels of purity, crystallinity, quality, monodispersity, and controlled physical and chemical attributes.[21]

1.5.3 Wet chemical process

The bottom-up method of wet chemical synthesis of nanoparticles is highly appealing, owing to its simplicity and versatility. The wet chemical synthesis method is deemed more advantageous than the sol-gel process due to the increased versatility and cost-effectiveness of alkoxides utilized in the former, as compared to the inorganic salt compounds employed in the latter.

1.6 Processes for incorporating nanomaterials

Until now, there have been two main approaches for incorporating nanomaterials into textiles: (i) applying them to the textile during the coating or finishing process (a top-down approach) and (ii) applying them to the textile during the spinning stage of fiber production (a bottom-up approach).[22] Nanomaterials can be added to finishing/coating step of fabrics through various lamination or coating techniques and dyeing or printing processes to produce multifunctional textiles.[7] Due to their high cost-effectiveness, shorter production times, minor infrastructure requirements, and need for less equipment than impregnation during the fiber production stage or spinning process, these processes are more widely adopted by textile manufacturers and producers. Contrarily, because fiber spinning technologies can create fine-tunable nanoengineered fibers, they offer enormous extensibility for the textile industry.[23] However, this stage is still evolving because it needs to be tuned before use.

1.7 Nanofinishing

Nanofinishing enhances certain functionality by applying colloidal solutions of nanoparticles (NPs) or ultrafine dispersions to textile substrates. Nanofinishing uses a pad-dry-cure technique. Textiles are nano-finished with nanosol or nanoemulsion, which have droplet sizes of 100-500 nm. Semicontinuous or continuous padding mangle methods immerse the textile substrate in a nanomaterial dispersion. A roller pair presses the substrate to infiltrate nanoparticles into the cloth and remove surplus distribution. Figure 1.1 depicts this procedure.[24] Padding controls roller pressure and fabric velocity through the padded. After drying and curing the cloth, the solvent, mainly water, is removed, ensuring nanomaterial fixation. The nanomaterial must be evenly applied to the cloth

surface during dipping. Compared to weariness, the finishing path is the most convenient due to its simplicity, quickness, and cost-effectiveness.[25]
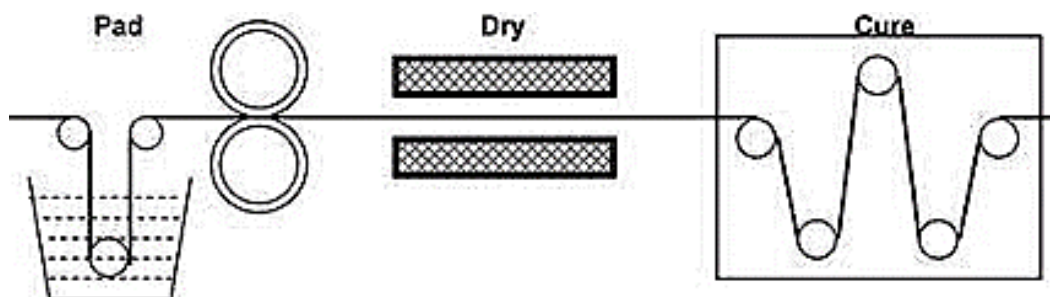
Figure 1.1: Typical padding process of textile fabrics[24]

This method outperforms typical finishing methods, using fewer NPs than bulk materials to obtain the same result. Moreover, nanofinishes are durable, do not affect shine or tactile feel of textile substrates, uniformly distribute NPs on textiles, and perform functions that standard finishing processes cannot. Nanomaterials in multifunctional finishes are popular due to their benefits. Many textile companies have effectively marketed their products by using nanoemulsions or nano sols to finish their textiles and adding helpful capabilities.[25]

1.8   Functional properties of nanotextiles

Nanotextiles are defined as the incorporation of nanomaterials into textile fibers or the application of coatings onto fabric. Besides their artistic and aesthetic applications, nanotextiles possess several valuable features that significantly enhance their overall performance. Nanofinishing and nanocoating are being increasingly utilized in various application domains on textile substrates. Diverse laminating, coating, or finishing methods have been employed to administer nanocomposites onto textiles. The potential for developing multifunctional nanotextiles has been greatly facilitated by the utilization of both nanocomposites and nanofibers, as illustrated in Figure 1.2.[26]
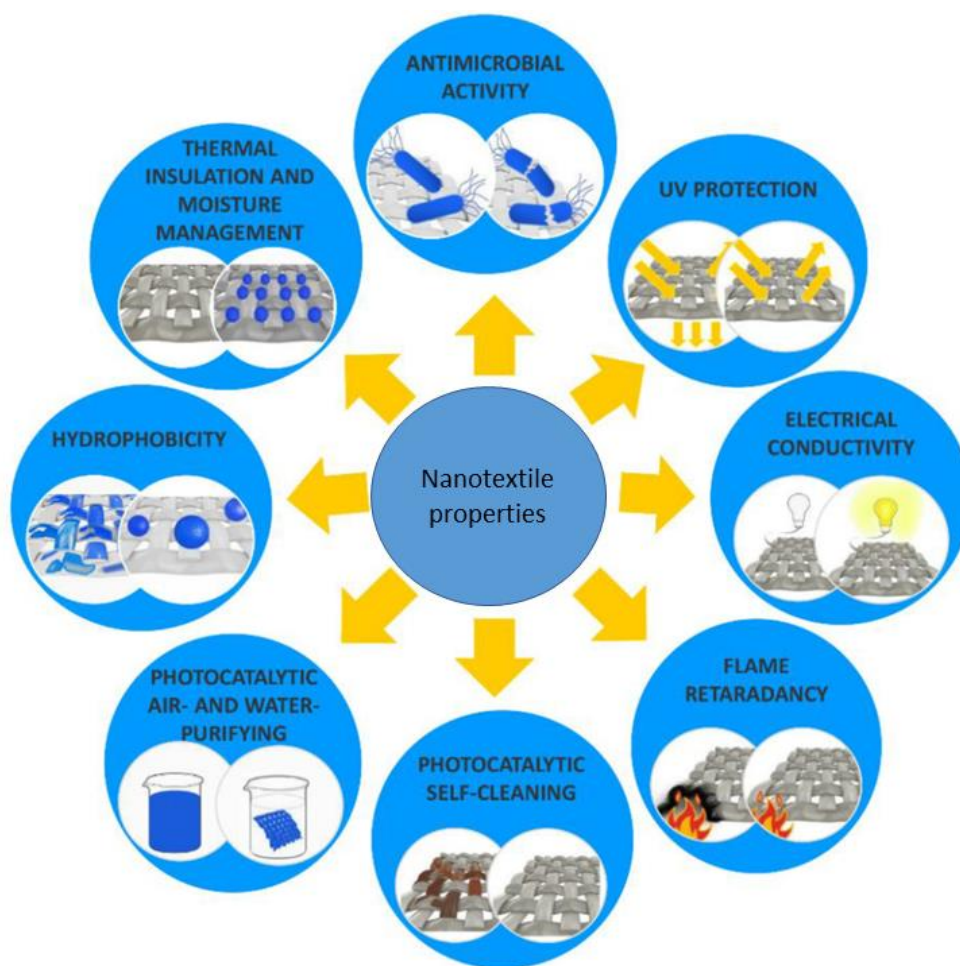
Figure 1.2: Various functional properties of multifunctional nanotextiles.[26]

1.8.1 Antimicrobial textiles

Nanoparticles have garnered significant interest as antimicrobial agents in academic and commercial spheres due to their biological efficiency against pathogens.[27] The ability of NPs to fight bacteria, protozoa, algae, fungi, viruses, and others determines their antibacterial potency. Various textile materials such as cotton, lyocell, viscose, linen, wool, and silk are susceptible to harboring numerous drug-resistant pathogens due to their favorable environmental conditions, including moisture, temperature, oxygen, and nutrients.[28] Textile companies worry about hazardous microorganism infestation. It discolors, smells terrible, causes allergic reactions, spreads infectious diseases, and lowers the aesthetic attractiveness of fabrics. Antimicrobial fabrics offer an innovative solution to

ongoing problems of healthcare and hygiene. Due to the growing awareness of hygiene and health, antimicrobial textile research is booming. Clothing must resist microorganisms.[29] Heavy metal ions, formaldehyde, organometallics, phenols, chitosan, quaternary ammonium salts, and organosilicon are used to give textiles antimicrobial properties through two distinct mechanisms, as illustrated in Figure 1.3.[30]
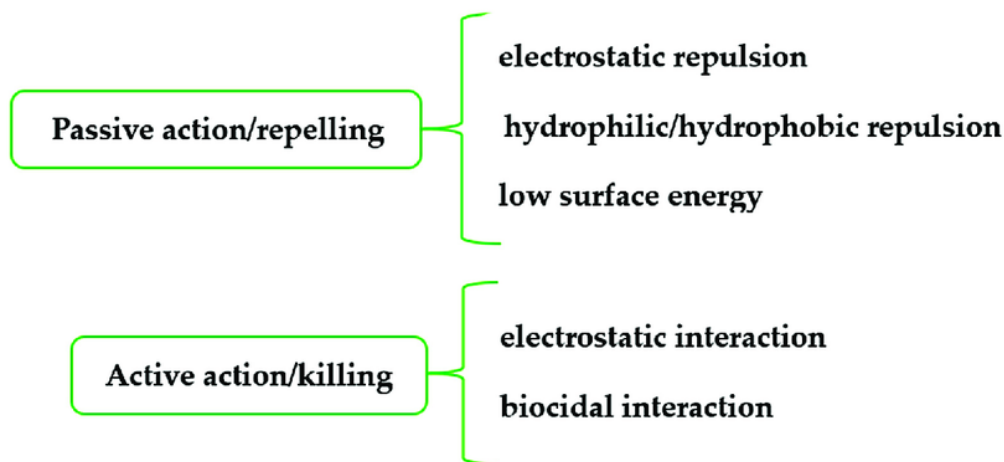
Figure 1.3: Classification of the mechanism of action of antimicrobial polymers.[30]

However, antimicrobial agents are often associated with various limitations, such as these can cause environmental toxicity, non-specific activity against non-target bacteria, and limited durability of the antimicrobial coating. NPs can solve these concerns. Nanoscience and nanotechnology have been studied in textile technologies with exceptionally functional finishing.[31] Non-peptide compounds outperform traditional antimicrobials. Antibacterial textile textiles use metal and metal oxide NPs. Gram-positive or gram-negative bacteria are characterized by their outer cell wall structure. Gram-negative bacteria have lipopolysaccharide outer membranes, while gram-positive bacteria have a thicker peptidoglycan layer.[32] Gram-negative bacteria have a periplasmic layer between their outer layer and plasma membrane. Antimicrobial NPs can penetrate this layer, killing the bacterial cell.[33] Figure 1.4 depicts a schematic representation of the bactericidal mechanism of metal ion NPs.
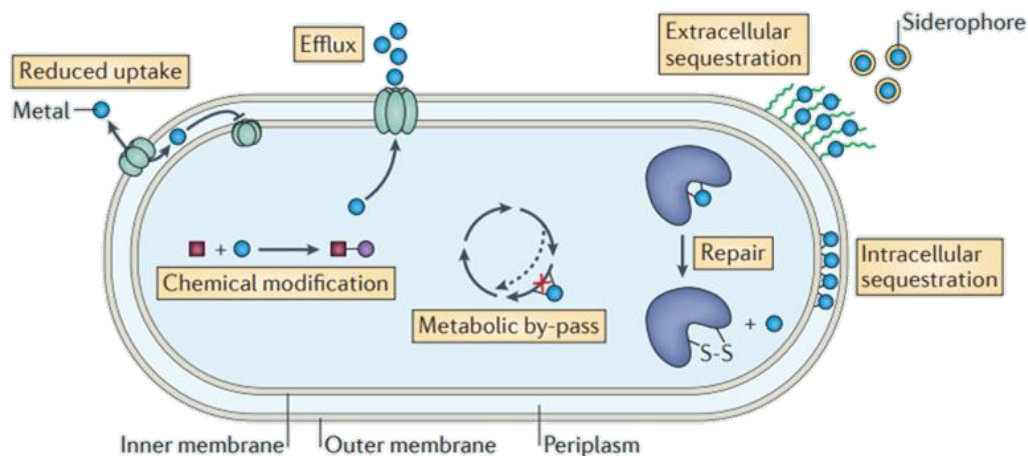
Figure 1.4: Schematic illustration showing the mechanism for the antimicrobial action of metal ions[32]

Nanoparticles are receiving considerable research attention as antimicrobial agents due to their antibacterial, antifungal, cost-effective, and low-toxicity qualities.[34] Metal oxide NPs have generated reactive oxygen species (ROS) such as superoxide anions, hydroxyl radicals, and hydrogen peroxide. These ROS can lead to polyunsaturated phospholipids' peroxidation, damaging cell structure and DNA and cause cell death.[35] Sharp nano-structured material edges can disrupt bacterial cell wall membranes. Nanomaterials adhering to the bacterial cell wall may damage the cell membrane and slow cytoplasmic outflow. Moreover, NPs emit metal ions that hinder DNA replication and ATP synthesis, damaging cells. ZnO NPs kill microbes by internalizing cells, generating ROS, and disorganizing plasma membranes. Among other metal NPs, silver (Ag) NPs have antimicrobial properties by generating oxygen radicals to oxidize bacterial structures, adhere to the bacterial cell wall, subsequently traversing the cell membrane and ultimately leading to bacterial demise via direct inhibition of its respiratory process, disrupting the cell wall and plasma membrane, reducing ATP levels, disintegrating the plasma membrane potential, introducing pits and gaps in the cell wall, inhibiting DNA replication, arresting the cell cycle at the G2/M phase, and reducing proton motive force. Additionally, Ag NPs limit the absorption and discharge of phosphate, succinate, mannitol, glutamine, and proline within *E.coli* bacteria cells.[36] Furthermore, the ionization of metallic silver occurs

through its reaction with moisture, resulting in the formation of highly active Ag^+ ions compared to metallic silver. The ionized silver particles generate many reactive species, including photo-generated hole-electron pairs and reactive oxygen species such as $\cdot O^{2-}$, $\cdot OH$, etc., when exposed to visible light on the surface of cellulose cotton. The cell wall structure is compromised by the presence of ionized Ag, ultimately leading to bacterial cell death.[32]

1.8.2 **Ultraviolet protection textiles**

Textile businesses face a significant and desirable challenge against UV protection. The solar radiation that reaches the Earth comprises 50% visible, 45% infrared, and 5% ultraviolet radiation. UV radiations are classified into three categories: UV-A, UV-B, and UV-C, based on their respective wavelength ranges of 400-320 nm, 320-280 nm, and 280-200 nm. UV-A and UV-B radiations damage skin and clothing the most. UV light can cause sunburn, tanning, photo dermatitis, erythema, and skin cancer.[37] Textiles exposed to UV light lose chemical, mechanical, and color qualities. Thus, clothing and materials must have UV protection. ZnO and TiO_2 NPs absorb both refractive and dispersing UV radiations and scatter UV light. Their band gap energies effectively shield UV light. Unlike many natural UV absorbers, NPs offer sustainable and improved UV protection.[38] Inorganic additives are preferred over organic ones because of their low toxicity, thermal and chemical stability, and UV resistance.[39] Previous investigations have shown that ZnO and TiO_2 nanoparticle chemical composition, particle size, shape, and crystallinity affect their protective efficiency.[39] Figure 1.5 illustrates UV protection on ZnO NPs coated fabric.
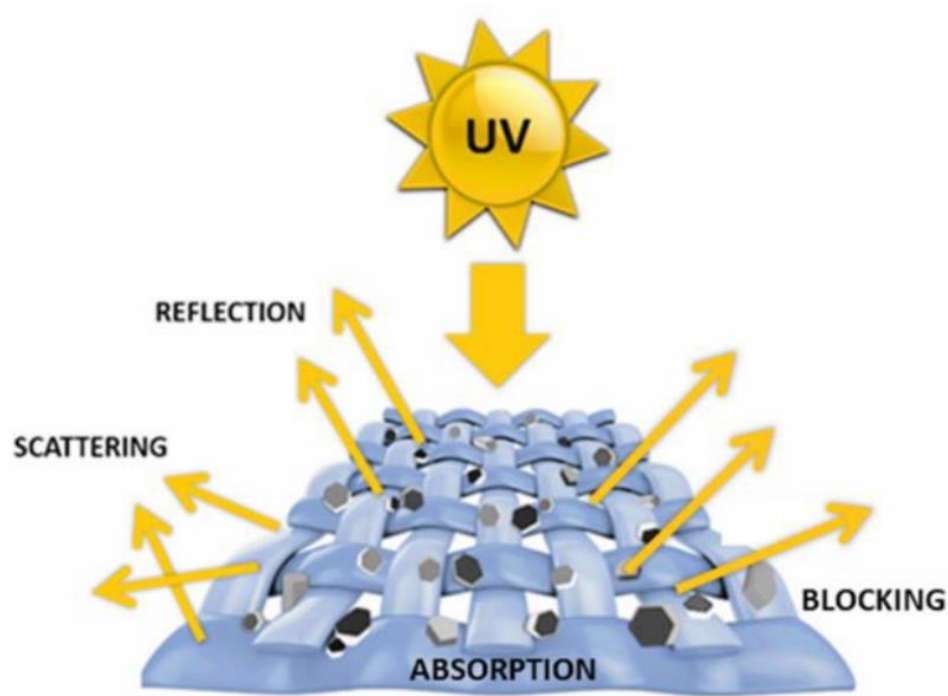
Figure 1.5: UV protection by ZnO NPs on coated textiles.[26]

The conventional practice for safeguarding against sun exposure involves evaluating the effectiveness of UV protection capabilities of fabrics through UV protection factor (UPF) values.[40] The UPF of a textile material is established through the following procedure (1.1,1.2):[41]

$$\text{UPF} = \frac{\sum_{\lambda=290}^{400} E(\lambda) \cdot \varepsilon(\lambda) \cdot \Delta(\lambda)}{\sum_{\lambda=290}^{400} E(\lambda) \cdot T(\lambda) \cdot \varepsilon(\lambda) \cdot \Delta(\lambda)} \qquad (1.1)$$

$$\text{Percent UV transmission} = \frac{\sum_{\lambda_1}^{\lambda_2} T(\lambda)}{(\lambda_2 - \lambda_1)} \qquad (1.2)$$

The solar irradiance, denoted as $E(\lambda)$ in units of W/m^2/nm, is a function of the spectral transmittance $T(\lambda)$ at the wavelength λ, the erythema action spectrum $\varepsilon(\lambda)$, and the wavelength interval $\Delta\lambda$. The UPF of textiles denotes their ability to block UV radiation, whereas a higher UPF value indicates a greater capacity for protection.[42] Table 1.1 classifies UPFs and their corresponding levels of protection.

Table 1.1: Classification of UPF category measured from relative transmittance and protection level. [40]

UPF range	Protection category	Transmittance (%)
<15	Insufficient protection	>6.7
15-24	Good protection	6.7-4.2
25-39	Very good protection	4.1-2.6
40-50, 50+	Excellent protection	<2.5

Several elements determine textile UV protection. Synthetic fibers transmit less UV than natural fibers. Tighter weaves transfer fewer UV rays. Darker hues absorb more UV rays and have higher UPFs than lighter ones. Higher stretchability decreases UPF. Wet fabrics have lower UV protection. UV-absorbing compounds boost UPF in the finishing process. Washed cotton and poly cotton fabrics have more excellent UPF ratings than worn and faded materials due to shrinkage.[43] Dye also improves textile UV blocking. Darker textiles provide better UV protection.[44]

1.8.3 Self-cleaning textiles

Nature inspires self-cleaning textiles. Due to its exceptionally pristine surface, the lotus leaf self-cleans. Natural processes created the "lotus effect," or highly repellent or self-cleaning surfaces. Hydrophobic and oleophobic lotus leaves repels water and dirt, making them self-cleaning. Due to lotus leaves' dual-size roughness, surface energy decreases. Figure 6 shows that epidermal cells on the leaves have nanoscale papillose and hair-like waxy crystals.[45] Self-cleaning textiles reduce environmental maintenance, production time, energy, material, and cost, wear time, and consumer laundry and cleaning costs. NPs can help build self-cleaning textiles for future fabrics. Technology can reduce pathogenic infection, detergent, dry-cleaning, water, and energy use. They can be used in hospital, military, athletic, and outdoor textiles, reducing cleaning costs, time, and labor efficiencies. Self-cleaning textiles can be utilized in various applications, such as hospital attire, military apparel, athletic wear, and outdoor textiles.[46]

Self-cleaning textiles can be classified into two categories: those based on superhydrophobic properties and those based on photocatalysis. Self-cleaning textiles can be divided into two categories, one is superhydrophobic-based self-cleaning textiles, and the other is photocatalysis-based self-cleaning textiles.[47]
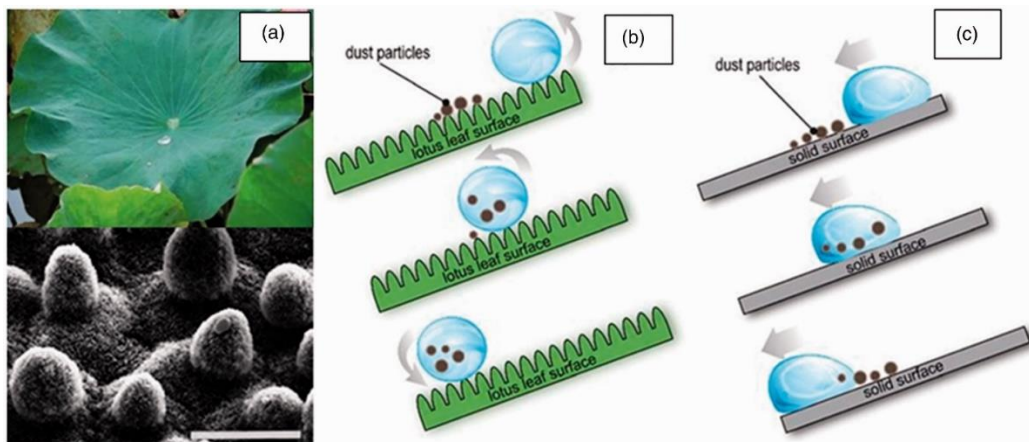
Figure 1.6: (a) A typical example of a superhydrophobic surface in nature, lotus effect, the effect of self-cleaning: a water droplet rolling off on (a) a lotus leaf rough surface (b) a normal smooth hydrophilic surface [48]

1.8.3.1   Superhydrophobic self-cleaning textiles

Nanotechnology could help create superhydrophobic textiles with the "lotus effect" shown in Figure 1.6. Superhydrophobic textile criteria are the material surface with a water contact angle larger than 150°, dual-size roughness like a lotus leaf, a low tilting angle of less than 10° for a water rolling on the surface, and a surface energy below 10 dynes/cm.[49] The textiles exhibit discoloration. It is caused by soil and aqueous solutions such as food and colored water. Textile materials possess the ability to assimilate a wide range of substances, thereby leading to the formation of blemishes. It is imperative to conduct testing on the stain resistance of coated cloth. The stain resistance of coated cotton is depicted in Figure 1.7(b). This investigation involved the dehydration of colored water droplets in the atmosphere, both with and without a coating. The sample that has been coated exhibits spherical absorption of water droplets, whereas the untreated surface demonstrates rapid absorption. Both specimens were subjected to air drying for 24 h. The application of heat

energy results in the transformation of liquid water into its gaseous state. The surface is covered with stains. Colored particles are deposited as water droplets evaporate on the covered sample. Rolling water droplets effectively eliminate pigmented particles and purifies the coated specimen.[50]
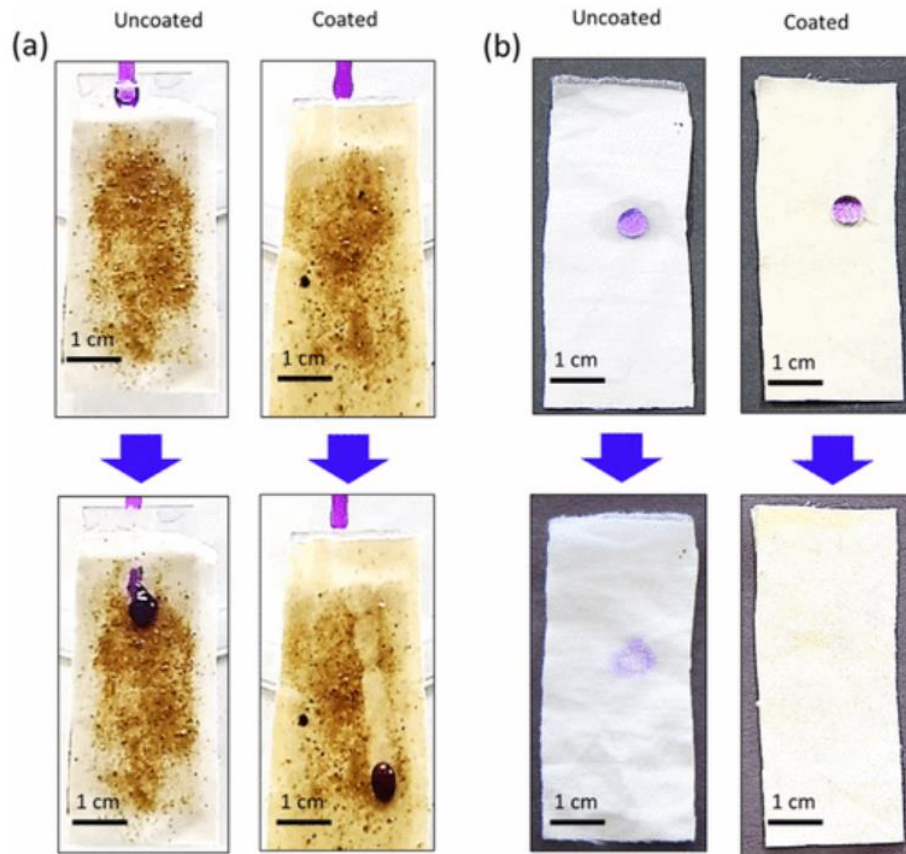
Figure 1.7: (a) Optical pictures of a uncoated non-self-cleaning cotton cloth. Coated cotton fabric with a heavy water drop displaying self-cleaning superhydrophobic surface. (b) Color water droplets on uncoated and coated cotton fabric before and after.

1.8.3.2   Photocatalytic self-cleaning textiles

After being stained with coffee, a cotton cloth coated with TiO_2 nanoparticles was UV-irradiated to test its photocatalytic efficiency (Figure 1.8). Photocatalysis degrades coffee stains by adsorbing the stain, absorbing light by the catalyst, and generating radicals through charge transfer reactions. Coffee stains textiles because of its water-

soluble and acidic chromophores, macromolecules, and colorants. Condensation reaction and heat degradation create coffee's oligomeric or polymeric chromophores. [51] Hydroxyl groups and conjugated double bonds in coffee stains on cotton fabric attract fibers by van der Waals or dispersion forces. Figure 1.8 shows dye stain photocatalysis.

Figure 1.8: Self-cleaning mechanism based on photocatalytic degradation of TiO_2 coated cotton.[51]

e_{CB}^- refers to electron conduction and h_{VB}^+ to hole valence. "*hv*" is the photon energy needed to excite a semiconductor electron from the valence band to the conduction band. Oxygen produces superoxide anion ($O_2^{\bullet-}$), and moisture (H_2O) converts hole (h^+) to hydroxyl radical ($OH^\bullet$). $O_2^{\bullet-}$ and H^+ become $HO_2^\bullet$ during conversion. Superoxide anion, hydroxyl radical, and perhydroxyl reduce stains. Organic molecules react with $OH^\bullet$ to create breakdown products. Organic compounds and h_{VB}^+ produce reduction products. TiO_2 at the nanoscale increases active sites, degrading coffee stains faster. The photocatalytic efficiency of TiO_2 coating depends on its phase, surface area, crystallinity, density of surface $OH^\bullet$ groups, and other characteristics.[52] High-crystallinity and anatase phases of TiO_2 exhibit excellent photocatalytic activity.[53]

1.8.3.3 Self-cleaning testing

Self-cleaning fabrics that utilize photocatalytic properties have the potential to undergo decontamination. The evaluation of textile photocatalysis is conducted through diverse techniques. The evaluation of photocatalytic efficiency involves the assessment of the degradation of model contaminants such as methylene blue or coffee and curry stain. Two different breakdown processes, solution discoloration and stain degradation, both are used

to address the photodegradation of the colorants.[54] In order to eliminate the dye stain, the fabric undergoes functionalization and subsequent dyeing and UV radiation. Following functionalization, the fabrics undergo a process of segmentation, where they are sectioned into smaller pieces and subjected to dyeing and UV radiation. The UV-Vis spectrophotometer is utilized to measure the absorbance of the dye solution.[55] Another technique is assessing the color strength (*K/S*) of the exposed and unexposed stained sample by a spectrophotometer. The *K/S* values of a given stain is used to evaluate the self-cleaning properties, where *K* is the absorption coefficient of the dye and *S* is the scattering coefficient.[56]

The formula for calculating the percentage decrease in *K/S* value is expressed as following equation (1.3):

$$\% \text{ Decrease in} \frac{K}{S} \text{value} = \frac{(\frac{K}{S})_{unexposed} - (\frac{K}{S})_{exposed}}{(\frac{K}{S})_{unexposed}} \times 100 \qquad (1.3)$$

The determination of *K/S* values is contingent upon the concentration of dye present on the fabric. The *K/S* value exhibits a decrease upon the disappearance of stains.[57] The assessment of self-cleaning fabrics can be performed through gas chromatography, which involves the quantification of highly oxidative intermediates formed on stained cotton textiles. According to Meilert et al., the presence of wine, coffee, and perspiration stains on treated materials results in the emission of CO_2. The evaluation of self-cleaning materials can be achieved by monitoring CO_2 emissions. The self-cleaning phenomenon is observed to be enhanced in the presence of CO_2.[58]

1.9 Current challenges and future scope

Nanotechnology has struggled to compete with existing technologies and goods, particularly in the textile industry. Nanotechnology and NPs may increase product costs. Nanomaterials at low concentrations can achieve bulk material characteristics or better. Thus, nanotechnology-enhanced multifunctional textiles can reduce production costs. Nanoengineered textiles have several benefits for society. However, global concern about their environmental and health implications is growing.[59] The textile and garment

industries account for 10% of global carbon emissions and 17-20% of industrial water pollution.[3] Additionally, high NPs concentrations can cause toxicity in creatures and harm the ecosystem. NPs' toxicity and leaching are ongoing environmental problems. Inhaling carbonaceous NPs can cause deadly illnesses. Textile producers must ensure that nanotechnology-based textile products, including manufacturing, use, and disposal, do not harm human health or the environment throughout their lifecycle. Thus, nanotechnology-based safety measures are essential.[59]

Most research and advancements in multifunctional textiles utilizing nanotechnology have been limited to laboratory settings, necessitating a transition to industrial-scale production. This undertaking presents a significant challenge for textile engineering and material science professionals. Despite the current challenges, scientists and researchers are eagerly exploring the potential of nanotechnology to create versatile textiles with multiple functions.

1.10   Conclusions

The durability and efficacy of various functional finishes on textile substrates are subject to significant challenges in traditional textile treatments. The field of nanotechnology has the potential to create fabrics that possess a multitude of desirable characteristics, such as self-cleaning capabilities, resistance to oil, water, and dirt, protection against UV radiation, antibacterial properties, durability against wear and tear, flame retardancy, wrinkle resistance, antistatic properties, and additional features. Implementing nano-finishing techniques has significantly improved textiles' function, comfort, and durability. Multifunctional fabrics treated with nanomaterials have been introduced into the commercial competitive market. The increasing demand for fashionable garments with advanced features has increased the multifunctional and intelligent fabrics market. Pursuing highly sophisticated, intelligent, and optimized multifunctional textiles could fuel the development of nano-enhanced textiles.

References:

(1)   Saleem, H.; Zaidi, S. J. Sustainable Use of Nanomaterials in Textiles and Their Environmental Impact. *Materials (Basel).* **2020**, *13* (22), 1–28. https://doi.org/10.3390/ma13225134.

(2)   Yang, M.; Liu, W.; Jiang, C.; Xie, Y.; Shi, H.; Zhang, F.; Wang, Z. Facile Construction of Robust Superhydrophobic Cotton Textiles for Effective UV Protection, Self-Cleaning and Oil-Water Separation. *Colloids Surfaces A Physicochem. Eng. Asp.* **2019**. https://doi.org/10.1016/j.colsurfa.2019.03.024.

(3)   Yetisen, A. K.; Qu, H.; Manbachi, A.; Butt, H.; Dokmeci, M. R.; Hinestroza, J. P.; Skorobogatiy, M.; Khademhosseini, A.; Yun, S. H. Nanotechnology in Textiles. *ACS Nano* **2016**, *10* (3), 3042–3068. https://doi.org/10.1021/acsnano.5b08176.

(4)   Nautiyal, A.; Shukla, S. R.; Prasad, V. ZnO-TiO2 Hybrid Nanocrystal-Loaded, Wash Durable, Multifunction Cotton Textiles. *Cellulose* **2022**. https://doi.org/10.1007/s10570-022-04595-6.

(5)   Taha, G. M.; Baseer, R. A.; Kassem, A. F.; Khalil, R. Designing of Semiconductive Cotton Fabrics Based on Poly (Propynyl Benzo Thiazolone) with UV Protection and Antibacterial Properties. *Mater. Sci. Eng. B Solid-State Mater. Adv. Technol.* **2022**. https://doi.org/10.1016/j.mseb.2022.115857.

(6)   Zhao, H.; Wang, S.; Zhou, M.; Cai, Z.; Zhao, Y. Self-Cleaning and Sun-Resistant Photocatalytic Polyester Fabrics Shielding with Fe–g–C3N4/TiO2 by Sol–Gel Method. *J. Mater. Sci. Mater. Electron.* **2022**. https://doi.org/10.1007/s10854-022-09178-6.

(7)   Goda, E. S.; Abu Elella, M. H.; Hong, S. E.; Pandit, B.; Yoon, K. R.; Gamal, H. Smart Flame Retardant Coating Containing Carboxymethyl Chitosan Nanoparticles Decorated Graphene for Obtaining Multifunctional Textiles. *Cellulose* **2021**, *28* (8), 5087–5105. https://doi.org/10.1007/s10570-021-03833-7.

(8)   Yang, J.; He, T.; Li, X.; Wang, R.; Wang, S.; Zhao, Y.; Wang, H. Rapid Dipping Preparation of Superhydrophobic TiO2 Cotton Fabric for Multifunctional Highly Efficient Oil-Water Separation and Photocatalytic Degradation. *Colloids Surfaces A Physicochem. Eng. Asp.* **2023**. https://doi.org/10.1016/j.colsurfa.2022.130590.

(9)   Gao, D.; Liu, J.; Lyu, L.; Li, Y.; Ma, J.; Baig, W. Construct the Multifunction of Cotton Fabric by Synergism between Nano ZnO and Ag. *Fibers Polym.* **2020**, *21* (3), 505–512. https://doi.org/10.1007/s12221-020-9347-4.

(10)   Gao, D.; Lyu, L.; Lyu, B.; Ma, J.; Yang, L.; Zhang, J. Multifunctional Cotton Fabric Loaded with Ce Doped ZnO Nanorods. *Mater. Res. Bull.* **2017**. https://doi.org/10.1016/j.materresbull.2017.01.030.

(11)   International organization for standardization, 2008. Technical specification: Nanotechnologies – Terminology and definitions for nano-objects – Nanoparticle, nanofiber and nanoplate, 2008, ISO/TS 80004-2.

(12)   Danks, A. E.; Hall, S. R.; Schnepp, Z. The Evolution of "sol-Gel" Chemistry as a Technique for Materials Synthesis. *Mater. Horizons* **2016**, *3* (2), 91–112. https://doi.org/10.1039/c5mh00260e.

(13) Tseng, T. K.; Lin, Y. S.; Chen, Y. J.; Chu, H. A Review of Photocatalysts Prepared by Sol-Gel Method for VOCs Removal. *Int. J. Mol. Sci.* **2010**, *11* (6), 2336–2361. https://doi.org/10.3390/ijms11062336.

(14) Znaidi, L. Sol-Gel-Deposited ZnO Thin Films: A Review. *Mater. Sci. Eng. B Solid-State Mater. Adv. Technol.* **2010**, *174* (1–3), 18–30. https://doi.org/10.1016/j.mseb.2010.07.001.

(15) De Coelho Escobar, C.; Dos Santos, J. H. Z. Effect of the Sol-Gel Route on the Textural Characteristics of Silica Imprinted with Rhodamine B. *J. Sep. Sci.* **2014**, *37* (7), 868–875. https://doi.org/10.1002/jssc.201301143.

(16) Parashar, M.; Shukla, V. K.; Singh, R. Metal Oxides Nanoparticles via Sol–Gel Method: A Review on Synthesis, Characterization and Applications. *J. Mater. Sci. Mater. Electron.* **2020**, *31* (5), 3729–3749. https://doi.org/10.1007/s10854-020-02994-8.

(17) Khashaei, M.; Kafi-Ahmadi, L.; Khademinia, S.; Poursattar Marjani, A.; Nozad, E. A Facile Hydrothermal Synthesis of High-Efficient NiO Nanocatalyst for Preparation of 3,4-Dihydropyrimidin-2(1H)-Ones. *Sci. Rep.* **2022**, *12* (1), 1–15. https://doi.org/10.1038/s41598-022-12589-4.

(18) Hayashi, H.; Hakuta, Y. Hydrothermal Synthesis of Metal Oxide Nanoparticles in Supercritical Water. **2010**, 3794–3817. https://doi.org/10.3390/ma3073794.

(19) Darr, J. A.; Zhang, J.; Makwana, N. M.; Weng, X. Continuous Hydrothermal Synthesis of Inorganic Nanoparticles: Applications and Future Directions. *Chem. Rev.* **2017**, *117* (17), 11125–11238. https://doi.org/10.1021/acs.chemrev.6b00417.

(20) Nadimpalli, N. K. V.; Bandyopadhyaya, R.; Runkana, V. Thermodynamic Analysis of Hydrothermal Synthesis of Nanoparticles. *Fluid Phase Equilib.* **2018**, *456*, 33–45. https://doi.org/10.1016/j.fluid.2017.10.002.

(21) Daou, T. J.; Pourroy, G.; Bégin-Colin, S.; Grenèche, J. M.; Ulhaq-Bouillet, C.; Legaré, P.; Bernhardt, P.; Leuvrey, C.; Rogez, G. Hydrothermal Synthesis of Monodisperse Magnetite Nanoparticles. *Chem. Mater.* **2006**, *18* (18), 4399–4404. https://doi.org/10.1021/cm060805r.

(22) Hazarika, D.; Kalita, N. K.; Kumar, A.; Katiyar, V. Crystalline Titanium-Dioxide Nanofinish Impregnated on Electrospun Stereocomplex Poly (Lactic Acid) as Non-Woven Nanotextile with Superhydrophilic, Anti-Shrinkage, Dark Dyeing and Waste Dye Removal Ability for Sustainable Application. *Int. J. Biol. Macromol.* **2022**, 219. https://doi.org/10.1016/j.ijbiomac.2022.07.093.

(23) Reddy, K. R.; Gomes, V. G.; Hassan, M. Carbon Functionalized TiO2nanofibers for High Efficiency Photocatalysis. *Mater. Res. Express* **2014**. https://doi.org/10.1088/2053-1591/1/1/015012.

(24) Chakraborty, J. N.; Mohapatra, M. R.; Kumar, J. Differential Functional Finishes for Textiles Using Graphene Oxide. *Res. J. Text. Appar.* **2018**, *22* (1), 77–91. https://doi.org/10.1108/RJTA-08-2017-0040.

(25) Joshi, M.; Butola, B. S. *Application Technologies for Coating, Lamination and Finishing of Technical Textiles*; 2013. https://doi.org/10.1533/9780857097613.2.355.

(26) Verbič, A.; Gorjanc, M.; Simončič, B. Zinc Oxide for Functional Textile Coatings: Recent Advances. *Coatings* **2019**, *9* (9), 17–23. https://doi.org/10.3390/coatings9090550.

(27) Gao, Y.; Cranston, R. Recent Advances in Antimicrobial Treatments of Textiles. *Text. Res. J.* **2008**, *78* (1), 60–72. https://doi.org/10.1177/0040517507082332.

(28) Sadu, R. B.; Chen, D. H.; Kucknoor, A. S.; Guo, Z.; Gomes, A. J. Silver-Doped TiO2/Polyurethane Nanocomposites for Antibacterial Textile Coating. *Bionanoscience* **2014**, *4* (2), 136–148. https://doi.org/10.1007/s12668-014-0125-x.

(29) Murugesh Babu, K.; Ravindra, K. B. Bioactive Antimicrobial Agents for Finishing of Textiles for Health Care Products. *J. Text. Inst.* **2015**, *106* (7), 706–717. https://doi.org/10.1080/00405000.2014.936670.

(30) Tanasa, F.; Teaca, C.; Nechifor, M.; Ignat, M.; Duceac, I. A.; Ignat, L. Highly Specialized Textiles with Antimicrobial Functionality — Advances and Challenges. **2023**, 219–245.

(31) Dastjerdi, R.; Montazer, M. A Review on the Application of Inorganic Nano-Structured Materials in the Modification of Textiles: Focus on Anti-Microbial Properties. *Colloids Surfaces B Biointerfaces* **2010**, *79* (1), 5–18. https://doi.org/10.1016/j.colsurfb.2010.03.029.

(32) Lemire, J. A.; Harrison, J. J.; Turner, R. J. Antimicrobial Activity of Metals: Mechanisms, Molecular Targets and Applications. *Nat. Rev. Microbiol.* **2013**, *11* (6), 371–384. https://doi.org/10.1038/nrmicro3028.

(33) Ye, Z.; Li, S.; Zhao, S.; Deng, L.; Zhang, J.; Dong, A. Textile Coatings Configured by Double-Nanoparticles to Optimally Couple Superhydrophobic and Antibacterial Properties. *Chem. Eng. J.* **2021**. https://doi.org/10.1016/j.cej.2020.127680.

(34) Choudhary, M. K.; Kataria, J.; Bhardwaj, V. K.; Sharma, S. Green Biomimetic Preparation of Efficient Ag-ZnO Heterojunctions with Excellent Photocatalytic Performance under Solar Light Irradiation: A Novel Biogenic-Deposition-Precipitation Approach. *Nanoscale Adv.* **2019**, *1* (3), 1035–1044. https://doi.org/10.1039/c8na00318a.

(35) El-Nahhal, I. M.; Salem, J.; Anbar, R.; Kodeh, F. S.; Elmanama, A. Preparation and Antimicrobial Activity of ZnO-NPs Coated Cotton/Starch and Their Functionalized ZnO-Ag/Cotton and Zn(II) Curcumin/Cotton Materials. *Sci. Rep.* **2020**, *10* (1), 1–10. https://doi.org/10.1038/s41598-020-61306-6.

(36) Chauhan, A.; Verma, R.; Kumari, S.; Sharma, A.; Shandilya, P.; Li, X.; Batoo, K. M.; Imran, A.; Kulshrestha, S.; Kumar, R. Photocatalytic Dye Degradation and Antimicrobial Activities of Pure and Ag-Doped ZnO Using Cannabis Sativa Leaf Extract. *Sci. Rep.* **2020**, *10* (1), 1–16. https://doi.org/10.1038/s41598-020-64419-0.

(37) Dhineshbabu, N. R.; Bose, S. UV Resistant and Fire Retardant Properties in Fabrics Coated with Polymer Based Nanocomposites Derived from Sustainable and Natural Resources for Protective Clothing Application. *Compos. Part B Eng.* **2019**, *172* (May), 555–563. https://doi.org/10.1016/j.compositesb.2019.05.013.

(38) Noorian, S. A.; Hemmatinejad, N.; Navarro, J. A. R. *Ligand Modified Cellulose Fabrics as Support of Zinc Oxide Nanoparticles for UV Protection and Antimicrobial Activities*; Elsevier LTD, 2020; Vol. 154. https://doi.org/10.1016/j.ijbiomac.2019.10.276.

(39) Sedighi, A.; Montazer, M.; Mazinani, S. Fabrication of Electrically Conductive Superparamagnetic Fabric with Microwave Attenuation, Antibacterial Properties and UV Protection Using PEDOT/Magnetite Nanoparticles. *Mater. Des.* **2018**, *160*, 34–47. https://doi.org/10.1016/j.matdes.2018.08.046.

(40) Grifoni, D.; Bacci, L.; Zipoli, G.; Albanese, L.; Sabatini, F. The Role of Natural Dyes in the UV Protection of Fabrics Made of Vegetable Fibres. *Dye. Pigment.* **2011**, *91* (3), 279–285. https://doi.org/10.1016/j.dyepig.2011.04.006.

(41) Campos Payá, J.; Díaz-García, P.; Montava, I.; Miró-Martínez, P.; Bonet, M. A New Development for Determining the Ultraviolet Protection Factor. *J. Ind. Text.* **2016**, *45* (6), 1571–1586. https://doi.org/10.1177/1528083714567238.

(42) Awad, A.; Abou-Kandil, A. I.; Elsabbagh, I.; Elfass, M.; Gaafar, M.; Mwafy, E. Polymer Nanocomposites Part 1: Structural Characterization of Zinc Oxide Nanoparticles Synthesized via Novel Calcination Method. *J. Thermoplast. Compos. Mater.* **2015**, *28* (9), 1343–1358. https://doi.org/10.1177/0892705714551241.

(43) Shahidi, S. Novel Method for Ultraviolet Protection and Flame Retardancy of Cotton Fabrics by Low-Temperature Plasma. *Cellulose* **2014**, *21* (1), 757–768. https://doi.org/10.1007/s10570-013-0127-9.

(44) Wilson, C. A.; Bevin, N. K.; Laing, R. M.; Niven, B. E. Solar Protection — Effect of Selected Fabric and Use Characteristics on Ultraviolet Transmission. *Text. Res. J.* **2008**, *78* (2), 95–104. https://doi.org/10.1177/0040517508089660.

(45) Zhang, M.; Feng, S.; Wang, L.; Zheng, Y. Lotus Effect in Wetting and Self-Cleaning. *Biotribology* **2016**, *5*, 31–43. https://doi.org/10.1016/j.biotri.2015.08.002.

(46) Pillai, O. M.; Sundaramoorthy, S. Development of Photocatalytic Self-Cleaning Textiles Using Tin Oxide and Titanium Dioxide Nanoparticles Mixture. *J. Text. Inst.* **2022**. https://doi.org/10.1080/00405000.2022.2062859.

(47) Ahmad, I.; Kan, C. W.; Yao, Z. Photoactive Cotton Fabric for UV Protection and Self-Cleaning. *RSC Adv.* **2019**, *9* (32), 18106–18114. https://doi.org/10.1039/c9ra02023c.

(48) Ghasemlou, M.; Daver, F.; Ivanova, E. P.; Adhikari, B. Bio-Inspired Sustainable and Durable Superhydrophobic Materials: From Nature to Market. *J. Mater. Chem. A* **2019**, *7* (28), 16643–16670. https://doi.org/10.1039/c9ta05185f.

(49) Adak, B.; Mukhopadhyay, S. All-Cellulose Composite Laminates with Low Moisture and Water Sensitivity. *Polymer (Guildf).* **2018**, *141*, 79–85. https://doi.org/10.1016/j.polymer.2018.02.065.

(50) Tudu, B. K.; Sinhamahapatra, A.; Kumar, A. Surface Modification of Cotton Fabric Using TiO2 Nanoparticles for Self-Cleaning, Oil-Water Separation, Antistain, Anti-Water Absorption, and Antibacterial Properties. *ACS Omega* **2020**, *5* (14), 7850–7860. https://doi.org/10.1021/acsomega.9b04067.

(51) Rashid, M. M.; Simončič, B.; Tomšič, B. Recent Advances in TiO2-Functionalized Textile Surfaces. *Surfaces and Interfaces* **2021**, *22*. https://doi.org/10.1016/j.surfin.2020.100890.

(52) Yang, M.; Liu, W.; Jiang, C.; Liu, C.; He, S.; Xie, Y.; Wang, Z. Robust Fabrication of Superhydrophobic and Photocatalytic Self-Cleaning Cotton Textile Based on TiO2 and Fluoroalkylsilane. *J. Mater. Sci.* **2019**. https://doi.org/10.1007/s10853-018-3001-1.

(53) Houas, A.; Lachheb, H.; Ksibi, M.; Elaloui, E.; Guillard, C.; Herrmann, J. Photocatalytic Degradation Pathway of Methylene Blue in Water. **2001**, *31*, 145–157.

(54) Shishoo, R. Recent Developments in Materials for Use in Protective Clothing. *Int. J. Cloth. Sci. Technol.* **2002**, *14* (3–4), 201–215. https://doi.org/10.1108/09556220210437167.

(55) PATRA, K. Application of Nanotechnology in Textile Engineering: An Overview. *J. Eng. Technol. Res.* **2013**, *5* (5), 104–111. https://doi.org/10.5897/jetr2013.0309.

(56) Yaghoubi, H.; Taghavinia, N.; Alamdari, E. K. Self Cleaning TiO2 Coating on Polycarbonate: Surface Treatment, Photocatalytic and Nanomechanical Properties. *Surf. Coatings Technol.* **2010**, *204* (9–10), 1562–1568. https://doi.org/10.1016/j.surfcoat.2009.09.085.

(57) Ashraf, M.; Champagne, P.; Perwuelz, A.; Campagne, C.; Leriche, A. Photocatalytic Solution Discoloration and Self-Cleaning by Polyester Fabric Functionalized with ZnO Nanorods. *J. Ind. Text.* **2015**, *44* (6), 884–898. https://doi.org/10.1177/1528083713519662.

(58) Meilert, K. T.; Laub, D.; Kiwi, J. Photocatalytic Self-Cleaning of Modified Cotton Textiles by TiO$_2$ Clusters Attached by Chemical Spacers. *J. Mol. Catal. A Chem.* **2005**, *237* (1–2), 101–108. https://doi.org/10.1016/j.molcata.2005.03.040.

(59) Rovira, J.; Domingo, J. L. Human Health Risks Due to Exposure to Inorganic and Organic Chemicals from Textiles: A Review. *Environ. Res.* **2019**, *168*, 62–69. https://doi.org/10.1016/j.envres.2018.09.027.

2. Functional Photocatalytic and Self-cleaning Finish Fabric with TiO₂ Nanoparticles

Abstract

Functional cotton fabric with good photocatalytic activity and excellent self-cleaning properties has been produced by titanium dioxide (TiO_2) nanoparticle deposits. In the first step, the TiO_2 NPs were synthesized by a sol-gel process. The physical characteristics, such as particle size and microstructure of TiO2 NPs, were analyzed using various techniques, including dynamic light scattering (DLS), Fourier transform infrared (FTIR) spectroscopy, UV-vis spectroscopy, X-ray diffraction (XRD), and transmission electron microscopy (TEM). The synthesized TiO2 NPs were coated onto cotton knit fabric using the pad-dry-cure technique, which made a transparent, thin film of nanocrystalline TiO_2 on the fiber surface with an acrylic binder. TiO_2 NPs coated fabric's surface morphology was analyzed by scanning electron microscopy (SEM). The photocatalytic efficacy of fabric coated with TiO_2 NPs was investigated through the degradation of methylene blue under UV radiation. The results indicate that 75% of the dye was degraded within five h, implying that utilizing TiO_2 NPs coated fabric may be a viable option for developing self-cleaning clothing. The self-cleaning properties were examined using coffee and curry stains as model dirt. After a 20 h exposure to xenon UV light, it was observed that cotton textiles coated with TiO_2 NPs could remove 58% of coffee stains and 76% of curry stains.

Keywords
Photocatalytic, self-cleaning, textiles, titanium dioxide nanoparticle

2.1 Introduction

Research associated with functional finishes like photocatalytic activity and self-cleaning finishes has accepted significant recognition within the scientific community because of their future applications in industry and daily life.[1,2] The textile industry is not only oriented towards the basic demands of comfort and fashion but also revolutionized by new approaches in nanotechnology that have an incredible impact on daily life.[3,4] Nanotechnology still stands plentiful inquiry and confrontation regarding industrial scale operation that would permit commercial production of nanofinishing products despite their

23

tremendous progress.[5,6] Nanomaterials are vital for their exceptional surface attributes in developing and manufacturing smart and multifunctional textiles, like anti-ageing properties, UV-protection, superhydrophobicity, fire-retardancy, antibacterial performance, and self-cleaning properties.[6,7] Both photocatalytic activity and self-cleaning finishes can be helpful in textile products that are threatened by exposing prolonged sunlight and staining with huge contaminants like soot, oils, lubricants, or those are sensitive to wash because of their size or water and detergent sensitivity (i.e., curtains, blinds, etc.).[8] This textile finish also shows vast potential for military/combat clothing as it is exposed to harsh weather for a prolonged time. Also, there are time constraints for laundering in extreme conditions and business life when clothes get stained accidentally. Recently, two central concepts have been applied to establish self-cleaning textiles.[7] One concept is physical self-cleaning, mainly built on the super hydrophobic approach where water droplets achieve a spherical shape and roll off the surface captivating the dirt particles (lotus effect).[9] Another concept is chemical self-cleaning, built on photocatalysis, where the dirt or stain molecules decompose into small species like CO_2 and water under exposure to sunlight.[10] Coating with nano polycrystalline semiconductor oxides such as titanium dioxide (TiO_2) has been successfully applied to develop several photocatalytic active self-cleaning textiles by decomposing organic dirt and stain. Moreover, TiO_2 nanoparticles have become an attractive high-efficiency catalyst because of their impressive properties like wide bandgap (~3.2 eV for anatase), non-toxicity, high availability, low cost, biocompatibility, stability, good thermal and optical properties, high refraction coefficient, absorption in the UV range and high photocatalytic activity.[11,12] In this regard, applying TiO_2 NPs in textile finishing has become an exciting research area as it introduces photocatalytic activity and self-cleaning effects to the textile substrate.[13] TiO_2 NPs also provide more efficiency due to their large surface area per unit mass and volume.[13,14] It is reported that the particle size, the phase, the crystallite size, and the morphology play vital roles in the photocatalytic activity and self-cleaning property of TiO_2, which are primarily dependent on the synthesis method, reaction condition, precursor, pH value, reaction temperature, time and additives, etc.[15,16] Several pieces of research have been reported that the anatase form has the highest photocatalytic activity among the other crystalline phases

of TiO$_2$.[17,18] On the other hand, natural fibers are plentifully available, biodegradable and renewable resources in comparison to synthetic fibers. Cotton is a cellulosic fiber composed of glucose with β-1,4-glucoside bonds and has more than ten thousand D-glucopyranose sections left out branching. Cotton textiles have more importance in daily life due to their superb physical and chemical properties like strength, elasticity, water affinity, moisture regain, air permeability, and low cost.[19]

Daoud and Xin established self-cleaning cotton by applying anatase nano TiO$_2$ crystallite onto cotton and wool fabric surface.[20,21] Self-cleaning properties of coated fabrics were investigated by fading coffee and red wine stains by UV irradiation.[22,23] The textile substrate has low thermal stability, requiring low-temperature synthesis and crystallization. Jung *et al.* have reported the preparation of anatase TiO$_2$ sol at 80 ℃ using nitric acid to peptize amorphous TiO$_2$ sol, but the acidic condition can decrease mechanical strength.[24] Xie *et al.* prepared neodymium-ion modified TiO$_2$ sol at 72 ℃ using the chemical co-precipitation-peptization method, which is unsuitable for industrial production due to its highly acidic condition.[25] Gole *et al.* and Mrowetz *et al.* have reported the preparation of TiO$_2$ sol by adding triethylamine as a surface-protecting agent and then characterizing TiO$_2$ particles and evaluating the photocatalytic activity.[26,27]

This study aims to develop a simple, low temperature, mild condition, and repeatable process of the TiO$_2$ nanophase to the cellulose fibers with improved photocatalytic activity and self-cleaning properties. Titanium (IV) butoxide is used as a precursor via the sol-gel process to produce a thin coating on a textile substrate using a mechanical, thermal fixation (dip-pad-dry-cure) process to make feasible photocatalytic activity and self-cleaning properties textiles for garment application.

2.2   Experimental

2.2.1   Materials

Titanium (IV) butoxide (Sigma- Aldrich), both acetic acid and hydrochloric acid (RCI Labscan Limited, Thailand), binder of aqueous acrylate dispersion (Forbind OB 45, Fortune Top Pte Ltd, New Taipei City, Taiwan) and softener (Nonionic surfactant, Forsoft NID, Taiwan) were used without further purification. De-ionized water (conductivity:

0.055 µScm^{-1}), collected from the HPLC quality water purification system (BOECO), was used for the sol-gel preparation. All lab work was done on single jersey cotton knit fabric scoured and bleached.

2.2.2 Synthesis of TiO$_2$ NPs by sol-gel method

This synthesis used 10 mL of de-ionized water to dissolve 0.2% HCl and 0.2% acetic acid. 3 mL of titanium (IV) butoxide was added dropwise to 7 mL of previously made solution at 60 ℃. After that, the mixture was rapidly stirred at 700 rpm for 48 h.

2.2.3 Preparation of TiO$_2$ NPs coated cotton fabric and TiO$_2$ powders

Previously synthesized TiO$_2$ NPs were diluted ten times using distilled water. Then 1% softener and 1% binder were added into the diluted TiO$_2$ NPs dispersion and applied on cotton fabric by a dip-pad-dry-cure method. At first, cotton fabric was dipped into TiO$_2$ NPs dispersion for 5 min under a magnetic stirrer to prevent precipitation of TiO$_2$ NPs. Padding was done by standard laboratory equipment with 2.5 m/min fabric speed and 2.8 kg/cm^2 padding pressure to maintain the wet pick-up% at about 75%. The pH value of the padding bath was maintained at about 5. The sample was dried at 80 ℃ for 5 min and cured (SDL mini-dryer steamer) at 145 ℃ for 2.5 min.

TiO$_2$ powder was extracted from the aforementioned made sol until precipitation occurred using enough 0.3% sodium carbonate aqueous solution. The liquid phase was removed from the generated suspensions by centrifuging them (Centrifuge Cencom II from J. P. Selecta, Spain) at 1000 rpm for 20 min. The sediments were cleaned three times with de-ionized water before being dried overnight at 100 ℃ in an oven and ground into powder.

2.2.4 **Characterization**

Average particle sizes and size distributions of the samples dispersed in water were measured using DLS measurements by a Malvern Zetasizer Nano ZS90 with a scattering angle of 90°. A He–Ne laser beam of 632.8 nm wavelength was used for the measurements. The average diameters were determined from cumulants mean of the intensity average of 50 runs using Stokes-Einstein equation, $d_H = k_B T / 3\pi\eta D_{ef}$, where d_H was the hydrodynamic diameter, k_B was the Boltzmann constant, T was the temperature, η was the solvent viscosity, and D_{ef} was the diffusion coefficient. The reproducibility was checked from at least three measurements. The sample temperature was controlled automatically within ±0.01 K by a built-in Peltier device.

FTIR spectrum was recorded by a Fourier transform spectrophotometer (Frontier, PerkinElmer) in transmittance mode for each KBr sample range between 400 and 4000 cm^{-1} at 4.0 cm^{-1} resolution. The crystallographic and phase identification properties were determined by an X-ray diffractometer (Philips PW 1724) with an X-ray generator using XDC-700 Guinier-Hagg focusing camera with monochromatized Cu Kα radiation (λ = 1.540598). According to Debye-Scherrer's equation, the crystallite diameters (D) were obtained from XRD peaks.

A double-beam UV–vis spectrophotometer (UVD-3500, LABOMED, INC, USA) recorded the UV- vis absorption spectrum, where cell length was 1 cm. Diffuse reflectance spectrum (DRS) was recorded using a double beam UV-vis spectrophotometer with an integrating sphere attachment DRA-CA-30I (Model: UV-1800, Shimadzu, Japan) to determine bandgap energy (E_g) of the solid NPs.

The surface morphology and structure of TiO_2 NPs were studied with tTEM, and the micrographs were attained using the LEO system (model 912 AB) at 120kV for samples. The morphological study used field emission scanning electron microscopy (FESEM) (ZEISS, Germany). The acceleration voltage of the electron gun was 20 kV with a probe current of 1.0 nA and magnifications ranging from 10,000 – 100,000. The images of samples were taken without sputtering and by mounting on the conducting carbon tape. The compositional study of the NPs is analyzed by EDX spectroscopy attached to the

FESEM. CImageJ 1.51k (Java 1.60-24 (64 bit), USA) was used to measure average particle size in both the TEM and the FESEM images of NPs. Thermal properties were studied under a nitrogen atmosphere by a Hitachi instrument (TG/ DTA 7200) in the 30–550 ℃ temperature at a heating rate of 20 ℃ min^{-1}. A double-beam Shimadzu UV–vis spectrophotometer (Model UV-1800) determined absorbance of methylene blue (MB) dye solution. Rectangular quartz cells of path length 1 cm were used throughout the investigation. The physical properties of the fabrics (weight, bursting strength, air permeability) were examined by ISO standards.

2.2.5 Photocatalytic activity of the coated fabric

The photocatalytic activity of the TiO$_2$ NPs coated cotton fabric was evaluated by analyzing the reduction in absorbance of MB after exposure to UV irradiation. 0.4 g of fabric was cut into small pieces (1 cm × 1 cm specimen). These pieces were placed in an 80 mL beaker containing 40 mL aqueous solution of MB dye (0.01 g/L), then exposed this beaker under UV irradiation by using a Philip UV lamp (365 nm, Philips TLD 18W/08) with 300 rpm shaking by magnetic stirrer (BOECO, Germany). After an interval of one h, one mL of the MB solution was removed, and its absorption spectra were measured using a double-beam Shimadzu UV-visible spectrophotometer (Model UVD-3500) at a wavelength of 664 nm.[28] The following formula (2.1) was used to calculate the rate of MB dye degradation:

$$\% \text{ Degradation} = \left[\frac{Ab_{s_0} - Ab_{s_t}}{Ab_{s_0}}\right] \times 100 \qquad (2.1)$$

Here Ab_{s_0} is the initial absorbance and Ab_{s_t} is an absorbance at 't' time.[29,30]

2.2.6 Whiteness test

The whiteness of control and TiO$_2$ NPs coated cotton were measured by Datacolor SF600 (Datacolor International, USA) with a D65 illuminant and 10° observer according to ISO 105-J02:1997 (Textiles-Tests for color fastness-Instrumental assessment of relative whiteness). The whiteness indexes (W_{10}) for the samples were calculated by using equation (2.2):

$$W_{10} = Y_{10} + 800(0.3138 - x_{10}) + 1700(0.3310 - y_{10}) \quad (2.2)$$

Where W_{10} is the whiteness value/index, Y_{10}, x_{10}, and y_{10} are the chromaticity coordinates of the sample, and 0.3138 and 0.3310 are the x_{10}, y_{10} chromaticity coordinates for the perfect diffuser.[31]

2.2.7 Evaluation of self-cleaning activity

The self-cleaning performance of the fabric was measured by the color strength change of coffee stain and curry stain on TiO_2 NPs coated fabric under UV irradiation. The coffee solution is produced by dissolving 0.6 g 100% pure soluble coffee powder (*Nestle*) in 50 mL hot water, and curry paste is produced by adding 0.5 g 100% curry powder (*Radhuni*) in 10 mL hot water. One drop of coffee solution and one drop of curry paste were dropped close on TiO_2 NPs coated fabric, allowed to spread and dried in the air, and then exposed to light irradiation. The irradiation of stained TiO_2 NPs coated fabric was carried out for 20 h in a light exposure and weathering test instrument (air-cooled xenon arc lamp, Xenotest Alpha LM, USA) by ISO 105 B02 test method. Half of each stain on the fabric was exposed to a Xenon arc lamp, while the other half was unexposed with a steel frame to prevent irradiation. The exposed part of the stain was compared with the unexposed part for self-cleaning action. The self-cleaning action was quantified by comparing the color strength (*K/S*) between the exposed part and the unexposed part of the same stain. The reflectance of the stained fabric was measured by the spectrophotometer (Datacolor SF600, Datacolor International, USA). The reflectance (R) was used to calculate the degradation rate as in the Kubelka-Munk equation (2.3):[32]

$$\frac{K}{S} = \frac{(1-R)^2}{2R} \quad (2.3)$$

K/S means color strength, and *K* and *S* are the absorptions and scattering coefficients. The *K/S* value of the unexposed part of the stain was taken as 100, and the relative reduction in the *K/S* value of the exposed part was calculated by using the below relation (2.4):[31]

$$\% \text{ Reduction in } \frac{K}{S} \text{ value} = \frac{\left(\frac{K}{S}\right)unexposed - \left(\frac{K}{S}\right)exposed}{\left(\frac{K}{S}\right)unexposed} \times 100 \quad (24)$$

2.3   Results and Discussion

2.3.1   Dynamic light scattering measurement

DLS engaged to determine the macromolecules and narrow particles in dilute suspension by coherent light sources based on the Brownian motion of the particles in an aqueous solution.[33] DLS assessment is done in the aqueous suspension of TiO_2 NPs to point out the size distribution in Figure 2.1. TiO_2 NPs display multiple sinusoidal peaks with very short particles of 1 nm hydrodynamic diameter (d_H), medium particles of 1 to 20 nm, and particles of d_H about 50-220 nm confess their presence. The peak maxima of intensity and narrow width near 1 and 10 nm demonstrate that higher no and minor ranges of hydrodynamic diameter of particles are present in that range. DLS expresses the particle size in solution form that can be swelled with time while measuring.[34] Additionally, DLS analysis signifies that the NPs formed had relatively well-defined dimensions.[28] Smaller the size of the NPs is, the higher the surface area is, which facilitates higher UV protection and self-cleaning activity.[35]
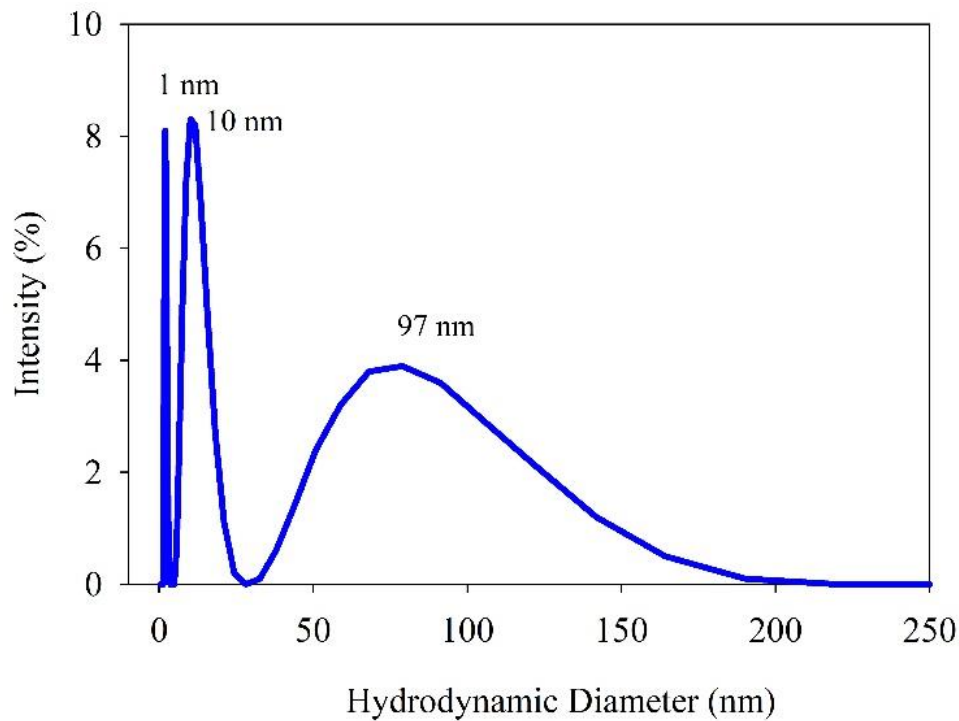
Figure 2.1: The average hydrodynamic diameter of TiO$_2$ NPs.

2.3.2 FTIR spectrophotometer measurement

FTIR spectrum of TiO$_2$ NPs is shown in Figure 2.2, where the band at around 3350 cm^{-1} is assigned to the stretching mode of water hydroxyl bonds.[36,37] The band near 3350 cm^{-1} is because of the stretching mode of the O-H bond due to free water, and the band near 1624 cm^{-1} is due to the vibration of the C=O bond due to acetic acid residue. Only one absorption peak is shown at 500-1000 cm^{-1} that is assigned for TiO$_2$ at 580 cm^{-1} corresponding Ti-O-Ti bond.[38,39]
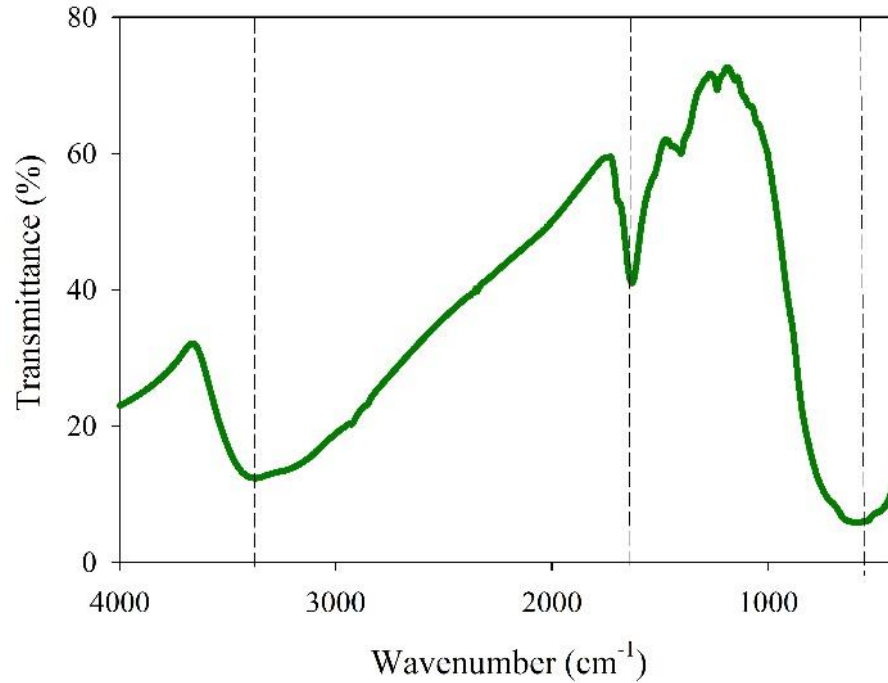
Figure 2.2: FTIR spectrum of TiO$_2$ NPs.

2.3.3 **X-ray diffraction**

XRD pattern was used to study the crystallographic structure and phase of pure TiO$_2$ nanopowders prepared by the sol-gel process, which is shown. (Figures 2.3 (a) and 2.3 (b)). The diffraction peaks of products can be indexed to the anatase form of TiO$_2$ NPs (JCPDS no. 96-900-8217; Joint Committee on Powder Diffraction Standards). The lattice parameters a, b, and c of the sample were calculated by using the following equations (2.5, 2.6).[40,41]

$$2d_{hkl}\sin\theta = n\lambda \qquad (2.5)$$

$$\frac{1}{d^2} = \frac{h^2 + k^2}{a^2} + \frac{l^2}{c^2} \qquad (2.6)$$

Where λ is the wavelength of the XRD, *n* is the order of diffraction (for first order *n* = 1), *d$_{hkl}$* is the interplanar spacing (d-spacing), and *hkl* is the Miller indices. The average lattice parameters for TiO$_2$ NPs were a = b = 3.7928 Å, c = 9.4753 Å. These values are close

enough to the JCPDS file no 96-900-8217 (a = b = 3.8040 Å, c = 9.6140 Å). The diffraction pattern of TiO$_2$ NPs is well indexed to anatase tetragonal structure with five sharp diffraction peaks (2θ) at 25.3º, 37.7º, 47.88º, 54.42º and 62.59º associated with the lattice planes designated by Miller indices (101), (104), (200), (105) and (204). Good crystallization is also exhibited from sharp diffraction peaks. The average crystallite diameter D was calculated from Debye-Scherrer's equation (2.7):

$$D = \frac{K\lambda}{\beta\cos\theta} \qquad (2.7)$$

Where D is the crystallite size, $K = 0.89$, λ = the wavelength of X-ray radiation (1.540598 Å), β = the full-width half maximum intensity (FWHM) of diffraction peak in radians, and θ = the Braggs diffraction angle.[13] Lattice stain was calculated by equation (2.8):

$$\eta = \frac{\beta}{\tan\theta} \qquad (2.8)$$

Where η = Lattice stain in the material, β = the full-width half maximum of diffraction peak, and θ = the Braggs diffraction angle. The dislocation density (δ), which represents the number of defects in the crystal, was calculated by using the Williamson-Hall equation (2.9):

$$\delta = \frac{1}{D^2} \qquad (2.9)$$

Where D is the crystallite size, the dislocation density is inversely proportional to D^2 where λ = the wavelength of X-ray radiation (1.5406 Å) and θ = the Braggs diffraction angle.[42] Crystallite size, lattice stain, dislocation density, lattice planes, and d-spacing values are listed in Table 2.1.
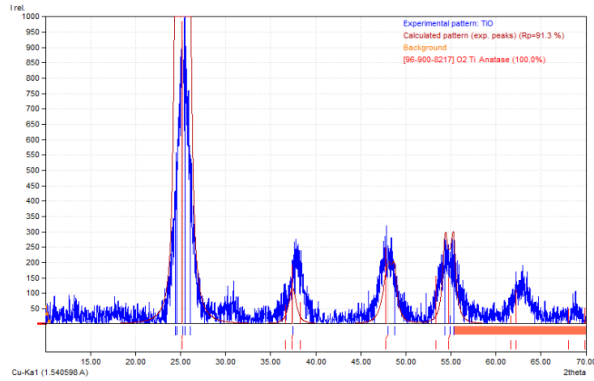
(a)   (b)
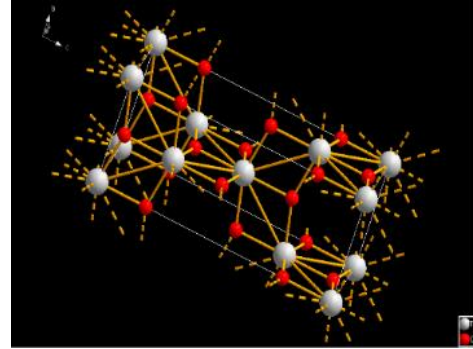
Figure 2.3: (a) XRD pattern of TiO_2 NPs and (b) crystal structure of anatase TiO_2 NPs.

Table 2.1: 2θ, crystallite size, lattice stain, dislocation density, *hkl,* d-spacing of TiO_2 NPs as presented in XRD patterns analysis

2θ (degree)	Full-width half maximum FWHM $[\beta]$	Crystallite size D (nm)	Lattice stain $\eta= \beta/tan\theta$	Dislocation density δ (nm^{-2})	*hkl*	d-spacing $d_{hkl} = \lambda/2sin\theta$
25.33	1.92	4.25	0.1489	0.0554	101	0.3513
37.95	1.88	4.47	0.0955	0.0501	004	0.2369
47.93	1.77	4.90	0.0696	0.0416	200	0.1896
54.65	2.17	4.11	0.0734	0.0591	105	0.1678
62.91	1.70	5.49	0.0484	0.0331	204	0.1476

2.3.4 **UV-vis absorption analysis**

The UV-vis absorption spectrum of TiO_2 NPs is expressed in Figure 4a, which displays an absorbance at 251 nm characteristic of TiO_2 NPs, leading to the absorption edge in the blue region. The band gap is determined by Tauc-equation (2.10):

$$\alpha h v = A(h v - E_g)^n \qquad (2.10)$$

Where α, v, A, and E_g are absorption coefficient, light frequency, a constant, and direct optical bandgap energy, respectively, and n = ½ (for direct transition mode material). The band gap can be measured by extrapolating the linear part of a plot of $(\alpha h v)^2$ versus photon energy $(h v)$ of the exciting light reported in Figure 2.4. The intersection of the tangent line with the x-axis provides a better resemblance of the band gap energy of TiO_2 NPs that have a direct band gap transition.[43]
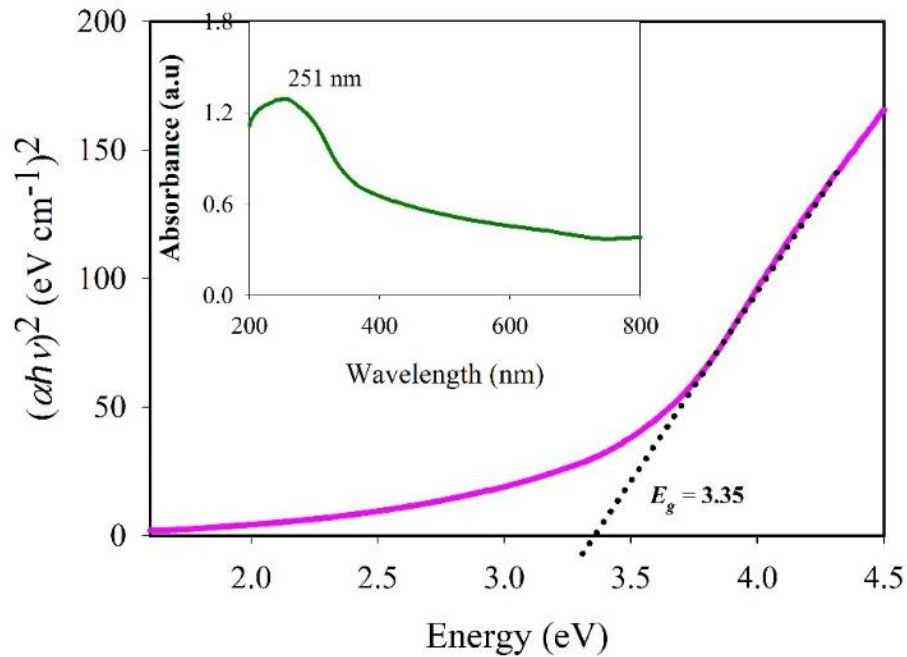
Figure 2.4: Tauc plot for band gap determination, the inset is UV-vis absorption spectrum of an aqueous dispersion of TiO_2 NPs.

2.3.5 Determination of optical band gap and the nature of optical charge carrier transitions

The optical band gap of TiO_2 is calculated by using the derivation of absorption spectrum fitting (DASF) method and is deduced as equations 2.11 and 2.12:[44]

$$\ln\left[\frac{f(R)}{\lambda}\right] + \ln s = \ln[B(hc)^{m-1}] + m\ln(\frac{1}{\lambda} - \frac{1}{\lambda_g}) \qquad (2.11)$$

Now,

$$\frac{d\{\ln\left[\frac{f(R)}{\lambda}\right]\}}{d(\frac{1}{\lambda})} = \frac{m}{\frac{1}{\lambda} - \frac{1}{\lambda_g}} \qquad (2.12)$$

As $f(R)$ is determined by using Kubelka–Munk method that is based on the following equation (2.13):[1]

Where R is the reflectance and $f(R)$ is proportional to the absorption coefficient (α).[45]

$$f(R) = \frac{(1-R)^2}{2R} \qquad (2.13)$$

Where λ is the wavelength, c is the velocity of light, λ_g is the wavelength corresponding to the optical band gap, B is a constant, and s is the scattering coefficient. $h\nu$ is the energy of photon energy, and E_g is the band gap energy of the sample. The optical band gap of the sample is calculated by the extrapolation of a linear portion in the plot $dln[\alpha(\lambda)\lambda^{-1}]/d\lambda^{-1}$ against $h\nu$ extended in Figure 2.5 . The calculated band gap of TiO_2 is 3.16 eV.
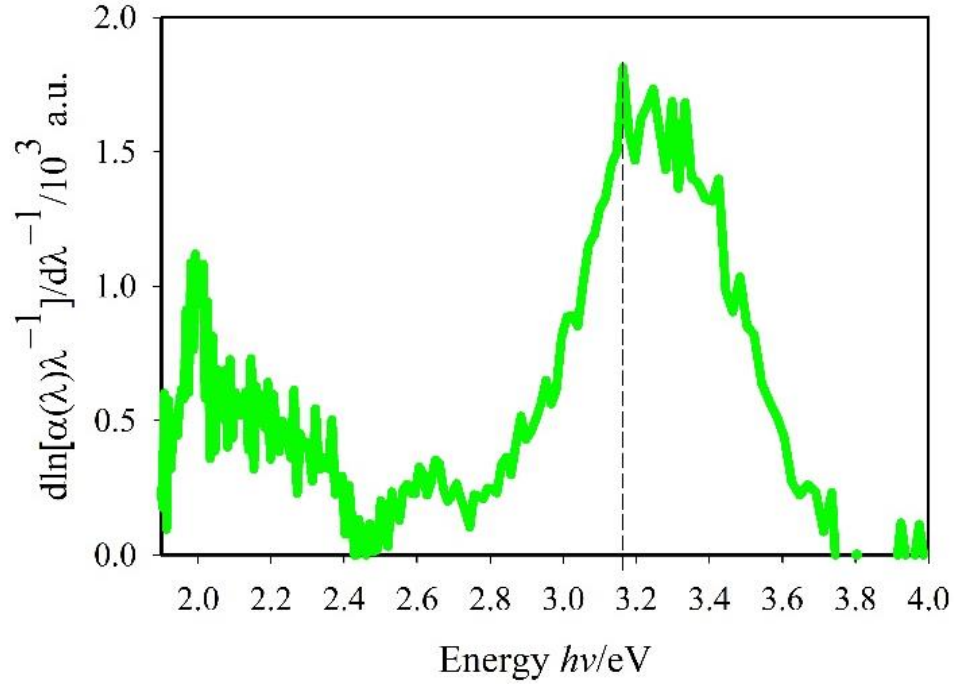
Figure 2.5: DASF method calculated for band gap by plotting of dln[α(λ)λ-1]/d λ-1 versus hv.

The corresponding coefficient (*m*) of the sample is calculated by the extrapolation of a linear portion in the plot of *ln[α(λ)λ⁻¹]* versus *ln[λ⁻¹ – λ_g⁻¹]* extended in Figure 2.6. The corresponding coefficient (*m*) associated with an electronic transition is calculated and found that *m* = 1/2 defines the direct allowed transition.
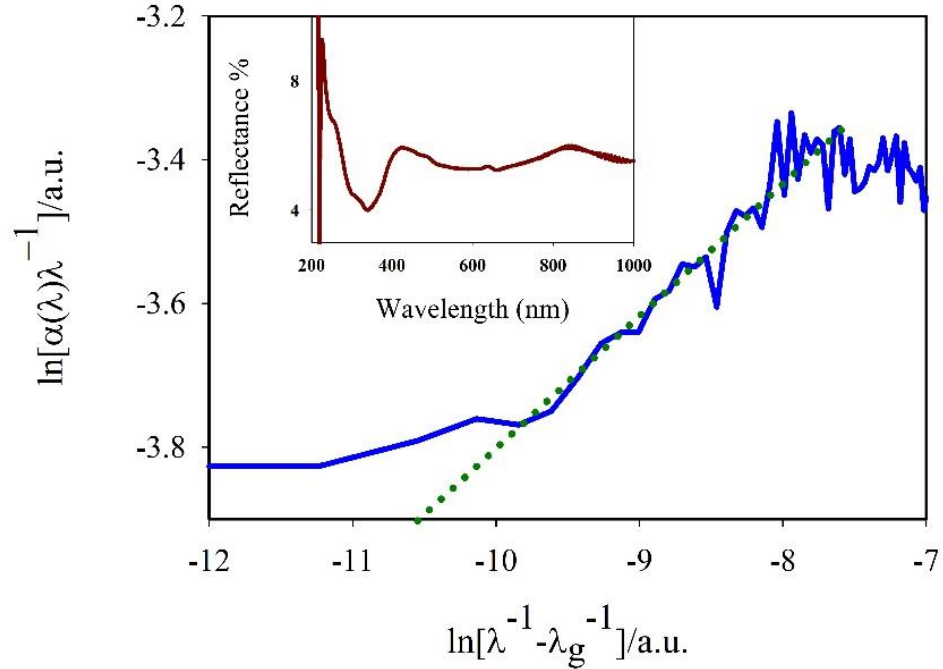
Figure 2.6: DASF method calculated for corresponding coefficient (m) by plotting ln[α(λ)λ-1] versus ln[λ-1 – λg-1], inset the reflectance spectra of TiO$_2$ NPs.

2.3.6 TEM analysis

Fig. 2.7 (a-b) shows TEM pictures of the TiO$_2$ NPs. TiO$_2$ NPs' form and size are revealed by TEM examination. The NPs are spherical in the TEM images. Nanocrystals with a spherical shape and restricted size distribution are created. It was unable to discern between these NPs.[63] Using image analysis software, the average particle size of these NPs is determined, and it is discovered that the TiO$_2$ NPs are agglomerated and have a size in the range of 20 to 60 nm that is shown in the histogram in Figure 2.7 (c) . Selected area diffraction pattern (SAED pattern) of TiO$_2$ NPs is shown in Figure 2.7 (d). The sharp diffraction rings show the polycrystalline structure with tiny grain sizes.[64] These agree with findings from the XRD pattern seen in Figure 2.3.
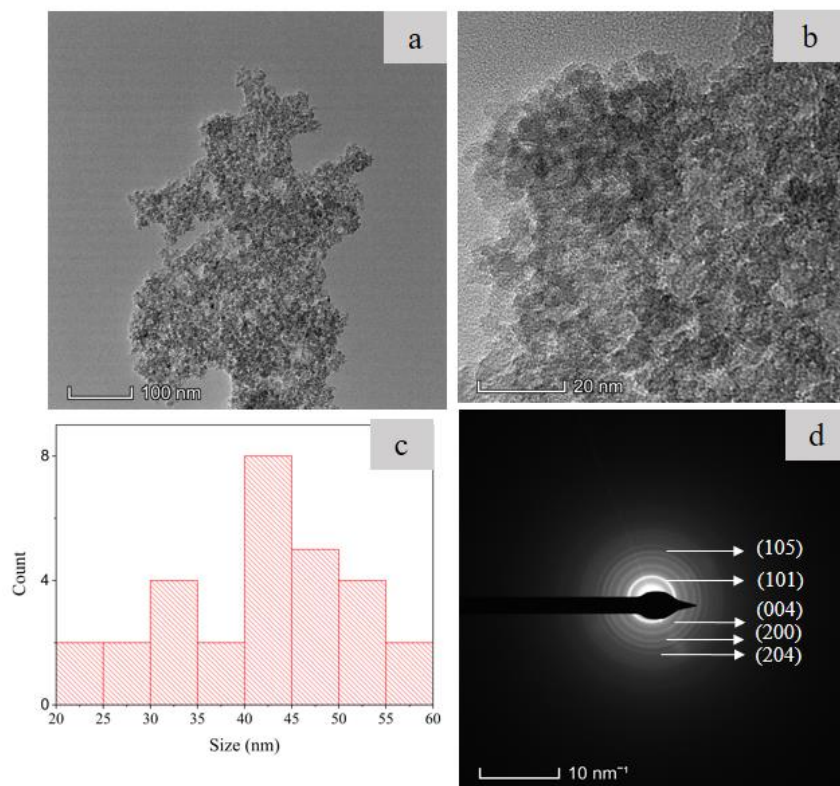
Figure 2.7: TEM images of (a, b) TiO$_2$ NPs with different magnifications, (c) histogram and (d) SAED pattern.

The diffraction ring pattern corresponds to the (101), (004), (200), (105), and (204) lattice planes of anatase TiO$_2$. As they demonstrate the deeply crystalline character, it is examined that these absolute circular rings are well coordinated with the XRD pattern of TiO$_2$ NPs.

2.3.7 Scanning electron microscopic analysis

The control cotton fiber surfaces were seen in the SEM images from Figure 2.8 (a-b) to comprise closely spaced, diagonal lines that entangle to form spiral fibrils with a twisted ribbon-like pattern. They had a clean, smooth surface, which showed that the pre-treatment procedure had removed any surface flaws. Clean surfaces are essential for a uniform distribution during the subsequent coating procedure. The surface of TiO$_2$ NPs coated fibers had slanted lines but weren't as visible as in Figures 2.8 (c-d). The grooves between the fibrils on the fiber surface were equally coated with TiO$_2$ NPs. Histograms (Figure 2.8 (e)) showed the particle size distributions of TiO$_2$ NPs within the 40 to 200 nm range. The

control cotton fabric displayed a clear surface with no accumulation of NPs.

On the other hand, NPs are homogeneously dispersed onto the coated fiber surface though some TiO_2 NPs clusters are found due to aggregation. The sizes of the TiO_2 NPs agglomerates on the coated fabric were less than 5 μm. Some hypotheses noticing these agglomerates could be NPs are sediment and remained at the vessel's bottom because of lack of stirring throughout the impregnation process, or nanoparticles are aggregated in aqueous solution due to their low dimension, or the surfactant that is used to make a relatively stable dispersion of TiO_2 NPs could hinder the adhesion of particles on the fabric surface. The wettability and absorption capacity of the fabric determines how many NPs are evenly distributed on the fiber surface, which in turn determines the quality of the coated fabric. According to reports, the EDX spectrum (Figure 2.8 (f)) identifies the components contained in the coated cotton. This spectrum demonstrated that the elements C, O, and Ti were on the surface.

(a)   (b)   (c)

(d)   (e)   (f)
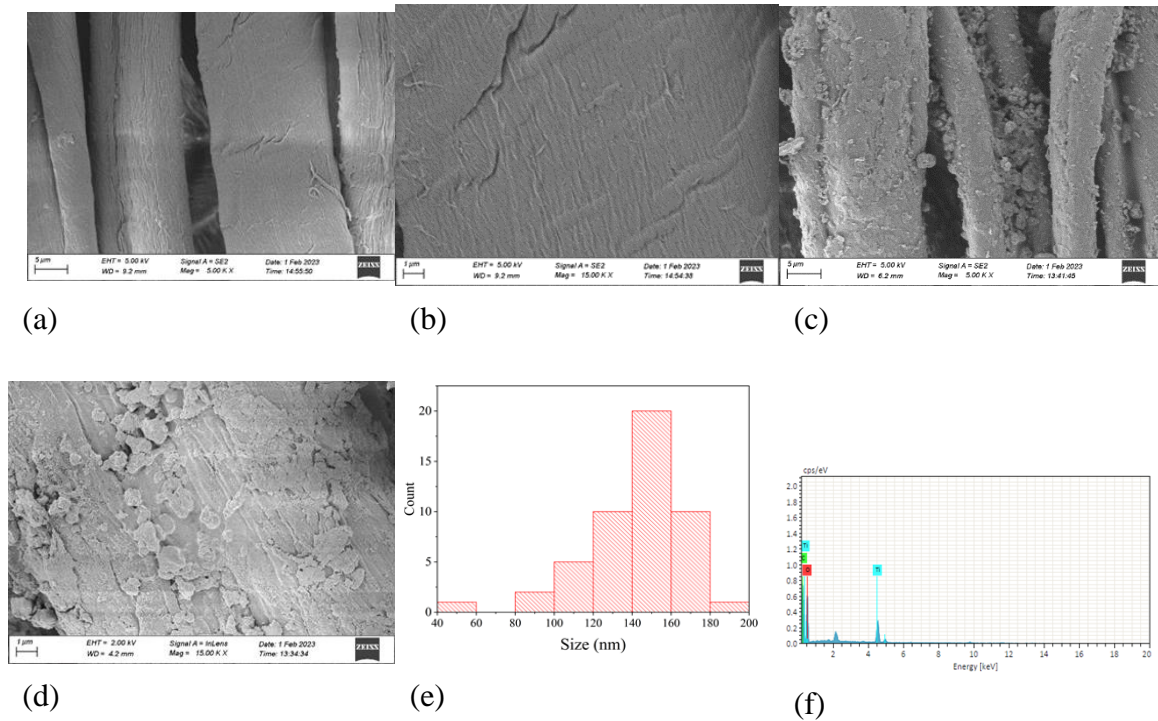
Figure 2.8: (a-b) SEM images of control fabric, (c-d) TiO_2 NPs coated fabric with different magnifications, (e) histogram of diameter size, (f) EDX spectrum of TiO_2 NPs coated cotton fabric.

2.3.8　**Thermogravimetric analysis**

The thermal behavior of TiO_2 NPs coated cotton fabric is examined from room temperature to 550 ℃ temperature range to investigate the effect of performed treatment on the cellulose pyrolysis process. TGA and DTA curves of control and coated cotton fabric with TiO_2 NPs are presented in Figure 2.8. Pyrolysis is a complex reaction in which various reactions such as endothermic, bond rupture, volatilization, and exothermic bond formation can coincide. The TGA thermogram shows the weight loss of fabrics in each pyrolysis stage though the DTA curve shows only the net change.[46] The control cotton fabric's TGA thermogram indicates three significant weight loss steps. In the first step, the TGA curve is linear because of the initial pyrolysis stage, where the damage of celluloses is done primarily on the amorphous region of the polymer. Some physical properties of the fabric can be changed by showing gradual weight loss (4.5%) up to around 254 ℃ due to the removal of absorbed and adsorbed water. In the second step, a massive slope in curves is seen due to the immense weight loss of the sample as cellulose pyrolysis occurred in the crystalline region of the polymer. A gradual weight loss line shows up to 320 ℃, and then drastic weight loss (around 83%) shows an endothermic peak up to 390 ℃ due to the formation of pyrolysis products like levoglucosan is produced.[47] In the third step, above 550 ℃, the residual weight (13%) finally curves, possibly due only to char/ash matter. On the other hand, TiO_2 NPs coated cotton fabric shows the same pattern of the endothermic peak in DTA curves except 320-360 ℃ showing slightly more thermal stability than the control c
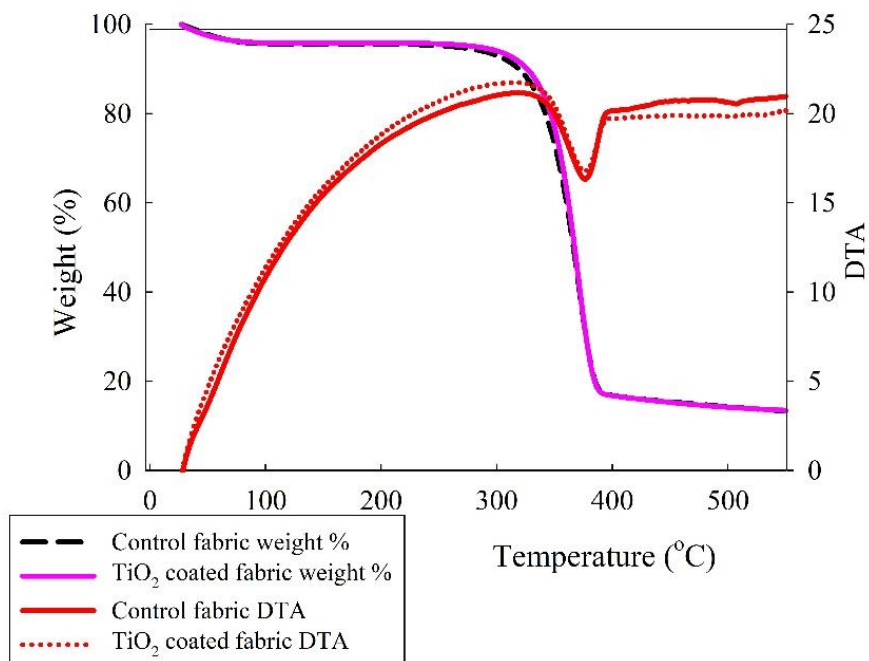
Figure 2.9: TGA and DTA analysis of control and coated cotton fabric with TiO_2 NPs.

2.3.9 Physical properties of coated fabric

All examined physical parameters revealed minor differences, as indicated in Table 2.2. The results demonstrated that the deposited TiO_2 NPs on the surface of the fabric resulted in weight loss and fabric density on the course and wales. The little drop in bursting strength may be caused by increased curing temperature, weight and fabric density decrease, or both. The deposition of TiO_2 NPs all over the surface may cause a decrease in air permeability since they increase the surface's cover factor.

Table 2.2: Physical properties of control and coated cotton fabrics parameters

Physical properties		Control fabric	Coated fabric	Standard
Weight (g/m^2)		147	142	ISO 12127:2003
Fabric density (number of yarns/10 cm)	Wales	161	158	ISO1049-2:2000
	Course	185	181	
Bursting strength (KPa)		180.5	177.8	ISO 13938-1:1999
Air permeability (cm^3 cm^{-2} s^{-1})		75.1	68.9	ISO 9237:1999

2.3.10 Photocatalytic activity of coated fabric

TiO_2 NPs can extortion solar energy to produce hydroxyl radicals for dye degradation due to their suitable band gap energy (3.16 eV from the DASF method). However, photocatalytic activity depends on the titanium phase, crystallinity, surface area, surface $OH^•$ group density, particle size, and morphology.[48] The UV-absorption spectra of methylene blue dye sol after immersion of the anatase-coated cotton under UV irradiation over time are shown in Figure 9. The shift in the absorption spectra of MB solution was evaluated through photocatalytic degradation analysis of the TiO_2 NPs coated cotton fabric immersed in MB sol under exposure to UV irradiation. Several researchers have examined the photocatalytic degradation of MB. It involves three steps; (a) adsorption of the dye, (b) adsorption of the light by the used catalyst, and (c) charge transfer reactions to generate necessary radicals for dye degradation.[49] The mechanism of photocatalytic degradation of MB dye is described below:

$$TiO_2 + h\nu(UV) \longrightarrow TiO_2(e_{CB}^- + h_{VB}^+)$$

$$TiO_2(h_{VB}^+) + H_2O \longrightarrow TiO_2 + H^+ + OH^•$$

$$TiO_2(e_{CB}^-) + O_2 \longrightarrow TiO_2 + O_2^•$$

$$O_2^• + H^+ \longrightarrow HO_2^•$$

$$Dye + OH^• \longrightarrow degradation\ products$$

$$Dye + h_{VB}^+ \longrightarrow reduction\ products$$
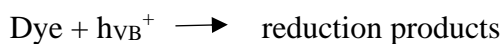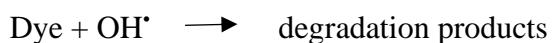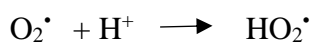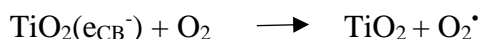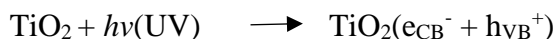
Here, photon energy *(hv)* is necessary to excite the semiconductor electron to travel to the conduction band (e_{CB}^-) from the valence band region (h_{VB}^+). Superoxide anion ($O_2^•$) is produced by oxygen. In contrast, the produced hole (h^+) is converted to hydroxyl radical ($OH^•$) by the moisture (H_2O) present in the air and superoxide anion ($O_2^•$) and hydrogen ion (H^+) are converted to perhydroxyl ion ($HO_2^•$).[50] All superoxide anion, hydroxyl radical, and perhydroxyl ions are responsible for the reduction in absorption peaks as these ions were assigned to split the aromatic ring of the MB dye molecules and initiate its

degradation by producing $C_8H_9NO_2$, C_9H_9NOS, and $C_7H_6N_2S$ intermediate product and finally producing single ring structure product by degraded to CO_2, H_2O, Cl^-, SO_4^{2-} and NO_3.[51] Moreover, nano TiO_2 provides a good no of active sites to enhance the degradation of MB as anatase has high crystallinity that shows better photocatalytic activity due to low disruption in its electronic band structure.[52,53]
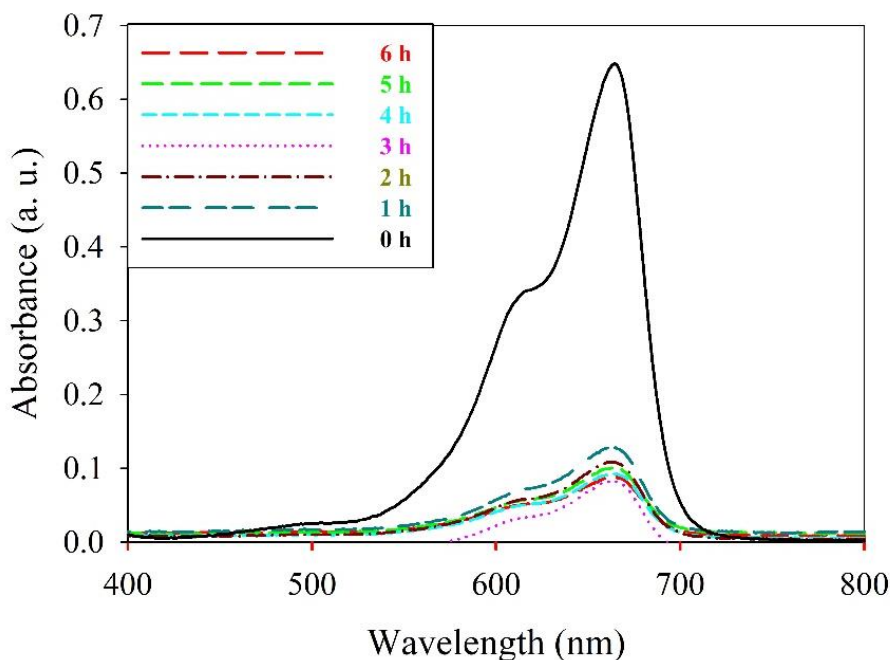
Figure 2.10: UV-vis absorption spectrum of MB dye using TiO2 NPs coated cotton under UV irradiation.

The reduction of absorbance for TiO_2 NPs coated cotton fabric, as shown in Figure 2.10, was measured by UV–vis spectrophotometer under one h interval. The maximum absorption peak of the MB dye solution was at 663 nm, which reduced slowly due to dye degradation and attained its lowest value at 5 h.
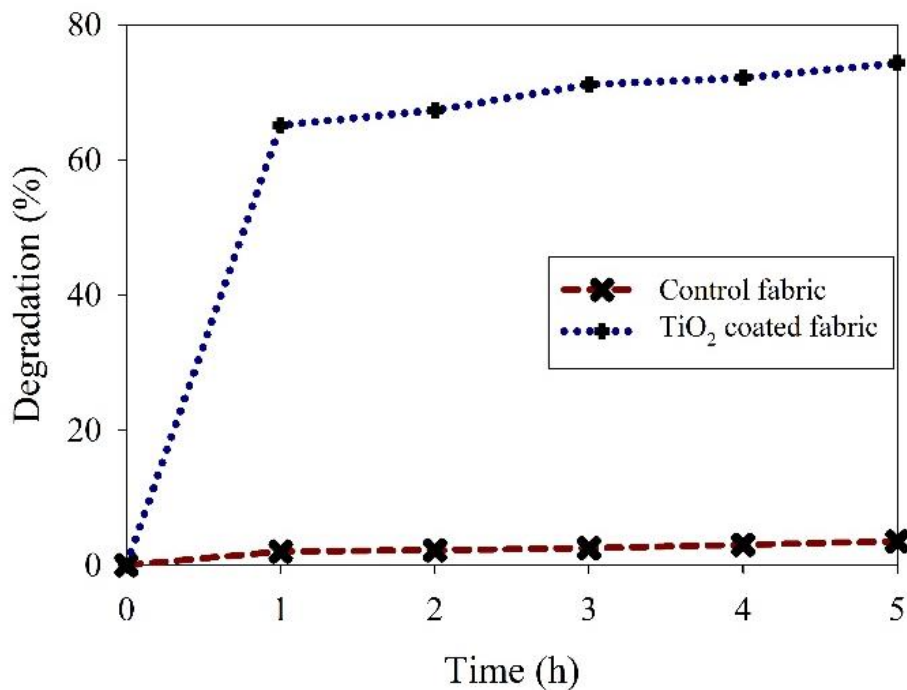
Figure 2.11: Dye degradation (%) of control and TiO$_2$ NPs coated cotton fabrics.

The dye degradation (%) of both control and TiO$_2$ NPs coated cotton fabrics are shown in Figure 2.11, where degradation (%) of coated fabric is drastically reduced to 75% compared with control one to 4%. However, dye degradation (%) of TiO$_2$ NPs coated cotton fabric doesn't change much regardless of more irradiation time (2-5 h).

2.3.11 Whiteness Test

The standard CIE whiteness of control cotton is 72.39, whereas TiO$_2$ NPs coated cotton fabric is 70.83. Though whiteness is slightly reduced after coating, it is acceptable as whiteness is more than 70 and expresses a good whiteness level.

2.3.12 The self-cleaning activity of coated fabric

Coffee is a complex mixture, and the main components in coffee are caffeine, 2-5%; acids, 7-17%; trigonelline, 1-2%; protein, 1-6%; sugar, 1-5%; polymeric carbohydrates, 30-50% and colored ingredients, 20-35% (Approximately). [54] Coffee stains on textiles are mainly caused by the water-soluble and acidic colored materials, pigments, and polymers in coffee. The colored substances in coffee are oligomeric or olymeric, formed by thermal

45

degradation and condensation reaction. Most colored substances and pigments in coffee contain hydroxyl groups and conjugated double bond that causes the attraction to fibers by van der Waals or dispersion forces, and these forces make the affinity of coffee stain to cotton fabric.[54] On the other hand, curry masala is a mixture of different ingredients such as turmeric, coriander seed, cumin, red chillies, black paper, salt, ginger, garlic, cloves, mustard, etc. Though the curry stain is produced by mixing this masala in hot water, the curry stain mainly shows the turmeric (Curcuma longa) stain on cotton. The yellow stain of curry stain on cotton fabrics is mainly because of the binding of the yellow pigments, which are most of the curcumin and its derivatives, with the cellulose of cotton. Curcumin is yellow with about 3-5% of turmeric constituents. Curcumin has two phenolic hydroxyl groups and two centrally located carbonyl groups, which can exist in solution keto-enol tautomers.[55,56] Curcumin molecule binding to TiO_2 NPs forming a 6-membered ring between Ti (IV) and β-diketo moiety. Figure 2.12 shows the *K/S* values of the coffee and the curry stains of (a) control and (b) coated fabric after 20 h irradiation.
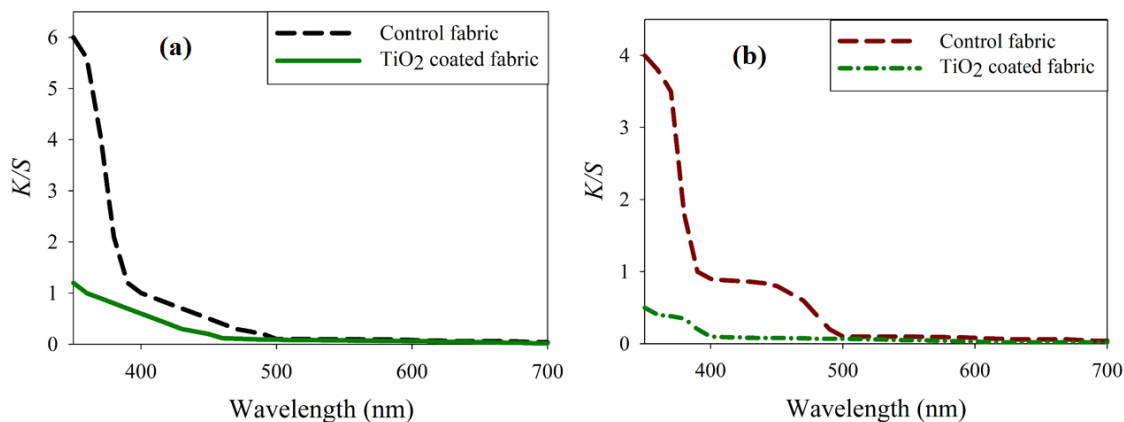
Figure 2.12: *K/S* values of the coffee and the curry stains of (a) control and (b) coated fabric after 20 h irradiation.

The *K/S* values (absorption and scattering coefficients; color strength) of exposed and unexposed parts of the samples were measured after 20 h irradiation. In Table 2.3, the percentage (%) decrease in *K/S* value for the exposed sample of the coffee stain is 58.28%, whereas, for the exposed sample of the curry stain is 75.9%.

Table 2.3: % of the decrease in *K/S* of TiO_2 NPs coated fabric

Types of stains	Unexposed Stain (*K/S*)	Exposed Stain (*K/S*)	% of the decrease in *K/S* value
Coffee stain	100	41.7	58.3%
Curry stain	100	24.1	75.9%

The colored substances (high molecular weight organic compound) of coffee and curry sensitize the stain discoloration on TiO_2 NPs coated cotton by the mechanism suggested in Figure2.12. When TiO_2 NPs are exposed to ultraviolet (UV) rays, photon energy is higher than the band gap of TiO_2 (3.2 eV). The electrons of TiO_2 will be excited and travel to the conduction band from the valence band, which produces two oppositely charged carriers, i.e., hole (h^+) and electron (e^-). The electron (e^-) is converted to superoxide anion ($^\bullet O_2^-$) by oxygen, whereas the produced hole (h^+) is converted to hydroxyl radical ($^\bullet OH$) by the moisture (H_2O) present in the air.
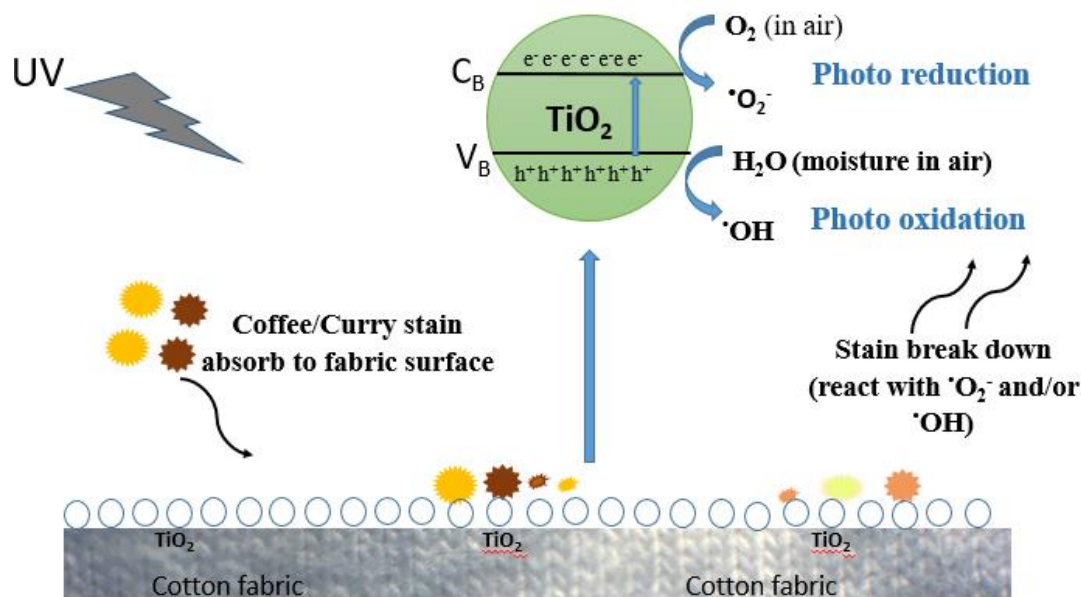
Figure 2.13: Schematic representation of ultraviolet photo excitation of TiO_2 NPs followed by the self-cleaning process.[24]

These superoxide anion and hydroxyl radicals are incredibly reactive particles that are responsible for redox reactions and the leading cause for the degradation of organic materials (coffee stain and curry stain) into small molecules (CO_2 and H_2O) by UV irradiation of the hydrated anatase TiO_2 NPs.[25] Summarized data of related NPs used for achieving self-cleaning performances are listed in Table 2.4.

Table 2.4: Summarized data of related NPs used for achieving self-cleaning performances

Types of NPs	Deposition process	Functionalized textile	Light irradiation	Self-cleaning property	Ref.
TiO_2	Pad-dry-cure	Woven fabric with 100% polyester, high-performance polyethylene: viscose blend, viscose: modacrylic blend	Visible light	Reduction in K/S value (%) is up to 54% for coffee stain after 24 h exposure	57
TiO_2	Functionalized - grafted	Cotton fabric	UV light (Philips 200W/m^2)	MB Stain removal ΔE is satisfactory after 24 h exposure	58
TiO_2	Functionalized	Cotton fabric	UV light irradiation for 65 h	A visually satisfactory Oleic acid color stain removed	59
TiO_2	Pad-dry-cure	Cotton fabric	Visible light	Reduction in K/S value (%) is up to 69% for coffee stain after 48 h exposure	60
Reactive blue 21+ TiO_2	Dip-pad-dry-cure	Cotton fabric	Visible light (45–95 mW cm^2)	Visually satisfactory removed	61
TiO_2	Dip-pad-dry-cure	Cotton fabric	UV light (1.2–1.3 mW cm^2)	Visually satisfactory removed coffee and wine stain	22
TiO_2-CNT	Dip-pad-dry-cure	Cotton and nylon fabric	Sunlight	Reduction in K/S value (%) is up to 36% for wine stain after 24 h exposure	62

TiO$_2$	Dip-pad-dry-cure	Cotton fabric	Xenon lamp	Reduction in K/S value (%) is up to 58% for coffee stain and 76% for curry stain after 20 h exposure.	Present study

2.4   Conclusions

Synthesis, characterization, and homogeneous application of TiO$_2$ NPs to the fabric surface could be successfully performed. By degrading methylene blue with UV light, the photocatalytic activity of fabrics coated with TiO$_2$ NPs was tested. In 5 hrs of UV exposure, 75% of the methylene blue dye was degraded. After 20 h of exposure to xenon UV radiation, TiO$_2$ NPs coated cotton textile can remove 58% of coffee stains and 76% of curry stains. Coated textiles have high photocatalytic activity and self-cleaning capabilities. This highly valuable multifunctional fabric has a variety of practical applications and follows new fashion trends. There are scopes for intriguing applications for this multifunctional fabric in the textile sector. This simple and repeatable technique can be applied with the TiO$_2$ nanophase to the cellulose fibers for improved photocatalytic activity and self-cleaning properties of the TiO$_2$ NPs coated fabrics to make feasible textiles and garment applications.

References:

(1) Esfandiari, A.; Firouzi-Pouyaei, E.; Aghaei-Meibodi, P. Effect of Enzymatic and Mechanical Treatment on Combined Desizing and Bio-Polishing of Cotton Fabrics. *J. Text. Inst.* **2014**, *105* (11), 1193–1202. https://doi.org/10.1080/00405000.2014.880222.

(2) Wang, J.; Zhao, J.; Sun, L.; Wang, X. A Review on the Application of Photocatalytic Materials on Textiles. *Text. Res. J.* **2015**, *85* (10), 1104–1118. https://doi.org/10.1177/0040517514559583.

(3) Gowri, S.; Almeida, L.; Amorim, T.; Carneiro, N.; Pedro Souto, A.; Fátima Esteves, M. Polymer Nanocomposites for Multifunctional Finishing of Textiles - a Review. *Text. Res. J.* **2010**, *80* (13), 1290–1306. https://doi.org/10.1177/0040517509357652.

(4) Czajkowski, W.; Paluszkiewicz, J.; Stolarski, R.; Kaźmierska, M.; Grzesiak, E. Synthesis of Reactive UV Absorbers, Derivatives of Monochlorotriazine, for Improvement in Protecting Properties of Cellulose Fabrics. *Dye. Pigment.* **2006**, *71* (3), 224–230. https://doi.org/10.1016/j.dyepig.2005.07.004.

(5) Gugliuzza, A.; Drioli, E. A Review on Membrane Engineering for Innovation in Wearable Fabrics and Protective Textiles. *J. Memb. Sci.* **2013**, *446*, 350–375. https://doi.org/10.1016/j.memsci.2013.07.014.

(6) Xu, L.; Zheng, G.; Wu, H.; Wang, J.; Gu, F.; Su, J.; Xian, F.; Liu, Z. Strong Ultraviolet and Violet Emissions from ZnO/TiO2 Multilayer Thin Films. *Opt. Mater. (Amst).* **2013**, *35* (8), 1582–1586. https://doi.org/10.1016/j.optmat.2013.04.001.

(7) Stan, M. S.; Nica, I. C.; Popa, M.; Chifiriuc, M. C.; Iordache, O.; Dumitrescu, I.; Diamandescu, L.; Dinischiotu, A. Reduced Graphene Oxide/TiO$_2$ Nanocomposites Coating of Cotton Fabrics with Antibacterial and Self-Cleaning Properties. *J. Ind. Text.* **2019**, *49* (3), 277–293. https://doi.org/10.1177/1528083718779447.

(8) Sobczyk-Guzenda, A.; Szymanowski, H.; Jakubowski, W.; Błasińska, A.; Kowalski, J.; Gazicki-Lipman, M. Morphology, Photocleaning and Water Wetting Properties of Cotton Fabrics, Modified with Titanium Dioxide Coatings Synthesized with Plasma Enhanced Chemical Vapor Deposition Technique. *Surf. Coatings Technol.* **2013**, *217*, 51–57. https://doi.org/10.1016/j.surfcoat.2012.11.071.

(9) Li, S.; Huang, J.; Ge, M.; Cao, C.; Deng, S.; Zhang, S.; Chen, G.; Zhang, K.; Al-Deyab, S. S.; Lai, Y. Robust Flower-Like TiO$_2$@Cotton Fabrics with Special Wettability for Effective Self-Cleaning and Versatile Oil/Water Separation. *Adv. Mater. Interfaces* **2015**, *2* (14), 1–11. https://doi.org/10.1002/admi.201500220.

(10) Du, Z.; Cheng, C.; Tan, L.; Lan, J.; Jiang, S.; Zhao, L.; Guo, R. Enhanced Photocatalytic Activity of Bi_2WO_6 /TiO_2 Composite Coated Polyester Fabric under Visible Light Irradiation. *Appl. Surf. Sci.* **2018**, *435*, 626–634. https://doi.org/10.1016/j.apsusc.2017.11.136.

(11) Afzal, S.; Daoud, W. A.; Langford, S. J. Superhydrophobic and Photocatalytic Self-Cleaning Cotton. *J. Mater. Chem. A* **2014**, *2* (42), 18005–18011. https://doi.org/10.1039/c4ta02764g.

(12) Zhang, H.; Chen, G.; Bahnemann, D. W. Photoelectrocatalytic Materials for Environmental Applications. *J. Mater. Chem.* **2009**, *19* (29), 5089–5121. https://doi.org/10.1039/b821991e.

(13) Ojstršek, A.; Kleinschek, K. S.; Fakin, D. Characterization of Nano-Sized TiO_2 Suspensions for Functional Modification of Polyester Fabric. *Surf. Coatings Technol.* **2013**, *226*, 68–74. https://doi.org/10.1016/j.surfcoat.2013.03.037.

(14) Zhang, H.; Zhu, H.; Sun, R. Fabrication of Photocatalytic TiO_2 Nanoparticle Film on PET Fabric by Hydrothermal Method. *Text. Res. J.* **2012**, *82* (8), 747–754. https://doi.org/10.1177/0040517511424526.

(15) Ge, S.; Wang, B.; Li, D.; Fa, W.; Yang, Z.; Yang, Z.; Jia, G.; Zheng, Z. Surface Controlled Photocatalytic Degradation of RhB over Flower-like Rutile TiO_2 Superstructures. *Appl. Surf. Sci.* **2014**, *295*, 123–129. https://doi.org/10.1016/j.apsusc.2014.01.015.

(16) Yuenyongsuwan, J.; Nithiyakorn, N.; Sabkird, P.; O'Rear, E. A.; Pongprayoon, T. Surfactant Effect on Phase-Controlled Synthesis and Photocatalyst Property of TiO_2 Nanoparticles. *Mater. Chem. Phys.* **2018**, *214*, 330–336. https://doi.org/10.1016/j.matchemphys.2018.04.111.

(17) Sandell, A.; Andersson, M. P.; Johansson, M. K. J.; Karlsson, P. G.; Alfredsson, Y.; Schnadt, J.; Siegbahn, H.; Uvdal, P. Metalorganic Chemical Vapor Deposition of Anatase Titanium Dioxide on Si: Modifying the Interface by Pre-Oxidation. *Surf. Sci.* **2003**, *530* (1–2), 63–70. https://doi.org/10.1016/S0039-6028(03)00386-8.

(18) Li, W. Di; Gao, J.; Wang, L. Enhancement of Durable Photocatalytic Properties of Cotton/Polyester Fabrics Using TiO2/SiO2 via One Step Sonosynthesis. *J. Ind. Text.* **2017**, *46* (8), 1633–1655. https://doi.org/10.1177/1528083716629138.

(19) Pinho, E.; Henriques, M.; Oliveira, R.; Dias, A.; Soares, G. Development of Biofunctional Textiles by the Application of Resveratrol to Cotton, Bamboo, and Silk. *Fibers Polym.* **2010**, *11* (2), 271–276. https://doi.org/10.1007/s12221-010-0271-x.

(20)   Daoud, W. A.; Xin, J. H. Nucleation and Growth of Anatase Crystallites on Cotton Fabrics at Low Temperatures. *J. Am. Ceram. Soc.* **2004**, *87* (5), 953–955. https://doi.org/10.1111/j.1551-2916.2004.00953.x.

(21)   Daoud, W. A.; Leung, S. K.; Tung, W. S.; Xin, J. H.; Cheuk, K.; Qi, K. Self-Cleaning Keratins. *Chem. Mater.* **2008**, *20* (4), 1242–1244. https://doi.org/10.1021/cm702661k.

(22)   Qi, K.; Daoud, W. A.; Xin, J. H.; Mak, C. L.; Tang, W.; Cheung, W. P. Self-Cleaning Cotton. *J. Mater. Chem.* **2006**, *16* (47), 4567–4574. https://doi.org/10.1039/b610861j.

(23)   Tung, W. S.; Daoud, W. A. Photocatalytic Self-Cleaning Keratins: A Feasibility Study. *Acta Biomater.* **2009**, *5* (1), 50–56. https://doi.org/10.1016/j.actbio.2008.08.009.

(24)   Jung, H. S.; Shin, H.; Kim, J. R.; Kim, J. Y.; Hong, K. S.; Lee, J. K. In Situ Observation of the Stability of Anatase Nanoparticles and Their Transformation to Rutile in an Acidic Solution. *Langmuir* **2004**, *20* (26), 11732–11737. https://doi.org/10.1021/la048425c.

(25)   Xie, Y.; Yuan, C.; Li, X. Photocatalytic Degradation of X-3B Dye by Visible Light Using Lanthanide Ion Modified Titanium Dioxide Hydrosol System. *Colloids Surfaces A Physicochem. Eng. Asp.* **2005**, *252* (1), 87–94. https://doi.org/10.1016/j.colsurfa.2004.10.061.

(26)   Gole, J. L.; Stout, J. D.; Burda, C.; Lou, Y.; Chen, X. Highly Efficient Formation of Visible Light Tunable TiO_2-xNx Photocatalysts and Their Transformation at the Nanoscale. *J. Phys. Chem. B* **2004**, *108*(4), 1230-1240. https://doi.org/10.1021/jp030843n.

(27)   Mrowetz, M.; Balcerski, W.; Colussi, A. J.; Hoffmann, M. R. Oxidative Power of Nitrogen-Doped TiO_2 Photocatalysts under Visible Illumination. *J. Phys. Chem. B* **2004**, *108* (45), 17269–17273. https://doi.org/10.1021/jp0467090.

(28)   Ashraf, M.; Champagne, P.; Perwuelz, A.; Campagne, C.; Leriche, A. Photocatalytic Solution Discoloration and Self-Cleaning by Polyester Fabric Functionalized with ZnO Nanorods. *J. Ind. Text.* **2015**, *44* (6), 884–898. https://doi.org/10.1177/1528083713519662.

(29)   Zare, M.; Namratha, K.; Alghamdi, S.; Mohammad, Y. H. E.; Hezam, A.; Zare, M.; Drmosh, Q. A.; Byrappa, K.; Chandrashekar, B. N.; Ramakrishna, S.; Zhang, X. Novel Green Biomimetic Approach for Synthesis of ZnO-Ag Nanocomposite; Antimicrobial Activity against Food-Borne Pathogen, Biocompatibility and Solar Photocatalysis. *Sci. Rep.* **2019**, *9* (1), 1–15. https://doi.org/10.1038/s41598-019-44309-w.

(30)   Diacon, A.; Mocanu, A.; Răducanu, C. E.; Busuioc, C.; Șomoghi, R.; Tricǎ, B.; Dinescu, A.; Rusen, E. New Carbon/ZnO/Li$_2$O Nanocomposites with Enhanced Photocatalytic Activity. *Sci. Rep.* **2019**, *9* (1), 1–14. https://doi.org/10.1038/s41598-019-53335-7.

(31)   Lessan, F.; Montazer, M.; Moghadam, M. B. A Novel Durable Flame-Retardant Cotton Fabric Using Sodium Hypophosphite, Nano TiO$_2$ and Maleic Acid. *Thermochim. Acta* **2011**, *520* (1–2), 48–54. https://doi.org/10.1016/j.tca.2011.03.012.

(32)   Gupta, K. K.; Jassal, M.; Agrawal, A. K. Functional Finishing of Cotton Using Titanium Dioxide and Zinc Oxide Nanoparticles. *Res. J. Text. Appar.* **2007**, *11* (3), 1–10. https://doi.org/10.1108/RJTA-11-03-2007-B001.

(33)   Xu, R. Progress in Nanoparticles Characterization: Sizing and Zeta Potential Measurement. *Particuology* **2008**, *6* (2), 112–115. https://doi.org/10.1016/j.partic.2007.12.002.

(34)   Domingos, R. F.; B.; Ju-Nam, M. A.; Reid, Y.; Tufenkji, M. M.; Lead, N.; Leppard, J. R.; Wilkinson, G. G.;; J., K. Characterizing Manufactured Nanoparticles in the Environment: Multimethod Determination of Particle Sizes. *Env. Sci Technol* **2009**, *43*(19), 7277−7284. https://doi.org/10.1021/es900249m.

(35)   Paul, R.; Bautista, L.; de la Varga, M.; Botet, J. M.; Casals, E.; Puntes, V.; Marsal, F. Nano-Cotton Fabrics with High Ultraviolet Protection. *Text. Res. J.* **2010**, *80* (5), 454–462. https://doi.org/10.1177/0040517509342316.

(36)   Ni, W.; Wu, S.; Ren, Q. Silanized TiO2 Nanoparticles and Their Application in Toner as Charge Control Agents: Preparation and Characterization. *Chem. Eng. J.* **2013**, *214*, 272–277. https://doi.org/10.1016/j.cej.2012.09.125.

(37)   Wang, L.; Ding, Y.; Shen, Y.; Cai, Z.; Zhang, H.; Xu, L. Study on Properties of Modified Nano-TiO$_2$ and Its Application on Antibacterial Finishing of Textiles. *J. Ind. Text.* **2014**, *44* (3), 351–372. https://doi.org/10.1177/1528083713487758.

(38)   Wang, Y. M.; Liu, S. W.; Xiu, Z.; Jiao, X. B.; Cui, X. P.; Pan, J. Preparation and Photocatalytic Properties of Silica Gel-Supported TiO 2. *Mater. Lett.* **2006**, *60* (7), 974–978. https://doi.org/10.1016/j.matlet.2005.10.061.

(39)   Akhavan Sadr, F.; Montazer, M. In Situ Sonosynthesis of Nano TiO2 on Cotton Fabric. *Ultrason. Sonochem.* **2014**, *21* (2), 681–691. https://doi.org/10.1016/j.ultsonch.2013.09.018.

(40)   Seid, E. T.; Dejene, F. B. Co-Solvent Medium Volume Ratio Effect on the Properties of Re Fl Uxed Sol-Gel Synthesized ZnO Nanopowder. *J. Alloys Compd.* **2019**, *787*, 658–665. https://doi.org/10.1016/j.jallcom.2019.02.163.

(41) Thamri, S.; Sta, I.; Jlassi, M.; Hajji, M.; Ezzaouia, H. Fabrication of ZnO-NiO Nanocomposite Thin Fi Lms and Experimental Study of the e Ff Ect of the NiO, ZnO Concentration on Its Physical Properties. *Mater. Sci. Semicond. Process.* **2017**, *71* (April), 310–320. https://doi.org/10.1016/j.mssp.2017.08.017.

(42) Kumar, N. S.; Ganapathy, M.; Sharmila, S.; Shankar, M.; Vimalan, M.; Potheher, I. V. *ZnO/Ni(OH)$_2$ Core-Shell Nanoparticles: Synthesis, Optical, Electrical and Photoacoustic Property Analysis. J. Alloys Compd.* **2017**, *703*, 624-632. https://doi.org/10.1016/j.jallcom.2017.01.323.

(43) Azeez, F.; Al-Hetlani, E.; Arafa, M.; Abdelmonem, Y.; Nazeer, A. A.; Amin, M. O.; Madkour, M. The Effect of Surface Charge on Photocatalytic Degradation of Methylene Blue Dye Using Chargeable Titania Nanoparticles. *Sci. Rep.* **2018**, *8* (1), 1–9. https://doi.org/10.1038/s41598-018-25673-5.

(44) Tauc, J.; Grigorovici, R.; Vancu, A. Optical Properties and Electronic Structure of Amorphous Germanium. *Phys. Stat. Sol.* (b). **1966**, *15*(2), 627–637. https://doi.org/10.1002/pssb.19660150224.

(45) Joseph, D. P.; Venkateswaran, C. Bandgap Engineering in ZnO By Doping with 3d Transition Metal Ions. **2011**, *2011*. https://doi.org/10.1155/2011/270540.

(46) Perkins, R.; Drake, G. L.; Reeves, W. A. DTA and TGA Studies of Flame-Resistant Fabrics. *J. Appl. Polym. Sci.* **1966**, *10*, 1041–1066. https://doi.org/10.1002/app.1966.070100708.

(47) Lessan, F.; Montazer, M.; Moghadam, M. B. Thermochimica Acta A Novel Durable Flame-Retardant Cotton Fabric Using Sodium Hypophosphite, Nano TiO$_2$ and Maleic Acid. *Thermochim. Acta* **2011**, *520* (1–2), 48–54. https://doi.org/10.1016/j.tca.2011.03.012.

(48) Blanco, E.; González-Leal, J. M.; Ramírez-del Solar, M. Photocatalytic TiO2 Sol-Gel Thin Films: Optical and Morphological Characterization. *Sol. Energy* **2015**, *122*, 11–23. https://doi.org/10.1016/j.solener.2015.07.048.

(49) Lakshmi, S.; Renganathan, R. Study on TiO$_2$-Mediated Photocatalytic Degradation of Methylene Blue. *J. Photochem. Photobiol. A*. **1995**, *88*(2), 163–167. https://doi.org/10.1016/1010-6030(94)04030-6.

(50) Houas, A.; Lachheb, H.; Ksibi, M.; Elaloui, E.; Guillard, C.; Herrmann, J. Photocatalytic Degradation Pathway of Methylene Blue in Water. *Appl. Catal. B.* **2001**, 31(2), 145-157. https://doi.org/10.1016/S0926-3373(00)00276-9.

(51) Mondal, S.; Reyes, M. E. D. A.; Pal, U. RSC Advances Plasmon Induced Enhanced Photocatalytic Activity of Gold Loaded Hydroxyapatite Nanoparticles for Methylene Blue Degradation under Visible Light. *RSC Adv.* **2017**, *7*, 8633–8645. https://doi.org/10.1039/C6RA28640B.

(52) Ohtani, B.; Ogawa, Y.; Nishimoto, S. Photocatalytic Activity of Amorphous - Anatase Mixture of Titanium (IV) Oxide Particles Suspended in Aqueous Solutions. *J. Phys. Chem. B*, **1997**, *101* (19), 3746–3752. https://doi.org/10.1021/jp962702.

(53) Yanagisawa, K.; Ovenstone, J. Crystallization of Anatase from Amorphous Titania Using the Hydrothermal Technique : Effects of Starting Material and Temperature. *J. Phys. Chem. B.* **1999**, 103 (37), 7781–7787. https://doi.org/10.1021/jp990521c.

(54) Clifforda, M. N.; Wight, J. The Measurement of Feruloylquinic Acids and Caffeoylquinic Acids in Coffee Beans. Development of the Technique and Its Preliminary Application to Green Coffee Beans. *J. Sci. Food Agric.* **1976**, 27, 73-84. https://doi.org/10.1002/jsfa.2740270112.

(55) Singh, U.; Verma, S.; Ghosh, H. N.; Rath, M. C.; Priyadarsini, K. I.; Sharma, A.; Pushpa, K. K.; Sarkar, S. K.; Mukherjee, Chemical Photo-Degradation of Curcumin in the Presence of TiO_2 Nanoparticles : Fundamentals and Application. *J Mol Catal A Chem.* **2010**, *318*, 106–111. https://doi.org/10.1016/j.molcata.2009.11.018.

(56) Priyadarsini, K. I. Photophysics , Photochemistry and Photobiology of Curcumin : Studies from Organic Solutions , Bio-Mimetics and Living Cells. Journal of Photochemistry and Photobiology C. *J. Photochem. Photobiol. C: Photochem. Rev.* **2009**, *10*, 81–95. https://doi.org/10.1016/j.jphotochemrev.2009.05.001.

(57) Abbas, M.; Iftikhar, H.; Malik, M. H.; Nazir, A. Surface Coatings of TiO2 Nanoparticles onto the Designed Fabrics for Enhanced Self-Cleaning Properties. *Coatings* **2018**, *8* (1). https://doi.org/10.3390/coatings8010035.

(58) Wijesena, R. N.; Tissera, N. D.; Perera, R.; Nalin De Silva, K. M.; Amaratunga, G. A. J. Slightly Carbomethylated Cotton Supported TiO_2 Nanoparticles as Self-Cleaning Fabrics. *J. Mol. Catal. A Chem.* **2015**, *398*, 107–114. https://doi.org/10.1016/j.molcata.2014.11.012.

(59) Yu, M.; Wang, Z.; Liu, H.; Xie, S.; Wu, J.; Jiang, H.; Zhang, J.; Li, L.; Li, J. Laundering Durability of Photocatalyzed Self-Cleaning Cotton Fabric with TiO_2 Nanoparticles Covalently Immobilized. *ACS Appl. Mater. Interfaces* **2013**, *5* (9), 3697–3703. https://doi.org/10.1021/am400304s.

(60) Kumar, B. S. Self-Cleaning Finish on Cotton Textile Using Sol-Gel Derived TiO$_2$ Nano Finish\n. *IOSR J. Polym. Text. Eng.* **2015**, *2* (1), 01–05. https://doi.org/10.9790/019X-0210105.

(61) Ahmad, I.; Kan, C. W.; Yao, Z. Photoactive Cotton Fabric for UV Protection and Self-Cleaning. *RSC Adv.* **2019**, *9* (32), 18106–18114. https://doi.org/10.1039/c9ra02023c.

(62) Lee, H. J.; Kim, J.; Park, C. H. Fabrication of Self-Cleaning Textiles by TiO$_2$-Carbon Nanotube Treatment. *Text. Res. J.* **2014**, *84* (3), 267–278. https://doi.org/10.1177/0040517513494258.

3. Synthesis and Characterization of ZnO Nanoparticles for Application in Self-cleaning Textiles

Abstract

ZnO nanoparticles were synthesized using the hydrothermal method. The prepared ZnO NPs were coated onto cotton fabric using the pad-dry-cure technique. The particle size, optical, microstructure, and morphology of the coated cotton fabric were obtained by dynamic light scattering (DLS), Fourier transform infrared (FTIR) spectroscopy, UV-vis spectroscopy, X-ray diffraction (XRD), Transmission electron microscopy (TEM), and scanning electron microscopy (SEM), Thermogravimetry analysis (TGA) , respectively. The photocatalytic activity of the ZnO NPs coated fabric was examined by degrading methylene blue using UV radiation. 83% of the dye was degraded in 3h, suggesting that ZnO NPs coated fabric can be used in self-cleaning clothing. Coffee and curry stains were used as model dirt to examine self-cleaning properties. ZnO NP-coated cotton textiles are observed to clean 67% coffee stain and 82% curry stain after 20h of xenon UV light exposure.

Keywords

Photocatalytic activity, self-cleaning, textiles, zinc oxide nanoparticle.

3.1   Introduction

An emerging area of study in the textile industry is the development of textile materials with customized properties through coating with nanoparticles.[1,2] Apart from clothing, textiles or fabrics dominate in building materials, transportation, agriculture, and the healthcare industry.[3,4] Cotton fabrics are widely used daily because of their outstanding qualities, including ease, biodegradability, softness, moisture retention, and regeneration.[5] The use of cotton fabrics with various functional finishing by NPs has gained significant notice over the past few decades because people are becoming more aware of their health, hygiene, safety, and comfort.[6,7] The large number of hydroxyl groups in the cotton structure makes them highly absorbent and easily stained by liquids.[8] Different types of germs start to grow due to stains and liquids. Therefore, the need for self-cleaning textiles is a requirement in our day-to-day lives. Semiconductor-based NPs can impart desired

functional properties on textiles that broaden the functional areas of the final product.[9] The application of semiconductor-based NPs like ZnO NPs on textiles has recently grown huge as it imparts various functional properties like hydrophobicity[10,11,12], antimicrobial resistance,[13,14] photocatalytic activity, self-cleaning properties,[15,16] flame retardance,[17,18] UV-protection, electric conductivity, etc.[19,20] ZnO NPs are promising materials for photocatalytic activity and self-cleaning property because they a high excitation binding energy (60 meV), wide band gap energy (3.10 to 3.37 eV).[21] They are less toxic and chemically and thermally stable. The size, crystalline structure, crystallite size, porosity of the layers, morphology, and phase all significantly impact this property.[22] Though several pieces of research on the photocatalytic activity of ZnO NPs in textiles have been found, systematic investigation of self-cleaning activity in textiles is limited. Gupta *et al*.[23] reported the photocatalytic self-cleaning activity of coffee stain of the cotton fabric against solar light. Using a pad-dry-cure method, they individually applied TiO_2 and ZnO NPs (0.5-1% on the fabric weight) on cotton fabrics with a 1-10% acrylic binder. They assessed the self-cleaning property by quantifying the discoloration of coffee stains after exposure to solar light for 48 h. Khan *et al*.[24] also investigated and achieved excellent photocatalytic self-cleaning properties of co-polyester (1,4-cyclohexanedimethylene isosorbide terephthalate) nanofibre after embedded with nine weight% of ZnO NPs after three h exposure against sunlight. Functional finishes on textile fabrics have recently been crucial in upgrading textile products. So, to reduce process costs, a detailed and systematic analysis of photocatalytic activity and self-cleaning properties of textiles with lower UV exposure time is necessary.

This present research shed light on the photocatalytic activity and self-cleaning properties with adequate fundamental physical properties of ZnO NPs coated fabric. Here, ZnO NPs are synthesized using a simple hydrothermal technique because it has excellent control over the shape and size of the particle, a low degree of aggregation, a narrow crystallite size distribution, and an abundance of purity.[21] Dynamic light scattering, FTIR spectroscopy, UV-vis spectroscopy, and XRD are used to characterize ZnO NPs systematically. An acrylate binder is used to immobilize and improve the binding of ZnO NPs on the cotton fabric surface using a pad-dry-cure technique. Scanning electron microscopy with EDX

spectroscopy was used to assess the morphological characteristics of cotton fabric. The physical and thermal properties, whiteness, photocatalytic activity, and self-cleaning properties of cotton fabrics were also thoroughly investigated. These findings may benefit the development of functional fabrics with photocatalytic activity and self-cleaning properties.

3.2   Experimental

3.2.1   Materials

Zinc nitrate hexahydrate (>98%, Merck), ammonium chloride (Analar BDH chemical Ltd, England), urea (Uni-chem chemical reagent, China), binder of aqueous acrylate dispersion (Forbind OB 45, Fortune top Pte Ltd. New Taipei City, Taiwan) methylene blue (Janssen Chimica, Belgium) were used without further purification. Deionized water (conductivity: 0.055 µScm^{-1}), collected from the HPLC grade water purification system (BOECO), was used to prepare the solutions. Each experiment used a scoured and bleached 100% cotton single jersey knit fabric.

3.2.2   Synthesis of ZnO nanoparticles (NPs) by hydrothermal method

0.015 mol of $Zn(NO_3)_2.6H_2O$, 0.015 mol of NH_4Cl, and 0.06 mol of urea were dissolved in 80 mL of distilled water at 30 ℃. The solution was kept in the Teflon container, transferred into a hydrothermal reactor, and put in an oven at 160 ℃ for 24 h. A white precipitate of ZnO NPs was obtained. Then the solution was centrifuged (Centrifuge Cencom II from J. P. Selecta, Spain) at 1000 rpm for 5 min and washed with distilled water several times. The obtained product was then dried in an oven at 80 ℃ for 24 h.

ZnO NPs were synthesized according to the following reaction (equations3.1 (a-e)). In synthesis, NH_3 produced from NH_4Cl and $CO(NH_2)_2$ can be considered a pH buffer as it steadily releases OH^- (equations 6-8). In hydrothermal treatment, NH_3 reacts with Zn^{2+} ions to form $Zn(NH_3)_4^{2+}$ nanocluster in solution, and then these intermediates tend to form ZnO particles by reacting with OH^-.[25]

$$NH_4Cl + H_2O \quad \rightarrow \quad NH_3 . H_2O + HCl \qquad 3.1(a)$$

$$CO(NH_2)_2 + H_2O \quad \rightarrow \quad 2NH_3 . H_2O + CO_2 \qquad 3.1(b)$$

$$NH_3 \cdot H_2O \qquad \leftrightarrow \quad NH_4^+ + OH^- \qquad\qquad 3.1(c)$$

$$Zn^{2+} + 4NH_3 \qquad \leftrightarrow \quad Zn(NH_3)_4^{2+} \qquad\qquad 3.1(d)$$

$$Zn(NH_3)_4^{2+} + 2OH^- \rightarrow \quad ZnO + 4NH_3 + H_2O \qquad\qquad 3.1(e)$$
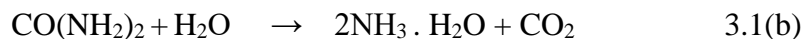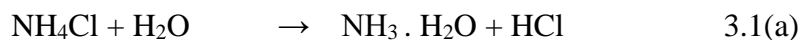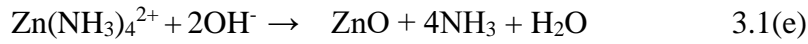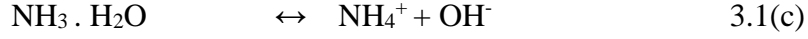
3.2.3   Application of ZnO NPs on cotton fabric

ZnO NPs can be coated on cotton fabric to preserve consistency with an existing textile finishing instrument which is shown in Scheme 1. 1% of ZnO NPs and 1% of the acrylic binder were dispersed in 100 mL distilled water and applied on pretreated cotton fabric by a dip-pad-dry-cure method. At first, cotton fabric was dipped into a dispersion of ZnO NPs for 5 min under magnetic stirring to prevent precipitation of ZnO NPs. Padding was done by standard laboratory equipment with 2.5 m/min fabric speed and 2.8 kg/cm^2 padding pressure to maintain about 70-75 pick-up percentage (%). The pH value of the padding bath was maintained at about 5. The samples were dried at 80 °C for 5 min and cured (SDL mini-dryer steamer) at 145 °C for 2.5 min to ensure good adhesion of the ZnO NPs to the substrate surface. The ZnO content of the coated cotton fabrics (W_{ZnO}) was calculated by using equation (3.2):

$$W_{ZnO} = P \times wt\% \qquad\qquad (3.2)$$

P is the pick-up%, and wt% is the weight ratio of ZnO NPs aqueous dispersion. The theoretical ZnO content on cotton fabrics was about 0.75% when one wt% of ZnO NPs dispersion was used. The ZnO NPs in colloidal dispersion concentration and pick-up% during the impregnation and padding processes are some controlling parameters of the ZnO content on coated fabrics.[26]
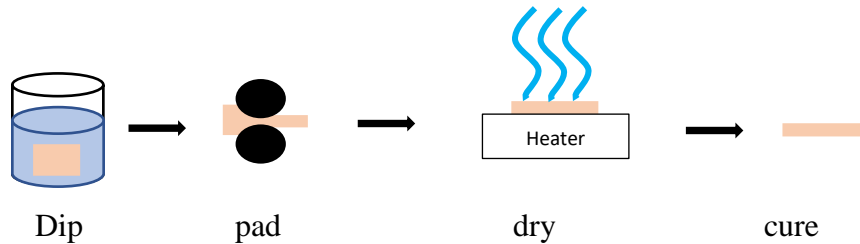
Figure 3.1: Schematic of ZnO NPs coating

3.2.4 Characterization

The average particle size and size distribution of the samples dispersed in water were measured using DLS measurements by a Malvern Zetasizer Nano ZS90 with a scattering angle of 90°. A He–Ne laser beam of 632.8 nm was used for the measurements. The average hydrodynamic diameters were determined from cumulants mean of the intensity average of 50 runs using Stokes–Einstein equation, $d_H = k_B T/3\pi\eta D_{ef}$, where d_H is the hydrodynamic diameter, k_B is the Boltzmann constant, T is the temperature, η is the solvent's viscosity, and D_{ef} is the diffusion coefficient. The reproducibility was checked from at least three measurements. The sample temperature was controlled automatically within ±0.01 K by a built-in Peltier device.

FTIR spectrum was recorded by a Fourier transform spectrophotometer (Frontier by Perkin-Elmer) in transmittance mode for each KBr sample range between 400 and 4000 cm^{-1} at 4.0 cm^{-1} resolution.

The optical absorption spectra for both ZnO NPs in dispersion solution and ZnO NPs coated cotton fabric in aqueous solution with methylene blue after UV irradiation (UV lamp) were recorded using a double-beam UV–visible spectrophotometer, Model UVD-3500, Shimadzu, Japan. Rectangular quartz cells of a path length of 1 cm were used throughout the investigation. UV-visible diffuse reflectance spectrum was recorded using a double-beam UV-visible spectrophotometer with an integrating sphere attachment DRA-CA-30I (Model: UV-1800, Shimadzu, Japan) to determine the band gap (E_g) energy of the solid NPs.

The crystallinity of the NPs was determined by an X-ray diffractometer (Philips PW 1724) with an X-ray generator using XDC-700 Guinier-Hagg focusing camera with monochromatized Cu Kα radiation ($\lambda = 1.540598$). According to Debye-Scherrer's $D = \dfrac{K\lambda}{\beta cos\theta}$ equation, the crystallite domain diameters (D) were obtained from XRD peaks.

Surface morphology and structure of ZnO NPs were studied with EM, and the micrographs were attained using the LEO system (model 912 AB) at 120kV for samples. The morphological study used field emission scanning electron microscopy (ZEISS, Germany).

The acceleration voltage of the electron gun was 20 kV with a probe current of 1.0 nA and magnifications ranging from 10,000 – 100,000. The images of samples were taken without sputtering and by mounting on the conducting carbon tape. The compositional study of the NPs is analyzed by EDX spectroscopy attached to the FESEM. mageJ 1.51k(java 1.60-24 (64 bit), USA) was used to measure the average particle size of NPs in both the TEM and the FESEM images of NPs. Thermal properties were studied under a nitrogen atmosphere by a Hitachi instrument (TG/ DTA 7200) in the 30–550 ℃ at a heating rate of 20° min^{-1}. The physical properties of the fabrics (weight, bursting strength, air permeability) were examined by ISO standards.

3.2.5   Assessment of photocatalytic properties of the coated fabrics

0.4 g of the fabric was cut into tiny pieces of 1cm × 1cm dimensions. These pieces were put in an 80 mL beaker with 40 mL of an aqueous MB dye solution (0.01g/L) and then exposed to UV irradiation using a Philips UV lamp (365 nm, Philips TLD 18W/08) at 300 rpm by magnetic stirrer (BOECO, Germany). After an interval of 1 h, 1 mL of the MB dye solution was removed, and its absorption spectra were measured using a double-beam Shimadzu UV-visible spectrophotometer (Model UVD-3500) at a wavelength of 664 nm.[27] The following formula (eq. 3.3) was used to calculate the rate of MB dye degradation:

$$\% \, Degradation = \left[\frac{Ab_{s_0} - Ab_{s_t}}{Ab_{s_0}}\right] \times 100 \qquad (3.3)$$

Here Ab_{s_0} is the initial absorbance and Ab_{s_t} is an absorbance at time t.[28,29]

3.2.6   Whiteness test

By ISO 105-J02:1997 (Textiles-Tests for color fastness-Instrumental assessment of relative whiteness), the Datacolor SF650 (Datacolor International, USA) with D65 illuminant and 10° observer was used to measure the whiteness of control and ZnO NPs coated cloth. The following equation (eq. 3.4) was used to determine the whiteness indices (W_{10}) of fabrics:

$$W_{10} = \, Y_{10} + 800(0.3138 - x_{10}) + 1700(0.3310 - y_{10}) \qquad (3.4)$$

Here, W_{10} is the brightness value or index, Y_{10}, x_{10}, and y_{10} are the chromaticity coordinates of the specimen, and 0.3138 and 0.3310 are the x_{10} and y_{10} chromaticity coordinates for the

ideal diffuser, respectively. When contrasted to the whiteness of the control fabric, the rate of whiteness reduction was expressed in percentage.[30]

3.2.7 Evaluation of self-cleaning activity

The color strength intensity of coffee and curry stains was used to gauge the self-cleaning ability of control and coated fabrics after UV irradiation. 0.3 g coffee powder (Nestle coffee powder) was mixed with 25 mL of hot water, and 0.5 g of curry powder (Radhuni meat curry masala) was mixed with 10 mL of hot water to prepare the coffee solution and curry paste, respectively. Both coffee and curry stains were produced by applying one drop of the respective solution onto a piece of ZnO NPs coated fabric, allowing it to disseminate and dry in the air and then exposing it to light irradiation. Both stains on the ZnO NPs coated fabric were irradiated for 20 h by ISO 105 B02 test technique in light exposure and weathering test instrument (air-cooled xenon arc lamp, Xenotest Alpha LM, USA). Each stain on the fabric was divided in half, with one side exposed to a xenon arc lamp and the other half protected by a steel frame from irradiation. The exposed and unexposed portions of the stain were examined for self-cleaning action. By comparing the color strength (K/S) between the exposed and unexposed portions of the same stain, the self-cleaning action was measured by the spectrophotometer to quantify the stained fabric's reflectance (Datacolor SF600, Datacolor International, USA) to determine the color strength by using following Kubelka-Munk equation (eq. 3.5).[23]

$$\frac{K}{S} = \frac{(1-R)^2}{2R} \qquad (3.5)$$

Here, K/S stands for color strength, K and S for absorption and scattering coefficients, respectively, and R is the reflectance. The K/S value of the stain's unexposed portion was set at 100, and the relative stain degradation in the exposed portion's K/S value was determined using the relationship below (eq. 3.6):[31]

$$\% \text{ Reduction in } \frac{K}{S} \text{ value } = \frac{\left(\frac{K}{S}\right)unexposed - \left(\frac{K}{S}\right)exposed}{\left(\frac{K}{S}\right)unexposed} \times 100 \qquad (3.6)$$

3.3   Results and Discussion

3.3.1   Dynamic light scattering measurement

The distribution of hydrodynamic diameter of the prepared ZnO NPs measured by DLS are depicted in Figure 3.1.[30] A sharp peak at 1 nm and a broader one at 18 to 38 nm suggests that the ZnO particles prepared are in the nano dimension range. These smaller particles will provide a higher surface area to be effective in photocatalytic and self-cleaning activity.[32]
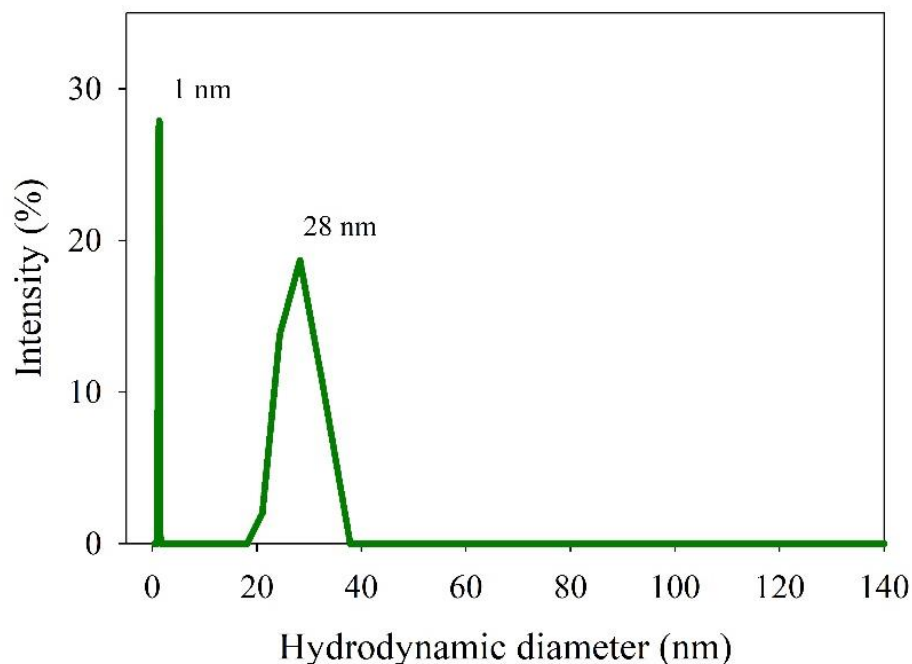
Figure 3.1: The average hydrodynamic diameter of ZnO NPs from DLS.

3.3.2   FTIR spectroscopy

The FTIR spectra of ZnO NPs are shown in Figure 3.2, and it has distinct bands at 460, 1050, 1383, 1635, and 3414 cm^{-1}. The broad absorption band at 3414 cm^{-1} correlates to the stretching vibration of the O-H mode, which may be caused by the OH groups of water present in the sample,[22,33] while the intense bnad at 460 cm^{-1} is the characteristic absorption of Zn-O vibrational bands of ZnO.[34] The C=O stretching vibration is responsible for the small band at 1635 cm^{-1} that may be small traces of precursor. The hydroxyl groups of

moisture are responsible for the band at 1383 cm^{-1}.[35] In 1050 cm^{-1}, Zn-O-Zn bridges are discovered.[8,36] From FTIR, it can be concluded that ZnO NPs are formed.
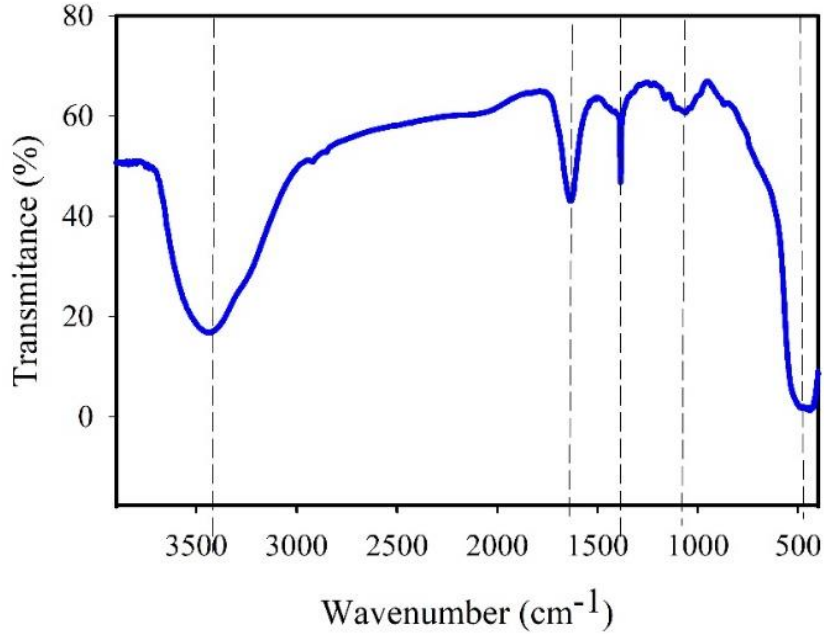
Figure 3.2: FTIR spectrum of ZnO NPs.

3.3.3 UV-visible absorption analysis

The UV-visible spectrum of ZnO NPs peaks at 372 nm, which can be attributed to the band gap energy of the prepared NPs. The band gap energy of ZnO NPs can be estimated by the formula (11):[37]

$$\alpha h v \ = \ A(h v - E_g)^n \qquad (3.7)$$

Where E_g, v, A, α are the direct optical band gap energy, light frequency, a constant, absorption coefficient, and $n = \frac{1}{2}$ (for direct transition mode material). The band gap can be calculated by extrapolating the linear area of the Tauc plot (a plot of $(\alpha h v)^2$ versus the photon energy $(h v)$) of the exciting light, shown in Figure 3.3. An improved representation of the band gap energy of ZnO NPs with a direct band gap transition can be found at the intersection of the tangent line and the X-axis.[38,39]
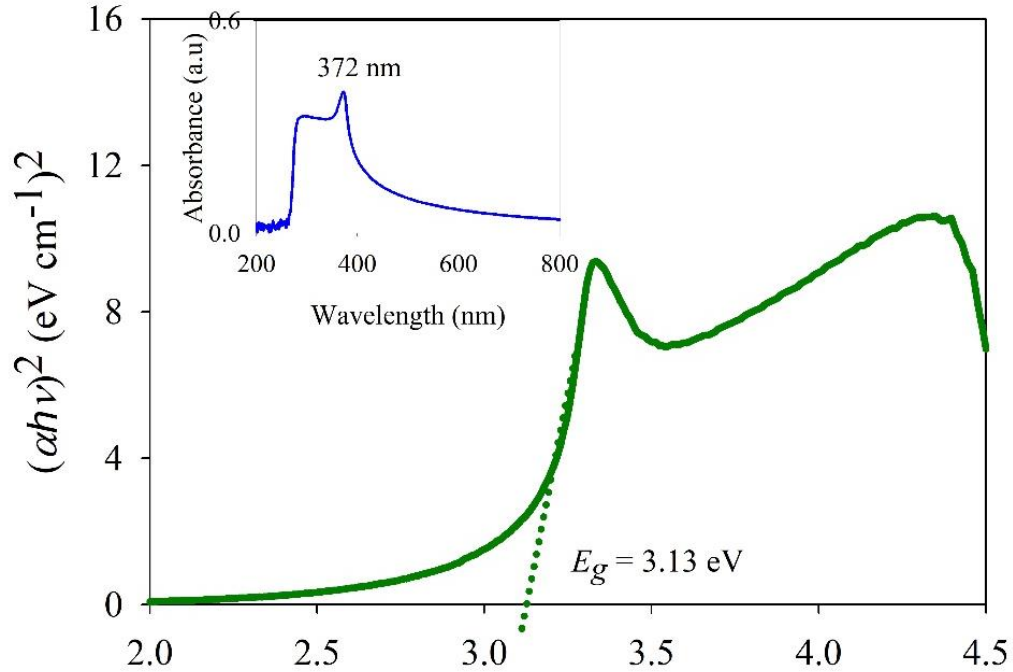
Figure 3.3: Tauc plot of the ZnO NPs. (The inset is the UV-vis absorption spectrum of an aqueous dispersion of ZnO NPs).

3.3.4 Determination of optical band gap and the nature of optical charge carrier transitions

In the DASF technique, the optical band gap of ZnO NPs can be calculated by eqs.3.8-9:[40]

$$ln\left[\frac{f(R)}{\lambda}\right] + ln\, s = ln[B(hc)^{m-1}] + m\, ln(\frac{1}{\lambda} - \frac{1}{\lambda_g}) \qquad (3.8)$$

Now,

$$\frac{d\{ln\left[\frac{f(R)}{\lambda}\right]\}}{d(\frac{1}{\lambda})} = \frac{m}{\frac{1}{\lambda} - \frac{1}{\lambda_g}} \qquad (3.9)$$

As R is the reflectance and $f(R)$ is proportional to the absorption coefficient (α), $f(R)$ is calculated using the Kubelka-Munk technique (equation3.10).

$$f(R) = \frac{(1-R)^2}{2R} \qquad (3.10)$$

66

Where c is the velocity of light, λ_g is the wavelength associated with the optical band gap, λ is the wavelength, s is the scattering coefficient, B is a constant, hv is the energy of a photon, and E_g is the band gap energy of the sample. By extrapolating a linear portion in the plot of $dln[\alpha(\lambda)\lambda^{-1}]/d\lambda^{-1}$ against hv extended in Figure 3.4, the optical band gap is determined, and the calculated E_g of ZnO NPs is 3.07 eV.
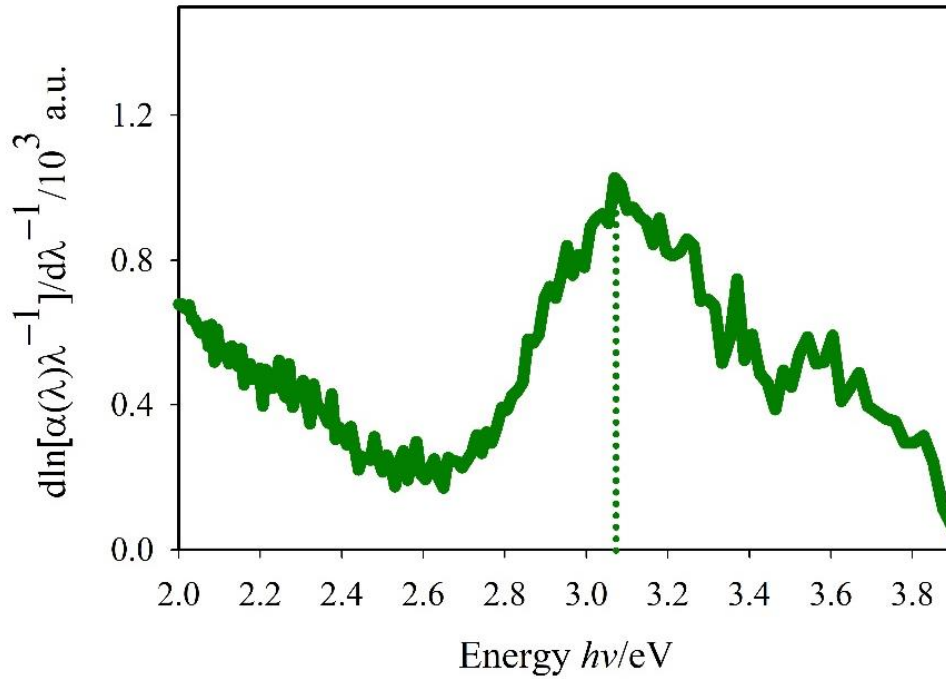
Figure 3.4: DASF method calculated for band gap by plotting of dln[α(λ)λ-1]/d λ-1 versus hv.

The band gap of ZnO NPs can vary depending on structural factors, carrier content, and grain size. By extrapolating a linear section of the plot of $ln[\alpha(\lambda)\lambda^{-1}]$ versus $ln[\lambda^{-1} - \lambda_g^{-1}]$ extended in Figure 3.5, where the inset is the reflectance spectra of ZnO NPs, one can determine the corresponding coefficient (m) of the sample. When an electronic transition occurs, the corresponding coefficient (m) is calculated, and it is found that $m = 1/2$ for the direct permitted transition.[41]
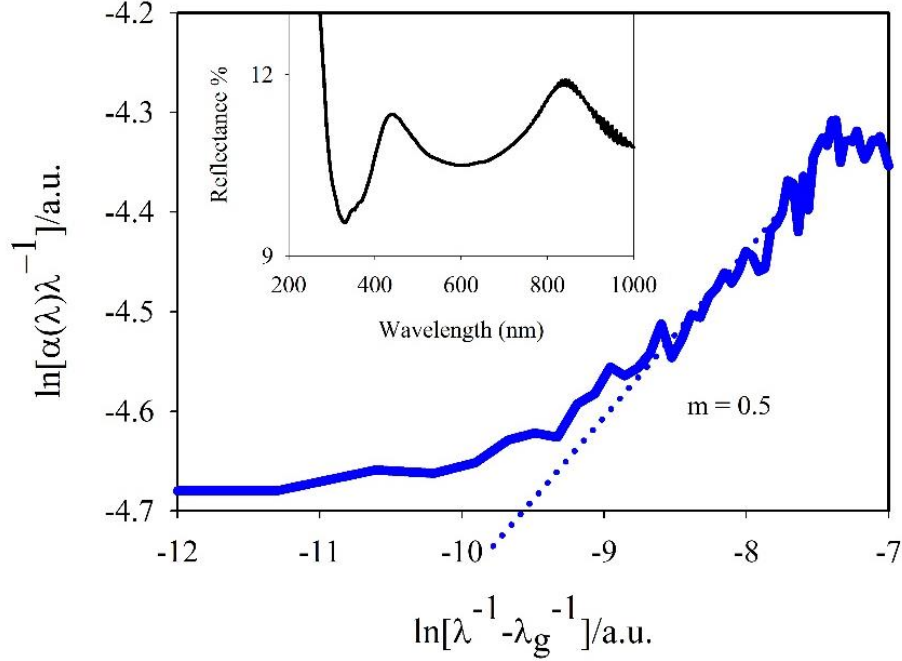
Figure 3.5: DASF method calculated the corresponding coefficient by plotting $\ln[\alpha(\lambda)\lambda\text{-}1]$ versus $\ln[\lambda\text{-}1 - \lambda g\text{-}1]$. The inset is the reflectance spectra of ZnO NPs.

3.3.5 X-ray diffraction

Figure 3.6 shows the XRD pattern of ZnO NPs. With nine diffraction peaks (2θ) at 31.82°, 34.47°, 36.31°, 47.60°, 56.67°, 62.93°, 66.46°, 68.03°, and 69.15°, ZnO NPs can be accurately indexed to wurtzite hexagonal structure (JCPDS no. 891397). These diffraction peaks are correlated to the lattice planes denoted by Miller indices (100), (002), (101), (102), (110), (103), (200), (112), and (201). Sharp diffraction patterns indicate significant crystallization. The eqs, 3.11-12 were used to compute the lattice parameters *a*, *b*, and *c* of the sample.[42,43]

$$2d_{hkl}sin\theta = n\lambda \qquad (3.11)$$

$$\frac{1}{d^2} = \frac{h^2 + k^2}{a^2} + \frac{l^2}{c^2} \qquad (3.12)$$

d_{hkl} is the interplanar spacing (d-spacing), *hkl* are the Miller indices, *n* is the diffraction order (for first order $n = 1$), and λ is the XRD wavelength. ZnO NPs had average lattice parameters of a = b = 2.8101 Å, and c = 5.1998 Å. The slight difference between the

68

experimental lattice constant and the bulk value is due to microstructural stain from certain intrinsic and non-intrinsic defects like oxygen vacancies, zinc antisites, and extended defects like threading dislocation. Debye-Scherrer's equation (17) was used to determine the average crystallite diameter (D).[44]

$$D = \frac{K\lambda}{\beta cos\theta} \qquad (17)$$
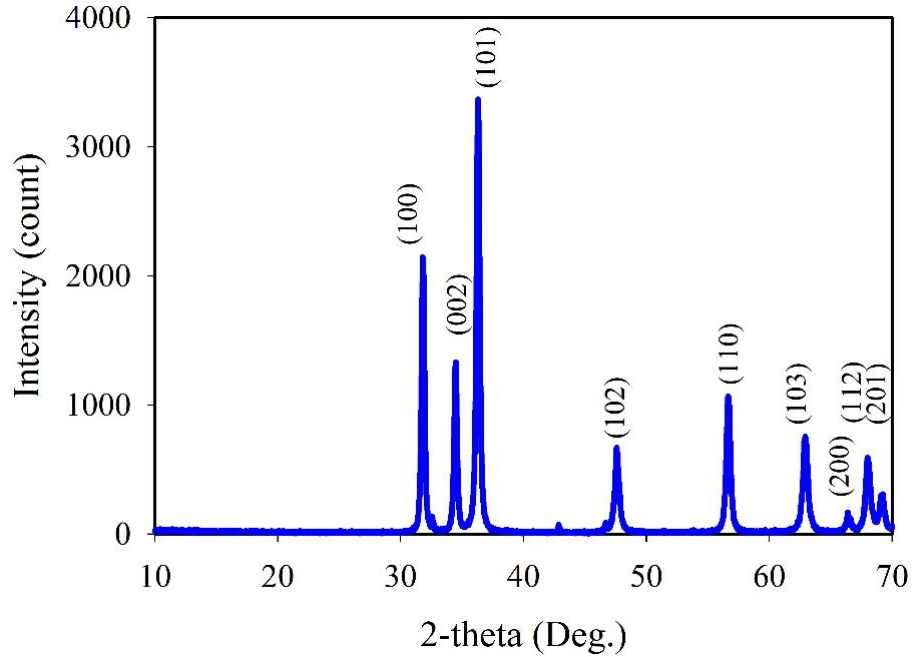
Figure 3.6: XRD patterns of ZnO NPs.

Lattice stain was calculated by equation (3.13):

$$\eta = \frac{\beta}{tan\theta} \qquad (3.13)$$

Using the Williamson-Hall equation (19), the dislocation density (δ), which reflects the number of crystal defects, was calculated. The dislocation density is the inverse of D^2.

$$\delta = \frac{1}{D^2} \qquad (3.14)$$

Where D is the crystallite size, $K = 0.9$, λ is the wavelength of X-ray radiation (1.5406 Å), β is the full-width half maximum of the diffraction peak, θ is the Braggs diffraction angle, η is the lattice stain of the material.[45]

Equation (3.15provides the estimation of the Zn-O bond length L.[46]

$$L = \sqrt{\left(\frac{a^2}{3} + \left(\frac{1}{2} - u\right)^2 c^2\right)} \qquad (3.15)$$

Where u express (equation3.16) the positioning parameter of the wurtzite structure, which calculates how far apart each atom is from the one next to it along the 'c' axis.

$$u = \frac{a^2}{3c^2} + 0.25 \qquad (3.16)$$

For ZnO NPs, the value of u is 0.3473 Å. The relationship between the c/a ratio and u is that as the c/a ratio declines, u increases so that the distortion of the tetrahedral angles causes those four tetrahedral distances to remain virtually constant. The measured Zn-O bond length in the unit cell of ZnO and nearby atoms is close enough to the estimated Zn-O bond length (L), which is 1.8061 Å. The bond length of Zn-O in the unit cell and the estimated one are almost the same. The full-width half maximum (FWHM, β) crystallite size(D) lattice stain (η), dislocation density (δ) lattice planes (hkl), and d-spacing (d_{hkl}) values are tabulated in Table 3.1.[47]

Table 3.1: 2θ, crystallite size, lattice stain, dislocation density, hkl, d-spacing of ZnO NPs as presented in XRD pattern analysis.

2θ (degree)	β	D (nm)	$\eta = \beta/tan\theta$	δ (nm^{-2})	hkl	$d_{hkl} = \lambda/2sin\theta$
31.82	0.30	27.82	0.0182	0.0013	100	0.2810
34.47	0.31	26.96	0.0174	0.0014	002	0.2600
36.31	0.34	24.41	0.0182	0.0017	101	0.2472
47.60	0.46	18.73	0.0183	0.0028	102	0.1909
56.67	0.43	20.90	0.0140	0.0023	110	0.1623
62.93	0.53	17.64	0.0151	0.0032	103	0.1476
66.46	0.49	19.52	0.0130	0.0026	200	0.1406
68.03	0.52	18.38	0.0135	0.0030	112	0.1377
69.15	0.59	16.28	0.0150	0.0038	201	0.1357

3.3.6   TEM analysis

Figure 3.7 (a-b) displays TEM images of the Ag NPs, revealing Ag NPs' form. Particle sizes of ZnO are highlighted by histogram from TEM examination (Figure3.7 (c)). The selected area diffraction pattern (SAED pattern) shows in Figure3.7. Nanocrystals with a wurtzite hexagonal structure are created with a narrow size distribution. These NPs are challenging to distinguish from one another.[48] Using image analysis software, the average particle size of ZnO was determined to be between 4 and 22 nm, as indicated on the histogram and the particles were agglomerated. Figure 3.7 (d) displays the SAED patterns of the ZnO NPs. The microstructure was polycrystalline with tiny grain sizes, as the relatively diffuse diffraction rings indicated.[49]
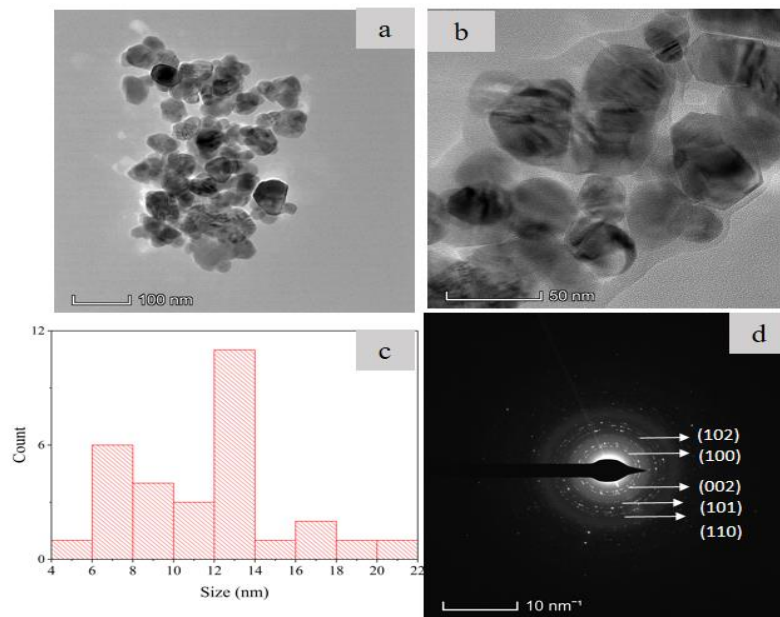
Figure 3.7: TEM images of (a, b) ZnO NPs with different magnifications, (c) histogram and (d) SAED pattern.

These rings are consistent with the result from the XRD pattern shown in Figure 3.6. The ring-like diffraction pattern coincides with the (100), (002), (004), (101), (102), and (110) lattice planes of ZnO NPs. It is inspected that these absolute circle rings with spots are well

coordinated with the XRD pattern of ZnO NPs as they clarify the profoundly crystalline nature.

3.3.7 SEM analysis

The SEM image from Figure 3.8 (a-b) depicted the morphology of the control cotton fiber surface as composed of tightly packed, diagonal lines that intertwine to produce spiral fibrils with a twisted ribbon-like shape. Their smooth and clean surfaces indicated that surface imperfections had been eliminated during pre-treatment. Clean surfaces are crucial for consistent distribution throughout the subsequent coating process. The diagonal lines on the surface of ZnO NPs coated fibers was less evident than in Figure 3.8 (c-d). ZnO NPs were evenly distributed across the grooves between the fibrils on the fiber surface. Histogram (Figure 3.8 (e)) showed the particle size distributions of ZnO NPs ranging from 40 to 240 nm. Higher size distributions were due to some clusters of ZnO NPs present on the coated cotton surface. The control cotton fabric exhibited a clear surface with no accumulation of ZnO NPs, while the sizes of the ZnO NPs agglomerates on the coated fabric were less than five μm. Some possible reasons regarding these agglomerates include the following: NPs were coagulated and remained at the bottom of the vessel due to lack of stirring during the impregnation process; NPs were aggregated in aqueous solution due to their low dimension; or the surfactant used to create a relatively stable dispersion of ZnO NPs may prevent the adhesion of particles on the fabric surface.[50] The quality of the coated fabric depends on the homogeneous allotment of NPs on the fiber surface, and the number of NPs deposited on the fiber surface depends on the wettability and absorbing quality of the fabric. The EDX spectrum (Figure 3.8 (f)) was reported to express the identification of elements in the coated cotton. This spectrum verified the presence of C, O, and Zn elements on the surface.
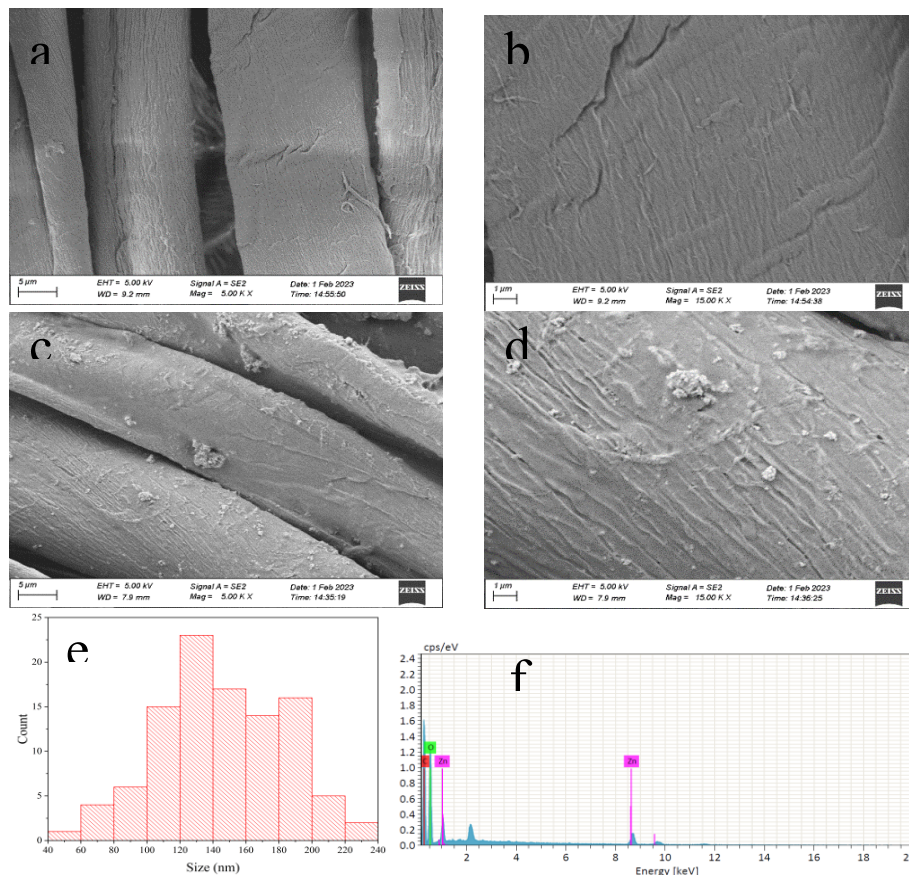
Figure 3.8: SEM images of (a-b) control fabric, (c-d) ZnO NPs coated fabric with different magnifications, (e) histogram of diameter size, and (f) EDX spectrum of ZnO NPs coated cotton fabric.

3.3.8 Thermogravimetric analysis

To explore the impact of the performed coating treatment on the cellulose pyrolysis process, the thermal behavior of ZnO NPs coated cotton fabric is investigated from room temperature to a temperature range of 550 ℃. Figure 3.9 displays the TGA and DTA curves of control, and ZnO NPs coated cotton fabrics. Pyrolysis is a complex process that allows for the simultaneous occurrence of endothermic bond rupture, volatilization, and exothermic bond formation. The DTA curve only displays the net change, whereas the TGA thermogram displays the weight loss of fabrics during each pyrolysis step.[51] TGA thermogram of the control cotton fabric showed three main weight reduction phases. Because of the initial pyrolysis stage, where celluloses are primarily damaged in the amorphous region of the polymer, the TGA curve is linear in the first step. However, some physical properties of the fabric can be altered by showing gradual weight loss (4.5%) up

to about 280 ℃ because of the removal of absorbed and adsorbed water.[52] Due to the significant weight loss of the sample in the second stage due to the pyrolysis of cellulose in the crystalline region of the polymer, the curves in this step have a steep slope. A line representing steady weight loss appears up to 320 °C. Then a line representing drastic weight loss (about 83%) appears with an endothermic peak at 383 °C due to the production of pyrolysis products like levoglucosan.[31,53] The remaining weight, around 13%, in the third step, above 500 ℃, may only be attributable to char/ash matter. The higher curing temperature may be weakening the cellulose linkages of cotton, as cotton cloth coated with ZnO NPs exhibits the same pattern of the endothermic peak in DTA curves but with less thermal stability above 390 ℃ with only 7% residual weight of char/ash matter.[26]
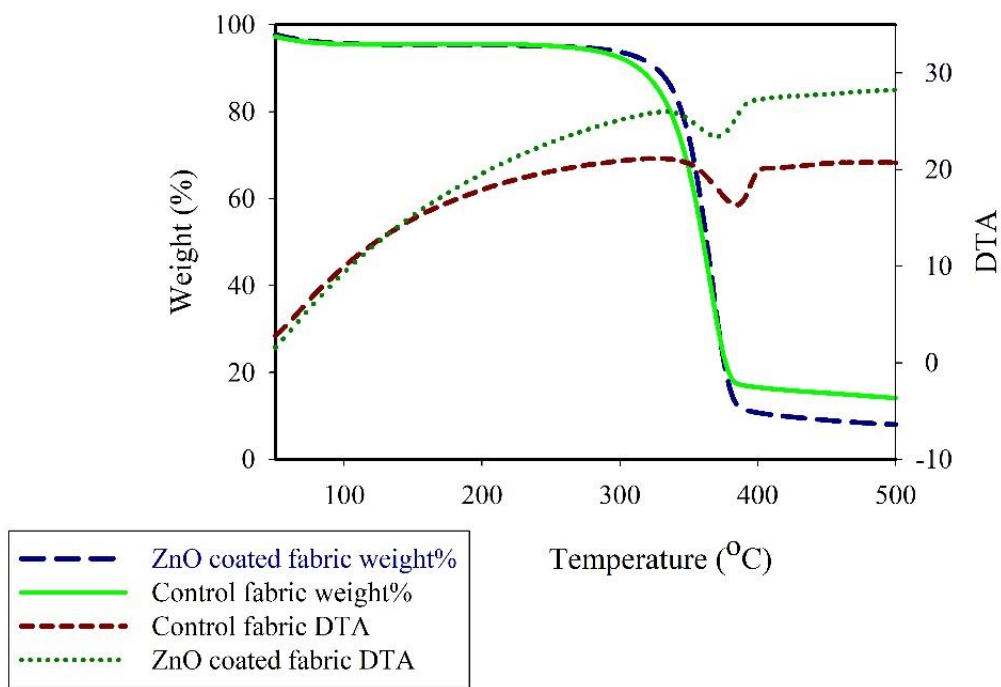
Figure 3.9: TGA and DTA analysis of control and coated cotton fabric with ZnO NPs. (N_2 atmosphere)

3.3.9 Physical properties of coated fabric

As shown in Table 3.2, all of the investigated physical properties exhibited minimal variations. The findings showed that the deposited NPs on the fabric surface caused a decrease in weight and fabric density on the wales and the course. A slight reduction of

bursting strength may be due to both weight and fabric density decreases and higher curing temperature. Air permeability decrease may be due to the deposition of ZnO NPs throughout the surface, which leads to a higher cover factor.

Table 3.2: Physical properties of control and ZnO NPs coated cotton fabrics.

Physical properties		Control fabric	Coated fabric	Standard
Weight (g/m^2)		147	142	ISO 12127:2003
Fabric density (number of yarns/10 cm)	Wales	161	158	ISO 1049-2:2000
	Course	185	181	
Bursting strength (KPa)		180.5	177.8	ISO 13938-1:1999
Air permeability (cm^3 cm^{-2} s^{-1})		75.1	73.9	ISO 9237:1999

3.3.10 Photocatalytic activity of coated fabric

The UV-vis spectrophotometer was used to track the photocatalytic activity of the coated fabric where methylene blue was used as a model dye. The kinetics of dye degradation was monitored at 663 nm, depicted in Figure3.10 (a). The UV radiation forms an electron-hole pair in the ZnO photocatalyst, which forms reactive oxygen species.[54,55] The formation of electrons in the conduction band and holes in the valence band occurs as a result of electron transfer when the energy of the incident radiation is equal to or higher than the band gap of ZnO NPs (3.07 eV according to the DASF method).[56] These ROS break down the MB dye. The photocatalytic activity of ZnO NPs was due to donor states produced by flaw sites like oxygen vacancies and interstitial zinc atoms and acceptor states produced by oxygen vacancies and zinc vacancies.[57] Interfacial electron transfer mainly occurs between oxygen vacancies when exposed to UV radiation.[50] The schematic diagram of the photocatalysis mechanism is shown in Figure 3.10 (b).
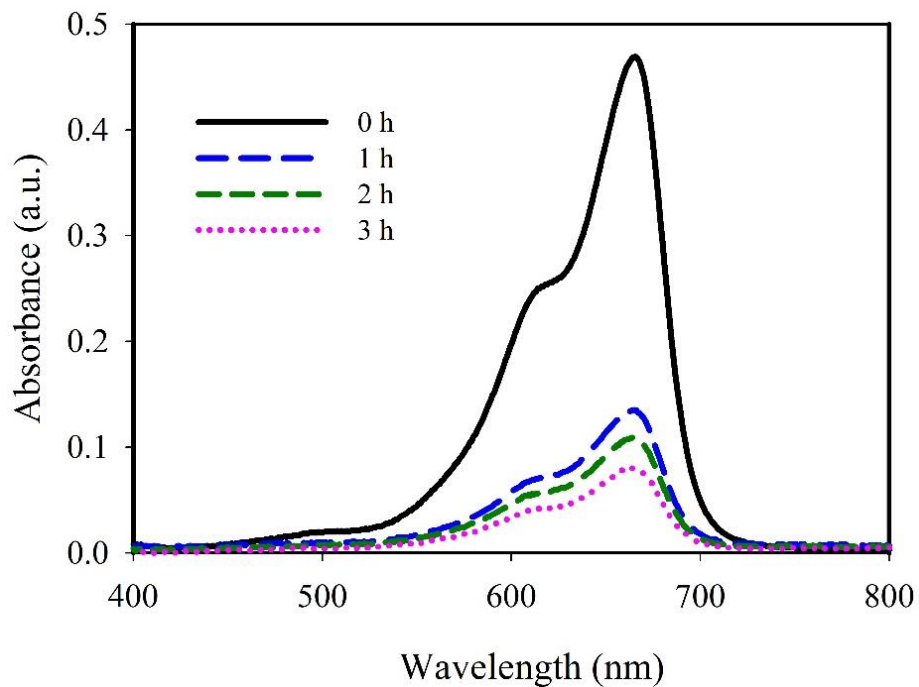
Figure 3.10: (a) UV-vis absorption spectrum of MB dye using ZnO NPs coated cotton fabric under UV irradiation.
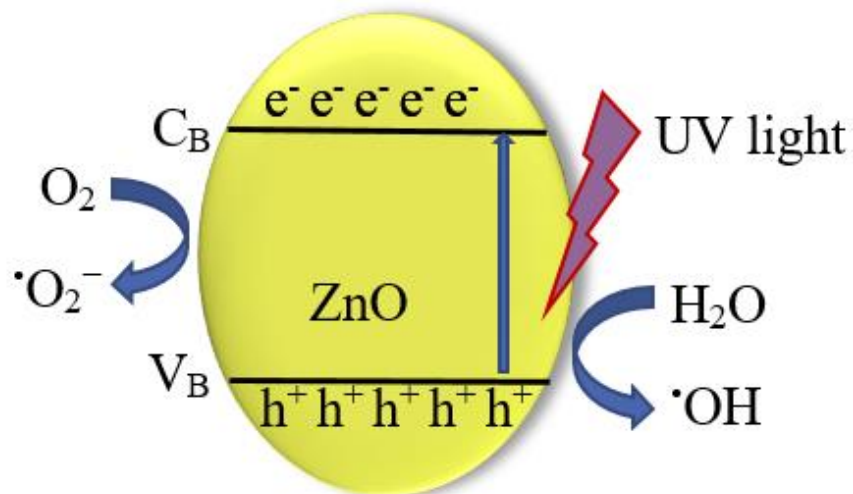
Figure 3.10: (b) Schematic illustration of the photocatalytic mechanism of ZnO NPs under UV light.

The mechanism of photocatalytic activities of ZnO NPs can be summarized in the following reactions (3.17 (a-l)):

$$ZnO + h\nu \rightarrow ZnO\ (e^- + h^+) \qquad (3.17(a))$$

$$ZnO(e^-) + O_2 \rightarrow ZnO + {}^{\bullet}O_2{}^- \qquad (3.17(b))$$

$$ZnO(h^+) + H_2O \rightarrow ZnO + {}^{\bullet}OH + H^+ \qquad (3.17(c))$$

$$ZnO(h^+) + 2H_2O \rightarrow ZnO + H_2O_2 + 2H^+ \qquad (3.17(d))$$

$${}^{\bullet}O_2{}^- + H^+ \rightarrow {}^{\bullet}HO_2 \qquad (3.17(e))$$

$${}^{\bullet}O_2{}^- + H_2O_2 \rightarrow {}^{\bullet}OH + OH^- + O_2 \qquad (3.17(f))$$

$$ZnO(h^+) + OH^- \rightarrow ZnO + {}^{\bullet}OH \qquad (3.17(g))$$

$$ZnO(e^-) + {}^{\bullet}HO_2 \rightarrow ZnO + HO_2{}^- \qquad (3.17(h))$$

$$HO_2{}^- + H^+ \rightarrow H_2O_2 \qquad (3.17(i))$$

$$2{}^{\bullet}HO_2 \rightarrow O_2 + H_2O_2 \qquad (3.17(j))$$

$$ZnO + H_2O_2 \rightarrow ZnO\ (e^-) + {}^{\bullet}O_2{}^- + 2H^+ \qquad (3.17(k))$$

$$ZnO(e^-) + H_2O_2 \rightarrow ZnO + {}^{\bullet}OH + OH^- \qquad (3.17(l))$$
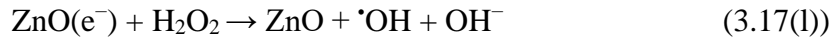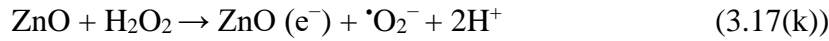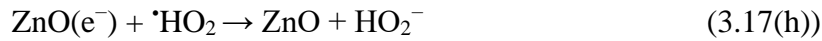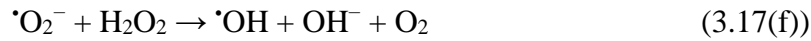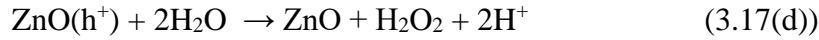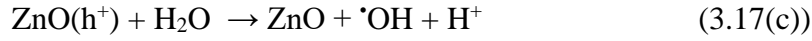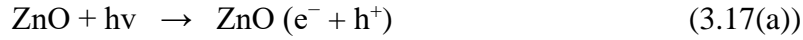
Negative electrons at the conduction band reduce oxygen molecules to form the superoxide radical anions, and holes at the valence band oxidize water molecules to form hydroxyl groups (${}^{\bullet}OH$).[27,58] Other organic compounds, including MB, are destroyed by these ROS.[59,60]
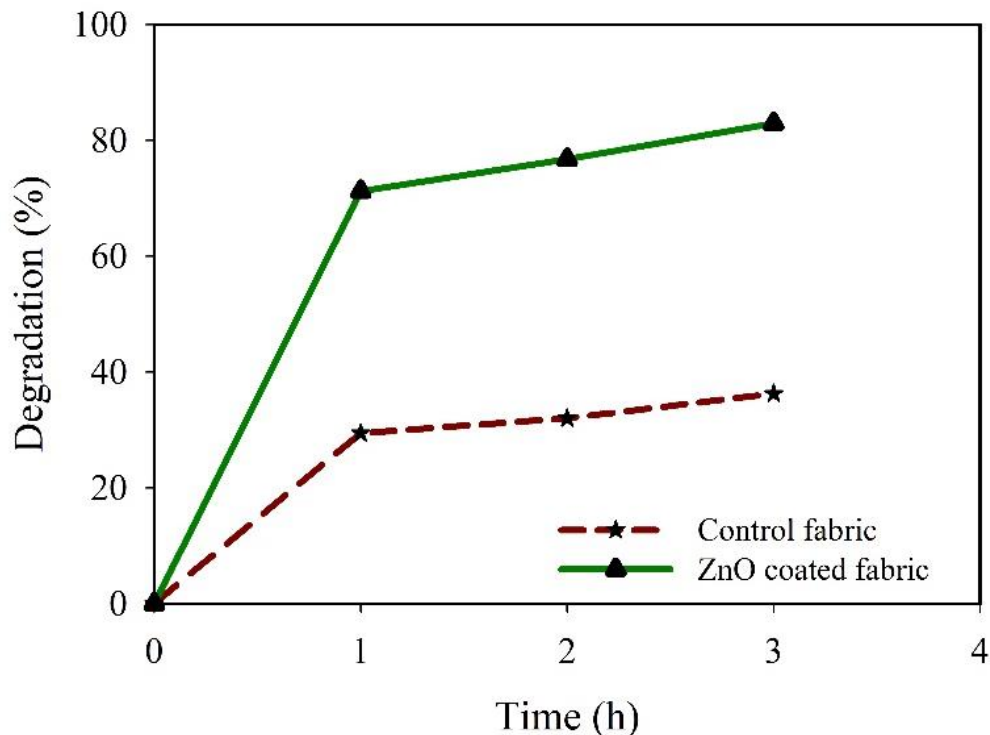
Figure 3.11: Dye degradation (%) of control and ZnO NPs coated cotton fabrics in an aqueous solution as a function of UV irradiation time.

The dye degradation (%) of both control and ZnO NPs coated cotton fabrics were shown in Figure 3.11, where degradation (%) of coated fabric is increased from 72% to 83% under 1 to 3 h irradiation time compared with control one.

3.3.11 Self-cleaning property of coated fabric

Coffee includes up to around 5% of caffeine, which also contains acids (7-17%), trigonelline (2%), sugar (5%), protein (6%), polymeric carbohydrates (30-50%), and colorful additives (20%-35%). (Approximately).[51] Coffee stains on clothing are caused mainly by the water-soluble and acidic colored components, pigments, and polymers in coffee. The condensation process and heat degradation produce coffee's oligomeric or polymeric coloring pigments. Coffee stains are compatible with cotton fabrics because the bulk of colorful components and pigments in coffee comprise hydroxyl groups and conjugated double bonds, which attach fibers via Van der Waals or dispersion forces. Contrarily, curry masala combines various components, including turmeric, cumin,

coriander seed, black paper, red chilies, ginger, salt, cloves, garlic, mustard, etc. Although this curry masala and hot water are used to create the curry stain, the turmeric (*Curcuma longa*) mark on cotton is what the curry stain primarily reveals. Curry paste causes yellow stains on cotton textiles primarily due to the binding of yellow pigments, most of which are curcumin and its derivatives, with cotton cellulose. The curcuminoid found in turmeric is mainly made up of curcumin (around 77%).[61] About 3-5% of the overall ingredients in turmeric are curcumin, a yellow substance composed of two carbonyl groups and two phenolic hydroxyl groups that allow it to reside in solution as keto-enol tautomers shown in Figure3.12.[62] Zinc from ZnO can form compounds with curcumin through its β-diketo group. Summarized data of related NPs used for achieving self-cleaning properties are shown in Table3.3.
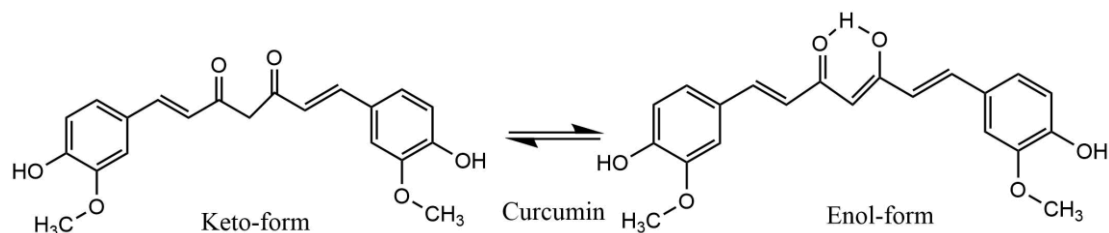
Figure 3.12: Schematic structure of curcumin.[62]

Table 3.3: Summarized data of related NPs for achieving self-cleaning properties.

Types of coating on the fiber	Types of self-cleaning	The efficiency of coating for self-cleaning	Ref.
Cotton and PC blend fabrics coated with ZnO NPs	Chemical self-cleaning	-eliminated the ketchup stain under sunlight irradiation for 24 h.	[63]
Cotton fabrics exploiting ZnO NPs by dip-pad-dry-cure method	Chemical self- cleaning	-exhibited good photocatalytic activity against methylene blue and Eosin yellowish under UV-vis irradiation.	[64]
Cotton fabrics treated with ZnO by dip-pad-dry-cure method	Chemical self- cleaning	-removal of Methylene Blue stains was used to evaluate the self-cleaning properties -showed the photocatalytic degradation rate of Methylene Blue increased with increasing ZnO NP content from 3 to 9 wt% against 6, 12, and 24 h of irradiation under the solar simulator.	[26]
In situ synthesis of polyester woven fabric with ZnO nanorods	Chemical self- cleaning	-exhibited good photocatalytic activity against C. I. acid blue 9 under UV light for 24 h.	[15]
Cotton fabrics coated with ZnO NPs by dip-pad-dry-cure method	Chemical self- cleaning	-eliminated coffee and curry stains under xenon light.	Present paper

The self-cleaning property of the ZnO NPs coated cotton can be assessed by the degradation of organic dirt such as coffee and curry stains. Figure 3.13showed the percentage of degradation of coffee and curry stains on control and ZnO NPs coated cotton fabrics under 20 h irradiation by Xenotest light exposure and weathering test instrument (Q-SUN, Xenon Test Chamber, Model Xe-2, USA). When ZnO NPs are subjected to UV radiation, the electrons in the valence band of ZnO will be excited to the conduction band, producing two types of opposing charged carriers: the hole (h^+) and electron (e^-). The produced hole (h^+) oxidizes the moisture (H_2O) in the air to a hydroxyl radical ($^•OH$), while

the electron (e^-) reduces oxygen into a superoxide anion ($^•O_2^-$). These superoxide anions and hydroxyl radicals are responsible for redox reactions that primarily cause the breakdown of organic materials (coffee stain and curry stain) into small molecules (CO_2 and H_2O).[65,66]
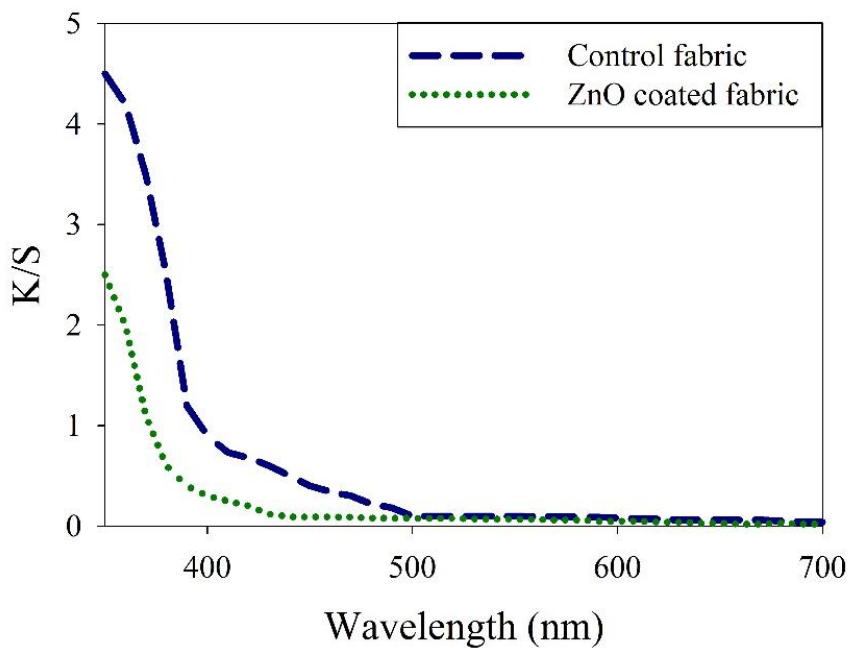
Figure 3.13: Color strength (*K/S*) of the coffee stain of control and coated cotton fabric after 20 h irradiation.
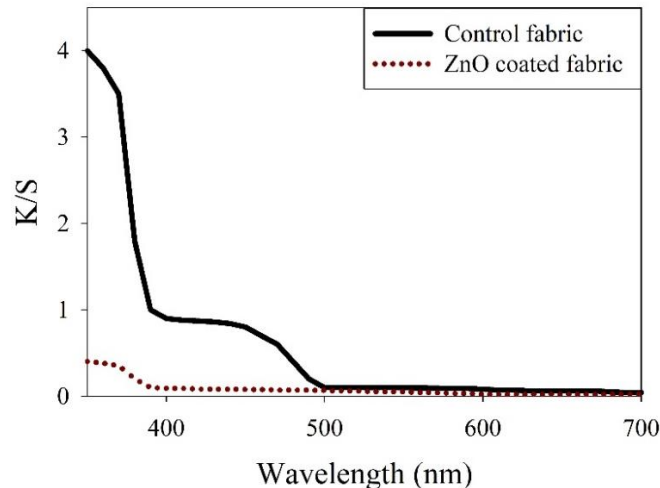
Figure 3.14: Color strength (*K/S*) of the curry stain of control and coated cotton fabric after 20 h irradiation.

The *K*/*S* values (absorption and scattering coefficients; color intensity) of exposed and unexposed portions of the stained samples were determined after 20 h of irradiation and expressed in Table 3.4. The percentage of decrease in *K*/*S* value for the exposed sample of the coffee stain is 67.1%, whereas, for the exposed sample of the curry stain is 81.8%.

Table 3.4: Percentage (%) decrease in *K*/*S* of ZnO NPs coated cotton fabric.

Types of stains	Unexposed Stain (*K/S*)	Exposed Stain (*K/S*)	% of the decrease in *K/S* value
Coffee stain	100	32.9	67.1%
Curry stain	100	18.2	81.8%

3.4 Conclusions

ZnO NPs have been synthesized successfully, characterized, and uniformly applied to the fabric surface. The photocatalytic activity of the ZnO NPs coated fabric was examined by degrading MB using UV radiation. 83% of MB was degraded in 3 h UV exposure. ZnO NP-coated cotton textiles can clean 67% coffee stain and 82% curry stain after 20 h of xenon UV light exposure. Coated textiles demonstrate excellent photocatalytic activity and outstanding self-cleaning properties. This multifunctional fabric with high value-added has

many real-world uses and keeps up with emerging trends. We think the textile industry can use this multifunctional fabric in exciting ways.

References:

(1) Arputharaj, A.; Nadanathangam, V.; Shukla, S. R. A Simple and Efficient Protocol to Develop Durable Multifunctional Property to Cellulosic Materials Using in Situ Generated Nano-ZnO. *Cellulose* **2017**, *24* (8), 3399–3410. https://doi.org/10.1007/s10570-017-1335-5.

(2) Avazpour, S.; Karimi, L.; Zohoori, S. Simultaneous Coloration and Functional Finishing of Cotton Fabric Using Ag/ZnO Nanocomposite. *Color. Technol.* **2017**, *133* (5), 423–430. https://doi.org/10.1111/cote.12296.

(3) Nourbakhsh, S.; Montazer, M.; khandaghabadi, Z. Zinc Oxide Nano Particles Coating on Polyester Fabric Functionalized through Alkali Treatment. *J. Ind. Text.* **2018**, *47* (6), 1006–1023. https://doi.org/10.1177/1528083716657819.

(4) Mohammadi, M.; Karimi, L.; Mirjalili, M. Simultaneous Synthesis of Nano ZnO and Surface Modification of Polyester Fabric. *Fibers Polym.* **2016**, *17* (9), 1371–1377. https://doi.org/10.1007/s12221-016-6497-5.

(5) Sivakumar, A.; Murugan, R.; Sundaresan, K. Certain Investigations on the Effect of Nano Metal Oxide Finishes on the Multifunctional Characteristics of Cotton Fabrics. *J. Ind. Text.* **2013**, *43* (2), 155–173. https://doi.org/10.1177/1528083712450741.

(6) Shahidi, S.; Zarei, L.; Elahi, S. M. Fabrication of ZnO Nano Particles Using Sonochemical Method and Applying on Cotton Fabric Using in Situ and Pad-Dry-Cure Methods. *Fibers Polym.* **2014**, *15* (12), 2472–2479. https://doi.org/10.1007/s12221-014-2472-1.

(7) El-Nahhal, I. M.; Zourab, S. M.; Kodeh, F. S.; Elmanama, A. A.; Selmane, M.; Genois, I.; Babonneau, F. Nano-Structured Zinc Oxide-Cotton Fibers: Synthesis, Characterization and Applications. *J. Mater. Sci. Mater. Electron.* **2013**, *24* (10), 3970–3975. https://doi.org/10.1007/s10854-013-1349-1.

(8) Zhang, D.; Chen, L.; Fang, di; Toh, G. W.; Yue, X.; Chen, Y.; Lin, H. In Situ Generation and Deposition of Nano-ZnO on Cotton Fabric by Hyperbranched Polymer for Its Functional Finishing. *Text. Res. J.* **2013**, *83* (15), 1625–1633. https://doi.org/10.1177/0040517512474362.

(9)   Khanjani, S.; Morsali, A.; Joo, S. W. In Situ Formation Deposited ZnO Nanoparticles on Silk Fabrics under Ultrasound Irradiation. *Ultrason. Sonochem.* **2013**, *20* (2), 734–739. https://doi.org/10.1016/j.ultsonch.2012.09.013.

(10)   Boticas, I.; Dias, D.; Ferreira, D.; Magalhães, P.; Silva, R.; Fangueiro, R. Superhydrophobic Cotton Fabrics Based on ZnO Nanoparticles Functionalization. *SN Appl. Sci.* **2019**, *1* (11), 1–9. https://doi.org/10.1007/s42452-019-1423-2.

(11)   Wang, M.; Peng, M.; Weng, Y. X.; Li, Y. D.; Zeng, J. B. Toward Durable and Robust Superhydrophobic Cotton Fabric through Hydrothermal Growth of ZnO for Oil/Water Separation. *Cellulose* **2019**, *26* (13–14), 8121–8133. https://doi.org/10.1007/s10570-019-02635-2.

(12)   Jin, G. W.; Kim, J. Y.; Min, B. G. Superhydrophobic and Antibacterial Properties of Cotton Fabrics Treated with PVDF and Nano-ZnO through Phase Inversion Process. *Fibers Polym.* **2018**, *19* (9), 1835–1842. https://doi.org/10.1007/s12221-018-8313-x.

(13)   Arciniegas-Grijalba, P. A.; Patiño-Portela, M. C.; Mosquera-Sánchez, L. P.; Guerrero-Vargas, J. A.; Rodríguez-Páez, J. E. ZnO Nanoparticles (ZnO-NPs) and Their Antifungal Activity against Coffee Fungus Erythricium Salmonicolor. *Appl. Nanosci.* **2017**, *7* (5), 225–241. https://doi.org/10.1007/s13204-017-0561-3.

(14)   Shaker, K.; Ashraf, M.; Jabbar, M.; Shahid, S.; Nawab, Y.; Zia, J.; Rehman, A. Bioactive Woven Flax-Based Composites: Development and Characterisation. *J. Ind. Text.* **2016**, *46* (2), 549–561. https://doi.org/10.1177/1528083715591579.

(15)   Ashraf, M.; Champagne, P.; Campagne, C.; Perwuelz, A.; Dumont, F.; Leriche, A. Study the Multi Self-Cleaning Characteristics of ZnO Nanorods Functionalized Polyester Fabric. *J. Ind. Text.* **2016**, *45* (6), 1440–1456. https://doi.org/10.1177/1528083714562086.

(16)   Çakir, B. A.; Budama, L.; Topel, Ö.; Hoda, N. Synthesis of ZnO Nanoparticles Using PS-b-PAA Reverse Micelle Cores for UV Protective, Self-Cleaning and Antibacterial Textile Applications. *Colloids Surfaces A Physicochem. Eng. Asp.* **2012**, *414*, 132–139. https://doi.org/10.1016/j.colsurfa.2012.08.015.

(17)   Samanta, A. K.; Bhattacharyya, R.; Jose, S.; Basu, G.; Chowdhury, R. Fire Retardant Finish of Jute Fabric with Nano Zinc Oxide. *Cellulose* **2017**, *24* (2), 1143–1157. https://doi.org/10.1007/s10570-016-1171-z.

(18)   El-Hameed El-Ebissy, A. A.; Michael, M. N.; Eldin Abdelhameed, S. K. Effect of Nano Zinc Oxide on the Structural Characteristic, Tensile Thermal Properties of Textile Fabrics. *J. Ind. Text.* **2016**, *46* (1), 130–142. https://doi.org/10.1177/1528083715576321.

(19)   Wasim, M.; Naeem, M. A.; Khan, M. R.; Mushtaq, M.; Wei, Q. Preparation and Characterization of Copper/Zinc Nanoparticles-Loaded Bacterial Cellulose for Electromagnetic Interference Shielding. *J. Ind. Text.* **2022**, *51* (4), 7072S-7088S. https://doi.org/10.1177/1528083720921531.

(20)   Abou Taleb, M.; Mowafi, S.; El-Sayed, H.; El-Newashy, R. Facile Development of Electrically Conductive Comfortable Fabrics Using Metal Ions. *J. Ind. Text.* **2022**, *51* (7), 1100–1120. https://doi.org/10.1177/1528083719893713.

(21)   Senthilkumar, N.; Vivek, E.; Shankar, M.; Meena, M.; Vimalan, M.; Potheher, I. V. Synthesis of ZnO Nanorods by One Step Microwave-Assisted Hydrothermal Route for Electronic Device Applications. *J. Mater. Sci. Mater. Electron.* **2018**, *29* (4), 2927–2938. https://doi.org/10.1007/s10854-017-8223-5.

(22)   Perelshtein, I.; Applerot, G.; Perkas, N.; Wehrschetz-Sigl, E.; Hasmann, A.; Guebitz, G. M.; Gedanken, A. Antibacterial Properties of an in Situ Generated and Simultaneously Deposited Nanocrystalline ZnO on Fabrics. *ACS Appl. Mater. Interfaces* **2009**, *1* (2), 361–366. https://doi.org/10.1021/am8000743.

(23)   Gupta, K. K.; Jassal, M.; Agrawal, A. K. Functional Finishing of Cotton Using Titanium Dioxide and Zinc Oxide Nanoparticles. *Res. J. Text. Appar.* **2007**, *11* (3), 1–10. https://doi.org/10.1108/RJTA-11-03-2007-B001.

(24)   Khan, M. Q.; Lee, H.; Koo, J. M.; Khatri, Z.; Sui, J.; Im, S. S.; Zhu, C.; Kim, I. S. Self-Cleaning Effect of Electrospun Poly (1,4-Cyclohexanedimethylene Isosorbide Terephthalate) Nanofibers Embedded with Zinc Oxide Nanoparticles. *Text. Res. J.* **2018**, *88* (21), 2493–2498. https://doi.org/10.1177/0040517517723026.

(25)   Wang, Y.; Zhu, S.; Chen, X.; Tang, Y.; Jiang, Y.; Peng, Z.; Wang, H. One-Step Template-Free Fabrication of Mesoporous ZnO/TiO 2 Hollow Microspheres with Enhanced Photocatalytic Activity. *Appl. Surf. Sci.* **2014**, *307*, 263–271. https://doi.org/10.1016/j.apsusc.2014.04.023.

(26)   Zhu, C.; Shi, J.; Xu, S.; Ishimori, M.; Sui, J.; Morikawa, H. Design and Characterization of Self-Cleaning Cotton Fabrics Exploiting Zinc Oxide Nanoparticle-Triggered Photocatalytic Degradation. *Cellulose* **2017**, *24* (6), 2657–2667. https://doi.org/10.1007/s10570-017-1289-7.

(27)   Ashraf, M.; Champagne, P.; Perwuelz, A.; Campagne, C.; Leriche, A. Photocatalytic Solution Discoloration and Self-Cleaning by Polyester Fabric Functionalized with ZnO Nanorods. *J. Ind. Text.* **2015**, *44* (6), 884–898. https://doi.org/10.1177/1528083713519662.

(28)   Zare, M.; Namratha, K.; Alghamdi, S.; Mohammad, Y. H. E.; Hezam, A.; Zare, M.; Drmosh, Q. A.; Byrappa, K.; Chandrashekar, B. N.; Ramakrishna, S.; Zhang, X. Novel Green Biomimetic Approach for Synthesis of ZnO-Ag Nanocomposite; Antimicrobial Activity against Food-Borne Pathogen, Biocompatibility and Solar Photocatalysis. *Sci. Rep.* **2019**, *9* (1), 1–15. https://doi.org/10.1038/s41598-019-44309-w.

(29)   Diacon, A.; Mocanu, A.; Răducanu, C. E.; Busuioc, C.; Șomoghi, R.; Trică, B.; Dinescu, A.; Rusen, E. New Carbon/ZnO/Li$_2$O Nanocomposites with Enhanced Photocatalytic Activity. *Sci. Rep.* **2019**, *9* (1), 1–14. https://doi.org/10.1038/s41598-019-53335-7.

(30)   Xu, R. Progress in Nanoparticles Characterization: Sizing and Zeta Potential Measurement. *Particuology* **2008**, *6* (2), 112–115. https://doi.org/10.1016/j.partic.2007.12.002.

(31)   Lessan, F.; Montazer, M.; Moghadam, M. B. Thermochimica Acta A Novel Durable Flame-Retardant Cotton Fabric Using Sodium Hypophosphite , Nano TiO$_2$ and Maleic Acid. *Thermochim. Acta* **2011**, *520* (1–2), 48–54. https://doi.org/10.1016/j.tca.2011.03.012.

(32)   Chandra, H.; Patel, D.; Kumari, P.; Jangwan, J. S.; Yadav, S. Phyto-Mediated Synthesis of Zinc Oxide Nanoparticles of Berberis Aristata: Characterization, Antioxidant Activity and Antibacterial Activity with Special Reference to Urinary Tract Pathogens. *Mater. Sci. Eng. C* **2019**, *102* (July 2018), 212–220. https://doi.org/10.1016/j.msec.2019.04.035.

(33)   Wang, L.; Ding, Y.; Shen, Y.; Cai, Z.; Zhang, H.; Xu, L. Study on Properties of Modified Nano-TiO2 and Its Application on Antibacterial Finishing of Textiles. *J. Ind. Text.* **2014**, *44* (3), 351–372. https://doi.org/10.1177/1528083713487758.

(34)   Niu, H.; Zhou, D.; Yang, X.; Li, X.; Wang, Q.; Qu, F. Towards Three-Dimensional Hierarchical ZnO Nanofiber@Ni(OH)$_2$ Nanoflake Core-Shell Heterostructures for High-Performance Asymmetric Supercapacitors. *J. Mater. Chem. A* **2015**, *3* (36), 18413–18421. https://doi.org/10.1039/c5ta04311e.

(35)   Tarigh, G. D.; Shemirani, F.; Maz'hari, N. S. Fabrication of a Reusable Magnetic Multi-Walled Carbon Nanotube-TiO$_2$ Nanocomposite by Electrostatic Adsorption: Enhanced Photodegradation of Malachite Green. *RSC Adv.* **2015**, *5* (44), 35070–35079. https://doi.org/10.1039/c4ra15593a.

(36)   Gharpure, S.; Yadwade, R.; Ankamwar, B. Non-Antimicrobial and Non-Anticancer Properties of ZnO Nanoparticles Biosynthesized Using Different Plant Parts of Bixa Orellana. *ACS Omega* **2022**, *7* (2), 1914–1933. https://doi.org/10.1021/acsomega.1c05324.

(37) Sharwani, A. A.; Narayanan, K. B.; Khan, M. E.; Han, S. S. Photocatalytic Degradation Activity of Goji Berry Extract Synthesized Silver-Loaded Mesoporous Zinc Oxide (Ag@ZnO) Nanocomposites under Simulated Solar Light Irradiation. *Sci. Rep.* **2022**, *12* (1), 1–18. https://doi.org/10.1038/s41598-022-14117-w.

(38) Jadhav, J.; Biswas, S. Structural and Electrical Properties of ZnO:Ag Core-Shell Nanoparticles Synthesized by a Polymer Precursor Method. *Ceram. Int.* **2016**, *42* (15), 16598–16610. https://doi.org/10.1016/j.ceramint.2016.07.081.

(39) Shaban, M.; Mohamed, F.; Abdallah, S. Production and Characterization of Superhydrophobic and Antibacterial Coated Fabrics Utilizing ZnO Nanocatalyst. *Sci. Rep.* **2018**, *8* (1), 1–15. https://doi.org/10.1038/s41598-018-22324-7.

(40) Tauc, J.; Grigorovici, R.; Vancu, A. Optical Properties and Electronic Structure of Amorphous Germanium. *Phys. Stat. Sol.* (b) **1966**, *15*(2), 627–637. https://doi.org/10.1002/pssb.19660150224.

(41) Shahmoradi, Y.; Souri, D. Growth of Silver Nanoparticles within the Tellurovanadate Amorphous Matrix: Optical Band Gap and Band Tailing Properties, beside the Williamson-Hall Estimation of Crystallite Size and Lattice Strain. *Ceram. Int.* **2019**, *45* (6), 7857–7864. https://doi.org/10.1016/j.ceramint.2019.01.094.

(42) Seid, E. T.; Dejene, F. B. Co-Solvent Medium Volume Ratio Effect on the Properties of Re Fl Uxed Sol-Gel Synthesized ZnO Nanopowder. *J. Alloys Compd.* **2019**, *787*, 658–665. https://doi.org/10.1016/j.jallcom.2019.02.163.

(43) Thamri, S.; Sta, I.; Jlassi, M.; Hajji, M.; Ezzaouia, H. Materials Science in Semiconductor Processing Fabrication of ZnO-NiO Nanocomposite Thin Fi Lms and Experimental Study of the e Ff Ect of the NiO , ZnO Concentration on Its Physical Properties. **2017**, *71* (April), 310–320. https://doi.org/10.1016/j.mssp.2017.08.017.

(44) Król-Górniak, A.; Railean, V.; Pomastowski, P.; Płociński, T.; Gloc, M.; Dobrucka, R.; Kurzydłowski, K. J.; Buszewski, B. Comprehensive Study upon Physicochemical Properties of Bio-ZnO NCs. *Sci. Rep.* **2023**, *13* (1), 1–21. https://doi.org/10.1038/s41598-023-27564-w.

(45) Chauhan, A.; Verma, R.; Kumari, S.; Sharma, A.; Shandilya, P.; Li, X.; Batoo, K. M.; Imran, A.; Kulshrestha, S.; Kumar, R. Photocatalytic Dye Degradation and Antimicrobial Activities of Pure and Ag-Doped ZnO Using Cannabis Sativa Leaf Extract. *Sci. Rep.* **2020**, *10* (1), 1–16. https://doi.org/10.1038/s41598-020-64419-0.

(46)   Bindu, P.; Thomas, S. Estimation of Lattice Strain in ZnO Nanoparticles: X-Ray Peak Profile Analysis. *J. Theor. Appl. Phys.* **2014**, *8* (4), 123–134. https://doi.org/10.1007/s40094-014-0141-9.

(47)   Zamiri, R.; Rebelo, A.; Zamiri, G.; Adnani, A.; Kuashal, A.; Belsley, M. S.; Ferreira, J. M. F. Far-Infrared Optical Constants of ZnO and ZnO/Ag Nanostructures. *RSC Adv.* **2014**, *4* (40), 20902–20908. https://doi.org/10.1039/c4ra01563k.

(48)   Yang, H. G.; Sun, C. H.; Qiao, S. Z.; Zou, J.; Liu, G.; Smith, S. C.; Cheng, H. M.; Lu, G. Q. Anatase TiO2 Single Crystals with a Large Percentage of Reactive Facets. *Nature* **2008**, *453* (7195), 638–641. https://doi.org/10.1038/nature06964.

(49)   Xia, Y.; Xiong, Y.; Lim, B.; Skrabalak, S. E. Shape-Controlled Synthesis of Metal Nanocrystals: Simple Chemistry Meets Complex Physics? *Angew. Chemie - Int. Ed.* **2009**, *48* (1), 60–103. https://doi.org/10.1002/anie.200802248.

(50)   Shateri-Khalilabad, M.; Yazdanshenas, M. E. Bifunctionalization of Cotton Textiles by ZnO Nanostructures: Antimicrobial Activity and Ultraviolet Protection. *Text. Res. J.* **2013**, *83* (10), 993–1004. https://doi.org/10.1177/0040517512468812.

(51)   Perkins, R.; Drake, G. L.; Reeves, W. A. DTA and TGA Studies of Flame-Resistant Fabrics. *Appl. Polym. Sci.* **1966**, *10*, 1041–1066. https://doi.org/10.1002/app.1966.070100708.

(52)   Noorian, S. A.; Hemmatinejad, N.; Navarro, J. A. R. Ligand modified cellulose fabrics as support of zinc oxide nanoparticles for UV protection and antimicrobial activities, *Int. J. Biol. Macromol*, **2020**, 154, 1215 – 1226. https://doi.org/10.1016/j.ijbiomac.2019.10.276

(53)   Siller, M.; Amer, H.; Bacher, M.; Roggenstein, W.; Rosenau, T.; Potthast, A. Effects of Periodate Oxidation on Cellulose Polymorphs. *Cellulose* **2015**, *22* (4), 2245–2261. https://doi.org/10.1007/s10570-015-0648-5.

(54)   EL-Dafrawy, S. M.; Tarek, M.; Samra, S.; Hassan, S. M. Synthesis, Photocatalytic and Antidiabetic Properties of ZnO/PVA Nanoparticles. *Sci. Rep.* **2021**, *11* (1), 1–11. https://doi.org/10.1038/s41598-021-90846-8.

(55)   Chauhan, M.; Jasrotia, T.; Kaur, G.; Prakash, C.; Kumar, R.; Dilbaghi, N.; Chaudhary, G. R.; Kumar, S. Investigating the Efficiency of α-Bismuth Zinc Oxide Heterostructure Composite/UV-LED in Methylene Blue Dye Removal and Evaluation of Its Antimicrobial Activity. *Environ. Res.* **2020**, *180*, 108857. https://doi.org/10.1016/j.envres.2019.108857.

(56)   Sun, Z. P.; Liu, L.; Zhang, L.; Jia, D. Z. Rapid Synthesis of ZnO Nano-Rods by One-Step, Room-Temperature, Solid-State Reaction and Their Gas-Sensing Properties. *Nanotechnology* **2006**, *17* (9), 2266–2270. https://doi.org/10.1088/0957-4484/17/9/032.

(57)   Nair, M. G.; Nirmala, M.; Rekha, K.; Anukaliani, A. Structural, Optical, Photo Catalytic and Antibacterial Activity of ZnO and Co Doped ZnO Nanoparticles. *Mater. Lett.* **2011**, *65* (12), 1797–1800. https://doi.org/10.1016/j.matlet.2011.03.079.

(58)   Krishnakumar, B.; Imae, T. Chemically Modified Novel Pamam-Zno Nanocomposite: Synthesis, Characterization and Photocatalytic Activity. *Appl. Catal. A Gen.* **2014**, *486*, 170–175. https://doi.org/10.1016/j.apcata.2014.08.010.

(59)   Peng, H.; Liu, X.; Tang, W.; Ma, R. Facile Synthesis and Characterization of ZnO Nanoparticles Grown on Halloysite Nanotubes for Enhanced Photocatalytic Properties. *Sci. Rep.* **2017**, *7* (1), 1–10. https://doi.org/10.1038/s41598-017-02501-w.

(60)   Wang, X.; Yang, F.; Yang, W.; Yang, X. A Study on the Antibacterial Activity of One-Dimensional ZnO Nanowire Arrays: Effects of the Orientation and Plane Surface. *Chem. Commun.* **2007**, No. 42, 4419–4421. https://doi.org/10.1039/b708662h.

(61)   Buddee, S.; Wongnawa, S.; Sriprang, P.; Sriwong, C. Curcumin-Sensitized TiO2for Enhanced Photodegradation of Dyes under Visible Light. *J. Nanoparticle Res.* **2014**, *16* (4). https://doi.org/10.1007/s11051-014-2336-z.

(62)   Moussawi, R. N.; Patra, D. Modification of Nanostructured ZnO Surfaces with Curcumin: Fluorescence-Based Sensing for Arsenic and Improving Arsenic Removal by ZnO. *RSC Adv.* **2016**, *6* (21), 17256–17268. https://doi.org/10.1039/c5ra20221c.

(63)   Kathirvelu, S.; D'Souza, L.; Dhurai, B. Study of Stain-Eliminating Textiles Using ZnO Nanoparticles. *J. Text. Inst.* **2010**, *101* (6), 520–526. https://doi.org/10.1080/00405000802563693.

(64)   Moafi, H. F.; Shojaie, A. F.; Zanjanchi, M. A. Photocatalytic Self-Cleaning Properties of Cellulosic Fibers Modified by Nano-Sized Zinc Oxide. *Thin Solid Films* **2011**, *519* (11), 3641–3646. https://doi.org/10.1016/j.tsf.2011.01.347.

(65)   Sricharussin, W.; Threepopnatkul, P.; Neamjan, N. Effect of Various Shapes of Zinc Oxide Nanoparticles on Cotton Fabric for UV-Blocking and Anti-Bacterial Properties. *Fibers Polym.* **2011**, *12* (8), 1037–1041. https://doi.org/10.1007/s12221-011-1037-9.

(66) Wang, Y.; Baheti, V.; Khan, M. Z.; Viková, M.; Yang, K.; Yang, T.; Militký, J. A Facile Approach to Develop Multifunctional Cotton Fabrics with Hydrophobic, Self-Cleaning and UV Protection Properties Using ZnO Particles and Fluorocarbon. *J. Text. Inst.* **2021**. https://doi.org/10.1080/00405000.2021.1975905.

4. Silver Nanoparticles Coated Cotton Fabric for UV Protection, Self-cleaning, and Antibacterial Textiles

Abstract

Silver nanoparticles were synthesized by wet chemical methods and characterized using dynamic light scattering , Fourier transform infrared spectroscopy, UV-vis spectroscopy, X-ray diffraction , and transmission electron microscopy. The cotton fabric was coated with Ag NPs using an acrylic binder by a pad-dry-cure technique. The morphological characteristics of Ag NPs coated fabric were assessed through scanning electron microscopy . The antibacterial effectiveness of Ag NPs coated cotton fabric was evaluated separately against *Staphylococcus aureus*, a Gram-positive bacterium, and *Escherichia coli*, a Gram-negative bacterium. The results indicated a reduction of over 98% for *Staphylococcus aureus* and around 99.9% for *Escherichia coli* bacteria. The coated fabric demonstrated a favorable ultraviolet protection factor 26. The self-cleaning properties were examined using curry stains as model dirt. The coated fabric effectively removed curry stains following a 20 h exposure to xenon UV light.

4.1 Introduction

The application of nanotechnology in the textile industry is primarily aimed at developing functional textiles that exhibit desirable properties such as antistatic behavior, wrinkle resistance, water and oil repellency, self-cleaning capabilities, flame retardancy, antimicrobial activity, UV protection, enhanced comfort of synthetic fabrics, etc.[1] Functional textiles can be produced by applying metallic nanoparticles using various coating methods. Due to their distinctive and improved optical, electrical, magnetic, biomedical, and catalytic properties in comparison to conventional macroscopic materials, metallic nanoparticles have garnered significant interest in the textile research.[2] The exceptional characteristics of these materials can be attributed primarily to their elevated surface area-to-volume ratios and augmented proportion of atoms located at the grain

boundaries. In this study, the Ag NPs coated cotton fabric is investigated as a means to confer ultraviolet (UV) protection, antimicrobial efficacy, and self-cleaning attributes.[3] Cotton is a highly esteemed textile fiber for use in clothing due to its exceptional properties, including biodegradability, regenerative capacity, hydrophilicity, softness, and skin affinity. Notwithstanding their widespread use, cotton fabrics cannot provide adequate protection against UV radiation and may create a conducive environment for the proliferation of microorganisms. Additionally, their high surface area and propensity to absorb moisture render them susceptible to bacterial attack. The addition of microorganisms to cotton fabric can result in unpleasant odors. The transmission of UV rays through cotton fabric has been found to lead to dermal infections and potential allergic reactions. So, production of cotton fabrics that possess a range of functionalities, such as UV protection, antibacterial activity, and self-cleaning capabilities is a crucial and urgent matter for application in smart and versatile textiles. Ag NPs have been widely employed to achieve these functionalities due to their wide range of antibacterial properties. The size of Ag NPs is a determining factor in their antimicrobial efficacy. The heightened antimicrobial effect is attributed to the extensive surface area resulting from the diminutive size of the particles.[4] While extensive research has been conducted on the antibacterial properties of fabrics coated with Ag NPs, there remains a dearth of studies on their effectiveness in terms of UV-protection and self-cleaning capabilities.

The current study elucidates the antibacterial efficacy, ultraviolet shielding capacity, and self-cleaning attributes of fabric coated with Ag NPs while ensuring sufficient underlying physical properties. The synthesis of Ag NPs is carried out via a wet chemical method. The systematic characterization of Ag NPs involves the utilization of various analytical techniques, including DLS, FTIR spectroscopy, UV-vis spectroscopy, XRD, and TEM. Using an acrylate binder in a pad-dry-cure technique immobilizes and enhances the binding of Ag NPs onto the surface of cotton fabric. The morphological characteristics of cotton fabric were evaluated SEM in conjunction with EDX spectroscopy. The study comprehensively examines the physical and thermal characteristics, colorimetric measurements, antibacterial efficacy, UV shielding, and self-cleansing attributes of Ag-coated cotton fabrics. The previous results have the potential to facilitate the advancement

of multifaceted textiles that possess antibacterial properties, safeguard against ultraviolet radiation, and exhibit self-cleaning characteristics.

4.2   Materials and methods

4.2.1   Materials

Silver nitrate (AgNO$_3$, reagent grade, Scharlau, Spain), cetyltrimethylammonium bromide (CTAB, >98%, Merck), NaBH$_4$ (>98%, ACROS organics, Belgium), binder of aqueous acrylate dispersion (Forbind OB 45, Fortune top Pte Ltd. New Taipei City, Taiwan) were used in the experiments without further purifications. HPLC grade water purification system (BOECO) was used for deionized water (conductivity: 0.055 µScm^{-1}) to produce all solutions. 100% cotton knit fabric with a single jersey structure after scouring and bleaching was used throughout all experiments.

4.2.2   Synthesis of Ag NPs

To synthesize Ag NPs, 0.09 mmol of CTAB was mixed in 50 mL deionized water as a capping and stabilizing agent under constant stirring at 300 rpm by a magnetic stirrer and heating at 40   ℃. Then the temperature of the solution was slowly decreased to room temperature. Afterward, a 25 mL aqueous solution of AgNO$_3$ was gradually added drop-wise to the above solution for 1 h. Then another 25 mL of 28 mM aqueous solution of NaBH$_4$ was slowly added to reduce Ag NPs. The color of the solution changed from white to dark brown because of surface plasmon resonance indicating the onset of the formation of Ag NPs. Then the solution was aged overnight and dried at 60 ℃ to get Ag NPs.[5]

4.2.3   Preparation of Ag NPs coated cotton fabric

Ag NPs were applied on cotton knit fabric (20 cm × 20 cm) by a dip-pad-dry-cure method. At first, padding was done by a standard laboratory instrument after immersion into 100 mL of Ag NPs dispersion for 5 min under constant stirring to prevent precipitation of NPs. Then padding was done with 1% binder in 100 mL distilled water with 2.5 m/min fabric speed and 2.8 kg/cm^2 padding pressure to maintain the pick-up% at about 70-75%. The pH value of the padding bath was maintained at about 6. The padded fabric was dried at 80 ℃ ℃ for 5 minutes and cured (SDL mini-dryer steamer) at 140 ℃ for 2.5 min.

4.2.4 Characterization of materials

The average particle sizes and size distributions of the samples dispersed in water were measured using DLS measurements by a Malvern Zetasizer Nano ZS90 with a scattering angle of 90°. He–Ne laser beam of 632.8 nm was used for the measurements. The average diameters were determined from cumulants mean of the intensity average of 50 runs using Stokes–Einstein equation, $d_H = k_B T/3\pi\eta D_{ef}$, where d_H is the hydrodynamic radius, k_B is the Boltzmann constant, T is the temperature, η is the viscosity of solvent, and D_{ef} is the diffusion coefficient. The reproducibility was checked from at least three measurements. The sample temperature was controlled automatically within ±0.01 K by a built-in Peltier device.

FTIR spectrum was recorded by a Fourier transform spectrophotometer Frontier by PerkinElmer in transmittance mode for each KBr sample range between 400 and 4000 cm^{-1} at 4.0 cm^{-1} resolution. UV–vis absorption spectrum was recorded by a double-beam UV-vis spectrophotometer (UVD-3500, LABOMED, INC, USA), where cell length is 1 cm. UV-vis diffuse reflectance spectra were recorded using a double-beam UV-visible spectrophotometer with an integrating sphere attachment DRA-CA-30I (Model: UV-1800, Shimadzu, Japan) to determine the band gap (E_g) energies of the solid nanoparticle.

The crystallographic and phase-dependent properties were analyzed by X-ray diffractometer (Philips PW 1724) with an X-ray generator using XDC-700 Guinier-Hagg focusing camera with monochromatic Cu $K\alpha$ radiation ($\lambda = 1.540598$ Å). The measurement was performed continuously with a scan speed of 3.0 deg/min within 10-70 °C while the scan width was 0.026 degree. The crystallite domain diameters (D) were obtained from XRD peaks from Debye-Scherrer's equation.

$$D = \frac{K\lambda}{\beta cos\theta}.$$

The surface morphology and structure were studied with TEM, and the micrographs were attained by using the LEO system (model 912 AB) at 120kV for samples. Image J 1.51k (Java 1.60-24 (64 bit), USA) was used to measure average particle size in the TEM images of NPs. The morphological study used Field emission SEM (FESEM) (ZEISS, Germany).

Computer-adapted software (Image J 1.51k, java 1.60-24 (64 bit), USA) was used to measure average particle size in the SEM images of NPs. The compositional study of the nanoparticles was analyzed by EDX spectroscopy attached to the FESEM. The acceleration voltage of the electron gun was 20 kV with a probe current of 1.0 nA and magnifications ranging from 10,000 – 100,000. The images of samples were taken without sputtering and by mounting on the conducting carbon tape. Thermal properties were studied under a nitrogen atmosphere by a Hitachi instrument (TG/ DTA 7200) in the 30–550 °C at a heating rate of 20° min^{-1}. The physical properties of the fabrics (weight, bursting strength, air permeability) and fastness properties were examined by ISO standards.

4.2.5 Color measurements

The colorimetric difference within control and coated fabrics were determined by a spectrophotometer (Datacolor SF850, Datacolor International, USA) under D65 (average daylight), F11 (fluorescent lighting), A (tungsten-filament lighting) standard illuminants at a 10 observing angle with d/8 viewing geometry. The CIE *LCH* color coordinates (*L**, *C** *and H**) where *L** represents white to black, *C** means brighter duller, and *H** represents hue, whereas The CIE *Lab* color coordinates (*L**, *a** *and b**) where, *L** representing white to black, *a** and *b** meaning redness–greenness and yellowness–blueness, respectively. The difference (Δ*L*, Δ*a*, Δ*b*, Δ*C*, Δ*H*) between reference (control fabric) and sample (coated) fabrics were measured by the following equations (4.1-7):[6]

$$\Delta L^* = L^*_{reference} - L^*_{sample} \qquad (4.1)$$

$$\Delta a^* = a^*_{reference} - a^*_{sample} \qquad (4.2)$$

$$\Delta b^* = b^*_{reference} - b^*_{sample} \qquad (4.3)$$

$$C = \sqrt{\Delta a^{*2} + \Delta b^{*2}} \qquad (4.4)$$

$$\Delta C^* = C^*_{reference} - C^*_{sample} \qquad (4.5)$$

$$H = \tan^{-1} b/a \qquad (4.6)$$

$$\Delta H^* = H^*_{reference} - H^*_{sample} \qquad (4.7)$$

The color difference, ΔE^* computer color matching (CMC), provides the distance within the reference and coated fabric sample in the CIE CMC color space and was calculated by the following equation (4.8):

$$\Delta E^*CMC = \Delta L^*\Delta C^*\Delta H^* \qquad (4.8)$$

Where, $\Delta L^*, \Delta a^*, \Delta b^*, \Delta C^*, \Delta H^*$ are the differences between control (reference) and coated fabrics.

4.2.6 Assessment of the antibacterial properties

The antimicrobial properties of the coated and control fabrics were evaluated using the ASTM E2149-01 quantitative method, which estimates the effectiveness of non-leaching antimicrobial coatings in inhibiting the growth of microorganisms under dynamic contact conditions. The antimicrobial efficacy was assessed against Gram-positive *S. aureus* and Gram-negative *E. coli* bacteria. The cultures were each suspended in a limited amount of nutrient broth, subsequently transferred onto a nutrient agar plate, and subjected to incubation at 37 ℃ for 24 h. Two individual colonies were aseptically transferred using an inoculating loop from the agar plate onto coated and control fabrics in separate Petri dishes. The Petri dishes were then incubated at 37 ℃ for 24 h to facilitate the internalization of NPs into the microbial cells. Equation (eqn. 4.9) determines reduction of microorganisms, R (%) after coated and control fabrics exposure.[6]

$$R\ (\%) = \frac{B-A}{A} \times 100 \qquad (4.9)$$

The surviving cells, A and B, expressed as colony-forming units per milliliter (CFU/mL) were observed in a flask containing coated and control fabrics, respectively, following a 1 h contact time.

4.2.7 Assessment of the UV protection properties

The UV protection efficacy of the Ag NPs coated fabric was assessed through UV transmission spectra analysis using a double beam ultraviolet-visible (UV-vis) spectrometer (Cintra 2020, GBC, Australia). The UPF was determined by incorporating an integrating sphere attachment. A UPF of fabric is defined under the PN-EN 13758-1:2007 standard, utilizing equations (4.10-11).[7]

$$UPF = \frac{\sum_{\lambda=290}^{400} E(\lambda) \cdot \varepsilon(\lambda) \cdot \Delta(\lambda)}{\sum_{\lambda=290}^{400} E(\lambda) \cdot T(\lambda) \cdot \varepsilon(\lambda) \cdot \Delta(\lambda)} \qquad (4.10)$$

$$\text{Percent UV transmission} = \frac{\sum_{\lambda_1}^{\lambda_2} T(\lambda)}{(\lambda_2 - \lambda_1)} \qquad (4.11)$$

The solar irradiance, denoted as $E(\lambda)$ and measured in W/m^2/nm, is a function of the spectral transmittance at the wavelength λ, represented by $T(\lambda)$, the erythema action spectrum, denoted as $\varepsilon(\lambda)$, and the wavelength interval, marked as $\Delta\lambda$. The UPF of textiles represents their ability to block UV radiation, with greater UPF values indicating a higher capacity for protection.[8] According to Table 4.1, the Australian classification system can categorize fabrics based on their UPF values, which range from 15 to 50+, into three levels of protection: good, very good, and excellent.

Table 4.1: Classification of UPF category measured from relative transmittance and protection level.[9]

UPF range	Protection category	UVBE$_{eryt}$ transmittance (%)
<15	Insufficient protection	>6.7
15-24	Good protection	6.7-4.2
25-39	Very good protection	4.1-2.6
40-50, 50+	Excellent protection	<2.5

4.2.8 Evaluation of self-cleaning activity

The efficacy of the self-cleaning properties of the material was assessed by measuring the intensity of color difference induced by UV irradiation of curry stains. To prepare the curry paste 10 mL of hot water was mixed with 0.5 g of beef curry powder (*Radhuni*). A fabric sample coated with Ag NPs was utilized in an experiment wherein a single droplet of curry paste was applied, allowed to diffuse, air-dried, and subsequently exposed to light irradiation. The Ag NPs coated fabric stain was subjected to a light exposure and weathering test using an air-cooled xenon arc lamp, specifically the Xenotest Alpha LM device from the United States, for 20 h, in compliance with the ISO 105 B02 standard. To prevent irradiation, a steel frame was utilized to cover one side of each fabric stain, while the other half was subjected to exposure from a xenon arc lamp. The color strength (*K/S*)

of the exposed and unexposed portions of stain were analyzed to evaluate their self-cleaning performance. The reflectance of the fabric that had been stained was measured through a spectrophotometer (Datacolor SF850, Datacolor International, USA) to ascertain the degradation rate through the utilization of the Kubelka-Munk equation (eqn. 4.12)[10],

$$\frac{K}{S} = \frac{(1-R)^2}{2R} \qquad (4.12)$$

Here, *K/S* stands for color strength, and *K* and *S* stand for the absorptions and scattering coefficients, respectively.

4.3 Results and Discussion

4.3.1 DLS analysis

Figure 4.1 shows the size distribution for the aqueous solution of Ag NPs measured from DLS measurement. One small sinusoidal peak with a maximum at about 22 nm d_H and another peak with maxima at about 93 nm d_H are seen, respectively, and they both indicate the successful synthesis of Ag NPs. DLS typically measures the hydrodynamic diameter of the particles in solution based on the Brownian motion of the particles in aqueous solution. Since DLS measures particle size in a solution state, the NPs may swell during the measurement.[12] DLS analysis indicates that the generated NPs had relatively well-defined dimensions. The surface area of NPs increases with decreasing size, which enhances antibacterial effectiveness and self-cleaning activity.[13]
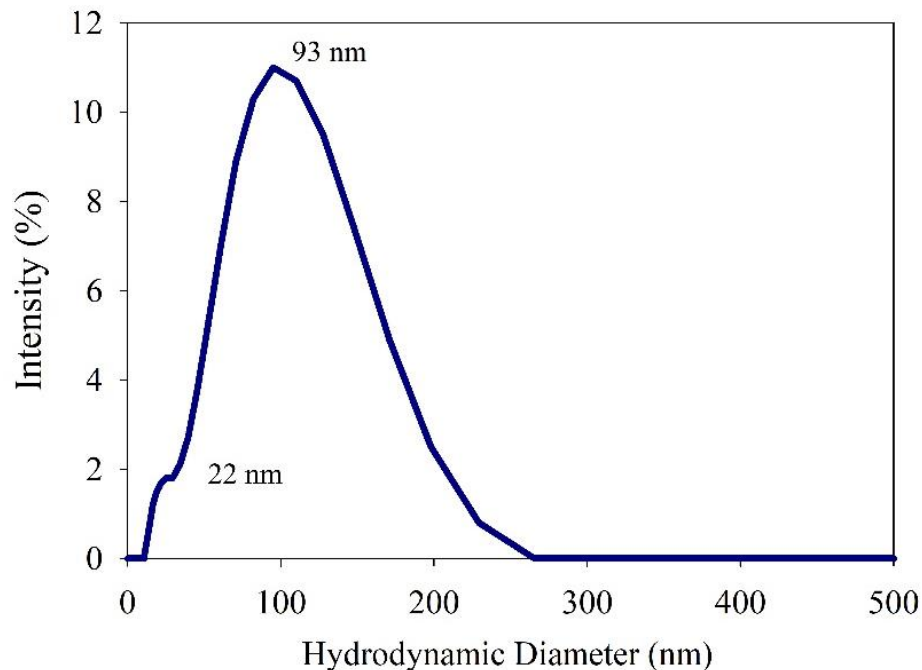
Figure 4.1: The average hydrodynamic diameter of Ag NPs.

4.3.2 **Fourier transform infrared spectroscopy measurement**

The FTIR spectrum of Ag NPs, shown in Figure 4.2 has sharp peaks at 527, 826, 932, 1104, 1397, 1637, and 3450 cm^{-1}, where a band around 527 cm^{-1} is associated with the bending vibration of the Ag-O bond of Ag NPs.[14,15] A broad and intense absorption band at 3450 cm^{-1} corresponds to the stretching vibration of the O-H mode due to the OH groups of water.[16] The small band at 1397 cm^{-1} is attributed to the hydroxyl groups of moisture.[17] The band at 1104 cm^{-1} is attributed to the stretching vibration of C–O. [18]
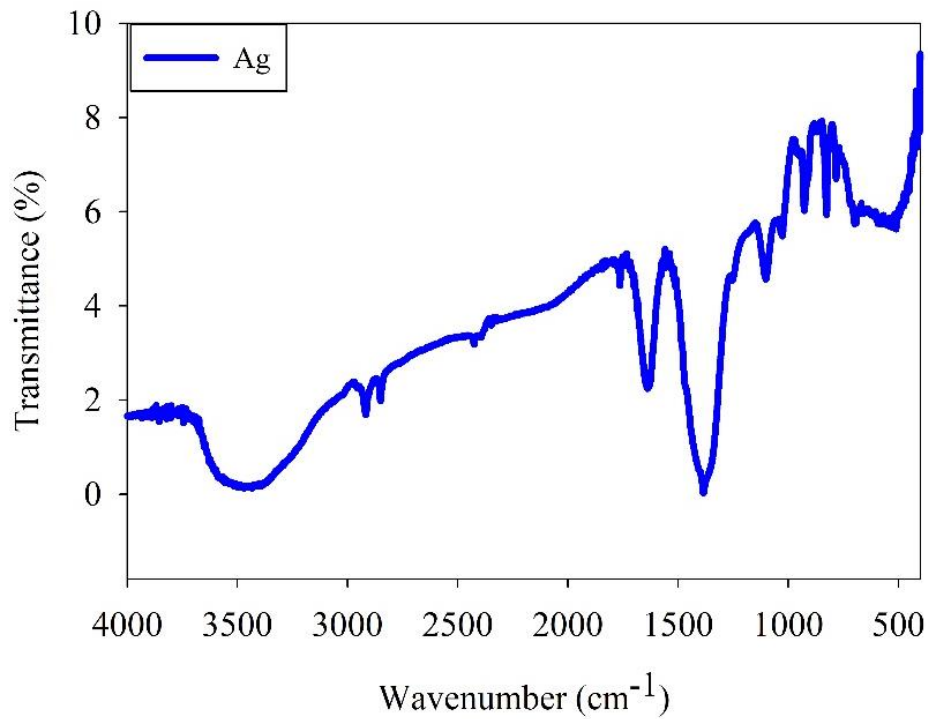
Figure 4.2: FTIR spectrum of Ag NPs.

4.3.3   Optical analysis (UV-visible absorbance spectrum analysis)

The UV-visible absorbance spectrum of Ag NPs is exhibited in Figure 4.3. The capacity of Ag NPs to absorb incoming electromagnetic radiation helps to explain localized surface plasmon resonance (LSPR).[19]
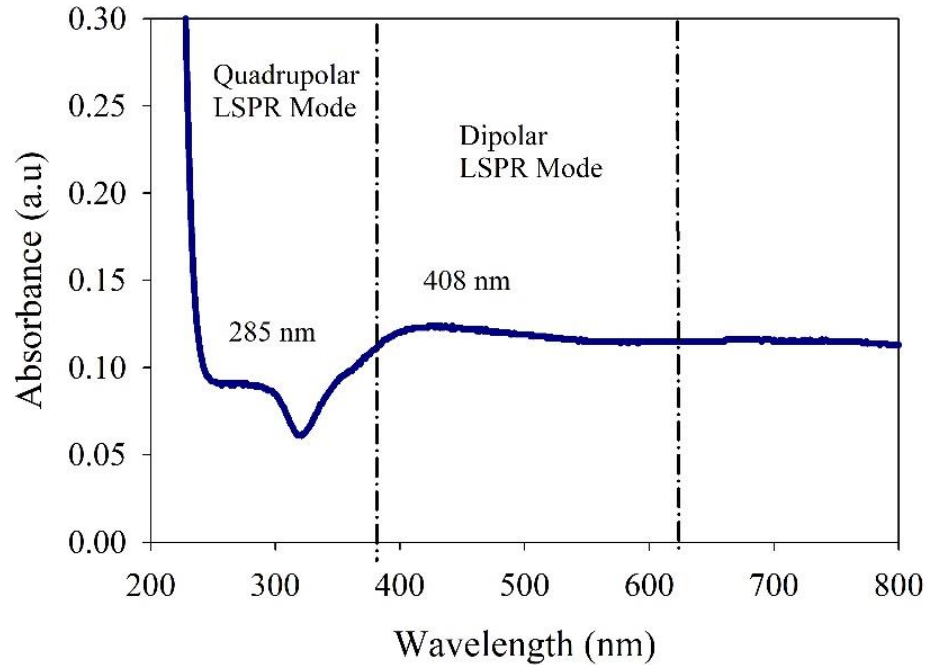
Figure 4.3: UV-vis absorption spectrum of a dispersion solution of Ag NPs.

LSPR occurs due to the collective oscillation of conduction electrons at the interface between metal NPs and their dielectric surroundings, triggered by the incoming light.[20] One of the significant advantages of plasmonic silver nanoparticles is their ability to generate artificially produced multipolar localized surface plasmon resonance modes, such as dipolar, quadrupolar, octupolar, and hexadecapolar modes. The sensitivity of multipolar LSPR modes is significantly influenced by their size, shape, and composition.[21] The observation of a dipolar LSPR mode at 408 nm and a quadrupolar LSPR mode at 285 nm in the Ag NPs with a peak d_H at approximately 93 nm provides evidence for the synthesis of Ag NPs. The dipolar and quadrupolar LSPR modes can distinguish the dimer-like structure featuring a nanogap. The presence of the quadruple mode in the absorption spectra is attributed to the size and retardation effects of Ag NPs. Spherical plasmonic NPs with an average 10-65 nm diameter exhibited a sole dipolar localized surface plasmon resonance band. As the dimensions of the system increased, the impact of phase retardation effects became more pronounced, resulting in the emergence of higher-order modes that could no longer be disregarded.[22] The estimation of the band gap energy of Ag NPs can be achieved by using the formula (eqn. 4.13).[23]

$$\alpha h v = A(h v - E_g)^n \tag{4.13}$$

Where v, α, E_g and A are light frequency, absorption coefficient, direct optical band gap energy, and a constant, respectively, and $n = \frac{1}{2}$ (for direct transition mode material), when plotting $(\alpha h v)^2$ vs. photon energy $(h v)$ of the stimulating light, as shown in Figure 4.4, the linear area may be used to extrapolate the band gap. The band gap energy of Ag NPs is more accurately represented at the point where the tangent line and the x-axis connect. It should be noted that Ag NPs have E_g of 3.6 eV.[24]
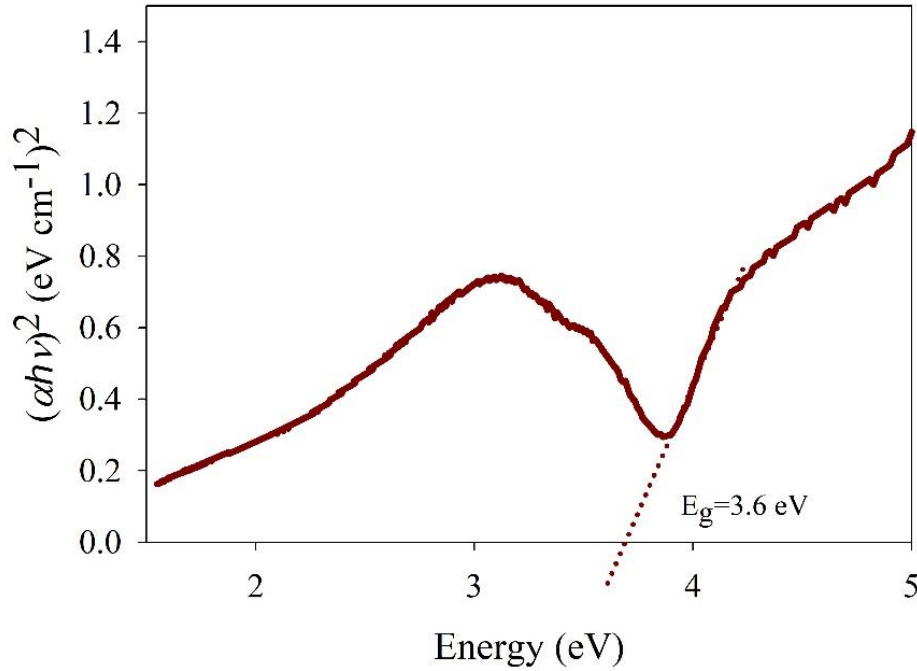
Figure 4.4: Tauc plot of the Ag NPs.

4.3.4 Determination of optical band gap and the nature of optical charge carrier transitions

By using the DASF approach and the accompanying equations (4.14–15), the optical band gap of Ag NPs is reported:[25]

$$ln\left[\frac{f(R)}{\lambda}\right] + ln\, s = ln[B(hc)^{m-1}] + m\, ln(\frac{1}{\lambda} - \frac{1}{\lambda_g}) \tag{4.14}$$

Now,

$$\frac{d\{ln\left[\frac{f(R)}{\lambda}\right]\}}{d\left(\frac{1}{\lambda}\right)} = \frac{m}{\frac{1}{\lambda} - \frac{1}{\lambda_g}} \tag{4.15}$$

As R is the reflectance and f® is proportional to the absorption coefficient (α), f® is calculated using the Kubelka-Munk technique (eqn. 4.16).

$$f(R) = \frac{(1-R)^2}{2R} \tag{4.16}$$

where, B is a constant, s is the scattering coefficient, λ_g is the wavelength connected to the optical band gap, c is the speed of light, and λ is the wavelength. E_g is the band gap energy of the sample, and hv is the energy of photon. The extrapolation of a linear part in Figure 5 of $dln[\alpha(\lambda)\lambda^{-1}]/d\lambda^{-1}$ against hv is used to determine optical band gap of the sample. Ag has an estimated E_g of 3.38 eV.
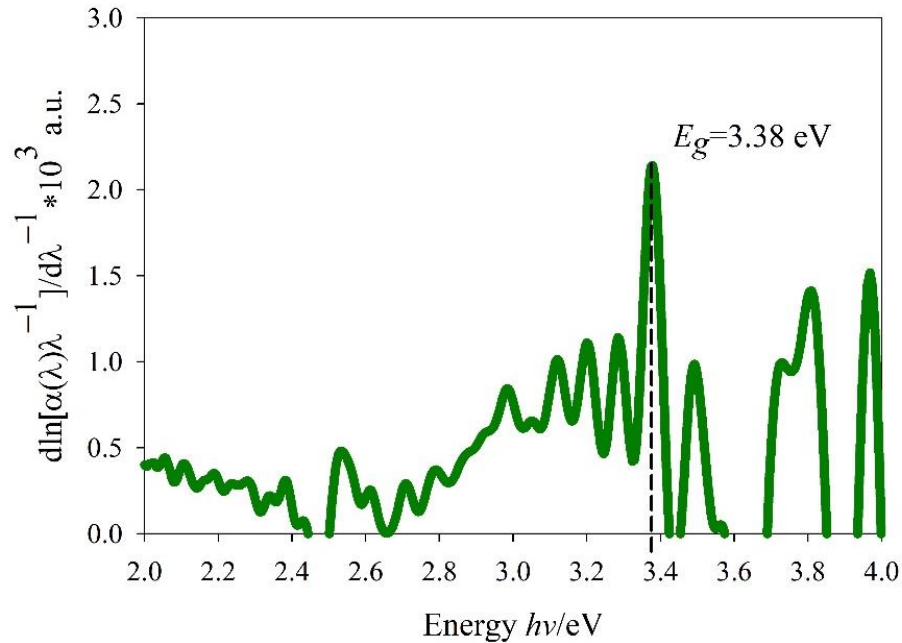
Figure 4.5: DASF method calculated for band gap by plotting of dln[α(λ)λ-1]/d λ-1 versus hv.

The extrapolation of a linear part in the plot of $ln[\alpha(\lambda)\lambda^{-1}]$ vs. $ln[\lambda^{-1} - \lambda_g^{-1}]$ expanded in Figure 4.6yields the corresponding coefficient (m) of the sample. Calculating the

corresponding coefficient (*m*) for an electronic transition, it is discovered that $m = 1/2$ determines the direct allowed transition.[26]
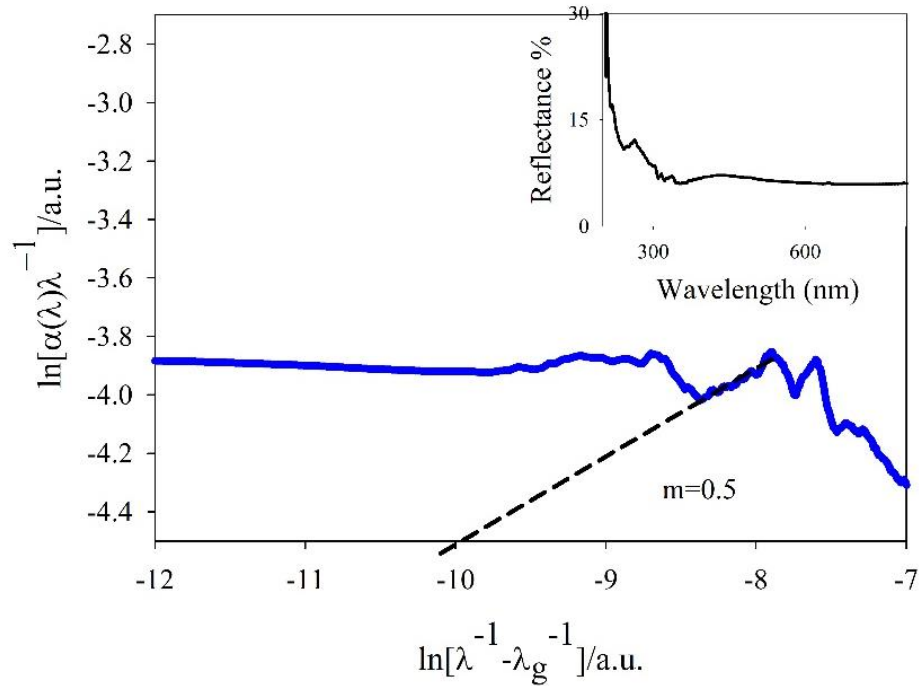
Figure 4.6: DASF method calculated for corresponding coefficient (m) by plotting ln[α(λ)λ-1] versus ln[λ-1 – λg-1]. The inset is the reflectance spectrum of Ag NPs.

4.3.5 XRD Analysis

Figure 4.7 shows the results of an XRD analysis of Ag NPs. Sharp diffraction peaks indicate substantial crystalline structure. The face-centered cubic (FCC) phase of the Ag NPs revealed peaks at 28.04°, 30.97°, 38.14°, 44.37°, 55.09°, and 64.52° which correspond to the (210), (122), (111), (200), (142), and (220) planes, respectively. It was well coordinated with JCPDS, No. 04-0783.[16,18] The d-spacing (d_{hkl}) and lattice parameters *a*, *b*, and *c* of the sample were calculated using the following equations (eqn. 4.17-18).[27,28]

$$2d_{hkl}sin\theta = n\lambda \qquad (4.17)$$

$$\frac{1}{d^2} = \frac{h^2 + k^2}{a^2} + \frac{l^2}{c^2} \qquad (4.18)$$

Where, λ is the wavelength of the XRD, *n* is the order of diffraction (for first order $n = 1$), d_{hkl} is the interplanar spacing (*d*-spacing), and *hkl* is the Miller indices. The average lattice

parameters for Ag NPs were $a = b = c = 4.0803$ Å. The Debye-Scherrer equation (4.19) was used to compute the average crystallite diameter D.[29]

$$D = \frac{K\lambda}{\beta\cos\theta} \qquad (4.19)$$
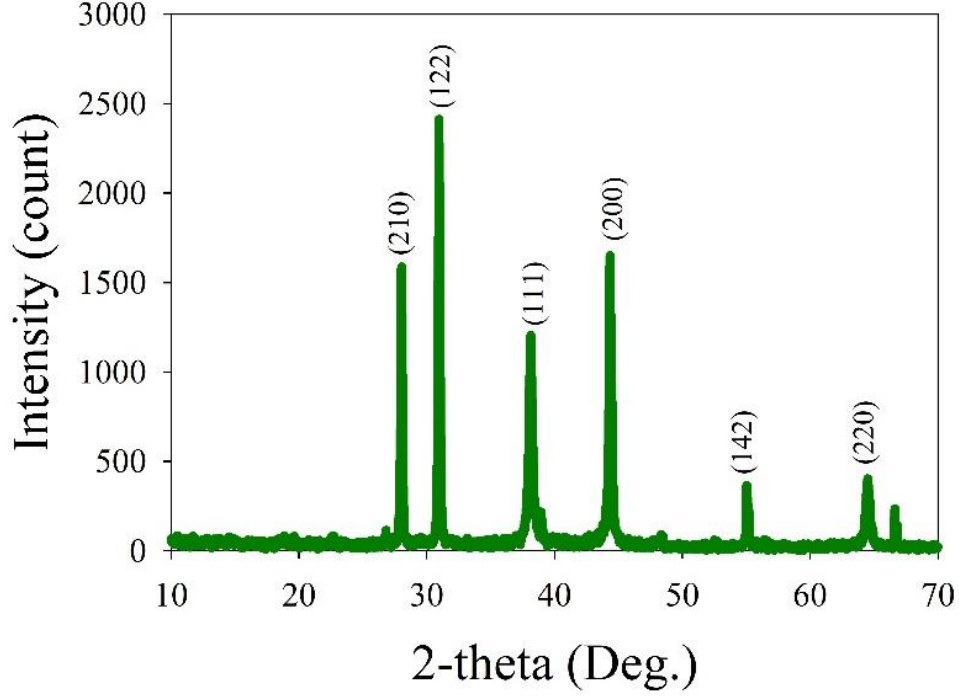
Figure 4.7: XRD pattern of Ag NPs.

Equation (4.20) was used to compute lattice strain.

$$\eta = \frac{\beta}{\tan\theta} \qquad (4.20)$$

Using the Williamson-Hall equation (21), the dislocation density (δ), which measures the number of crystal defects, was computed.

$$\delta = \frac{1}{D^2} \qquad (4.21)$$

where, D is the size of the crystallite, $K = 0.9$, λ is the X-ray radiation wavelength (1.5406 Å), β is the full-width half maximum (FWHM) of diffraction peak, θ is the Braggs diffraction angle, and η is the lattice strain of the material.[30,31] The crystallite size, lattice strain, dislocation density, lattice planes, and d-spacing values are listed in Table 4.2.

Table 4.2: 2θ, crystallite size, lattice strain, dislocation density, *hkl,* d-spacing of Ag NPs as presented in XRD pattern analysis.

2θ (degree)	B	D (nm)	$\eta = \beta/tan\theta$	$\delta(nm^{-2})$	hkl	$d_{hkl} = \lambda/2sin\theta$
28.04	0.18	46.14	0.0124	0.0005	210	0.3180
30.97	0.18	46.52	0.0112	0.0005	122	0.2885
38.14	0.41	20.75	0.0205	0.0023	111	0.2357
44.37	0.29	29.89	0.0123	0.0011	200	0.2040
55.09	0.25	36.33	0.0083	0.0008	142	0.1666
64.52	0.41	22.97	0.0113	0.0019	220	0.1443

4.3.6 TEM analysis

Figure 4.8 (a-b) presents the results of the TEM analysis conducted on Ag NPs, highlighting their structural characteristics, morphology, particle size, and shape. TEM images provide evidence of the development of nanostructures that exhibit a spherical morphology. The histogram (Figure 4.8 (c)) indicates that the average particle size of the Ag NPs falls within the range of 20 to 160 nm. The diffraction ring patterns observed in the SAED pattern depicted in Figure 6d are significantly diffused, indicating that the NPs were polycrystalline, with small grain sizes corresponding to Ag. These findings are consistent with the results obtained from the XRD pattern.
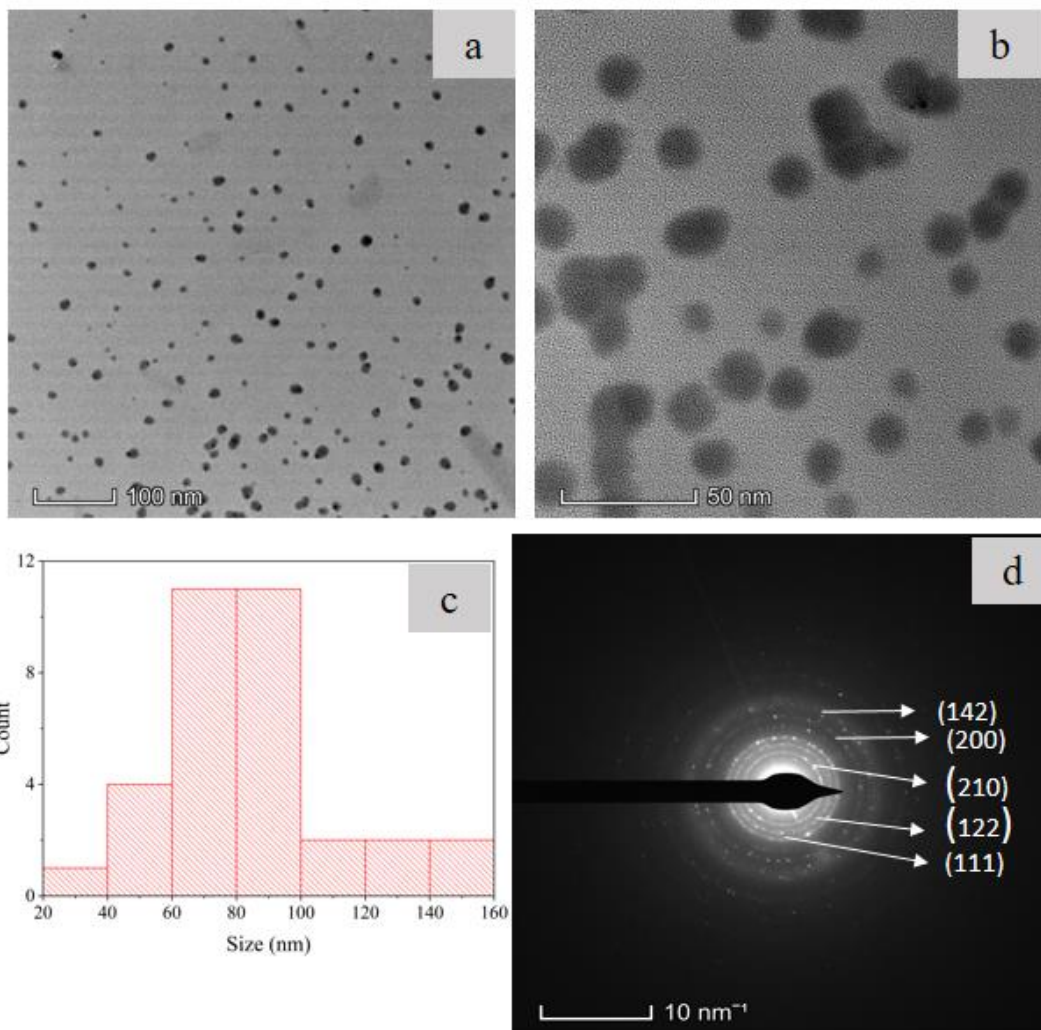
Figure 4.8: TEM images of (a, b) Ag NPs with different magnifications, (c) histogram and (d) SAED pattern.

The diffraction rings pattern exhibits a ring-like structure that corresponds to the (210), (122), (111), (200), and (142) lattice planes of Ag NPs. The observation has been made that the aforementioned circular rings containing spots exhibit a high degree of coordination with the XRD pattern of Ag NPs, thereby indicating their highly crystalline nature.

4.3.7 **SEM and EDX of coated fabrics**

Figure 4.9 (a-b) depicts the surface morphology evaluation of control and Ag NPs coated fabrics through SEM images. The image presented in Figure 4.9 (a) displays a control cotton fiber characterized by a highly uniform and diverse surface, featuring a well-defined "twisted ribbon" structure with visible micro-fibrils and an absence of any impurities.[32] The surface morphology undergoes modification after applying Ag NPs, as evidenced in Figure 4.9 (b). The presence of spherical Ag NPs on the coated fiber surface indicates the attachment of Ag NPs. The text elucidated that the acrylic binder is the binding agent between the NPs and the fiber surface, fulfilling the role of binding element. The histogram in Figure 4.9 (c) reports the particle size of Ag NPs on the coated cotton fabrics. The agglomerates of Ag NPs on the fabrics are attributed to the lack of stirring during the impregnation process and the low dimension of the Ag NPs, which occurred during the coating process by padding.
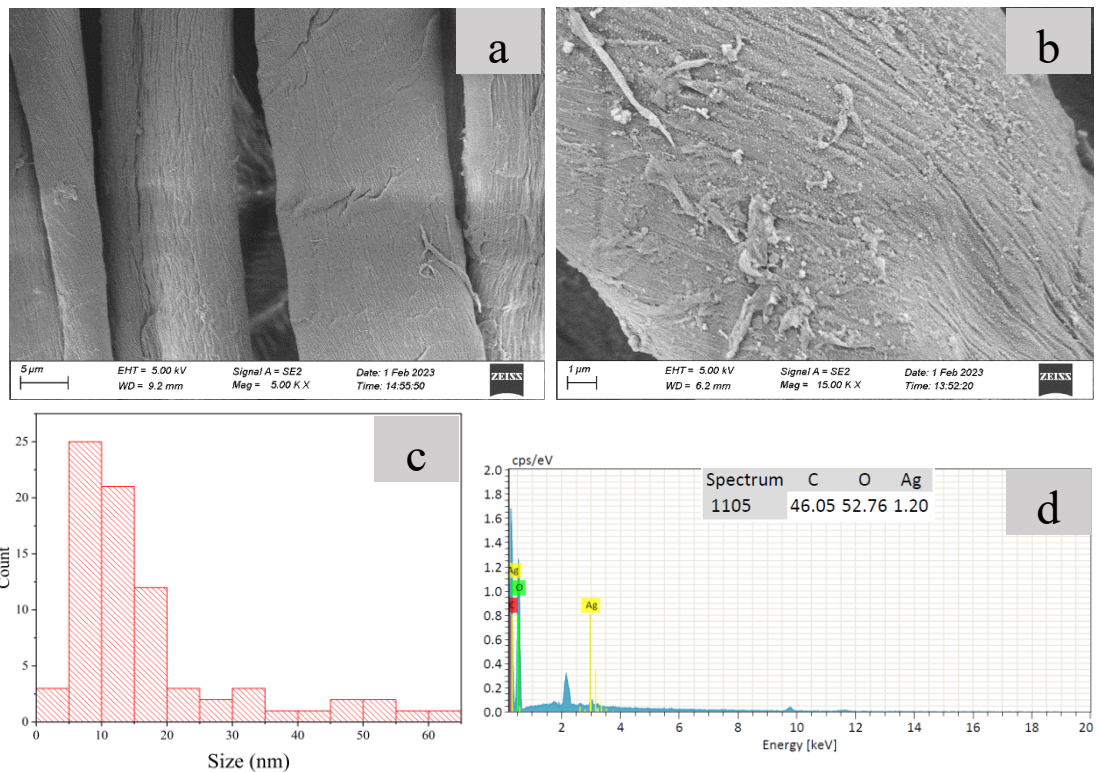
Figure 4.9: SEM images of (a) control cotton, (b) Ag NPs coated cotton, (c) histogram of particle size (d) EDX spectrum of Ag NPs coated cotton fabric.

The uniform distribution of NPs on the fiber surface is a critical factor in determining the quality of coated fabric. The quantity of NPs that adhere to the fiber surface is contingent upon the fabric wettability and absorption characteristics.[33] Figure 4.9 (d) is utilized to demonstrate the identification of the elements present on the coated cotton fabric through the EDX spectrum. The spectrum obtained provides evidence of existence of Ag on the surface of cotton fabric.

4.3.8 Thermogravimetric analysis

The present study examines the thermal properties of cotton fabric coated with Ag NPs at room temperature to 550 ºC. The aim is to investigate the impact of the treatment on the pyrolysis process of cellulose. Figure 4.10 displays the TGA curves for the control and cotton fabric coated with Ag NPs. Pyrolysis is a multifaceted process in which various reactions can coincide, including endothermic reactions, bond rupture, volatilization, and exothermic bond formation. The thermogram depicts the extent of mass reduction of textiles during individual pyrolysis phases.[34] The thermogram obtained from the cotton fabric under investigation displays three primary stages of mass reduction. During the initial pyrolysis stage, the TGA curve exhibits linearity as the amorphous region of the polymer undergoes significant damage, resulting in gradual weight loss (4.5%) up to approximately 254 ºC. This phenomenon can lead to alterations in specific physical properties of the fabric. Removing absorbed and adsorbed water is also responsible for the observed weight loss. The second step of the experiment reveals a significant increase in the slope of the curves, which can be attributed to the substantial reduction in the weight of the sample resulting from the pyrolysis of cellulose in the crystalline region. A gradual weight loss is observed until reaching a temperature of 320 ºC, followed by a significant weight loss of approximately 83%. This weight loss is accompanied by an endothermic peak at 390 ºC, which is attributed to the generation of pyrolysis by-products such as levoglucosan.[35] During the third stage, at temperatures exceeding 550 ºC, the residual weight curve indicates that the remaining weight (8%) could potentially be attributed solely to the presence of char/ash matter. In contrast, the cotton fabric coated with Ag NPs exhibits a similar curve pattern to the control fabric, except for the temperature range of 320-380 ºC. Notably, the Ag NPs coated fabric displays a faster onset of decomposition at

305 ºC and less percentage (4%) of char/ash formation, albeit demonstrating lower thermal stability than the control fabric.
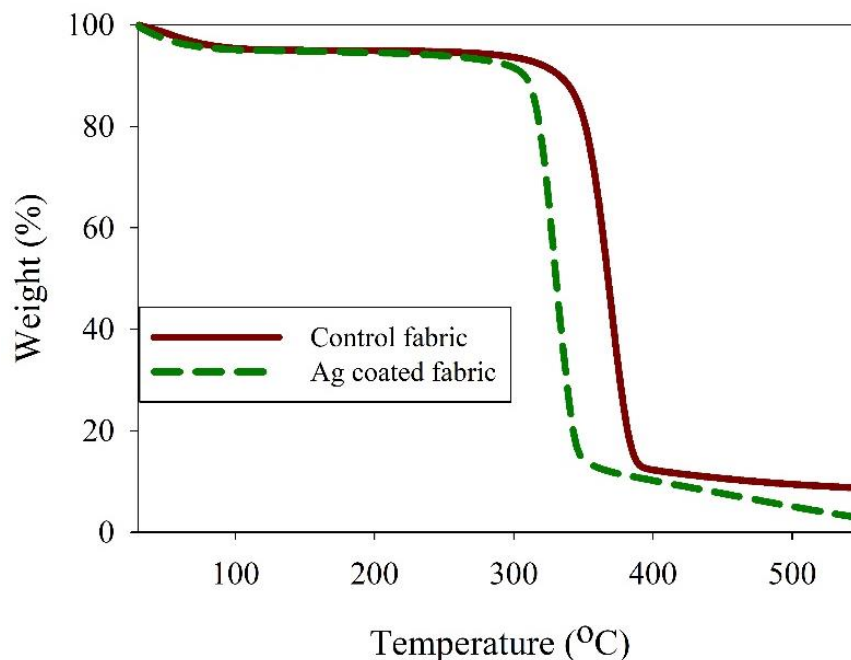
Figure 4.10: TGA analysis of control and Ag NPs coated cotton fabric.

4.3.9 Physical properties of coated fabric

Table 4.3 displays the slight modifications observed in the physical and color fastness properties of fabric. The weight, fabric density, bursting strength and air permeability decreased. These changes can be attributed to the deposition of NPs on the fabric surface. Using an acrylic binder facilitates the immobilization of NPs onto the surface of fibers, resulting in a reduction in bursting strength. After coating with a dispersion solution, the curing is done in a steamer, which contributes to decreased density due to fabric stretching. Furthermore, the reduction in air permeability can be attributed to the cross-linking of acrylic binding agents across the fabric surface. The fabric coated with Ag NPs exhibited favorable resistance to color fading when subjected to washing, perspiration, and rubbing, which can be attributed to the surface plasmon resonance of the Ag NPs.

Table 4.3: Physical and fastness properties of control and coated cotton fabrics parameters

Physical and fastness properties		Control fabric	Coated fabric	Standard
Weight (g/m^2)		147	145	ISO 12127:2003
Fabric density (number of yarns/10 cm)	Wales	161	159	ISO1049-2:2000
	Coarse	185	183	
Bursting strength (KPa)		180.5	155.8	ISO 13938-1:1999
Air permeability (cm^3 cm^{-2} s^{-1})		68.8	51.3	ISO 9237:1999
Colorfastness to wash		---	Color change: 4/5 Color staining:4/5	ISO 105-C06
Colorfastness to perspiration		---	Color change: 4/5 Color staining:4/5	ISO 105-E04
Colorfastness to rubbing		---	Dry rub:4/5 Wet rub: 4	ISO 105-X12

4.3.10 **Color differences between control and coated fabrics**

The ΔL^*, Δa^*, Δb^*, ΔC^*, and ΔH^* color coordinates of control and coated fabrics are presented in Table 4.4. A trend of reducing L^* values at different illuminants was seen. A drastic color-changing effect was observed both by visual and spectrophotometer within control and coated fabrics due to the surface plasmon resonance of Ag NPs.

Table 4.4: The color difference between control and coated fabrics.

Illuminants/Observer angle	CMC ΔE	ΔL^*	ΔC^*	ΔH^*	Δa^*	Δb^*
D65 10 Deg.	21.66	-49.58	11.46	-2.47	3.63	11.14
F11 10 Deg.	22.25	-48.96	13.04	-1.94	3.49	12.71
A 10 Deg.	22.61	-48.53	13.41	-1.74	5.56	12.32

4.3.11 **Antibacterial activity**

Summarized data of Ag NPs for achieving antibacterial performances are presented in Table 4.5. The study examined and expressed the antimicrobial characteristics of Ag NPs coated fabric in Figure 4.11 and Table 4.6 and demonstrated the efficacy with a higher decrease (>98%) against *Staphylococcus aureus* (*S. aureus*) (Gram-positive) and (>99.9%) against *Escherichia coli* (*E. coli*) (Gram-negative) bacterial strains. This antimicrobial activity in the coated fabric can be attributed to the inherent antimicrobial properties of Ag. Ag ions exhibit antimicrobial properties through various mechanisms. Initially, Ag NPs engage in the antibacterial activity by adhering to and infiltrating the bacterial cell wall, instigating the production of reactive oxygen species, and disrupting cellular processes by impeding oxygen diffusion and obstructing respiration.[36]

Table 4.5: Summarized data of Ag NPs for achieving antibacterial performances.

Types of NPs	Deposition process	Functionalized textile	Microbes used	Antimicrobial activity	Reference
Ag NPs	Dip-dry-cure	Cotton fabric	*S. aureus, E. coli, S. faecalis, P. aeruginosa*	Up to 99.99% reduction	[37]
Nano Ag	*In situ synthesis*	Cotton jersey knit and PES tricot knit fabric	*E. coli*	Observable inhibition zone	[38]
Ag NPs	Pad-dry-cure	Cotton fabric	*S. aureus* and *E. coli*	Upto 98% reduction	[39]
Ag NPs	Pad-dry-cure	Cotton fabric	*S. aureus* and *E. coli*	>98% reduction	Present work
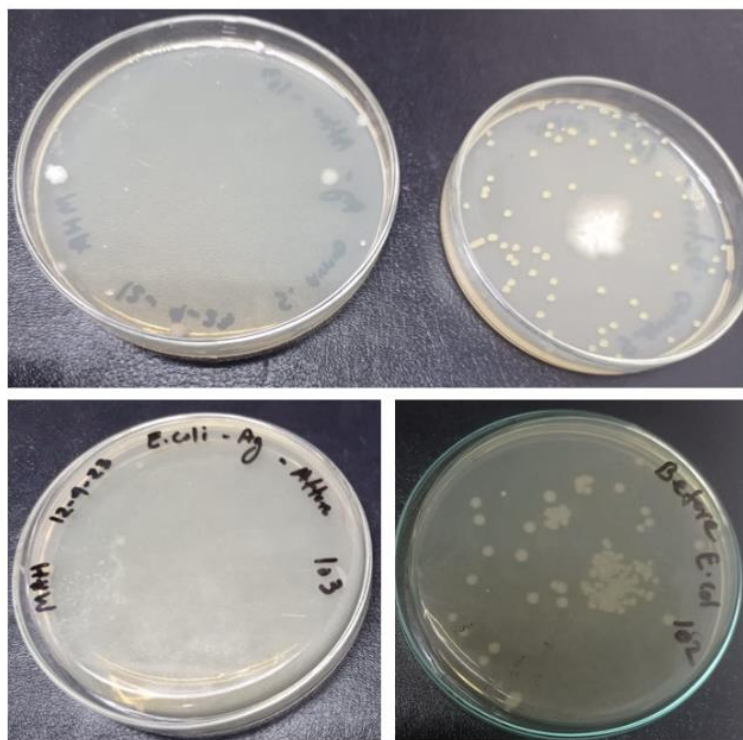
Figure 4.11: Antibacterial efficiency of control and Ag coated fabrics specimens against (a) Staphylococcus aureus, (2) Escherichia coli.

Table 4.6: The reduction (%) of surviving cells after disinfection of cotton with Ag NPs.

Microorganism	Surviving cells (CFU/mL)		Reduction (%)
	Control fabric	Coated fabric	
Staphylococcus aureus	9.99×10^3	1.89×10^2	98.1
Escherichia coli	1.11×10^3	0.01×10^2	99.9

The perturbation mentioned above induces alterations in the structural integrity of the cytoplasmic membrane around the cell, resulting in an elevation of cellular permeability membrane impairment and ultimately culminating in cellular demise.[40] The bactericidal properties of Ag NPs can be attributed to the presence of Ag^+ ions. The influx of Ag^+ ions into the cellular environment generates reactive oxygen species, damaging the membrane. The cellular mechanisms for extruding Ag^+ ions appear insufficient, thereby restricting their efficacy by penetrating the bacterial cell and inserting themselves between the purine and pyrimidine base pairs in DNA. The base pairs exhibited a disruptive impact on the hydrogen bonding between the two antiparallel strands, ultimately resulting in the

denaturation of the DNA molecule.[41] The second approach to eliminating bacteria entails the infiltration of specific ions into the bacterial cell, which subsequently hinders enzyme reactions, leading to the cessation of metabolic processes and eventual bacterial death. The bacterial cell undergoes binary fission with a frequency of once every 20 minutes. An additional antibacterial mechanism involves the infiltration of Ag^+ ions into cells, forming strong interactions with thiol groups found in essential enzymes and phosphorus-containing bases. This interaction may result in damage to DNA caused by the interaction between Ag NPs and DNA.[42] This particular interaction has the potential to impede the process of cell division and DNA replication, which could ultimately result in the cessation of cellular activity. Ag NPs have been found to modulate the phosphotyrosine profile of bacterial peptides, potentially impacting cellular signaling and resulting in the growth inhibition of bacteria. The growth of bacteria is hindered by the inactivation of proteins by utilizing Ag NPs. The deactivation of enzymes occurs due to the binding of silver atoms to thiol groups (-SH) present in them. The formation of a stable S-Ag bond between silver and the thiol group of compounds in the cell membrane is known to modify their function.[43] This modification is crucial for transmembrane energy generation and ion transport. Ag functions as a catalyst during disulfide bond formation, which involves the reaction between oxygen molecules within the cell and hydrogen atoms in thiol groups (R-S-H).[44] The catalytic activity of Ag facilitates the formation of disulfide bonds that are accountable for the conformational alterations of cellular enzymes, ultimately influencing their functional properties. The efficacy of antimicrobial activity is contingent upon various factors, including the dosage of chemicals, the size of particles, substrate structure, percentage of pickup, and application method.[45]

4.3.12 UV protection factor of Ag NPs coated fabric

Solar UV radiation encompasses UV-A (400-315 nm), UV-B (315-290 nm), and UV-C (290-200 nm) radiation, which collectively constitutes 3-5% of UV radiation and pose a potential threat to human health. The radiations mentioned above are present in natural terrestrial sunlight. They are subject to the filtering capacity of the upper atmosphere and local conditions such as latitude, altitude, and cloud cover. It is worth noting that the ozone layer filters out UV-C and the majority of UV-B radiation. Cotton fabric lacking UV-

absorbing properties may have adverse effects on human skin. The utilization of UV protection fabric has been found to effectively safeguard human skin from the harmful effects of UV radiation. These are achieved through increased absorption and reflection and reduced transmittance in the UV region. The UV protection characteristics of Ag NPs coated and control fabrics were evaluated using equations (4.10) and (4.11), as illustrated in Figure 4.12 and presented in Table 4.7. The Ag NPs that have been coated demonstrate UPF value of approximately 26.01. The significant attenuation of UV-B and UV-A radiation can be attributed to the coating of Ag NPs on cotton fabric.
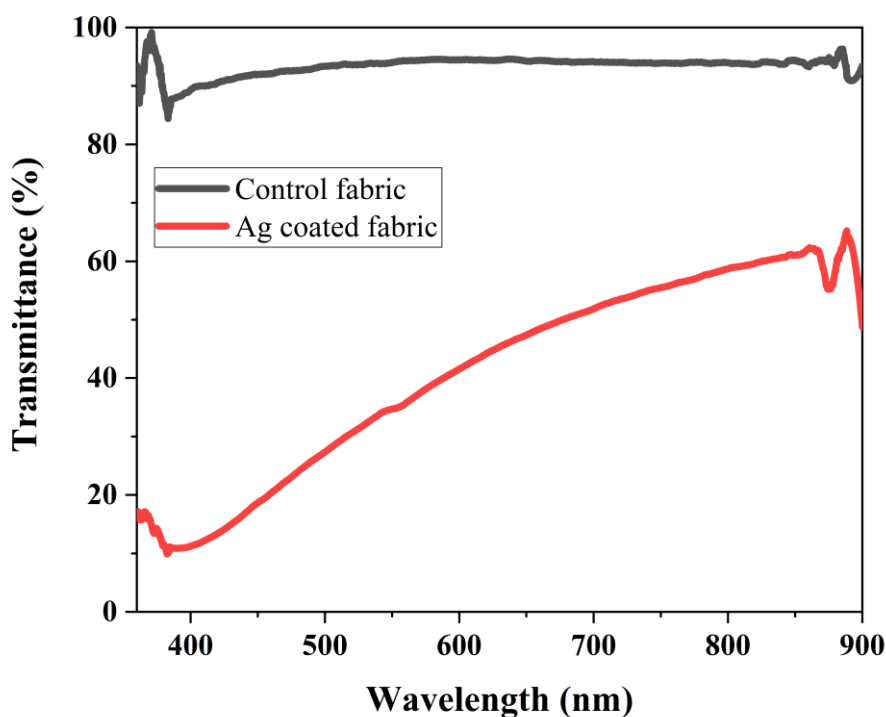
Figure 4.12: UV-protection of control and Ag NPs coated fabrics.

The effectiveness of UV protection is influenced by various factors such as the refractive index, scattering efficiency of UV rays, dimensions, and morphology of Ag NPs.[46] The incorporation of larger nanoparticles in the coating results in an improved dispersion of UV-blocking agents and a concomitant reduction in the overall reflection of UV radiation.[47] The observed phenomenon can be ascribed to the non-uniform and repeated reflection of ultraviolet radiation at the boundary between nanoparticles and the fabric

surface, resulting in a notable enhancement of photon absorption. The UV protection property of the fabric is primarily attributed to the plasmon structure of Ag NPs. This study demonstrates that the coating of Ag NPs enables the absorption and scattering of UV rays.[48] Table 4.8 summarizes UV protection performances of the Ag coated fabric.

Table 4.7: UPF and UV transmission for control and coated fabrics against UV-A and UV-B radiation.

Sample	UPF	UV-A transmission (%)	UV-B transmission (%)
Control fabric	1.20	84.27	79.49
Ag NPs coated fabric	26.01	4.50	1.40

Table 4.8: Summarized data of Ag NPs for achieving UV-protection performances.

NPs	Deposition process	Functionalized textile	UV protection factor	Ref.
Ag NPs	Dyeing bath	Woven cotton fabric	>50	[48]
Ag NPs	Shaking bath-dry	Woven cotton fabric	Slightly improve	[47]
Ag NPs	*In situ synthesis*	Woven cotton fabric	>50	[49]
Ag-doped ZnO composite	Pad-dry-cure	Cotton fabric	>50	[50]
Ag NPs	Pad-dry-cure	Cotton fabric	26.01	Present work

4.3.13 **Self-cleaning properties**

Curry masala comprises a variety of ingredients, including turmeric, cumin, coriander seed, black pepper, cloves, red chilies, ginger, salt, garlic, and mustard, among others. The formation of a curry stain is typically attributed to the infusion of curry masala in heated water. However, it is important to note that the primary culprit responsible for the

discoloration of cotton fabric is the turmeric (*Curcuma longa*) stain. These are due to the binding of yellow pigments, predominantly curcumin and its derivatives, with the cellulose fibers of the cotton material. Curcumin constitutes approximately 3-5% of the total constituents of turmeric. It is a yellow-colored substance that comprises two phenolic hydroxyl groups and two centrally located carbonyl groups. In solution, curcumin can exist in keto-enol tautomers.[51] The XRD studies have revealed that Ag NPs exhibit a face-centered cubic (FCC) arrangement. Additionally, TEM analysis has determined that the average size of the nanoparticles ranges from 60 to 100 nm. The discoloration of high molecular weight organic compounds in curry stains under UV exposure caused by Ag NPs coated cotton is attributed to the excitation of electrons in Ag NPs. NPs with smaller dimensions have a higher atom count, increasing active sites. In particular, the phenomenon occurs whereby electrons are elevated from the valence band to the conduction band in silver atoms when the photon energy derived from visible light surpasses the band gap of Ag NPs, measured at 3.38 eV. The excited electrons react with the oxygen that is dissolved in the reaction mixture, producing free radicals such as HO, HOO, and O_2^{-2} at the catalyst's surface. These sites are commonly referred to as "active sites." The active sites are generated through the utilization of the vacant d-orbitals and unpaired electrons that are present in the silver atoms. The process by which a curry stain undergoes degradation is explicated as follows (4.22(a-e)).[52]

$$Ag + h\nu \text{ (UV)} \longrightarrow Ag^+ + e^- \qquad\qquad (4.22(a))$$

$$e^- + O_2 \longrightarrow {}^*O_2^- \qquad\qquad (4.22(b))$$

$$Ag^+ \longrightarrow Ag + h^+ \qquad\qquad 4.22(c))$$

$$h^+ + H_2O/OH^- \longrightarrow {}^*OH \qquad\qquad 4.22(d))$$

$$\text{Curcumin dye} + {}^*OH \longrightarrow \text{degradation products} \qquad 4.22(e))$$

The generation of active sites is primarily accountable for the decomposition of organic substances (such as curry stains) into smaller molecules (namely, CO_2 and H_2O) upon exposure to UV radiation of Ag NPs.[45] Figure 4.13 depicts the *K/S* values, which refer to

the absorption and scattering coefficients, also known as color strength, of the control fabric that was unexposed, as well as the curry stain that was unexposed and exposed to light for 20 h under the ISO 105 B02:2013 standard for assessing self-cleaning efficacy.
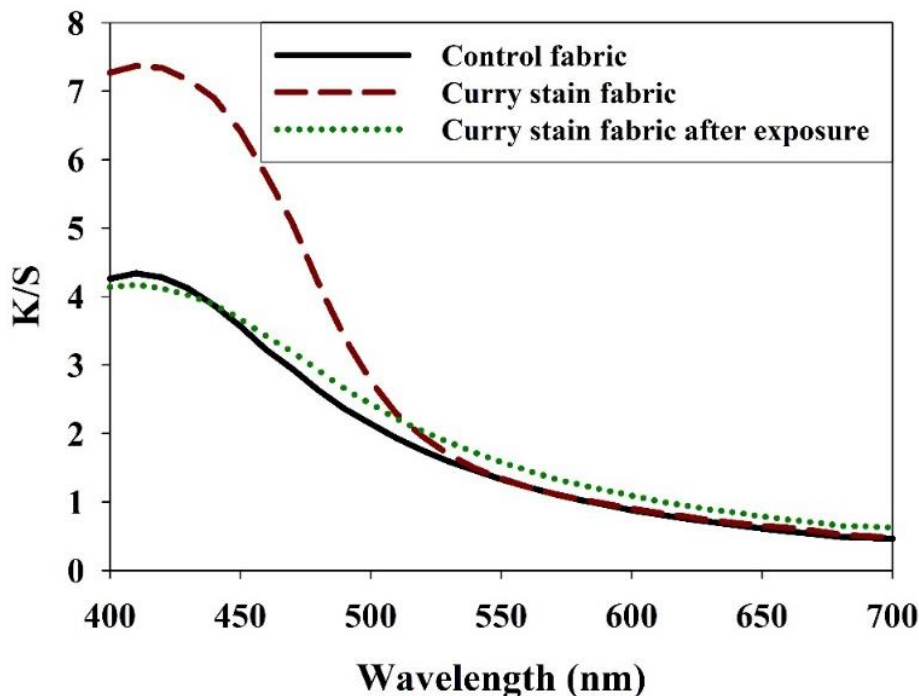
Figure 4.13: *K/S* values of control fabric, curry stain on Ag NPs coated fabric and curry stain on Ag NPs coated fabric after exposure against 20 h irradiation.

The Ag NPs coated fabric exhibits exceptional self-cleaning properties, as evidenced by its relative color strength (*K/S*) compared to the unstained control fabric indicating that all stains are effectively removed from the fabric's surface.

4.4   Conclusions

Cotton fabric was utilized as a substrate to fabricate a multifunctional material by depositing Ag NPs onto its surface. The synthesis and characterization of Ag nanoparticles have been conducted and evenly dispersed on the fabric's surface. The coated fabric demonstrates commendable UV protection, synergistic and remarkable antibacterial efficacy against gram-positive (*S. aureus*) and gram-negative (*E. coli*) bacteria, and exhibits exceptional self-cleaning characteristics. This multifunctional fabric with high

value-added features has a diverse range of practical applications and is aligned with the emerging trends of the future. This versatile textile possesses considerable potential for utilization within the textile sector.

References:

(1)   Sawhney, A. P. S.; Condon, B.; Singh, K. V.; Pang, S. S.; li, G.; Hui, D. Modern Applications of Nanotechnology in Textiles. *Text. Res. J.* **2008**, *78* (8), 731–739. https://doi.org/10.1177/0040517508091066.

(2)   Hong, H. R.; Kim, J.; Park, C. H. Facile Fabrication of Multifunctional Fabrics: Use of Copper and Silver Nanoparticles for Antibacterial, Superhydrophobic, Conductive Fabrics. *RSC Adv.* **2018**, *8* (73), 41782–41794. https://doi.org/10.1039/c8ra08310j.

(3)   Senthilkumar, N.; Vivek, E.; Shankar, M.; Meena, M.; Vimalan, M.; Potheher, I. V. Synthesis of ZnO Nanorods by One Step Microwave-Assisted Hydrothermal Route for Electronic Device Applications. *J. Mater. Sci. Mater. Electron.* **2018**, *29* (4), 2927–2938. https://doi.org/10.1007/s10854-017-8223-5.

(4)   Liu, G.; Xiang, J.; Xia, Q.; Li, K.; Yan, H.; Yu, L. Fabrication of Durably Antibacterial Cotton Fabrics by Robust and Uniform Immobilization of Silver Nanoparticles via Mussel-Inspired Polydopamine/Polyethyleneimine Coating. *Ind. Eng. Chem. Res.* **2020**, *59* (20), 9666–9678. https://doi.org/10.1021/acs.iecr.9b07076.

(5)   Kumar, N. S.; Ganapathy, M.; Sharmila, S.; Shankar, M.; Vimalan, M.; Potheher, I. V. ZnO/Ni(OH)2 Core-Shell Nanoparticles: Synthesis, Optical, Electrical and Photoacoustic Property Analysis. *J. Alloys Compd.* **2017**, *703*, 624-632. https://doi.org/10.1016/j.jallcom.2017.01.323.

(6)   Pietrzak, K.; Gutarowska, B.; Machnowski, W.; Mikołajczyk, U. Antimicrobial Properties of Silver Nanoparticles Misting on Cotton Fabrics. *Text. Res. J.* **2016**, *86* (8), 812–822. https://doi.org/10.1177/0040517515596933.

(7)   Campos Payá, J.; Díaz-García, P.; Montava, I.; Miró-Martínez, P.; Bonet, M. A New Development for Determining the Ultraviolet Protection Factor. *J. Ind. Text.* **2016**, *45* (6), 1571–1586. https://doi.org/10.1177/1528083714567238.

(8)   Awad, A.; Abou-Kandil, A. I.; Elsabbagh, I.; Elfass, M.; Gaafar, M.; Mwafy, E. Polymer Nanocomposites Part 1: Structural Characterization of Zinc Oxide Nanoparticles Synthesized via Novel Calcination Method. *J. Thermoplast. Compos. Mater.* **2015**, *28* (9), 1343–1358. https://doi.org/10.1177/0892705714551241.

(9)   Grifoni, D.; Bacci, L.; Zipoli, G.; Albanese, L.; Sabatini, F. The Role of Natural Dyes in the UV Protection of Fabrics Made of Vegetable Fibres. *Dye. Pigment.* **2011**, *91* (3), 279–285. https://doi.org/10.1016/j.dyepig.2011.04.006.

(10) Gupta, K. K.; Jassal, M.; Agrawal, A. K. Functional Finishing of Cotton Using Titanium Dioxide and Zinc Oxide Nanoparticles. *Res. J Text. Appl*. **2007**, 11(3), 1560-6074. https://doi.org/10.1108/RJTA-11-03-2007-B001.

(11) Xu, R. Progress in Nanoparticles Characterization: Sizing and Zeta Potential Measurement. *Particuology* **2008**, *6* (2), 112–115. https://doi.org/10.1016/j.partic.2007.12.002.

(12) Mohamed, F.; Enaiet Allah, A.; Abu Al-Ola, K. A.; Shaban, M. Design and Characterization of a Novel Zno–Ag/Polypyrrole Core–Shell Nanocomposite for Water Bioremediation. *Nanomaterials* **2021**, *11* (7). https://doi.org/10.3390/nano11071688.

(13) Rozalen, M.; Sánchez-Polo, M.; Fernández-Perales, M.; Widmann, T. J.; Rivera-Utrilla, J. Synthesis of Controlled-Size Silver Nanoparticles for the Administration of Methotrexate Drug and Its Activity in Colon and Lung Cancer Cells. *RSC Adv.* **2020**, *10* (18), 10646–10660. https://doi.org/10.1039/c9ra08657a.

(14) Goudarzi, M.; Mir, N.; Mousavi-Kamazani, M.; Bagheri, S.; Salavati-Niasari, M. Biosynthesis and Characterization of Silver Nanoparticles Prepared from Two Novel Natural Precursors by Facile Thermal Decomposition Methods. *Sci. Rep.* **2016**, *6* (August), 1–13. https://doi.org/10.1038/srep32539.

(15) Kumar, I.; Gangwar, C.; Yaseen, B.; Pandey, P. K.; Mishra, S. K.; Naik, R. M. Kinetic and Mechanistic Studies of the Formation of Silver Nanoparticles by Nicotinamide as a Reducing Agent. *ACS Omega* **2022**, *7* (16), 13778–13788. https://doi.org/10.1021/acsomega.2c00046.

(16) Goswami, M.; Baruah, D.; Das, A. M. Green Synthesis of Silver Nanoparticles Supported on Cellulose and Their Catalytic Application in the Scavenging of Organic Dyes. *New J. Chem.* **2018**, *42* (13), 10868–10878. https://doi.org/10.1039/c8nj00526e.

(17) Chakraborty, B.; Pal, R.; Ali, M.; Singh, L. M.; Rahman, D. S.; Ghosh, S. K.; Sengupta, M. Immunomodulatory Properties of Silver Nanoparticles Contribute to Anticancer Strategy for Murine Fibrosarcoma. *Cell. Mol. Immunol.* **2016**, *13* (2), 191–205. https://doi.org/10.1038/cmi.2015.05.

(18) Meng, Y. A Sustainable Approach to Fabricating Ag Nanoparticles/PVA Hybrid Nanofiber and Its Catalytic Activity. *Nanomaterials* **2015**, *5* (2), 1124–1135. https://doi.org/10.3390/nano5021124.

(19) Pyne, S.; Sarkar, P.; Basu, S.; Sahoo, G. P.; Bhui, D. K.; Bar, H.; Misra, A. Synthesis and Photo Physical Properties of Au @ Ag (Core @ Shell) Nanoparticles Disperse in Poly Vinyl Alcohol Matrix. *J. Nanoparticle Res.* **2011**, *13* (4), 1759–1767. https://doi.org/10.1007/s11051-010-9955-9.

(20) Zhang, C.; Chen, B. Q.; Li, Z. Y.; Xia, Y.; Chen, Y. G. Surface Plasmon Resonance in Bimetallic Core-Shell Nanoparticles. *J. Phys. Chem. C* **2015**, *119* (29), 16836–16845. https://doi.org/10.1021/acs.jpcc.5b04232.

(21) Bastús, N. G.; Piella, J.; Puntes, V. Quantifying the Sensitivity of Multipolar (Dipolar, Quadrupolar, and Octapolar) Surface Plasmon Resonances in Silver Nanoparticles: The Effect of Size, Composition, and Surface Coating. *Langmuir* **2016**, *32* (1), 290–300. https://doi.org/10.1021/acs.langmuir.5b03859.

(22) Garcia, M. A. Surface Plasmons in Metallic Nanoparticles: Fundamentals and Applications. *J. Phys. D. Appl. Phys.* **2011**, *44* (28). https://doi.org/10.1088/0022-3727/44/28/283001.

(23) Sharwani, A. A.; Narayanan, K. B.; Khan, M. E.; Han, S. S. Photocatalytic Degradation Activity of Goji Berry Extract Synthesized Silver-Loaded Mesoporous Zinc Oxide (Ag@ZnO) Nanocomposites under Simulated Solar Light Irradiation. *Sci. Rep.* **2022**, *12* (1), 1–18. https://doi.org/10.1038/s41598-022-14117-w.

(24) Choudhary, M. K.; Kataria, J.; Bhardwaj, V. K.; Sharma, S. Green Biomimetic Preparation of Efficient Ag-ZnO Heterojunctions with Excellent Photocatalytic Performance under Solar Light Irradiation: A Novel Biogenic-Deposition-Precipitation Approach. *Nanoscale Adv.* **2019**, *1* (3), 1035–1044. https://doi.org/10.1039/c8na00318a.

(25) Grigorovici, R.; Vancu, A. Optical Properties and Electronic Structure of Amorphous Germanium. **1966**, *627*, 627–637.

(26) Shahmoradi, Y.; Souri, D. Growth of Silver Nanoparticles within the Tellurovanadate Amorphous Matrix: Optical Band Gap and Band Tailing Properties, beside the Williamson-Hall Estimation of Crystallite Size and Lattice Stain. *Ceram. Int.* **2019**, *45* (6), 7857–7864. https://doi.org/10.1016/j.ceramint.2019.01.094.

(27) Seid, E. T.; Dejene, F. B. Co-Solvent Medium Volume Ratio Effect on the Properties of Re Fl Uxed Sol-Gel Synthesized ZnO Nanopowder. *J. Alloys Compd.* **2019**, *787*, 658–665. https://doi.org/10.1016/j.jallcom.2019.02.163.

(28) Thamri, S.; Sta, I.; Jlassi, M.; Hajji, M.; Ezzaouia, H. Materials Science in Semiconductor Processing Fabrication of ZnO-NiO Nanocomposite Thin Fi Lms and Experimental Study of the e Ff Ect of the NiO , ZnO Concentration on Its Physical Properties. **2017**, *71* (April), 310–320. https://doi.org/10.1016/j.mssp.2017.08.017.

(29) Pal, S.; Nisi, R.; Stoppa, M.; Licciulli, A. Silver-Functionalized Bacterial Cellulose as Antibacterial Membrane for Wound-Healing Applications. *ACS Omega* **2017**, *2* (7), 3632–3639. https://doi.org/10.1021/acsomega.7b00442.

(30) Chauhan, A.; Verma, R.; Kumari, S.; Sharma, A.; Shandilya, P.; Li, X.; Batoo, K. M.; Imran, A.; Kulshrestha, S.; Kumar, R. Photocatalytic Dye Degradation and Antimicrobial Activities of Pure and Ag-Doped ZnO Using Cannabis Sativa Leaf Extract. *Sci. Rep.* **2020**, *10* (1), 1–16. https://doi.org/10.1038/s41598-020-64419-0.

(31) Zamiri, R.; Rebelo, A.; Zamiri, G.; Adnani, A.; Kuashal, A.; Belsley, M. S.; Ferreira, J. M. F. Far-Infrared Optical Constants of ZnO and ZnO/Ag Nanostructures. *RSC Adv.* **2014**, *4* (40), 20902–20908. https://doi.org/10.1039/c4ra01563k.

(32) Kim, T. S.; Cha, J. R.; Gong, M. S. Investigation of the Antimicrobial and Wound Healing Properties of Silver Nanoparticle-Loaded Cotton Prepared Using Silver Carbamate. *Text. Res. J.* **2018**, *88* (7), 766–776. https://doi.org/10.1177/0040517516688630.

(33)   Gao, D.; Chen, C.; Ma, J.; Duan, X.; Zhang, J. Preparation, Characterization and Antibacterial Functionalization of Cotton Fabric Using Dimethyl Diallyl Ammonium Chloride-Allyl Glycidyl Ether-Methacrylic/Nano-ZnO Composite. *Chem. Eng. J.* **2014**, *258*, 85–92. https://doi.org/10.1016/j.cej.2014.07.072.

(34)   Perkins, R.; Drake, G. L.; Reeves, W. A. DTA and TGA Studies of Flame-Resistant Fabrics. *J. Appl. Polym. Sci.* **1966**, *10*, 1041–1066. https://doi.org/10.1002/app.1966.070100708.

(35)   Lessan, F.; Montazer, M.; Moghadam, M. B. Thermochimica Acta A Novel Durable Flame-Retardant Cotton Fabric Using Sodium Hypophosphite , Nano TiO 2 and Maleic Acid. *Thermochim. Acta* **2011**, *520* (1–2), 48–54. https://doi.org/10.1016/j.tca.2011.03.012.

(36)   Kim, J. S.; Kuk, E.; Yu, K. N.; Kim, J. H.; Park, S. J.; Lee, H. J.; Kim, S. H.; Park, Y. K.; Park, Y. H.; Hwang, C. Y.; Kim, Y. K.; Lee, Y. S.; Jeong, D. H.; Cho, M. H. Antimicrobial Effects of Silver Nanoparticles. *Nanomedicine Nanotechnology, Biol. Med.* **2007**, *3* (1), 95–101. https://doi.org/10.1016/j.nano.2006.12.001.

(37)   Gorjanc, M.; Kovač, F.; Gorenšek, M. The Influence of Vat Dyeing on the Adsorption of Synthesized Colloidal Silver onto Cotton Fabrics. *Text. Res. J.* **2012**, *82* (1), 62–69. https://doi.org/10.1177/0040517511420754.

(38)   Li, R.; Yang, J.; Xiang, C.; Song, G. Assessment of Thermal Comfort of Nanosilver-Treated Functional Sportswear Fabrics Using a Dynamic Thermal Model with Human/Clothing/Environmental Factors. *Text. Res. J.* **2018**, *88* (4), 413–425. https://doi.org/10.1177/0040517516679147.

(39)   Hebeish, A.; Ramadan, M. A.; El-Naggar, M. E.; El-Rafie, M. H. Rendering Cotton Fabrics Antibacterial Properties Using Silver Nanoparticle-Based Finishing Formulation. *Res. J. Text. Appar.* **2011**, *15* (2), 114–120. https://doi.org/10.1108/RJTA-15-02-2011-B013.

(40)   Jyoti, K.; Baunthiyal, M.; Singh, A. Characterization of Silver Nanoparticles Synthesized Using Urtica Dioica Linn. Leaves and Their Synergistic Effects with Antibiotics. *J. Radiat. Res. Appl. Sci.* **2016**, *9* (3), 217–227. https://doi.org/10.1016/j.jrras.2015.10.002.

(41)   Jain, A. S.; Pawar, P. S.; Sarkar, A.; Junnuthula, V.; Dyawanapelly, S. Bionanofactories for Green Synthesis of Silver Nanoparticles: Toward Antimicrobial Applications. *Int. J. Mol. Sci.* **2021**, *22* (21). https://doi.org/10.3390/ijms222111993.

(42)   Xiu, Z. M.; Zhang, Q. B.; Puppala, H. L.; Colvin, V. L.; Alvarez, P. J. J. Negligible Particle-Specific Antibacterial Activity of Silver Nanoparticles. *Nano Lett.* **2012**, *12* (8), 4271–4275. https://doi.org/10.1021/nl301934w.

(43)   Morones, J. R.; Elechiguerra, J. L.; Camacho, A.; Holt, K.; Kouri, J. B.; Ramírez, J. T.; Yacaman, M. J. The Bactericidal Effect of Silver Nanoparticles. *Nanotechnology* **2005**, *16* (10), 2346–2353. https://doi.org/10.1088/0957-4484/16/10/059.

(44)   Lemire, J. A.; Harrison, J. J.; Turner, R. J. Antimicrobial Activity of Metals: Mechanisms, Molecular Targets and Applications. *Nat. Rev. Microbiol.* **2013**, *11* (6), 371–384. https://doi.org/10.1038/nrmicro3028.

(45) Zhu, W.; Li, Z.; Zhou, Y.; Yan, X. Deposition of Silver Nanoparticles onto Two Dimensional BiOCl Nanodiscs for Enhanced Visible Light Photocatalytic and Biocidal Activities. *RSC Adv.* **2016**, *6* (69), 64911–64920. https://doi.org/10.1039/c6ra09964e.

(46) Emam, H. E.; Bechtold, T. Cotton Fabrics with UV Blocking Properties through Metal Salts Deposition. *Appl. Surf. Sci.* **2015**, *357*, 1878–1889. https://doi.org/10.1016/j.apsusc.2015.09.095.

(47) Mahmud, S.; Pervez, N.; Taher, M. A.; Mohiuddin, K.; Liu, H. H. Multifunctional Organic Cotton Fabric Based on Silver Nanoparticles Green Synthesized from Sodium Alginate. *Text. Res. J.* **2020**, *90* (11–12), 1224–1236. https://doi.org/10.1177/0040517519887532.

(48) Gorenšek, M.; Recelj, P. Nanosilver Functionalized Cotton Fabric. *Text. Res. J.* **2007**, *77* (3), 138–141. https://doi.org/10.1177/0040517507076329.

(49) Čuk, N.; Šala, M.; Gorjanc, M. Development of Antibacterial and UV Protective Cotton Fabrics Using Plant Food Waste and Alien Invasive Plant Extracts as Reducing Agents for the In-Situ Synthesis of Silver Nanoparticles. *Cellulose* **2021**, *28* (5), 3215–3233. https://doi.org/10.1007/s10570-021-03715-y.

(50) Porrawatkul, P.; Pimsen, R.; Kuyyogsuy, A.; Teppaya, N.; Noypha, A.; Chanthai, S.; Nuengmatcha, P. Microwave-Assisted Synthesis of Ag/ZnO Nanoparticles Using Averrhoa Carambola Fruit Extract as the Reducing Agent and Their Application in Cotton Fabrics with Antibacterial and UV-Protection Properties. *RSC Adv.* **2022**, *12* (24), 15008–15019. https://doi.org/10.1039/d2ra01636b.

(51) Priyadarsini, K. I. Journal of Photochemistry and Photobiology C : Photochemistry Reviews Photophysics, Photochemistry and Photobiology of Curcumin : Studies from Organic Solutions, Bio-Mimetics and Living Cells. **2009**, *10*, 81–95. https://doi.org/10.1016/j.jphotochemrev.2009.05.001.

(52) Altaf, N. U. H.; Naz, M. Y.; Shukrullah, S.; Bhatti, H. N. Testing of Photocatalytic Potential of Silver Nanoparticles Produced through Nonthermal Plasma Reduction Reaction and Stabilized with Saccharides. *Main Gr. Chem.* **2021**, *20* (4), 475–488. https://doi.org/10.3233/MGC-210059.

5. Multifunctional finishing of cotton fabric by TiO₂@Ag nanoparticles

Abstract

Titanium dioxide@silver nanoparticles (TiO$_2$@Ag NPs) were synthesized by wet chemical methods, whereas TiO$_2$ NPs were previously synthesized by the sol-gel process. TiO$_2$@Ag NPs were characterized using dynamic light scattering , FTIR spectroscopy, UV-vis spectroscopy, XXRD), and TEM. The cotton fabric was coated with TiO$_2$@Ag NPs using an acrylic binder by a pad-dry-cure technique. The morphological characteristics of Ag NPs coated fabric were assessed through SEM. The antibacterial effectiveness of Ag NPs coated cotton fabric was evaluated separately against *Staphylococcus aureus*, a gram-positive bacterium, and *Escherichia coli*, a gram-negative bacterium. The results indicated a reduction of over 99.9% for *Staphylococcus aureus* and around 99.9% for *Escherichia coli* bacteria. The coated fabric demonstrated a favorable UPF of 26.14. The self-cleaning properties were examined using curry strains as model dirt. The coated fabric effectively removed curry stains following a 20 h exposure to xenon UV light.

Keywords

UV protection, antibacterial, self-cleaning, textiles, titanium dioxide, silver, core@shell

5.1 Introduction

Research associated with a multifunctional finish, like UV protection, antibacterial activity and self-cleaning finish has accepted significant recognition within the scientific community because of their future applications in industry and daily life.[12] The textile industry is not only oriented towards the basic demands of comfort and fashion but also revolutionized by the introduction of nanotechnology as nanomaterials play a vital role for its exceptional surface attributes to develop and manufacture smart and multifunctional textiles, like anti-aging properties, UV protection, superhydrophobicity, fire-retardancy, antibacterial performance and self-cleaning properties.[345] UV protection, antibacterial activity and self-cleaning finish can be helpful in textile products that are threatened by

exposing prolonged sunlight, exposure against bacteria and staining with huge contaminants like soot, oils, and lubricants as it may have a great potential of further widening the functional applications of cotton fabrics and imparting several new functional properties by the use of fiber surface modification by the deposition of various NPs coatings.[6] Recently, the study of core-shell metal NPs is an emerging field and has attracted attention, especially in the field of photocatalysis,[789] owing to its conducive and versatile compositions and structures to serve as potential material for various device applications. Moreover, it may also have synergistic properties between the cores and shells based on their interactions. These tailored properties have also advanced in NPs for various applications such as device fabrication.[10] The NPs consist of an inorganic semiconductor matrix covered, usually, with a shell of metal that has gained massive attention from the academic and industrial fraternity because of its vast intromission into different chapters of technological excellence.[11] The preparation of "core@shell" systems needs a cautious choice of both core and shell material to optimize the passivation and to reduce the structural defects induced by positive mismatch of their lattice parameters.[12] A plenty of synthetic strategies are available for these core@shell materials though they divide into two main categories: (a) a one-step preparation of core-shell nanoparticles require simultaneous development of noble metal oxide NPs and metal shells, and (b) coating of former prepared metal oxide NPs with a shell of metal oxide. This second approach generally conduct to upgrade monodispersity of the core@shell structures and is also captivating for the formation of non-centrosymmetric morphologies.[13,14] Some fascinating shapes of core-shell are yolk-shell [15] Janus,[16] flower-like[17] and eccentric[18], and many of these structures exhibit novel plasmonic properties. Inorganic semiconductor NPs have attained significant recognition due to their distinctive optical and electrical properties that can be applied in nanophotonics and nanoelectronics.[1920] Among these semiconductor NPs, TiO_2 is prime in various energy-related applications, mainly in the fields of photovoltaic,[21] optics[22] and field emission[23] because of its excellent properties, such as high redox potential, excellent chemical stability,[24] nontoxicity, and low cost. Anatase TiO_2 had a wide direct bandgap of 3.23 eV, which could only absorb radiations light below 384 nm to produce charges (electron/hole (e-/h+) pairs), resulting in low photocatalytic activity. To

increase the photocatalytic performance of TiO$_2$, it should not only improve visible light absorption efficiency but also efficiently restrain the recombination of charges.[24] Silver has been chosen as shell material, playing the most important role in developing plasmonics. Surface plasmon resonance (SPR) is an exciting characteristic of silver that has been primarily employed for surface-enhanced spectroscopy, biological and chemical imaging, lithographic fabrication,[25] and other applications.[26]

Different methods for the synthesis of different kinds of NPs were reported. The combination of TiO$_2$ and Ag core-shell can effectively enhance photocatalytic properties[27] and antibacterial activity.[28],[29]

5.2   Experimental

5.2.1   Materials

Titanium (IV) butoxide (Sigma- Aldrich), acetic acid and hydrochloric acid (RCI Labscan Limited, Thailand), silver nitrate (AgNO$_3$, reagent grade, Scharlau, Spain), cetyltrimethylammonium bromide (CTAB,>98%, Merck), NaBH$_4$ (>98%, ACROS organics, Belgium), binder of aqueous acrylate dispersion (Forbind OB 45, Fortune top Pte Ltd. New Taipei City, Taiwan) were used without further purification. Deionized water (conductivity: 0.055 µScm^{-1}) collected from the HPLC grade water purification system (BOECO) was used to prepare all solutions. Scoured and bleached 100% cotton single jersey knit fabric was used throughout all experiments.

5.2.2   Synthesis of TiO$_2$ nanoparticles by sol-gel method

TiO$_2$ nanoparticles were synthesized through a particular sol-gel process using Titanium (IV) butoxide as a precursor material. This synthesis dissolved 0.2% HCl and 0.2% acetic acid in 10 mL of deionized water. Titanium (IV) butoxide of 3 mL was added dropwise into 7 mL of water containing acid at 60 ℃. The mixture was then vigorously stirred at 700 rpm for 48 hours at 60 ℃. The color of the solution changed rapidly from colorless acidic water and light yellow titanium (IV) butoxide to white, indicating the onset of the formation of TiO$_2$ NPs. TiO$_2$ powder was extracted from the above-prepared sol using a sufficient amount of 0.3% sodium carbonate aqueous solution until precipitation occurred. The produced suspensions were centrifuged (Centrifuge Cencom II from J. P. Selecta,

Spain) at 1000 rpm for 20 min by eliminating the liquid phase. The precipitates were washed thrice with deionized water, dried overnight in an oven at 100 °C, and ground into powder.[30]

5.2.3   Preparation of TiO₂@Ag nanoparticles

To synthesize the TiO$_2$@Ag NPs, 0.7 mmol of TiO$_2$ NPs were dispersed in 50 mL deionized water by ultrasonication for 30 min. After completing sonication, 0.09 mmol of CTAB, which was used as a capping and stabilizing agent, was dissolved in the above solution by stirring at 300 rpm by a magnetic stirrer. Then, the temperature was raised to 40 °C under constant stirring, and the solution temperature was slowly reduced to room temperature. Afterward, a 25 mL aqueous solution of AgNO$_3$ was gradually added dropwise to the above solution under constant stirring for one h at room temperature. Then a 25 mL aqueous solution of 0.7 mmol of NaBH$_4$ was added slowly under constant stirring to reduce Ag NPs. The color of the solution changed from white to green color, with surface plasmon resonance indicating the onset of the formation of TiO$_2$@Ag NPs. Then the solution was aged overnight and dried at 60 °C. Finally, TiO$_2$@Ag NPs were synthesized.[31]

5.2.4   Preparation of TiO₂@Ag NPs coated cotton fabric

TiO$_2$@Ag NPs were applied to cotton knit fabrics by a pad dry cure method. At first, cotton fabric (20 cm × 20 cm) was dipped into 100 mL of TiO$_2$@Ag NPs sol after completing 5 min stirring by a magnetic stirrer to prevent precipitation of NPs, and then padding was done to apply TiO$_2$@Ag NPs on cotton fabrics. The fabric was second time padded by adding 1% binder in 100 mL distilled water. A standard laboratory machine was used for padding with 2.5 m/min fabric speed and 2.8 kg/cm^2 padding pressure to maintain pick up is about 70-75%. The pH value of the padding bath was maintained at around 6. The sample was dried at 80 °C for 5 min by an oven machine, and an SDL Mini-dryer steamer was used for curing at 140 °C for 2.5 min.

5.2.5 Material Characterization

The average particle size and size distribution of the samples dispersed in water were measured using DLS measurements by a Malvern Zetasizer Nano ZS90 with a scattering angle of 90°. A He–Ne laser beam of 632.8 nm was used for the measurements. The average diameters were determined from cumulants mean of the intensity average of 50 runs using Stokes–Einstein equation, $d_H = k_B T / 3\pi\eta D_{ef}$, where d_H is the hydrodynamic diameter, k_B is the Boltzmann constant, T is the temperature, η is the solvent viscosity, and D_{ef} is the diffusion coefficient. The reproducibility was checked from at least three measurements. The sample temperature was controlled automatically within ±0.01 K by a built-in Peltier device.

FTIR spectra were recorded by a Fourier transform spectrophotometer FrontierTM by PerkinElmer in transmittance mode for each KBr sample range between 400 and 4000 cm^{-1} at 4.0 cm^{-1} resolution. Attenuated total reflectance-Fourier transform infrared (ATR-FTIR) spectra was recorded by a Courier' transform Infrared (MB3000, ABB Analytical, Canada) in transmittance mode for each sample in the range between 400 and 4000 cm^{-1} at 4.0 cm^{-1} resolution.

The crystallographic and phase-dependent properties were analyzed by an X-ray diffractometer (Philips PW 1724) with an X-ray generator using XDC-700 Guinier-Hagg focusing camera with monochromatized Cu Kα radiation (λ = 1.540598 Å). The measurement was performed in the continuous mode with a scan speed of 3.0 deg/min within the 10-70 ºC range while the scan width was 0.026 deg. According to Debye-Scherrer's equation $D = \frac{K\lambda}{\beta cos\theta}$, the crystallite domain diameters (D) were obtained from XRD peaks.

The surface morphology, structure and attachment of Ag on TiO_2 were studied with TEM, and the micrographs were attained using the LEO system (model 912 AB) at 120kV for samples.

UV–vis absorption spectra were recorded by a double-beam UV–vis spectrophotometer (UVD-3500, LABOMED, INC, USA), where cell length is 1 cm. UV-vis diffuse

reflectance spectra were recorded using a double-beam UV-visible spectrophotometer with an integrating sphere attachment DRA-CA-30I (Model: UV-1800, Shimadzu, Japan) to determine the solid nanoparticle band gap (energies.

The morphological study used FESEM (ZEISS, Germany). The acceleration voltage of the electron gun was 20 kV with a probe current of 1.0 nA and magnifications ranging from 10,000 – 100,000. The images of samples were taken without sputtering and by mounting on the conducting carbon tape. Compositional study of the nanoparticles is analyzed by EDX attached to the FESEM. ImageJ 1.51k (Java 1.60-24 (64 bit), USA) was used to measure average particle size in both the TEM and the FESEM images of NPs. Thermal properties were studied under a nitrogen atmosphere by a Hitachi instrument (TG/ DTA 7200) in the 30–550 °C at a heating rate of 20° min^{-1}. The physical properties of the fabrics (weight, bursting strength, air permeability) were examined by ISO standards.

5.2.6 Color measurements

A spectrophotometer (Datacolor SF850, Datacolor International, USA) measured the colorimetric analysis of the control and coated fabrics. Measurements were done by D65 (average daylight), F11 (fluorescent lighting), and A (tungsten-filament lighting) standard illuminants at a 10 observing angle with d/8 viewing geometry. The CIE Lab color coordinates (L^*, a^* and b^*) where L^* represents white black, a^* and b^* represent redness–greenness and yellowness–blueness, respectively. The CIE computer color matching (CMC) color coordinates (L^*, C^* and H^*) where, L^*, represents white black, C^* represents brighter duller, H^* represents hue and the color difference (ΔE) between reference (control fabric) and sample (coated) fabrics were measured by the following equation (5.1-8):[32]

$$\Delta L^* = L^*_{reference} - L^*_{sample} \qquad (5.1)$$

$$\Delta a^* = a^*_{reference} - a^*_{sample} \qquad (5.2)$$

$$\Delta b^* = b^*_{reference} - b^*_{sample} \qquad (5.3)$$

$$\Delta C^* = C^*_{reference} - C^*_{sample} \qquad (5.4)$$

$$\Delta H^* = H^*_{reference} - H^*_{sample} \qquad (5.5)$$

$$C = \sqrt{\Delta a^{*2} + \Delta b^{*2}} \qquad\qquad (5.6)$$

$$H = tan^{-1} b/a \qquad\qquad (5.7)$$

The color difference, ΔE^*, provided the distance within the reference and the textile sample in the CIE Lab color space and was calculated by the following equation:

$$\Delta E^* CMC = \Delta L^* \Delta C^* \Delta H^* \qquad\qquad (5.8)$$

Where, $\Delta L^*, \Delta a^* \Delta b^* \Delta C^*, \Delta H^*$ are the respective differences between control and coated fabrics.

5.2.7 Assessment of antibacterial properties

Antibacterial property was carried out to demonstrate the efficiency of the coated fabric against microorganism development. The coated and control fabric specimens were used to assess the antimicrobial property according to ASTM E2149-01, a quantitative method used to evaluate the protection of non-leaching antimicrobial coated samples to the advancement of microbes against dynamic contact situations. The antimicrobial property was assessed by *S. aureus* (gram-positive) and *E. coli* (gram-negative) bacteria. Each culture was suspended in a low amount of nutrient broth, swept on the nutrient agar plate and incubated at 37 °C for 24 h. Two single colonies were grasped with an inoculating loop from the agar plate, put down on both coated and control fabrics in two different Petri dishes and incubated at 37 °C for 24 h to permit the insertion of NPs into the microorganism cells. The antimicrobial activity of testing specimens was evaluated by percent reduction of the microorganisms after contact with coated and control fabrics.[33]

The reduction R (%) in microorganisms was determined by the following equation:

$$R\ (\%) = \frac{B-A}{A} \times 100 \qquad\qquad (5.9)$$

A and B express the surviving cells (colony forming units per mililitre (CFU/mL) in a flask containing coated and control fabrics, respectively, after a contact time of 1 h.

5.2.8 Assessment of UV protection properties

The UV protection properties of the $TiO_2@Ag$ NPs attached fabric are evaluated by the ultraviolet protection factor (UPF) and UV transmission spectra, which were reported by using a double beam ultraviolet-visible (UV-vis) spectrometer (Cintra 2020, GBC, Australia), with an integrating sphere attachment. The tests were reported following standard PN-EN 13758-1:2007.

The UPF of fabric is determined as following equation (5.10-11):[34]

$$UPF = \frac{\sum_{\lambda=290}^{400} E(\lambda) \cdot \varepsilon(\lambda) \cdot \Delta(\lambda)}{\sum_{\lambda=290}^{400} E(\lambda) \cdot T(\lambda) \cdot \varepsilon(\lambda) \cdot \Delta(\lambda)} \qquad (5.10)$$

$$\text{Percent UV transmission} = \frac{\sum_{\lambda_1}^{\lambda_2} T(\lambda)}{(\lambda_2 - \lambda_1)} \qquad (5.11)$$

Where $E(\lambda)$ expressed in $W/m^2/nm$ = solar irradiance, $T(\lambda)$ = spectral transmittance at the wavelength λ, $\varepsilon(\lambda)$ = erythema action spectrum, and $\Delta\lambda$ = wavelength interval. The UPF values of textiles represent their UV radiation blocking capabilities, as higher UPF values mean higher protection capacity.[35]

Fabrics can be classified as providing good, very good or excellent protection based on their UPF values ranging from 15 to 50+ following the Australian classification scheme (Table 5.1).

Table 5.1: Classification of UPF category measured from relative transmittance and protection level.[36]

UPF range	Protection category	UVBE$_{eryt}$ transmittance (%)
<15	Insufficient protection	>6.7
15-24	Good protection	6.7-4.2
25-39	Very good protection	4.1-2.6
40-50, 50+	Excellent protection	<2.5

5.2.9 **Evaluation of self-cleaning activity**

The self-cleaning performance of TiO$_2$@Ag NPs coated fabric was measured by the color strength change of curry stain under UV irradiation. Curry paste is made in addition to 0.5 g 100% curry powder (Radhuni, meat curry powder) in 10 mL hot water. One drop of curry solution is dropped close on TiO$_2$@Ag NPs coated fabric, allowed to spread and dried in air and then exposed to light irradiation. The irradiation of stained TiO$_2$@Ag NPs treated fabric was carried out for 20 h in a Xenotest Alpha LM light exposure and weathering test instrument (air-cooled xenon arc lamp, Xenotest Alpha LM, USA). One-half of each stain on the fabric was exposed to a Xenon arc lamp, while the other half was unexposed with a steel frame to prevent its irradiation. The exposed part of the stain was compared with the unexposed part for self-cleaning action. The self-cleaning action was quantified by comparing the color strength (*K/S*) between the exposed part and the unexposed part of the same stain. The reflectance of the stained fabric was measured by the spectrophotometer (Datacolor SF850, Datacolor International, USA). The reflectance (*R*) was used to calculate the degradation rate as in the Kubelka-Munk equation (eqn. 5.12).[37]

$$\frac{K}{S} = \frac{(1-R)^2}{2R} \qquad (5.12)$$

Here, *K/S* means color strength, and *K* and *S* are the absorption and scattering coefficients.

5.3   Result and Discussion

5.3.1   **DLS analysis**

DLS employed to evaluate the macromolecules and small particles in dilute suspension with the help of coherent light sources.[38] DLS measurement was carried out in the aqueous suspension of TiO$_2$@Ag NPs and TiO$_2$ NPs to express the size distribution in Figure 5.1. Two sinusoidal peaks are observed and the maxima, with the highest probability of the particles to be found at around 144 nm hydrodynamic diameter of TiO$_2$@Ag NPs whereas TiO$_2$ NPs show multiple sinusoidal peaks with very small particles with hydrodynamic diameter (d_h) around 1 nm, moderate-sized particles (1 to 20 nm) and particles of d_h about 50-220 nm reveal their existence. The peak maxima to be found, are near 1 and 10 nm as the intensity is far more than another peak. The narrow width of the peaks indicates that

particles consist a small range of hydrodynamic diameter. DLS usually measures the hydrodynamic diameter of the particles in solution which is based on the Brownian motion of the particles in aqueous solution. Particle size found from DLS takes place in a solution form, so the nanoparticles may be swelled with time while measuring.[39] Additionally, DLS analysis signifies that the NPs formed had quite well-defined dimensions.[40] Smaller the size of the NPs, is higher the surface area is, which facilitate higher UV protection and self-cleaning activity.[41]
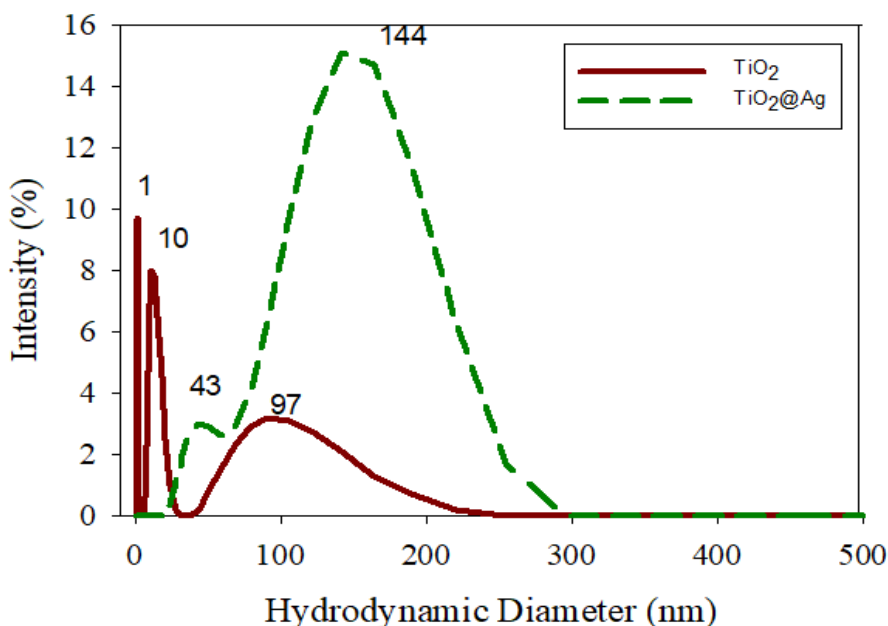
Figure 5.1: Average hydrodynamic diameter of TiO$_2$ and TiO$_2$@Ag core@shells NPs from DLS measurements.

5.3.2 **FTIR spectra analysis**

The elucidation of structural attribute by FTIR spectrum is shown in Figure 5.2 and the spectra was analyzed within 4000 to 400 cm^{-1}. The spectra of TiO$_2$@Ag nanocrystals exhibit prominent peaks at 407, 507, 1029, 1383.2 cm^{-1}. The nanocrystals showed intense peak around 507 cm^{-1} indicating the presence of Ti-O-Ti band of TiO$_2$ from the longitudinal optical mode (LOM).[42,43] The red shift of the LO mode of TiO$_2$ from 580 cm^{-1} to 507 cm^{-1} was a significance of the existence of Ag nanograins.[44] A small peak at 1383.2 cm^{-1} is attributed to the hydroxyl groups of moisture.[45] Two sharp broad and intense absorption

133

peaks located at 3450 cm^{-1} and 1624 cm^{-1} corresponding to the stretching and bending vibration of the O-H mode that may be due to the OH groups of water physiosorbed of TiO$_2$.[46] The peak that attributed to the vibration of the Ag-Ag metallic bonds cannot be seen in this graph because the FTIR uses the mid-infrared ray (4000-400 cm^{-1}) that is not suitable to measure the vibration frequency of metal-metal bonds.[47] The weak band near 407 and 1029 cm^{-1} may correspond to the stretching and vibration of Ag-O.[48]
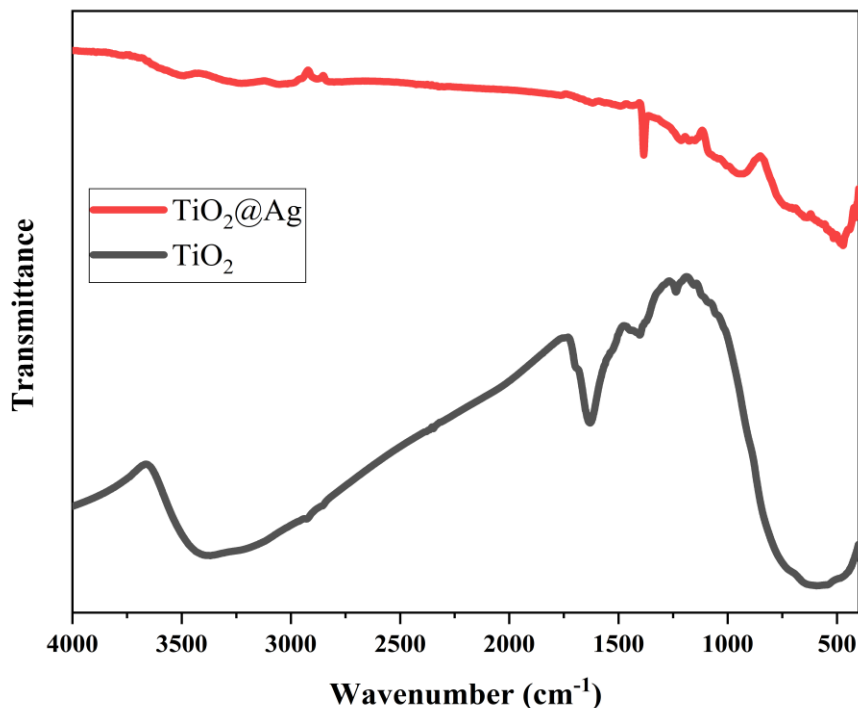
Figure 5.2: FTIR spectra of TiO$_2$ and TiO$_2$@Ag NPs.

Table 5.2: The FTIR transmittance characteristic peaks of TiO$_2$ NPs and TiO$_2$@Ag NPs

TiO$_2$ NPs	TiO$_2$@Ag NPs	Mode of vibration
----------	407 cm^{-1}	(Ag+) ion of silver [44]
580 cm^{-1}	507 cm^{-1}	Ti-O and Ti-O-Ti [4243]
----------	1029 cm^{-1}	[Ag-O] [48]
1389.7 cm^{-1}	1383 cm^{-1}	-OH bending[46]
1624 cm^{-1}	----------	-OH bond of vibration of the surface adsorbed of Ti-OH[45]
3450 cm^{-1}	3450 cm^{-1}	Surface -OH groups and absorbed water [46]

5.3.3 Determination of optical band gap and the nature of optical charge carrier transitions

By using the DASFapproach and the accompanying equations (5.13-14), the optical band gap of TiO_2@Ag NPs is reported:[49]

$$ln\left[\frac{f(R)}{\lambda}\right] + ln\,s = ln[B(hc)^{m-1}] + m\,ln(\frac{1}{\lambda} - \frac{1}{\lambda_g}) \qquad (5.13)$$

Now,

$$\frac{d\{ln\left[\frac{f(R)}{\lambda}\right]\}}{d(\frac{1}{\lambda})} = \frac{m}{\frac{1}{\lambda} - \frac{1}{\lambda_g}} \qquad (5.14)$$

As R is the reflectance and $f®$ is proportional to the absorption coefficient (α), $f®$ is calculated using the Kubelka-Munk technique (eqn. 5.15).

$$f(R) = \frac{(1-R)^2}{2R} \qquad (5.15)$$

Where, λ is the wavelength, c is the velocity of light, λ_g is the wavelength corresponding to the optical band gap, B is a constant and s is the scattering coefficient. hv is the energy of the photon and E_g is the bandgap energy of the sample. The optical bandgap of the sample is calculated by the extrapolation of a linear portion in the plot of $dln[\alpha(\lambda)\lambda^{-1}]/d\lambda^{-1}$ against hv extended in Figure 5.3. The calculated E_g of TiO_2@Ag NPs is 2.8 eV which is reduced from pure TiO_2 NPs (3.19 eV).
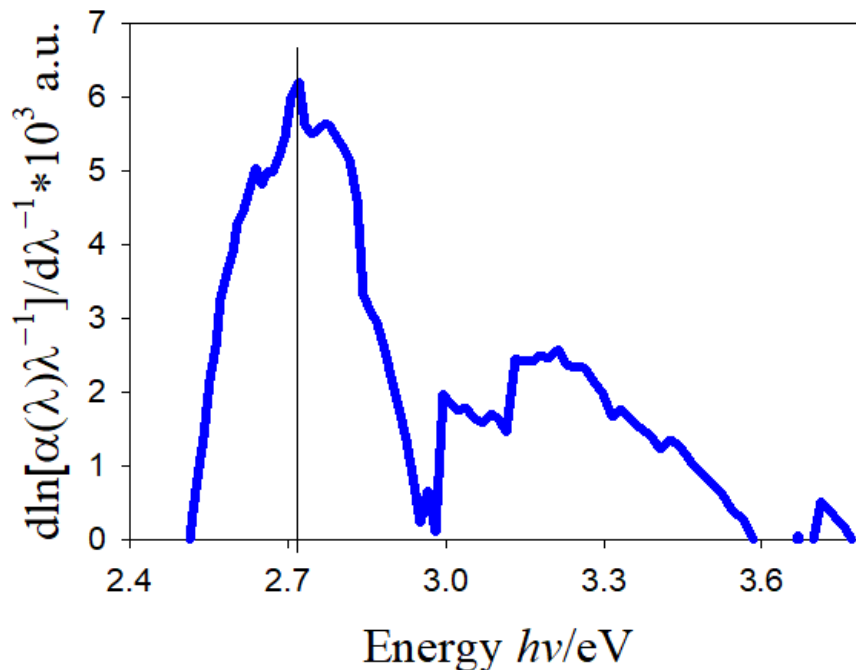
Figure 5.3: DASF method calculated for bandgap by plotting of dln[α(λ)λ^{-1}]/d λ^{-1} versus hν.

The reduction of E_g by addition of Ag may be indicated that Ag has substituted the Ti in the lattice that creates oxygen vacancies due to the valence difference between Ag^+ and Ti^{4+}. The created oxygen vacancies take part a significant role in the narrowing of E_g since they act as trap centers that decrease the recombination rate of photo-generated charge carriers by capturing the electrons.[50] Moreover, host TiO_2 states maybe interact by Ag state leading to create energy levels in TiO_2 band gap that reduce its optical band gap thus improve the photocatalytic properties of TiO_2 by widening the spectrum of the visible light response.[51] The variation within band gap values for TiO_2@Ag and TiO_2 are obtainable to structural parameter, grain size and concentration of carrier. [52,53] The corresponding coefficient (*m*) of the sample is calculated by the extrapolation of a linear portion in the plot of *ln[α(λ)λ^{-1}]* versus *ln[λ^{-1} − λ$_g$$^{-1}$]* extended in Figure 5.4. The corresponding coefficient (*m*) associated with an electronic transition is calculated and found *m* = 1/2 defines the direct allowed transition.

Figure 5.4: DASF method calculated for corresponding coefficient (m) by plotting of $\ln[\alpha(\lambda)\lambda^{-1}]$ versus $\ln[\lambda^{-1} - \lambda g^{-1}]$. The inset is the reflectance spectra of $TiO_2@Ag$ NPs.

5.3.4 **Optical properties (UV absorbance)**

UV-vis absorption spectra of aqueous solution of pure TiO_2 and $TiO_2@Ag$ NPs (Figure 5.5 (a)) exhibit that the surface plasmon resonance of $TiO_2@Ag$ NPs is shifted to the longer range of 287 nm from 251 nm of pure TiO_2 NPs due to the addition of the strong band of Ag NPs as the inter-band transition of the TiO_2 NPs is at 200 and 350 nm.[54] The band gap energy of TiO_2 and $TiO_2@Ag$ NPs can be estimated by the formula (eqn. 5.16):[55]

$$\alpha h v = A(h v - E_g)^n \qquad (5.16)$$

Where α, v, A and E_g are absorption coefficient, light frequency, a constant and direct optical bandgap energy respectively and $n = \frac{1}{2}$ (for direct transition mode material). Where bandgap can be measured by extrapolating the linear part of a plot of $(\alpha h v)^2$ versus photon energy $(h v)$ of the exciting light that is reported in Figure 5.5 (b). The intersection of the tangent line with the x axis provides a better resemblance of the bandgap energy of both TiO_2 (pink line) and $TiO_2@Ag$ (green line) NPs. TiO_2 has a direct band gap transition.[56] It can be noted that the bandgap energy (E_g) of $TiO_2@Ag$ NPs is decreased significantly to

137

2.61 eV from 3.35 eV of pure TiO_2 NPs as the reduction of E_g may be due to absorption edge shifting to longer wavelength (red shift) after the addition of Ag, maybe because of the grain boundary scattering and the SPR of Ag NPs, thus improved the absorption of light in the visible region.[57]

Figure 5.5: (a) UV-vis absorption spectra of dispersion solutions of TiO_2 and TiO_2@Ag NPs and (b) Tauc plot of the TiO_2 (pink line) and TiO_2@Ag (green line) NPs.

Table 5.3: Band gap energy of TiO_2 and TiO_2@Ag NPs estimated from Tauc plot and by using the DASF method.

Sample	Band gap energy (eV) by Tauc plot	Band gap energy (eV) by DASF method
TiO_2 NPs	3.35	3.19
TiO_2@Ag NPs	2.61	2.8

5.3.5   X-ray diffraction analysis

Figure 5.6 exhibits the XRD patterns of synthesized TiO_2 by sol gel method and TiO_2@Ag NPs by wet chemical method. As can be noticed, the sole TiO_2 can be well indexed to anatase tetragonal structure (JCPDS No. 65-5714) with five sharp diffraction peaks (2θ) at 25.3°, 37.7°, 47.88°, 54.42° and 62.59° associated with the lattice planes designated by Miller indices (101), (104), (200), (105) and (211). Good crystallization is also exhibited from sharp diffraction peaks. As for TiO_2@Ag NPs, it is captivating to record that the diffraction peaks of both anatase TiO_2 and Ag could be noticed in the as-prepared core-shell, suggested that the core@shell consist of TiO_2 and Ag. Moreover, TiO_2@Ag NPs

showed five fundamental peaks corresponding at 25.33°, 37.99°, 47.94°, 54.67°, 63.12° belonged respectively to (101), (004), (200), (105) and (211) of TiO_2 magnetite; meanwhile, there are additional peaks at 31.01°, 44.44°, 55.20° and 64.65° belonging respectively to the (122), (200), (142) and (220) planes of Ag (JCPDS, No. 04-0783). The average crystallite diameter D was calculated from Debye-Scherrer's equation (5.17):

$$D = \frac{K\lambda}{\beta cos\theta} \qquad (5.17)$$

Figure 5.6: XRD patterns of TiO_2-and TiO_2@Ag NPs.

Where D is the crystallite size, $K = 0.9$, λ = the wavelength of X-ray radiation (1.5406 Å), β = the full width half maximum of diffraction peak and θ = the Braggs diffraction angle.[58] Lattice strain was calculated by equation 5.18:

$$\eta = \frac{\beta}{tan\theta} \qquad (5.18)$$

Where, η = Lattice strain in the material, β = the full width half maximum of diffraction peak and θ = the Braggs diffraction angle. The dislocation density (δ), which represents the number of defects in the crystal, was calculated by using the Williamson-Hall equation5.19:

$$\delta = \frac{1}{D^2} \qquad (5.19)$$

Where D is the crystallite size. The dislocation density is inversely proportional to D^2 and d-spacing (d_{hkl}) was calculated by following equation5.20:

$$d_{hkl} = \frac{\lambda}{2sin\theta} \qquad (5.20)$$
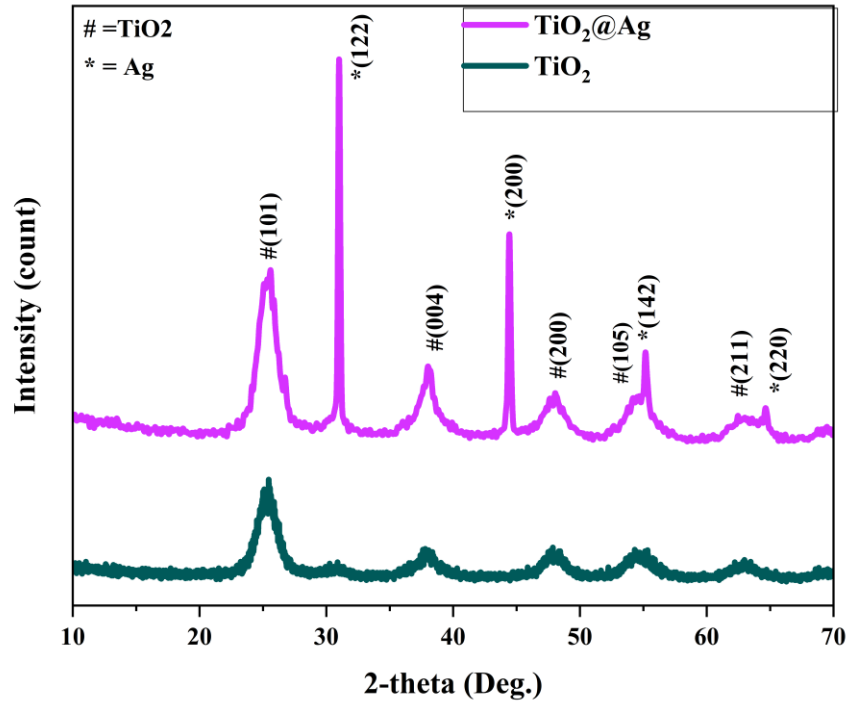
Where λ = the wavelength of X-ray radiation (1.5406 Å) and θ = the Braggs diffraction angle.[59] The crystallite size, lattice strain, dislocation density, lattice planes, and d-spacing values are listed in Table 5.4.

Table 5.4: 2θ, crystallite size, lattice strain, dislocation density, *hkl,* d-spacing of Ag NPs as presented in XRD pattern analysis.

Phase	2θ (degree)	β	D (nm)	η=β/tanθ	δ (nm⁻²)	hkl	d_{hkl}=λ/2sinθ
TiO₂	25.38	1.92	4.25	0.1486	0.0554	1 0 1	0.3506
Ag	31.01	1.88	4.38	0.1183	0.0520	1 2 2	0.2881
TiO₂	37.99	1.77	4.74	0.0899	0.0446	0 0 4	0.2366
Ag	44.44	2.17	3.95	0.0928	0.0641	2 0 0	0.2037
TiO₂	47.94	1.70	5.13	0.0666	0.0380	2 0 0	0.1896
TiO₂	54.67	1.70	5.27	0.0573	0.0359	1 0 5	0.1678
Ag	55.20	1.70	5.29	0.0566	0.0358	1 4 2	0.1663
TiO₂	63.12	1.70	5.50	0.0482	0.0331	2 1 1	0.1472
Ag	64.65	1.70	5.54	0.0468	0.0325	2 2 0	0.1441

5.3.6 TEM analysis

TEM images of the TiO₂@Ag NPs are shown in Figure 5.7(a–b). TEM analysis points out shape and particle size of TiO₂@Ag NPs. The TEM images, the SAED pattern (Figure 5.6 (c)c), and histogram (Figure 5.6 (d)) exhibits that core@shell is formed in spherical structure as Ag is surrounded throughout TiO₂ surface. It is evident that spherical shape

nanocrystals are formed with a narrow size distribution. These nano core@shell could not be plainly discriminated from each other.[60] The average particle size of this core@shell was measured by using image software and particle size of TiO_2@Ag NPs was at range from 20–90 nm that shown on histogram and were at agglomerated form. The SAED patterns of TiO_2@Ag NPs are shown in Figure 7c. The diffraction rings were slightly diffuse, indicating that the texture was polycrystalline with small grain sizes.[61]
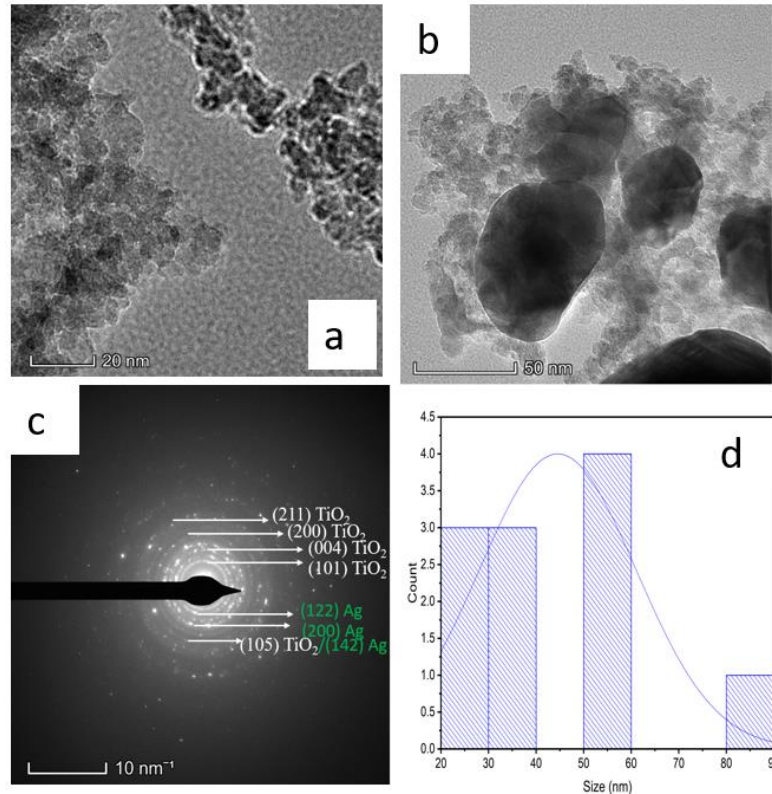
Figure 5.7: TEM images of (a-b) TiO_2 and TiO_2@Ag NPs with different magnifications, (c) SAED pattern and (d) histogram.

which was consistent with results from the XRD pattern that are shown in Figure 5.6. The diffraction rings evidently present the mixed phase of anatase TiO_2 and Ag as this unveils the ring-like diffraction pattern coincide to the (101), (122), (004), (200), (200), (105), (142) and (211) lattice planes of TiO_2 and Ag NPs. It is inspected that this absolute circle rings with spots are good coordinated with the XRD pattern of TiO_2@Ag NPs as that are clarify the profoundly crystalline nature.

5.3.7 SEM analysis

The SEM analysis was used to acknowledge the surface morphology of control and TiO_2@Ag NPs coated fabrics in Figure 5.8, control cotton fibre is expressed in Figure 5.8 (a) that exhibited a very smooth surface alongside a quality "twisted ribbon" and heterogeneous surface with evident micro-fibrils.[62] However, the surface morphology is altered after coating with TiO_2@Ag NPs that shown at Figure 5.8 (b-d) with different magnifications. Some spherical shaped NPs can be detected on the surface of coated fibre to expose the attachment of NPs. It also explained that acrylic binder accomplishes the duty of the ''binding element'' of NPs with the fiber surface. The diameter of NPs that found by histogram (Figure5.8 (e)) is slightly more than the diameter that found by TEM, as it may be because of some agglomerates of the NPs were formed when coating is done by padding due to lack of stirring throughout the impregnation process. Moreover, NPs are aggregated in aqueous solution due to their low dimension.
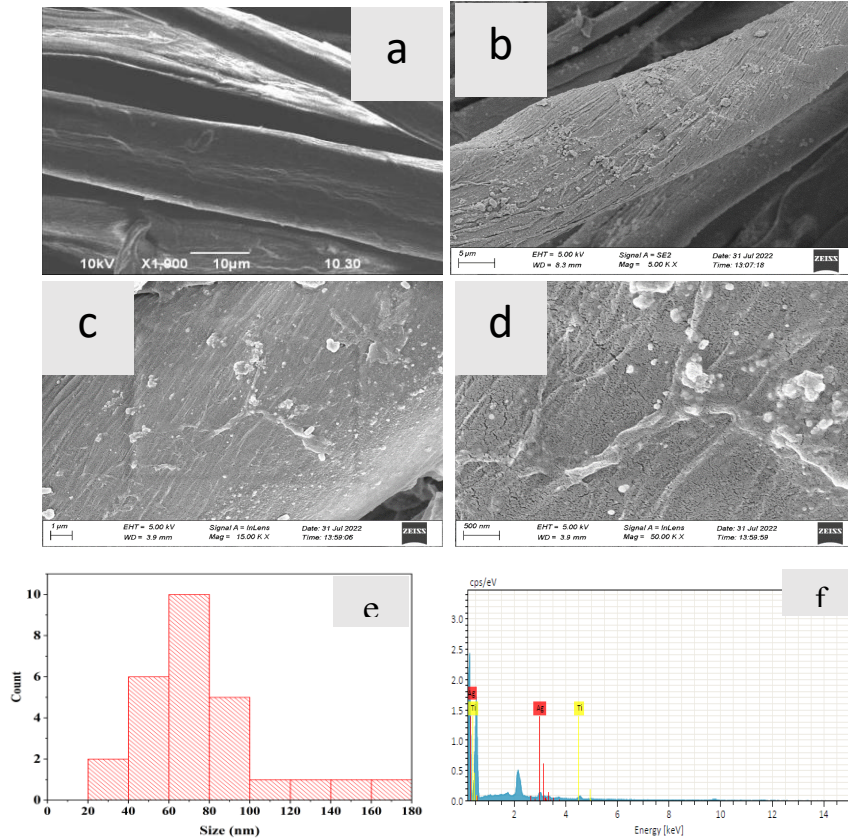
Figure 5.8: SEM images of (a) uncoated cotton and (b-d) TiO2@Ag NPs coated cotton with different magnifications, (e) histogram of diameter size (f) EDX spectrum of TiO$_2$@Ag NPs coated cotton.

The quality of the coated fabric depends on the homogeneous allotment of NPs on the fibre surface and the quantity of NPs deposited on the fiber surface depends on the wettability and absorbing quality of fabric. The EDX spectra was reported to express the identification of elements that present in the synthesized NPs coated cotton in Figure5.8 (f). This spectrum verified the presence of Ti, Ag chemical elements are existent on the surface.

5.3.8 FTIR-ATR spectral analysis

Cotton fabric untreated and treated (by coating) with TiO$_2$@Ag NPs were studied by FTIR-ATR analysis. The FTIR-ATR spectra are drawn in transmittance mode for TiO$_2$@Ag NPs coated and control cotton fabrics and are expressed in the Figure 5.9. All FTIR-ATR

transmittance characteristics bands are given in Table 5. There is a band at 3383 cm^{-1} suggesting O-H stretching vibration of hydrogen-bonded hydroxyl groups, band at 488 cm^{-1} suggesting Ti-O-Ti[4243] and 408 cm^{-1} indicating Ag-O.[44]
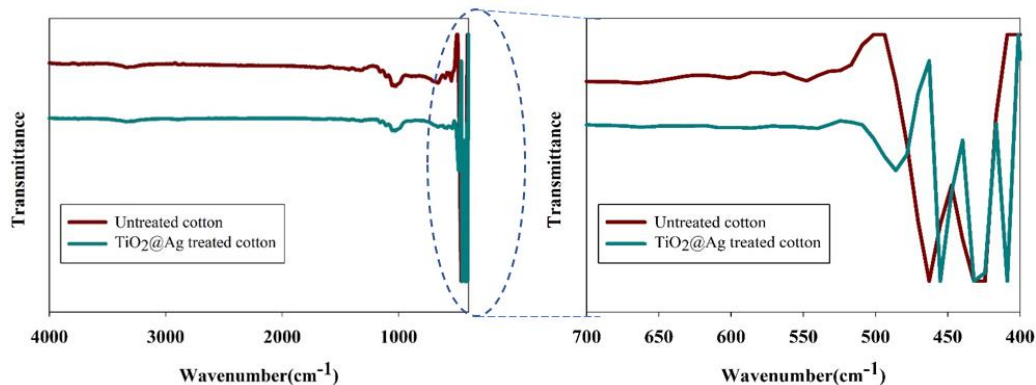
Figure 5.9: FTIR-ATR spectra of TiO2@Ag NPs control and coated fabrics.

Table 5.5: Assignment of FTIR-ATR transmittance characteristics peaks of TiO$_2$@Ag NPs coated and control fabrics.

Wavenumber (cm^{-1}) of TiO$_2$@Ag NPs treated cotton	Mode of vibration
3383	O-H stretching vibration of H-bonded hydroxyl groups[43]
2916	-CH$_2$ asymmetric stretching of long alkyl chain[63]
1645	Absorbed H$_2$O[42]
1433	-CH in plane bending[63]
1314	-CH wagging[63]
1163, 1103	Asymmetric bridge C-O-C[63]
1028	C-O stretch, Vibration of Ag+ ion of silver bonds[48]
896	Asymmetric stretching of C1-O-C4 of cellulose[63]
488	Ti-O and Ti-O-Ti stretching[4546]
407	Vibration of Ag-O[44]

5.3.9 Thermogravimetric analysis

Thermal behavior of TiO$_2$@Ag NPs coated cotton fabric is examined from room temperature to 500 °C temperature range to investigate effect of performed treatment on

cellulose pyrolysis process. TGA and DTA curves of control and coated cotton fabric with TiO$_2$@Ag NPs are presented in Figure 10. The pyrolysis is a complex reaction in which various reactions such as endothermic, bond rupture, volatilization and exothermic bond formation can be occurred at a time. The TGA thermogram shows the weight loss of fabrics in each pyrolysis stage though DTA curve shows only the net change.[64] The TGA thermogram of the control cotton fabric indicates three major steps of weight loss. In the first step, TGA curves are linear because of the initial pyrolysis stage where the damage of celluloses is done mostly in the amorphous region of polymer, some physical properties of the fabric can be changed by showing gradual weight loss (4.5%) up to around 254 °C due to the removal of absorbed and adsorbed water. In the second step, a huge slope in curves is seen due to the large weight loss of the sample as pyrolysis of cellulose occurred in the crystalline region of the polymer. A gradual weight loss line shows up to 320 °C and then drastic weight loss (around 83%) shows an endothermic peak up to 390 °C due to the formation of pyrolysis products like levoglucosan is produced.[65] In the third step, above 500 °C, finally curves the residual weight (8%) may be due to char/ash matter only. On the other hand, cotton fabric treated with TiO$_2$@Ag NPs shows the same pattern of the endothermic peak in DTA curves except 320-380 °C and decomposition starts at 355 °C quicker than control fabric though showing slightly more thermal stability than the control fabric due to the more char/ash formation (14%) because of TiO$_2$@Ag NPs .
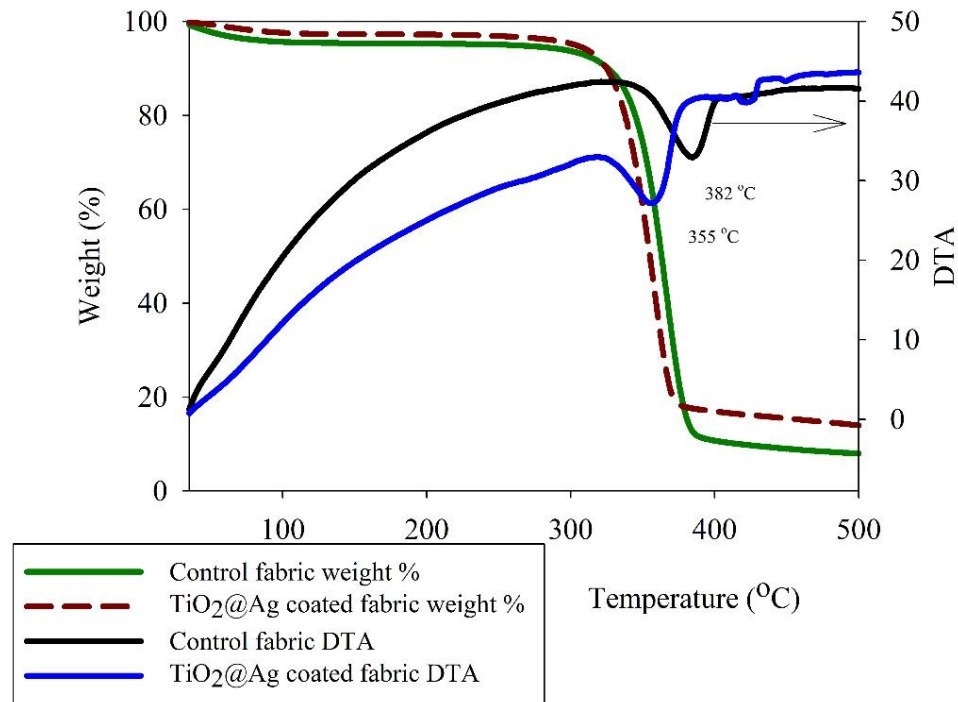
Figure 5.10: TGA and DTA analysis of control and coated cotton fabric with $TiO_2@Ag$ NPs.

5.3.10 Physical and colorfastness properties of coated fabric

All the examined physical and fastness properties showed slight modications which is shown in Table 5.6. The results expressed slight reduction on weight, fabric density, bursting strength and air permeability due to the deposited NPs on the fabric surface. Acrylic binder is used to immobilization of NPs on fiber surface that justify a decrease in bursting strength and coating is done in aqueous solution, it also justifies the increase in density as in water fabric become compact by shrink. Moreover, decrease in air permeability justify due to the cross linking of acrylic binding throughout the surface of fabric.

Table 5.6: Physical and colorfastness properties of control and coated fabrics parameters.

Physical properties		Control fabric	Coated fabric	Standard
Weight (g/m^2)		147	148	ISO 12127:2003
Fabric density (number of yarns/10 cm)	Wales	161	162	ISO1049-2:2000
	Coarse	185	186	
Bursting strength (KPa)		180.5	155.3	ISO 13938-1:1999
Air permeability (cm^3 cm^{-2} s^{-1})		68.8	50.6	ISO 9237:1999
Colorfastness to wash		-----	Color change:4/5 Color staining: 4/5	ISO 105-C06
Colorfastness to perspiration		-----	Color change: 4/5 Color staining:4/5	ISO 105-E04
Colorfastness to rubbing		-----	Dry rub:4/5 Wet rub: 4	ISO 105-X12

5.3.11 Color differences between control and coated fabrics

The ΔL^*, Δa^*, Δb^*, ΔC^*, ΔH^* color coordinates of control and coated fabrics are presented in Table 5.7.

Table 5.7: Color difference between control and coated fabrics

Illuminants/Observer angle	CMC ΔE	ΔL^*	ΔC^*	ΔH^*	Δa^*	Δb^*
D65 10 Deg.	24.50	-55.38	12.73	-4.22	7.12	11.36
F11 10 Deg.	24.75	-54.58	14.11	-3.39	6.42	13.01
A 10 Deg.	25.98	-53.93	15.80	-2.98	8.66	13.54

A trend of reducing of L^* values at different illuminants were seen. A drastic color-changing effect was observed both visually and by using the spectrophotometer within control and coated fabrics due to the presence of surface plasmon resonance of Ag NPs.

5.3.12 Antibacterial Activity

The maximum decrease (>99%) was accomplished with TiO$_2$@Ag NPs coated fabric for *S. aureus* and *E. coli* bacteria. The reduction in microorganism numbers were prominently

satisfactory. The antibacterial activity of TiO$_2$@Ag NPs has demonstrated various mechanisms to achieve superior antibacterial action.

Table 5.8: Summarized data of related NPs that used for achieving antibacterial performances.

Types of NPs	Deposition process	Functionalized textile	Microbes used	Antimicrobial activity	Ref.
Ag doped TiO$_2$	Pad-dry-cure for woven, Electrospraying for nonwoven	Woven cotton fabric, nonwoven Cotton/PET and polypropylene fabrics	*S. aureus* and *E. coli*	Upto 99% reduction	[66]
Ag or Pt on PET/TiO$_2$ filaments	Electro spinning then photo deposition	PET filaments	*S. aureus* and *K. pneumoniae*	99.9%	[67]
Ag-TiO$_2$ nanocomposite	Two extruder melt spinning	Polypropylene filaments	*S. aureus*	99.95%	[5]
Ag NPs-loaded TiO$_2$@cotton	In situ synthesis	Cotton fabric	*S. aureus* and *E. coli*	Inhibition rate 86%	[68]
Ag-TiO$_2$ nanocomposite	wet-spinning method	polyacrylonitrile filaments	*S. aureus*	99%	[69]
TiO$_2$@Ag	Pad-dry-cure	Silk fabric	*S. aureus, E. coli, P. aeruginosa*	Evident inhibition zone	[70]
TiO$_2$ NPs doped Ag, and TiO$_2$ nanowire doped Ag	Pad-dry-cure	Cotton	*S. aureus, E. coli, P. aeruginosa, B. cereus, C. albicans*	From 11-24 mm inhibition zone/cm sample	[71]
TiO$_2$@Ag NPs	Pad-dry-cure	Cotton	*S. aureus* and *E. coli*	>99.9%	Present work

Table 5.9: The reduction (R) of surviving cells of microorganism after disinfection of cotton with TiO_2@Ag NPs

Microorganism	Surviving cells (CFU/mL)		Reduction (%)
	Control fabric	**Coated fabric**	
Staphylococcus aureus	9.95×10^5	1×10^2	99.99
Escherichia coli	1.33×10^5	0.2×10^2	99.98

Some leading mechanisms to cause cell death are enzyme inhibition by metal, cell membrane disruption and the electrostatic attraction within the positive charge of Ag^+ and the negative
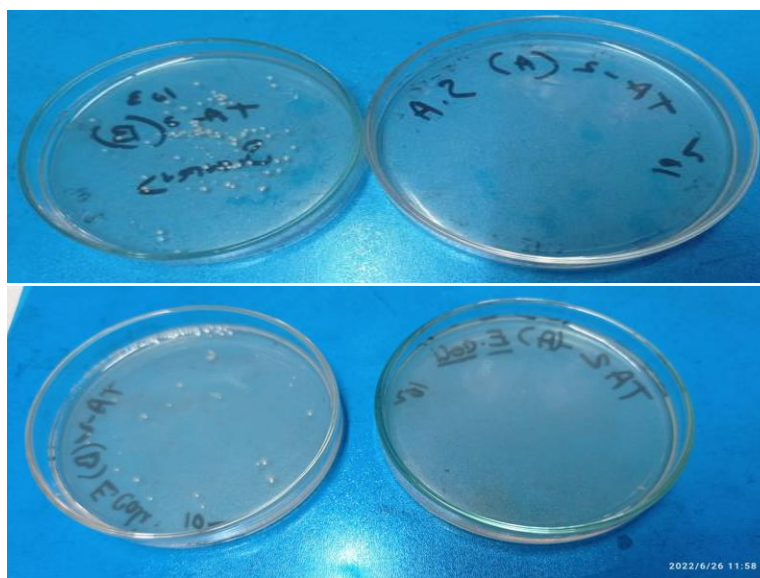
Figure 5.11: Antibacterial efficiency of control and coated fabrics specimens against (a) Staphylococcus aureus, (2) Escherichia coli.

charge of the bacterial membrane as Ag+ has capability to produce reactive oxygen species and natural antibiotic power. Moreover, nano size of TiO_2@Ag NPs can permit them to

penetrate into the bacteria and reacts with proteins thiol or sulfhydryl (-SH) groups and disband the protein by forming a stable S-metal complex structure thus causing protein denaturation and extinction of bacterial cell. Furthermore, Ag+ destabilized ATP (adenosine triphosphate) creation and destruct of DNA replication by lacking of hydrogen ion from protein that makes the ground for more entrance of TiO_2@Ag NPs within cells that prohibit the bacterial metabolism, causes the cell membrane damage and finally microbes' death. On above of that, TiO_2 lattice surge the oxygen vacancies and defects density causes to increase the antibacterial performance of Ag NPs. From the XRD results, the modest crystallite size of the TiO_2@Ag NPs is at around 4 nm and its narrow band gap energy absorbs the energy from visible light region which also causes to improve the antibacterial efficiency.[72]

5.3.13 UV protection factor (UPF) of TiO_2@Ag NPs coated fabric

The solar UV radiation is basically possessed of UV-A (400-315 nm), UV-B (315-290 nm) and UV-C (290-200 nm) radiation that contains 3-5% of UV radiation that are hazardous for human health. These 3-5% radiations that are present in natural terrestrial sunlight can depends on the upper atmosphere's filtering capacity and local conditions like latitude, altitude, clouds etc., though UV-C and maximum radiation of UV-B are filtered by the ozone layer. Control cotton fabric is incapable to absorb UV radiation resulting harmful effect on the human skin. UV protection fabric can prohibit human bodies from UV radiation by increasing both absorption and reflection, whereas by reducing transmittance not only in UV region but also in visible region. UV protection properties of coated and control fabrics were measured according to equation of (10) and (11) and tabulated at Table 10. TiO_2@Ag core-shell NPs coated fabric show high UV protection factor (UPF) value of around 28.4 by granting high reflection of UV radiation, thus provide high UV protection properties. This UV blocking properties also influenced by size and morphology of NPs. Moreover, larger NPs in coating promote the dispersion of UV blocking and decrease the total reflection of UV light due to the irregular and multiple reflection of UV light throughout the interface of NPs and fabric surface by improving the photons absorption greatly.
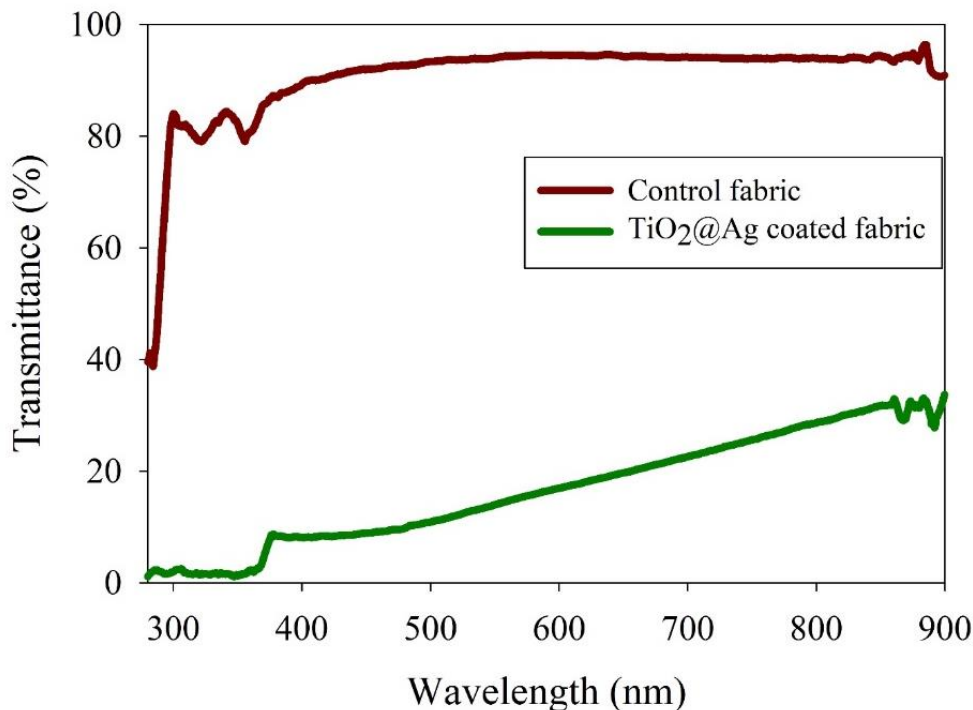
Figure 5.12: UV protection of control and TiO$_2$@Ag NPs coated fabric.

Table 5.10: UPF and % UV transmission for control and coated fabrics against UV-A (315-400 nm) and UV-B (290-315 nm) radiation

Sample	UPF	UV-A transmission (%)	UV-B transmission (%)
Control fabric	1.20	84.27	79.49
TiO$_2$@Ag NPs coated fabric	28.4	3.98	1.89

Table 5.11: Summarized data of related NPs that used for achieving UV protection performances.

NPs	Deposition process	Functionalized textile	UV protection factor	Reference
TiO$_2$@Ag	Pad-dry-cure	Silk fabric	48.7	[70]
Ag NPs-loaded TiO$_2$@cotton	*In situ* synthesis	Cotton fabric	>36	[68]
TiO$_2$@Ag core-shell	Pad-dry-cure	Cotton fabric	28.4	Present work

151

5.3.14 Self-cleaning properties
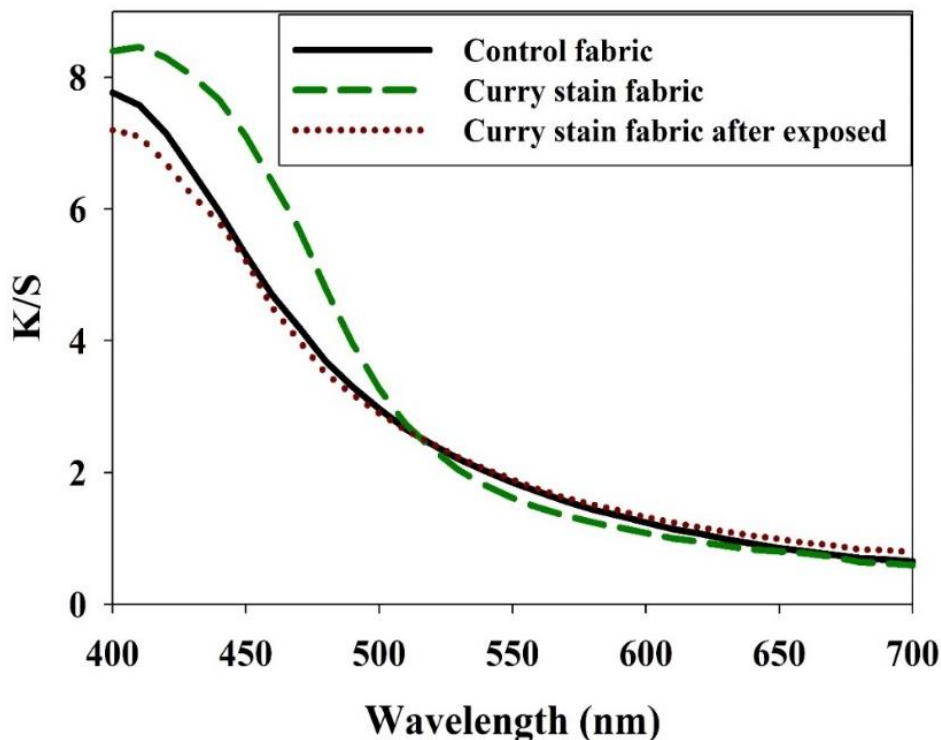
Figure 5.13: *K/S* values of control fabric, curry stain fabric and curry stain fabric after 20 h irradiation.

Curry masala is composed of various ingredients like turmeric, cumin, coriander seed, black paper, cloves, red chilies, ginger, salt, garlic, mustard etc. The curry stain is produced by mixing curry masala in hot water but this stain is mainly showing the turmeric (Curcuma longa) stain on cotton because of the binding of the yellow pigments which are most of the curcumin and its derivatives with the cellulose of cotton. Curcumin is about 3-5% of total turmeric constituents, is also a yellow-colored substance, consist of two phenolic hydroxyl groups and two centrally located carbonyl groups, that can exist in keto-enol tautomers in solution.[73] Curcumin molecule binding to TiO_2 NPs forming a 6-membered ring between Ti (IV) and β-diketo moiety. The mechanism behind the colored substances (high molecular weight organic compound) of curry sensitize the stain discoloration on TiO_2@Ag coated cotton is under exposure of ultraviolet (UV) rays the photon energy that

is higher than the band gap of TiO$_2$@Ag NPs (2.8 eV), the electrons of TiO$_2$@Ag will be excited and travel to the conduction band from the valence band thus results to the production of two kinds of opposite charged carriers, i.e. hole (h$^+$) and electron (e$^-$). The electron (e$^-$) is converted to superoxide anion ($^•$O$_2^-$) by oxygen, whereas the produced hole (h$^+$) is converted to hydroxyl radical ($^•$OH) by the moisture (H$_2$O) present in the air. These superoxide anion and hydroxyl radical are extremely reactive particles that are responsible for redox reaction and mainly cause for the degradation of organic materials (curry stain) into small molecules (CO$_2$ and H$_2$O) by UV irradiation of TiO$_2$@Ag NPs.[30] The *K/S* values (absorption and scattering coefficient; color strength) of control fabric unexposed and curry stain unexposed and curry stain exposed fabrics after 20 h irradiation under light source according to ISO 105 B02:2013 for self-cleaning efficiency were expressed in Figure 5.13. TiO$_2$@Ag core-shell NPs coated fabric show super self-cleaning results as pretty near color strength (*K/S*) of the curry stain fabric with control fabric without stain means all stains are removed from the surface.

5.4 Conclusions

Multifunctional cotton fabric was developed by coating with TiO$_2$@Ag NPs. TiO$_2$@Ag NPs has been synthesized, characterized and uniformly distributed on the fabric surface. TiO$_2$@Ag NPs coated fabric shows good UV protection capability, exhibits excellent antibacterial activity against gram-negative (*E. coli*), *and* against gram-positive (*S. aureus*), and outstanding self-cleaning properties. This high value-added multifunctional fabric has a wide range of practical applications and is in sync with developing future trends. This multifunctional fabric has promising applications in the textile industry.

References:

(1) Wang, J.; Zhao, J.; Sun, L.; Wang, X. A Review on the Application of Photocatalytic Materials on Textiles. *Text. Res. J.* **2015**, *85* (10), 1104–1118. https://doi.org/10.1177/0040517514559583.

(2) Gowri, S.; Almeida, L.; Amorim, T.; Carneiro, N.; Pedro Souto, A.; Fátima Esteves, M. Polymer Nanocomposites for Multifunctional Finishing of Textiles - a Review. *Text. Res. J.* **2010**, *80* (13), 1290–1306. https://doi.org/10.1177/0040517509357652.

(3) Ghoranneviss, M.; Shahidi, S. Effect of Various Metallic Salts on Antibacterial Activity and Physical Properties of Cotton Fabrics. *J. Ind. Text.* **2013**, *42* (3), 193–203. https://doi.org/10.1177/1528083711433230.

(4) Kowalczyk, D.; Brzeziński, S.; Kamińska, I. Multifunctional Nanocoating Finishing of Polyester/Cotton Woven Fabric by the Sol-Gel Method. *Text. Res. J.* **2018**, *88* (8), 946–956. https://doi.org/10.1177/0040517517693979.

(5) Dastjerdi, R.; Mojtahedi, M. R. M.; Shoshtari, A. M.; Khosroshahi, A. Investigating the Production and Properties of Ag/TiO2/PP Antibacterial Nanocomposite Filament Yarns. *J. Text. Inst.* **2010**, *101* (3), 204–213. https://doi.org/10.1080/00405000802346388.

(6) Sobczyk-Guzenda, A.; Szymanowski, H.; Jakubowski, W.; Błasińska, A.; Kowalski, J.; Gazicki-Lipman, M. Morphology, Photocleaning and Water Wetting Properties of Cotton Fabrics, Modified with Titanium Dioxide Coatings Synthesized with Plasma Enhanced Chemical Vapor Deposition Technique. *Surf. Coatings Technol.* **2013**, *217*, 51–57. https://doi.org/10.1016/j.surfcoat.2012.11.071.

(7) Awazu, K.; Fujimaki, M.; Rockstuhl, C.; Tominaga, J.; Murakami, H.; Ohki, Y.; Yoshida, N.; Watanabe, T. A Plasmonic Photocatalyst Consisting of Silver Nanoparticles Embedded in Titanium Dioxide. *J. Am. Chem. Soc.* **2008**, *130* (5), 1676–1680. https://doi.org/10.1021/ja076503n.

(8) Wang, P.; Huang, B.; Qin, X.; Zhang, X.; Dai, Y.; Wei, J.; Whangbo, M. H. Ag@AgCl: A Highly Efficient and Stable Photocatalyst Active under Visible Light. *Angew. Chemie - Int. Ed.* **2008**, *47* (41), 7931–7933. https://doi.org/10.1002/anie.200802483.

(9) Ma, X. C.; Dai, Y.; Yu, L.; Huang, B. B. Energy Transfer in Plasmonic Photocatalytic Composites. *Light Sci. Appl.* **2016**, *5* (August 2015). https://doi.org/10.1038/lsa.2016.17.

(10)   Karunakaran, C.; Vinayagamoorthy, P.; Jayabharathi, J. Electrical, Optical and Photocatalytic Properties of Polyethylene Glycol-Assisted Sol-Gel Synthesized Mn-Doped TiO2/ZnO Core-Shell Nanoparticles. *Superlattices Microstruct.* **2013**, *64*, 569–580. https://doi.org/10.1016/j.spmi.2013.10.021.

(11)   Kanmani, S. S.; Ramachandran, K. Synthesis and Characterization of TiO_2/ZnO Core/Shell Nanomaterials for Solar Cell Applications. *Renew. Energy* **2012**, *43*, 149–156. https://doi.org/10.1016/j.renene.2011.12.014.

(12)   Reiss, P.; Carayon, S.; Bleuse, J.; Pron, A. Low Polydispersity Core/Shell Nanocrystals of CdSe/ZnSe and CdSe/ZnSe/ZnS Type: Preparation and Optical Studies. *Synth. Met.* **2003**, *139* (3), 649–652. https://doi.org/10.1016/S0379-6779(03)00335-7.

(13)   Hassan, G. K.; Mahmoud, W. H.; Al-sayed, A.; Ismail, S. H.; El-Sherif, A. A.; Abd El Wahab, S. M. Multi-Functional of TiO_2@Ag Core–Shell Nanostructure to Prevent Hydrogen Sulfide Formation during Anaerobic Digestion of Sewage Sludge with Boosting of Bio-CH4 Production. *Fuel* **2023**. https://doi.org/10.1016/j.fuel.2022.126608.

(14)   Mayya, K. S.; Gittins, D. I.; Caruso, F. Gold-Titania Core-Shell Nanoparticles by Polyelectrolyte Complexation with a Titania Precursor. *Chem. Mater.* **2001**, *13* (11), 3833–3836. https://doi.org/10.1021/cm011128y.

(15)   Güttel, R.; Paul, M.; Schüth, F. Activity Improvement of Gold Yolk-Shell Catalysts for CO Oxidation by Doping with TiO2. *Catal. Sci. Technol.* **2011**, *1* (1), 65–68. https://doi.org/10.1039/c0cy00026d.

(16)   Seh, Z. W.; Liu, S.; Low, M.; Zhang, S. Y.; Liu, Z.; Mlayah, A.; Han, M. Y. Janus Au-TiO_2 Photocatalysts with Strong Localization of Plasmonic near-Fields for Efficient Visible-Light Hydrogen Generation. *Adv. Mater.* **2012**, *24* (17), 2310–2314. https://doi.org/10.1002/adma.201104241.

(17)   Zhang, N.; Liu, S.; Fu, X.; Xu, Y. J. Synthesis of M@TiO2 (M = Au, Pd, Pt) Core-Shell Nanocomposites with Tunable Photoreactivity. *J. Phys. Chem. C* **2011**, *115* (18), 9136–9145. https://doi.org/10.1021/jp2009989.

(18)   Lekeufack, D. D.; Brioude, A.; Mouti, A.; Alauzun, J. G.; Stadelmann, P.; Coleman, A. W.; Miele, P. Core-Shell Au (TiO2, SiO2) Nanoparticles with Tunable Morphology. *Chem. Commun.* **2010**, *46* (25), 4544–4546. https://doi.org/10.1039/c0cc00935k.

(19)   Miao, J.; Hu, C.; Liu, H.; Xiong, Y. BaTiO3 Nanocubes: Size-Selective Formation and Structure Analysis. *Mater. Lett.* **2008**, *62* (2), 235–238. https://doi.org/10.1016/j.matlet.2007.05.009.

(20)   Viswanadham, N.; Kamble, R.; Singh, M.; Kumar, M.; Murali Dhar, G. Catalytic Properties of Nano-Sized ZSM-5 Aggregates. *Catal. Today* **2009**, *141* (1–2), 182–186. https://doi.org/10.1016/j.cattod.2008.03.026.

(21)   Garnett, E. C.; Brongersma, M. L.; Cui, Y.; McGehee, M. D. Nanowire Solar Cells. *Annu. Rev. Mater. Res.* **2011**, *41*, 269–295. https://doi.org/10.1146/annurev-matsci-062910-100434.

(22)   Brönstrup, G.; Jahr, N.; Leiterer, C.; Csäki, A.; Fritzsche, W.; Christiansen, S. Optical Properties of Individual Silicon Nanowires for Photonic Devices. *ACS Nano* **2010**, *4* (12), 7113–7122. https://doi.org/10.1021/nn101076t.

(23)   Ye, C.; Bando, Y.; Fang, X.; Shen, G.; Golberg, D. Enhanced Field Emission Performance of ZnO Nanorods by Two Alternative Approaches. *J. Phys. Chem. C* **2007**, *111* (34), 12673–12676. https://doi.org/10.1021/jp073928n.

(24)   Ni, M.; Leung, M. K. H.; Leung, D. Y. C.; Sumathy, K. A Review and Recent Developments in Photocatalytic Water-Splitting Using TiO2 for Hydrogen Production. *Renew. Sustain. Energy Rev.* **2007**, *11* (3), 401–425. https://doi.org/10.1016/j.rser.2005.01.009.

(25)   Bouvrée, A.; D'Orlando, A.; Makiabadi, T.; Martin, S.; Louarn, G.; Mevellec, J. Y.; Humbert, B. Nanostructured and Nanopatterned Gold Surfaces: Application to the Surface-Enhanced Raman Spectroscopy. *Gold Bull.* **2013**, *46* (4), 283–290. https://doi.org/10.1007/s13404-013-0127-4.

(26)   Rehman, A. U.; Hassan, M.; Bano, S.; Farooq, K.; Raza, A.; Naeem Anjum, M. In Vitro and in Vivo Biocompatibility Study of Polyacrylate TiO_2@Ag Coated Nanoparticles for the Radiation Dose Enhancement. *Artificial Cells, Nanomedicine and Biotechnology.* 2021. https://doi.org/10.1080/21691401.2021.1889574.

(27)   Zhang, G.; Duan, H.; Lu, B.; Xu, Z. Electrospinning Directly Synthesized Metal Nanoparticles Decorated on Both Sidewalls of TiO2 Nanotubes and Their Applications. *Nanoscale* **2013**, *5* (13), 5801–5808. https://doi.org/10.1039/c3nr01085f.

(28)   Nithyadevi, D.; Suresh Kumar, P.; Mangalaraj, D.; Ponpandian, N.; Viswanathan, C.; Meena, P. Improved Microbial Growth Inhibition Activity of Bio-Surfactant Induced Ag-TiO 2 Core Shell Nanoparticles. *Appl. Surf. Sci.* **2015**. https://doi.org/10.1016/j.apsusc.2014.11.169.

(29)   Rai, M.; Yadav, A.; Gade, A. Silver Nanoparticles as a New Generation of Antimicrobials. *Biotechnology Advances.* 2009. https://doi.org/10.1016/j.biotechadv.2008.09.002.

(30)   Qi, K.; Wang, X.; Xin, J. h. Photocatalytic Self-Cleaning Textiles Based on Nanocrystalline Titanium Dioxide. *Text. Res. J.* **2011**, *81* (1), 101–110. https://doi.org/10.1177/0040517510383618.

(31)   Kumar, N. S.; Ganapathy, M.; Sharmila, S.; Shankar, M.; Vimalan, M.; Potheher, I. V. ZnO/Ni(OH)$_2$ Core-Shell Nanoparticles: Synthesis, Optical, Electrical and Photoacoustic Property Analysis. *J. Alloys Compd.* **2017**, *703*, 624-632. https://doi.org/10.1016/j.jallcom.2017.01.323.

(32)   Malm, V.; Strååt, M.; Walkenström, P. Effects of Surface Structure and Substrate Color on Color Differences in Textile Coatings Containing Effect Pigments. *Text. Res. J.* **2014**, *84* (2), 125–139. https://doi.org/10.1177/0040517513485626.

(33)   Pietrzak, K.; Gutarowska, B.; Machnowski, W.; Mikołajczyk, U. Antimicrobial Properties of Silver Nanoparticles Misting on Cotton Fabrics. *Text. Res. J.* **2016**, *86* (8), 812–822. https://doi.org/10.1177/0040517515596933.

(34)   Campos Payá, J.; Díaz-García, P.; Montava, I.; Miró-Martínez, P.; Bonet, M. A New Development for Determining the Ultraviolet Protection Factor. *J. Ind. Text.* **2016**, *45* (6), 1571–1586. https://doi.org/10.1177/1528083714567238.

(35)   Awad, A.; Abou-Kandil, A. I.; Elsabbagh, I.; Elfass, M.; Gaafar, M.; Mwafy, E. Polymer Nanocomposites Part 1: Structural Characterization of Zinc Oxide Nanoparticles Synthesized via Novel Calcination Method. *J. Thermoplast. Compos. Mater.* **2015**, *28* (9), 1343–1358. https://doi.org/10.1177/0892705714551241.

(36)   Grifoni, D.; Bacci, L.; Zipoli, G.; Albanese, L.; Sabatini, F. The Role of Natural Dyes in the UV Protection of Fabrics Made of Vegetable Fibres. *Dye. Pigment.* **2011**, *91* (3), 279–285. https://doi.org/10.1016/j.dyepig.2011.04.006.

(37)   Gupta, K. K.; Jassal, M.; Agrawal, A. K. Functional Finishing of Cotton Using Titanium Dioxide and Zinc Oxide Nanoparticles. **2007**.

(38)   Xu, R. Progress in Nanoparticles Characterization: Sizing and Zeta Potential Measurement. *Particuology* **2008**, *6* (2), 112–115. https://doi.org/10.1016/j.partic.2007.12.002.

(39)   Domingos, R. F. ; B.; Ju-Nam, M. A. ; Reid, Y. ; Tufenkji, M. M. ; Lead, N. ; Leppard, J. R. ; Wilkinson, G. G. ;; J., K. Characterizing Manufactured Nanoparticles in the Environment: Multimethod Determination of Particle Sizes. *Env. Sci Technol* **19AD**, *43*, 7277−7284.

(40)   Ashraf, M.; Champagne, P.; Perwuelz, A.; Campagne, C.; Leriche, A. Photocatalytic Solution Discoloration and Self-Cleaning by Polyester Fabric Functionalized with ZnO Nanorods. *J. Ind. Text.* **2015**, *44* (6), 884–898. https://doi.org/10.1177/1528083713519662.

(41) Paul, R.; Bautista, L.; de la Varga, M.; Botet, J. M.; Casals, E.; Puntes, V.; Marsal, F. Nano-Cotton Fabrics with High Ultraviolet Protection. *Text. Res. J.* **2010**, *80* (5), 454–462. https://doi.org/10.1177/0040517509342316.

(42) Wang, Y. M.; Liu, S. W.; Xiu, Z.; Jiao, X. B.; Cui, X. P.; Pan, J. Preparation and Photocatalytic Properties of Silica Gel-Supported TiO 2. *Mater. Lett.* **2006**, *60* (7), 974–978. https://doi.org/10.1016/j.matlet.2005.10.061.

(43) Akhavan Sadr, F.; Montazer, M. In Situ Sonosynthesis of Nano TiO2 on Cotton Fabric. *Ultrason. Sonochem.* **2014**, *21* (2), 681–691. https://doi.org/10.1016/j.ultsonch.2013.09.018.

(44) Al-Ariki, S.; Yahya, N. A. A.; Al-A'nsi, S. A.; Jumali, M. H. H.; Jannah, A. N.; Abd-Shukor, R. Synthesis and Comparative Study on the Structural and Optical Properties of ZnO Doped with Ni and Ag Nanopowders Fabricated by Sol Gel Technique. *Sci. Rep.* **2021**, *11* (1), 1–11. https://doi.org/10.1038/s41598-021-91439-1.

(45) Tarigh, G. D.; Shemirani, F.; Maz'hari, N. S. Fabrication of a Reusable Magnetic Multi-Walled Carbon Nanotube-TiO2 Nanocomposite by Electrostatic Adsorption: Enhanced Photodegradation of Malachite Green. *RSC Adv.* **2015**, *5* (44), 35070–35079. https://doi.org/10.1039/c4ra15593a.

(46) Wang, L.; Ding, Y.; Shen, Y.; Cai, Z.; Zhang, H.; Xu, L. Study on Properties of Modified Nano-TiO$_2$ and Its Application on Antibacterial Finishing of Textiles. *J. Ind. Text.* **2014**, *44* (3), 351–372. https://doi.org/10.1177/1528083713487758.

(47) Gharibshahi, L.; Saion, E.; Gharibshahi, E.; Shaari, A. H.; Matori, K. A. Structural and Optical Properties of Ag Nanoparticles Synthesized by Thermal Treatment Method. *Materials (Basel).* **2017**, *10* (4), 402. https://doi.org/10.3390/ma10040402.

(48) Tunc, I. The Effect of the Presence of Ag Nanoparticles on the Photocatalytic Degradation of Oxalic Acid Adsorbed on TiO2 Nanoparticles Monitored by ATR-FTIR. *Mater. Chem. Phys.* **2014**, *144* (3), 444–450. https://doi.org/10.1016/j.matchemphys.2014.01.018.

(49) Grigorovici, R.; Vancu, A. Optical Properties and Electronic Structure of Amorphous Germanium. **1966**, *627*, 627–637.

(50) Zhang, Q.; Xu, M.; You, B.; Zhang, Q.; Yuan, H.; Ostrikov, K. Oxygen Vacancy-Mediated ZnO Nanoparticle Photocatalyst for Degradation of Methylene Blue. *Appl. Sci.* **2018**, *8* (3), 1–12. https://doi.org/10.3390/app8030353.

(51)   Wang, J.; Wang, Z.; Huang, B.; Ma, Y.; Liu, Y.; Qin, X.; Zhang, X.; Dai, Y. Oxygen Vacancy Induced Band-Gap Narrowing and Enhanced Visible Light Photocatalytic Activity of ZnO. *ACS Appl. Mater. Interfaces* **2012**, *4* (8), 4024–4030. https://doi.org/10.1021/am300835p.

(52)   Goswami, N.; Sahai, A. Structural Transformation in Nickel Doped Zinc Oxide Nanostructures. *Mater. Res. Bull.* **2013**, *48* (2), 346–351. https://doi.org/10.1016/j.materresbull.2012.10.045.

(53)   Zhao, J.; Wang, L.; Yan, X.; Yang, Y.; Lei, Y.; Zhou, J.; Huang, Y.; Gu, Y.; Zhang, Y. Structure and Photocatalytic Activity of Ni-Doped ZnO Nanorods. *Mater. Res. Bull.* **2011**, *46* (8), 1207–1210. https://doi.org/10.1016/j.materresbull.2011.04.008.

(54)   Tsuji, T. Preparation of Silver Nanoparticles by Laser Ablation in Solution.Pdf. *Appl. Surf. Sci.* **2002**, *202*, 80.

(55)   Hamad, A.; Li, L.; Liu, Z.; Zhong, X. L.; Liu, H.; Wang, T. Generation of Silver Titania Nanoparticles from an Ag-Ti Alloy via Picosecond Laser Ablation and Their Antibacterial Activities. *RSC Adv.* **2015**, *5* (89), 72981–72994. https://doi.org/10.1039/c5ra16466d.

(56)   Tian, F.; Sun, J.; Yang, J.; Wu, P.; Wang, H. L.; Du, X. W. Preparation and Photocatalytic Properties of Mixed-Phase Titania Nanospheres by Laser Ablation. *Mater. Lett.* **2009**, *63* (27), 2384–2386. https://doi.org/10.1016/j.matlet.2009.08.018.

(57)   Tarwal, N. L.; Patil, P. S. Enhanced Photoelectrochemical Performance of Ag-ZnO Thin Films Synthesized by Spray Pyrolysis Technique. *Electrochim. Acta* **2011**, *56* (18), 6510–6516. https://doi.org/10.1016/j.electacta.2011.05.001.

(58)   Zhang, H.; Chen, G.; Bahnemann, D. W. Photoelectrocatalytic Materials for Environmental Applications. *J. Mater. Chem.* **2009**, *19* (29), 5089–5121. https://doi.org/10.1039/b821991e.

(59)   Ojstršek, A.; Kleinschek, K. S.; Fakin, D. Characterization of Nano-Sized TiO2 Suspensions for Functional Modification of Polyester Fabric. *Surf. Coatings Technol.* **2013**, *226*, 68–74. https://doi.org/10.1016/j.surfcoat.2013.03.037.

(60)   Yang, H. G.; Sun, C. H.; Qiao, S. Z.; Zou, J.; Liu, G.; Smith, S. C.; Cheng, H. M.; Lu, G. Q. Anatase TiO2 Single Crystals with a Large Percentage of Reactive Facets. *Nature* **2008**, *453* (7195), 638–641. https://doi.org/10.1038/nature06964.

(61)   Xia, Y.; Xiong, Y.; Lim, B.; Skrabalak, S. E. Shape-Controlled Synthesis of Metal Nanocrystals: Simple Chemistry Meets Complex Physics? *Angew. Chemie - Int. Ed.* **2009**, *48* (1), 60–103. https://doi.org/10.1002/anie.200802248.

(62)   Qi, K.; Daoud, W. A.; Xin, J. H.; Mak, C. L.; Tang, W.; Cheung, W. P. Self-Cleaning Cotton. *J. Mater. Chem.* **2006**, *16* (47), 4567–4574. https://doi.org/10.1039/b610861j.

(63)   Ahmad, I.; Kan, C. W.; Yao, Z. Photoactive Cotton Fabric for UV Protection and Self-Cleaning. *RSC Adv.* **2019**, *9* (32), 18106–18114. https://doi.org/10.1039/c9ra02023c.

(64)   Perkins, R.; Drake, G. L.; Reeves, W. A. DTA and TGA Studies of Flame-Resistant Fabrics. **1966**, *10*, 1041–1066.

(65)   Lessan, F.; Montazer, M.; Moghadam, M. B. Thermochimica Acta A Novel Durable Flame-Retardant Cotton Fabric Using Sodium Hypophosphite , Nano TiO 2 and Maleic Acid. *Thermochim. Acta* **2011**, *520* (1–2), 48–54. https://doi.org/10.1016/j.tca.2011.03.012.

(66)   Aksit, A.; Onar Camlibel, N.; Topel Zeren, E.; Kutlu, B. Development of Antibacterial Fabrics by Treatment with Ag-Doped TiO_2 Nanoparticles. *J. Text. Inst.* **2017**, *108* (12), 2046–2056. https://doi.org/10.1080/00405000.2017.1311766.

(67)   Hwang, S. H.; Lim, S. K.; Hong, S. H.; Kim, S.; Choi, W. M.; Han, J. S.; Lee, S. H. Anti-Bacterial Activity of Tetragonal and Cross-Pillar-Shaped Polyester/TiO_2 Filaments with Photo-Deposited Silver and Platinum Nanoparticles. *Text. Res. J.* **2016**, *86* (12), 1231–1240. https://doi.org/10.1177/0040517515609256.

(68)   Li, S.; Zhu, T.; Huang, J.; Guo, Q.; Chen, G.; Lai, Y. Durable Antibacterial and UV-Protective Ag/TiO2@fabrics for Sustainable Biomedical Application. *Int. J. Nanomedicine* **2017**, *12*, 2593–2606. https://doi.org/10.2147/IJN.S132035.

(69)   Kizildag, N.; Ucar, N.; Onen, A. Nanocomposite Polyacrylonitrile Filaments with Titanium Dioxide and Silver Nanoparticles for Multifunctionality. *J. Ind. Text.* **2018**, *47* (7), 1716–1738. https://doi.org/10.1177/1528083717708482.

(70)   Li, G.; Liu, H.; Zhao, H.; Gao, Y.; Wang, J.; Jiang, H.; Boughton, R. I. Chemical Assembly of TiO_2 and TiO_2@Ag Nanoparticles on Silk Fiber to Produce Multifunctional Fabrics. *J. Colloid Interface Sci.* **2011**, *358* (1), 307–315. https://doi.org/10.1016/j.jcis.2011.02.053.

(71)   Hebeish, A. A.; Abdelhady, M. M.; Youssef, A. M. TiO2 Nanowire and TiO_2 Nanowire Doped Ag-PVP Nanocomposite for Antimicrobial and Self-Cleaning Cotton Textile. *Carbohydr. Polym.* **2013**, *91* (2), 549–559. https://doi.org/10.1016/j.carbpol.2012.08.068.

(72)   Perera, S.; Bhushan, B.; Bandara, R.; Rajapakse, G.; Rajapakse, S.; Bandara, C. Morphological, Antimicrobial, Durability, and Physical Properties of Untreated and Treated Textiles Using Silver-Nanoparticles. *Colloids Surfaces A Physicochem.   Eng.   Asp.* **2013**, *436*, 975–989. https://doi.org/10.1016/j.colsurfa.2013.08.038.

(73)   Priyadarsini, K. I. Journal of Photochemistry and Photobiology C : Photochemistry Reviews Photophysics , Photochemistry and Photobiology of Curcumin : Studies from Organic Solutions , Bio-Mimetics and Living Cells. **2009**, *10*, 81–95. https://doi.org/10.1016/j.jphotochemrev.2009.05.001.

6. Multifunctional ZnO@Ag Nanoparticles on Cotton Fabric for UV protection, Self-cleaning, and Antibacterial Activity

Abstract

Developing multifunctional cotton fabrics with UV protection, antibacterial activity, and self-cleaning capabilities are desirable and pressing issues for the sustainability of natural fibers. Here, the wet chemical technique was used to synthesize ZnO@Ag NPs) while ZnO NPs were synthesized by the hydrothermal method. The particle size, microstructure, and morphology of NPs were obtained by DLS, FTIR spectroscopy, UV-vis spectroscopy, XRD, and TEM. ZnO@Ag NPs were applied with acrylic binder on cotton knit fabric by a pad-dry-cure method. The morphology of NPs coated fabric was evaluated by SEM. The antimicrobial efficacy of ZnO@Ag NPs assessed towards the Gram-positive bacteria *Staphylococcus aureus* and the Gram-negative bacteria *Escherichia coli* and possessed >99.9% reduction of both bacteria. The coated fabric exhibited a good UPF of 26.14. Curry stains were used as model dirt to examine self-cleaning properties. ZnO@Ag NPs coated cotton fabric showed satisfactory curry stain removal after 20 h of xenon UV light exposure.

Keywords

UV protection, antibacterial, self-cleaning, textiles, zinc oxide, silver, core@shell

6.1   Introduction

Cotton is a bountiful natural fiber on earth. It is trendy and extensively used in clothing and technical textiles due to its remarkable properties like large specific surface, softness, immense moisture absorption proficiency, porous structure, and cheap bio-degradability.[1] Cotton is restricted from high-end applications like functional textiles, self-cleaning, and health and hygiene textiles because of its incompetent antimicrobial property, poor strength, naturally hydrophilic capability, low awareness to ultraviolet radiation as these properties conduct to high discoloration, deterioration of mechanical strength by decomposition.[2] Multifunctional cotton not only solve these existing problems but also initiate value addition and propagate significant academic and industrial consideration because of its increasing demand for advanced materials for consumers.[3] The use of

162

modern nanotechnology is promptly increased in the textile industry, leading advance opportunities in multifunctional cotton by depositing semiconductor and metal NPs onto cotton fibers as these NPs showed improved antimicrobial properties, superior photocatalytic activity by making active species with reacting oxygen and water, outstanding self-cleaning property.[4,5] Multifunctional textiles are fabricated using various NPs of different shapes, sizes, and structures.[6] Moreover, core@shell NPs is a modern field that has gained massive attraction in photocatalysis,[7] due to its structure that possesses synergistic properties within the cores and shells based on their interactions. These tailored properties of inorganic semiconductor cores covered with a metal shell have gained massive attention from academic, industrial, and technical applications. ZnO is a famous semiconductor that is widely used to impart functional properties on textiles due to its wide-bandgap, photocatalytic, optical, binding energy, electrical, and antimicrobial properties whereas Ag possesses some outstanding properties like antimicrobial properties, etc. Semiconductor-metal-based core@shell NPs have been widely studied due to their synergistic photocatalytic activity. Danish et al.[7] synthesized ZnO@Ag core@shell hetero-junction nanorods by hydrothermal and seed-mediated growth techniques and evaluated its photocatalytic activity against rhodamine 6G dye, congo red and amido black 10B under UV and visible light (solar) irradiations. Vivek et al.[8] reported a novel plasmon-green mediated method for synthesizing ZnO@Ag core@shell nanocomposites and detailed their structural, optical, and electrical characterization. To the best of my understanding, there is a limited of research investigating the antibacterial, UV protection, and self-cleaning properties of cotton fabric coated with ZnO@Ag NPs.

This work aimed to synthesize ZnO@Ag NPs by wet chemical method and characterization by DLS, UV spectroscopy, XRD, and TEM for application on cotton knit fabric by a pad-dry-cure method. The morphological property of cotton fabric was evaluated by SEM equipped with EDXspectroscopy. UV protection, thermal characteristics, self-cleaning and antibacterial properties of coated fabrics also analyzed in detail.

6.2 Experimental

6.2.1 Materials

Zinc nitrate hexahydrate (>98%, Merck), Ammonium chloride (Analar BDH chemical Ltd, England), Urea (Uni-chem chemical reagent, China), silver nitrate ($AgNO_3$, reagent grade, Scharlau, Spain), cetyltrimethylammonium bromide (CTAB, >98%, Merck), $NaBH_4$ (>98%, ACROS organics, Belgium), binder of aqueous acrylate dispersion (Forbind OB 45, Fortune top Pte Ltd. New Taipei City, Taiwan) were utilized beyond additional purification. HPLC grade water purification system (BOECO) was used for deionized water (conductivity: 0.055 μScm^{-1}) to produce all solutions. 100% cotton knit fabric with a single jersey structure after scouring and bleaching was used throughout all experiments.

6.2.2 Synthesis of ZnO nanoparticles by hydrothermal method

To synthesize ZnO NPs, 0.015 mol $Zn(NO_3)_2 . 6 H_2O$, 0.06 mol urea, and 0.015 mol NH_4Cl were dissolved in 80 mL distilled water and stirred at 400 rpm for 30 min at 30 °C. Then the prepared solution was transferred into a Teflon container, lidded with a stainless-steel container, and put in an oven at 160 °C. White precipitation of ZnO NPs appeared after 24 h, and these precipitates were centrifuged (Centrifuge Cencom II from J. P. Selecta, Spain) at 1000 rpm for 5-10 min, washed several times and were kept in an oven at 80 °C for 24 h.[9]

6.2.3 Synthesis of ZnO@Ag nanoparticles

To synthesize of ZnO@Ag NPs, 0.7 mmol of ZnO NPs were dispersed in 50 mL deionized water by ultrasonication for about 30 min, and then 0.09 mmol of CTAB was mixed as capping and stabilizing agent in the above solution by stirring at 300 rpm by a magnetic stirrer accompanied with heating at 40 °C. The temperature of the solution slowly decreased to room temperature. Afterward, a 25 mL aqueous solution of $AgNO_3$ was gradually added drop-wise to the above solution under constant stirring for one h, followed by another 25 mL aqueous solution of 0.7 mmol of $NaBH_4$ addition slowly to reduce Ag NPs. The color of the solution changed from white to dark brown because of surface

plasmon resonance indicating the onset of the formation of ZnO@Ag NPs. Then the solution was aged overnight and dried at 60 °C. Finally, ZnO@Ag NPs were synthesized.[10]

6.2.4 Preparation of ZnO@Ag NPs coated cotton fabric

ZnO@Ag NPs were applied to cotton knit fabrics by a pad-dry-cure method. At first, cotton fabric (20 cm×20 cm) was immersed into 100 mL of ZnO@Ag NPs sol for 5 min under stirring to prevent precipitation of NPs and followed by padding and afterward again padded by 1% acrylic binder (Forbind OB 45, Taiwan) in 100 mL distilled water. Padding is done by a standard laboratory instrument with 2.5 m/min fabric speed and 2.8 kg/cm^2 padding pressure to maintain a pick-up% of about 70-75%. The pH value of the padding bath was maintained at around 6. The sample was dried at 80 °C for 5 min in an oven and cured (SDL mini-dryer steamer) at 140 °C for 2.5 min.

6.2.5 Material characterization

The average particle size and size distribution of the samples dispersed in water were measured using dynamic light scattering (DLS) measurements by a Malvern Zetasizer Nano ZS90 with a scattering angle of 90°. A He–Ne laser beam of 632.8 nm was used for the measurements. The average diameters were determined from cumulants mean of the intensity average of 50 runs using Stokes–Einstein equation, $d_H = k_B T / 3\pi\eta D_{ef}$, where d_H is the hydrodynamic diameter, k_B is the Boltzmann constant, T is the temperature, η is the solvent viscosity, and D_{ef} is the diffusion coefficient. The reproducibility was checked from at least three measurements. The sample temperature was controlled automatically within ±0.01 K by a built-in Peltier device.

UV–vis absorption spectra were recorded by a double-beam UV-vis spectrophotometer (UVD-3500, LABOMED, INC, USA), where cell length is 1 cm. Rectangular quartz cells of path length 1 cm were used throughout the investigation. UV-visible diffuse reflectance spectrum was recorded using a double-beam UV-visible spectrophotometer with an integrating sphere attachment DRA-CA-30I (Model: UV-1800, Shimadzu, Japan) to determine the band gap (E_g) energy of the solid NPs.

The crystallographic and phase-dependent properties were analyzed by an X-ray diffractometer (Philips PW 1724) with an X-ray generator using XDC-700 Guinier-Hagg focusing camera with monochromatized Cu Kα radiation (λ = 1.540598 Å). The measurement was performed continuously with a scan speed of 3.0 deg/min within the 10-70 degrees range while the scan width was 0.026 deg. According to Debye-Scherrer's equation $D = \dfrac{K\lambda}{\beta cos\theta}$, the crystallite domain diameters were obtained from XRD peaks.

The surface morphology, structure, and attachment of Ag on ZnO were studied with TEM, and the micrographs were attained using the LEO system (model 912 AB) at 120kV for samples.

The morphological study used Field emission scanning electron microscopy (ZEISS, Germany). The acceleration voltage of the electron gun was 20 kV with a probe current of 1.0 nA and magnifications ranging from 10,000 – 100,000. The images of samples were taken without sputtering and by mounting on the conducting carbon tape. The compositional study of the NPs is analyzed by EDX spectroscopy attached to the FESEM. Computer-adapted software (ImageJ 1.51k, java 1.60-24 (64 bit), USA) was used to measure average particle size in both the TEM and the FESEM images of NPs. ATR-FTIR spectra' transform Infrared (MB3000, ABB Analytical, Canada) in transmittance mode for each sample in the range between 400 and 4000 cm^{-1} at 4.0 cm^{-1} resolution was recorded. Thermal properties were studied under a nitrogen atmosphere by a Hitachi instrument (TG/ DTA 7200) in the 30–550 °C at a heating rate of 20° min^{-1}. The physical properties of the fabrics (weight, bursting strength, air permeability) were examined by ISO standards.

6.2.6 Color measurements

The colorimetric difference within control and coated fabrics were determined by a spectrophotometer (Datacolor SF850, Datacolor International, USA) under D65 (average daylight), F11 (fluorescent lighting), A (tungsten-filament lighting) standard illuminants at a 10 observing angle with d/8 viewing geometry. The CIE CMC color coordinates (L^*, C^* and H^*) where L^* represents white to black, C^* represents brighter duller, and H^* represents hue, whereas The CIE *Lab* color coordinates (L^*, a^* and b^*) where, L^* representing white black, a^* and b^* representing redness–greenness and yellowness–blueness, respectively.

The color difference $(\Delta L^*, \Delta a^*, \Delta b^*, \Delta C^*, \Delta H^*$ between reference (control fabric) and sample (coated) fabrics were measured by the following equations (6.1-7):[4]

$$\Delta L^* = L^*_{reference} - L^*_{sample} \qquad (6.1)$$

$$\Delta a^* = a^*_{reference} - a^*_{sample} \qquad (6.2)$$

$$\Delta b^* = b^*_{reference} - b^*_{sample} \qquad (6.3)$$

$$\Delta C^* = C^*_{reference} - C^*_{sample} \qquad (6.4)$$

$$\Delta H^* = H^*_{reference} - H^*_{sample} \qquad (6.5)$$

$$C = \sqrt{\Delta a^{*2} + \Delta b^{*2}} \qquad (6.6)$$

$$H = tan^{-1} b/a \qquad (6.7)$$

The color difference of computer color matching, ΔE^*CMC, provided the distance within the control (reference) and coated fabric sample in the CIE CMC color space and was calculated by following equation (eqn. 6.8):

$$\Delta E^*CMC = \Delta L^* \Delta C^* \Delta H^* \qquad (6.8)$$

Where, $\Delta L^*, \Delta a^*, \Delta b^*, \Delta C^*,$ and ΔH^* are the differences in respective values between control and coated fabrics.

6.2.7 Assessment of the antibacterial properties

The antibacterial properties of the coated and control fabrics are accomplished by ASTM E2149-01 quantitative method to estimate the conservation of non-leaching antimicrobial coated samples to advance microbes under dynamic contact situations. The antimicrobial property was evaluated by *S. aureus* (gram-positive) and *E. coli* (gram-negative) bacteria. Each culture was suspended in a small quantity of nutrient broth, swept on the nutrient agar plate, and incubated at 37 °C for 24 h. Two single colonies were grasped with an inoculating loop from the agar plate, put down on both coated and control fabrics in two particular Petri dishes, and leave it to incubate at 37 °C for 24 h to allow the insertion of

NPs into the microorganism cells. The reduction R (%) of the microorganisms after coming into contact with both coated and control fabrics is determined by the following equation (eqn. 6.9):[11]

$$R \ (\%) = \frac{B-A}{A} \times 100 \qquad (6.9)$$

Aand B express the surviving cells (colony forming units per milliliter (CFU/mL) in a flask containing coated and control fabrics, respectively, after a contact time of one h.

6.2.8 Assessment of the UV protection properties

The UV protection of the ZnO@Ag NPs attached fabric is reported by UV transmission spectra by using a double beam ultraviolet-visible (UV-vis) spectrometer (Cintra 2020, GBC, Australia), with an integrating sphere attachment to evaluated by the UPF. The UPF of fabric is determined per standard PN-EN 13758-1:2007 by following equation (eqn. 6.10-11):[12]

$$\text{UPF} = \frac{\sum_{\lambda=290}^{400} E(\lambda) . \ \varepsilon(\lambda) . \ \Delta(\lambda)}{\sum_{\lambda=290}^{400} E(\lambda) . \ T(\lambda) . \ \varepsilon(\lambda) . \Delta(\lambda)} \qquad (6.10)$$

$$\text{Percent UV transmission} = \frac{\sum_{\lambda_1}^{\lambda_2} T(\lambda)}{(\lambda_2 - \lambda_1)} \qquad (6.11)$$

Where $E(\lambda)$ expressed in $W/m^2/nm$ = solar irradiance, $T(\lambda)$ = spectral transmittance at the wavelength λ, $\varepsilon(\lambda)$ = erythema action spectrum, and $\Delta\lambda$ = wavelength interval. The UPF values of textiles represent their UV radiation blocking capabilities, as higher UPF values mean higher protection capacity.[13]

The Australian classification scheme can classify fabrics as providing good, very good, or excellent protection according to their UPF values ranging from 15 to 50+ (Table 6.1).

Table 6.1: Classification of UPF category measured from relative transmittance and protection level.[14]

UPF range	Protection category	UVBE$_{eryt}$ transmittance (%)
<15	Insufficient protection	>6.7
15-24	Good protection	6.7-4.2
25-39	Very good protection	4.1-2.6
40-50, 50+	Excellent protection	<2.5

6.2.9 Evaluation of the self-cleaning activity

The difference in color strength of the curry stain under UV irradiation determined the self-cleaning performance. Curry solution is prepared by adding 0.5 g curry powder (*Radhuni*) in 10 mL of hot water. One drop of curry solution is dropped close on ZnO@Ag NPs coated fabric, allowed to spread, dried in the air, and then exposed to light irradiation. The irradiation of stained ZnO@Ag NPs coated fabric was carried out for 20 h in a Xenotest Alpha LM light exposure and weathering test instrument (air-cooled xenon arc lamp, Xenotest Alpha LM, USA) by ISO 105 B02 standard. Half of each stain on the fabric was exposed to a xenon arc lamp, while the other half was unexposed with a steel frame to prevent irradiation. The exposed part of the stain was compared with the unexposed part for self-cleaning action. The self-cleaning action was determined by comparing the color strength (*K/S*) within the exposed and the unexposed parts of the same stain. The reflectance of the stained fabric was measured by the spectrophotometer (Datacolor SF850, Datacolor International, USA) to calculate the degradation rate per the Kubelka-Munk equation (eqn. 6.12).[15]

$$\frac{K}{S} = \frac{(1-R)^2}{2R} \qquad (6.12)$$

K/S means color strength, and *K* and *S* are the absorptions and scattering coefficients.

6.3   Results and Discussion

6.3.1   DLS analysis

DLS engaged in assessing the macromolecules and small particles in dilute suspension with the help of coherent light sources.[16] DLS measurement was compelled in the aqueous suspension of ZnO@Ag NPs and ZnO NPs to express the hydrodynamic diameter of size distribution in Figure 6.1. One broad sinusoidal peak is observed, and the maxima at around 104 nm hydrodynamic diameter of ZnO@Ag NPs, increases due to the introduction of Ag shells. In contrast, ZnO NPs show two sinusoidal peaks with tiny particles with a hydrodynamic diameter (d_H) around 1 nm and particles of d_H about 17-38 nm reveal their existence. The peak maxima to be found are near 1 and 28 nm. The narrow width of the peaks indicates that particles consist of a small range of hydrodynamic diameter. DLS usually measures the hydrodynamic diameter of the particles in solution based on the

169

Brownian motion of the particles in aqueous solution. Particle size found from DLS takes place in a solution form, so the nanoparticles may be swelled with time while measuring.[17] DLS analysis also signifies that the NPs formed had well-defined dimensions. A larger hydrodynamic size than the primary particle size was also mentioned in other studies.[18] Smaller the size of the NPs, the higher the surface area, which facilitates higher UV protection and self-cleaning activity.[19]
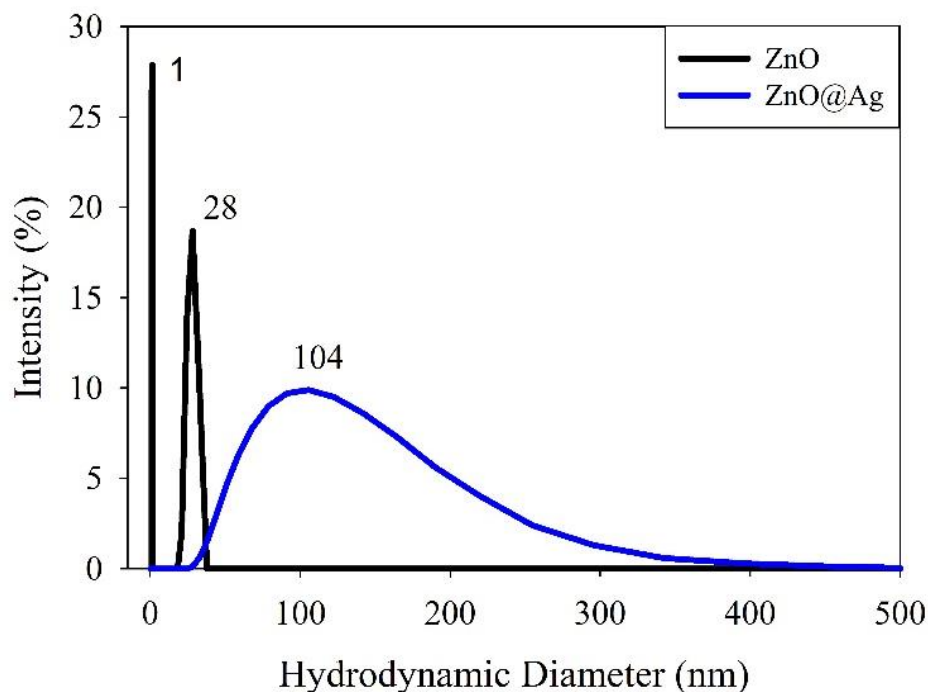
Figure 6.1: The average hydrodynamic diameter of ZnO and ZnO@Ag NPs from DLS.

6.3.2 **Optical analysis (UV-vis absorbance)**

UV-visible absorbance spectra of pure ZnO and ZnO@Ag NPs are exhibited in Figure 6.2(a), showing that the characteristic peak at 372 nm resembles the excitonic ground peak of pure ZnO NPs.[20] In ZnO@Ag NPs, a red-shifted peak at 418 nm was reported due to the solid interfacial electronic coupling within the ZnO and Ag atoms, and an electron transfer process occurs from ZnO and Ag attributing to a divergence in the Fermi levels exposes the SPR of Ag NPs.[8] The red-shift of light absorption results from decreased bandgap energy due to the lower Fermi level of Ag than those of ZnO. The shifting of the light absorption edge of metal oxide NPs after shelling metal ions was also reported in other

studies.[21] The bandgap energy of ZnO and ZnO@Ag NPs can be estimated by the formula (eqn. 6.13):[22]

$$\alpha h v = A(h v - E_g)^n \qquad (6.13)$$

Where α, v, A, and E_g are absorption coefficient, light frequency, a constant, and direct optical bandgap energy, respectively, and $n = \frac{1}{2}$ (for direct transition mode material). Band gap can be measured by extrapolating the linear region of the plot of $(\alpha h v)^2$ versus photon energy $(h v)$ of the exciting light reported in Figure 6.2 (b).
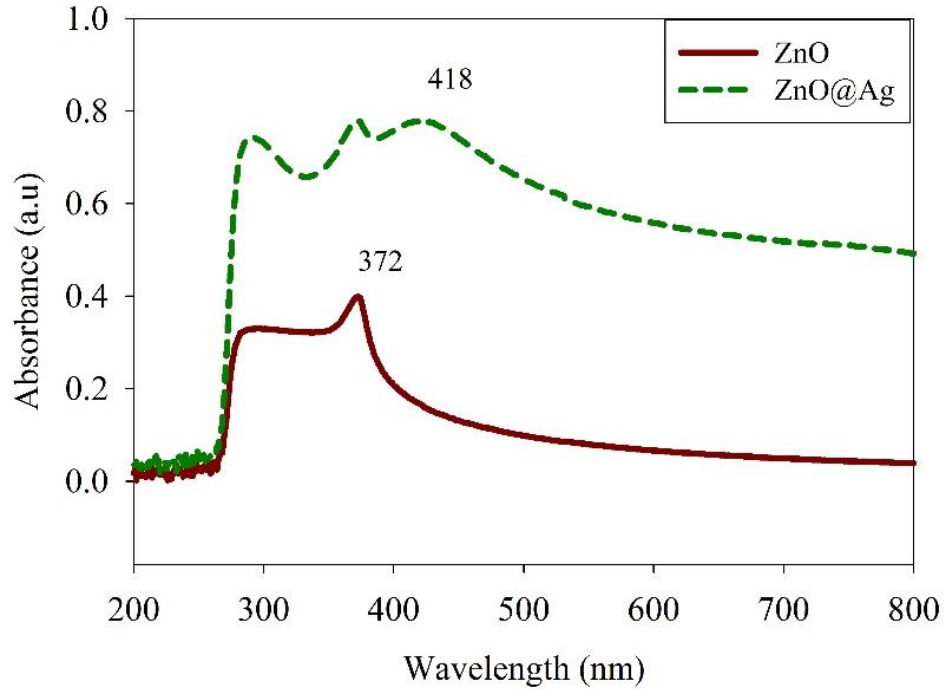
Figure 6.2: (a) UV-vis absorption spectra of a dispersion solution of ZnO and ZnO@Ag NPs.

The intersection of the tangent line with the X-axis provides a better resemblance of the band gap energy of both ZnO (maroon line) and ZnO@Ag (green line) NPs. ZnO has a direct band gap transition.[23] It can be noted that the E_g of ZnO@Ag NPs is decreased significantly to 2.13 eV from 3.13 eV of pure ZnO NPs as the reduction of E_g may be due to the addition of Ag that shift the absorption edge to longer wavelength (red-shift), maybe because of the grain boundary scattering and the SPR of Ag NPs, thus improved the absorption of light in the visible region.[24]
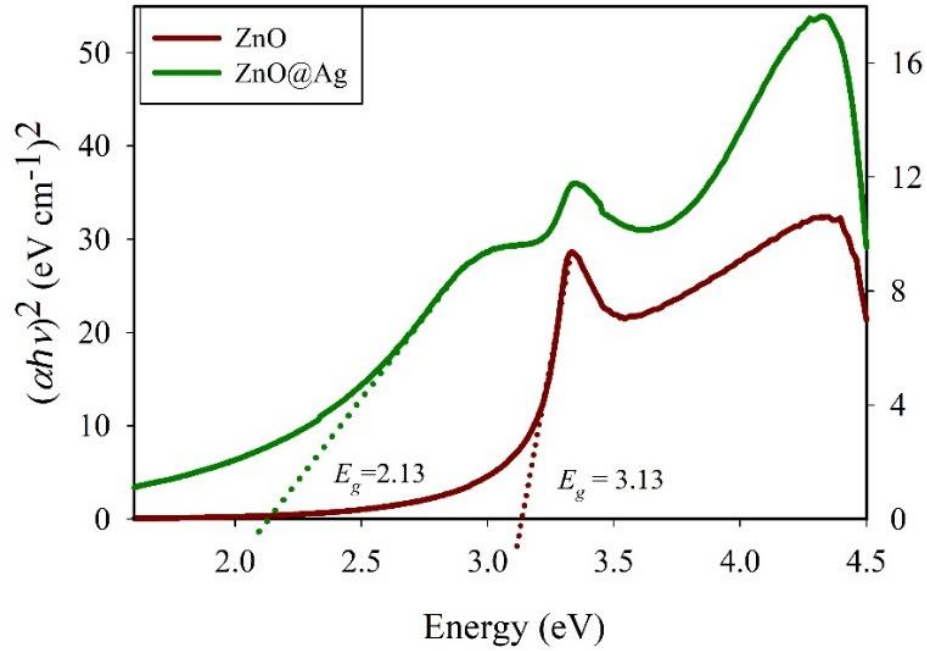
Figure 6.2: (b) Tauc plot of the ZnO and ZnO@Ag NPs.

6.3.3 Determination of optical band gap and the nature of optical charge carrier transitions

The optical band gap of ZnO@Ag NPs is reported by the DASF method under the following equations (6.14-15):[25]

$$ln\left[\frac{f(R)}{\lambda}\right] + ln\,s = ln[B(hc)^{m-1}] + m\,ln(\frac{1}{\lambda} - \frac{1}{\lambda_g}) \qquad (6.14)$$

Now,

$$\frac{d\{ln\left[\frac{f(R)}{\lambda}\right]\}}{d(\frac{1}{\lambda})} = \frac{m}{\frac{1}{\lambda} - \frac{1}{\lambda_g}} \qquad (6.15)$$

As $f(R)$ is determined by using Kubelka–Munk method (eqn.6.16) where R is the reflectance and $f(R)$ is proportional to the absorption coefficient (α).

$$f(R) = \frac{(1-R)^2}{2R} \qquad (6.16)$$

where λ is the wavelength, c is the velocity of light, λ_g is the wavelength associated with the optical bandgap, B is a constant, and s is the scattering coefficient. hv is the photon's energy, and E_g is the bandgap energy of the sample. The optical bandgap of the sample is measured by the extrapolation of a linear portion in the plot of $dln[\alpha(\lambda)\lambda^{-1}]/d\lambda^{-1}$ against hv extended in Figure 6.3 (a). The calculated E_g of ZnO@Ag is 3.21 and 2.12 eV, which is reduced from pure ZnO (3.11 eV).
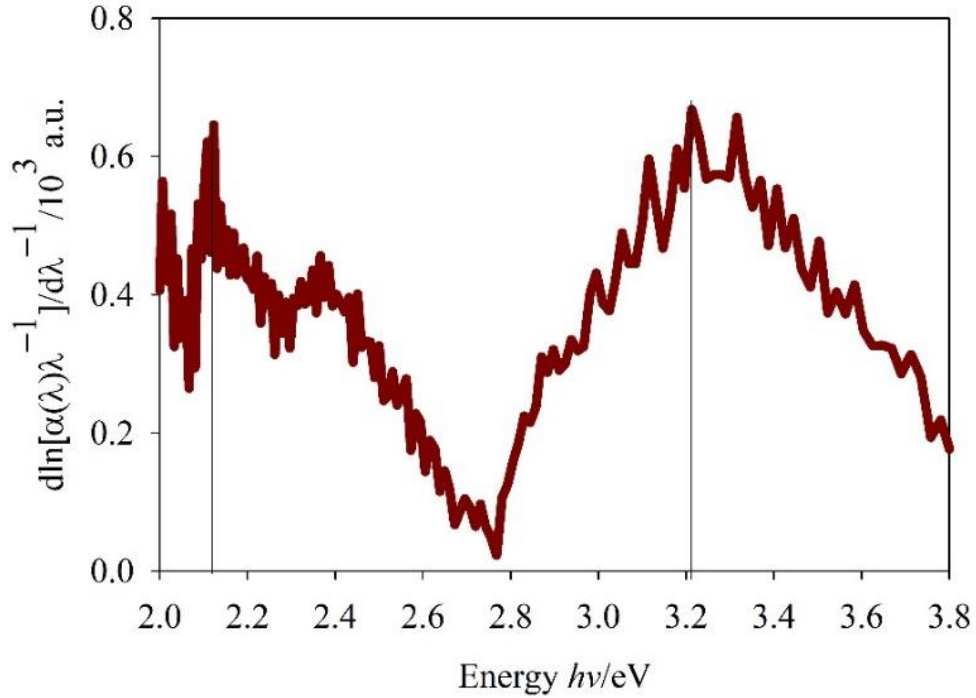
Figure 6.3: (a) DASF method calculated for bandgap by plotting of $dln[\alpha(\lambda)\lambda^{-1}]/d\lambda^{-1}$ versus hv.

The increase of E_g or higher the optical gap by adding Ag may be due to the lower localized state, which may occur by the quantum confinement effect generated by oxygen vacancies in the inter-granular regions.[8] This reduction of E_g by adding Ag may indicate that Ag has substituted the Zn in the lattice creating oxygen vacancies due to the valence difference between Ag^+ and Zn^{2+}. The created oxygen vacancies play a significant role in the narrowing of E_g. They act as trap centers that decrease the recombination rate of photo-generated charge carriers by capturing the electrons.[26] First mechanism of E_g reduction may be due to direct electron transfer from SPR of Ag to the conduction band of ZnO. The

second mechanism may be due to the excited electron transfer to the Fermi state of the Ag NPs from the conduction band of ZnO. The third mechanism may be due to the electron transfer to ZnO's defect level from the Ag NPs' Fermi state. Moreover, the Fermi level of ZnO is located below the Ag Fermi level, which guides electron transfer smoothly from Ag NPs to ZnO NPs, when the two systems are not in equilibrium. Furthermore, host ZnO states may interact with the Ag state, creating energy levels in the ZnO bandgap that reduce its optical bandgap, thus improving the photocatalytic properties of ZnO by widening the spectrum of the visible light response.[27] The variation within bandgap values for ZnO@Ag and ZnO are obtainable to structural parameters, grain size, and carrier concentration. The corresponding coefficient (*m*) of the sample is calculated by the extrapolation of a linear portion in the plot of $\ln[\alpha(\lambda)\lambda^{-1}]$ versus $\ln(\lambda^{-1} - \lambda_g^{-1})$ extended in Figure6.3 (b). The corresponding coefficient (*m*) associated with an electronic transition is calculated, and found that $m = 1/2$ defines the direct allowed transition.[28]
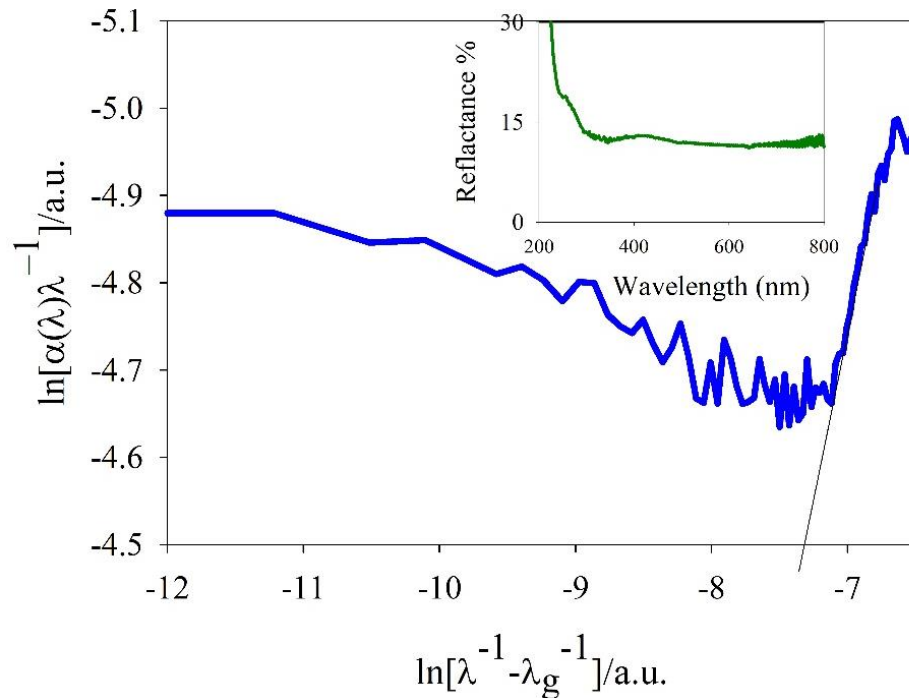
Figure 6.3: (b) DASF method calculated for corresponding coefficient (m) by plotting $\ln[\alpha(\lambda)\lambda^{-1}]$ versus $\ln[\lambda\text{-}1 - \lambda g^{-1}]$. The inset is the reflectance spectrum of ZnO@Ag NPs.

Table 6.2: Bandgap energy of ZnO and ZnO@Ag NPs estimated from Tauc plot and the absorption spectrum fitting (DASF) method derivation.

NPs	Band gap energy (eV) by Tauc plot	Band gap energy (eV) by the DASF method
ZnO NPs	3.13	3.11
ZnO@Ag NPs	2.13	3.21 and 2.12

6.3.4 XRD analysis

The phase and composition of ZnO and ZnO@Ag were analyzed with XRD in Figure 6.4. ZnO can be well indexed to wurtzite hexagonal structure (JCPDS no. 891397) with nine diffraction peaks (2θ) at 31.82°, 34.47°, 36.31°, 47.60°, 56.67°, 62.93°, 66.46°, 68.03° and 69.15° corresponds with the lattice planes designated by Miller indices (100), (002), (101), (102), (110), (103), (200), (112) and (201). These nine diffraction peaks are present without any shift in ZnO@Ag NPs. Also, shelling Ag NPs did not change the crystal structure of the ZnO domains. Sharp diffraction peaks indicate good crystallization. Moreover, ZnO@Ag NPs showed additional peaks at 31.01°, 38.14°, 44.42°, 55.16° and 64.59° belonging respectively to the (122), (111), (200), (142), and (220) planes of face-centered cubic (FCC) phase of the Ag NPs and it was well coordinated with JCPDS, No. 04-0783. The average crystallite diameter D was calculated from Debye-Scherrer's equation (eqn. 6.17):[29]

$$D = \frac{K\lambda}{\beta cos\theta} \qquad (6.17)$$
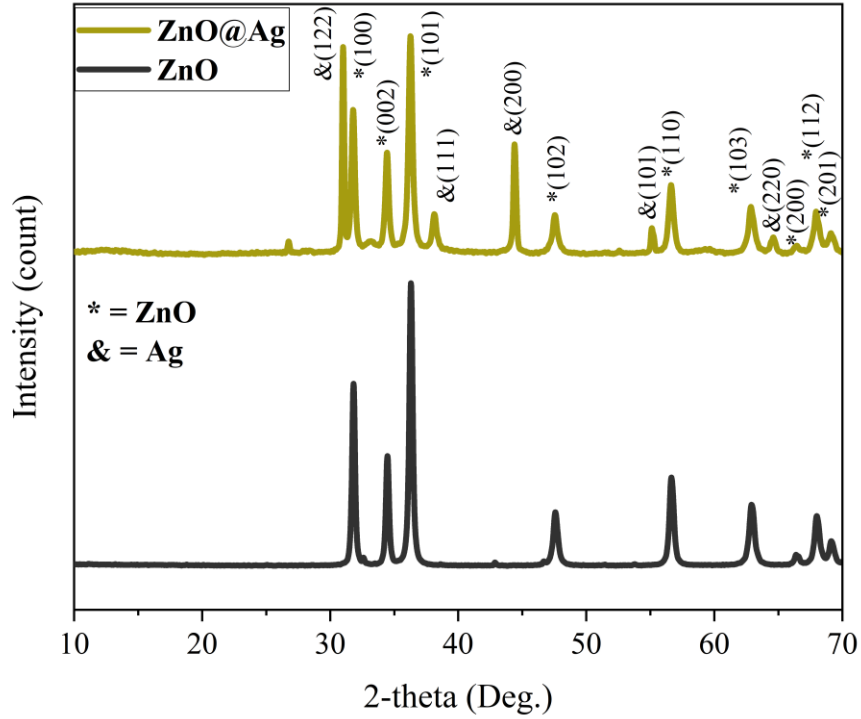
Figure 6.4: XRD patterns of ZnO and ZnO@Ag core@shell NPs.

Lattice strain (η) was calculated by equation 6.18:

$$\eta = \frac{\beta}{\tan\theta} \qquad (6.18)$$

The dislocation density (δ), which represents the number of defects in the crystal, was calculated by using the Williamson-Hall equation 6.19:

$$\delta = \frac{1}{D^2} \qquad (6.19)$$

The dislocation density is inversely proportional to D^2, and d-spacing was calculated by the following equation 6.20:

$$d_{hkl} = \frac{\lambda}{2\sin\theta} \qquad (6.20)$$

Where D is the crystallite size, $K = 0.9$, λ = the wavelength of X-ray radiation (1.5406 Å), β = the full-width half maximum of diffraction peak, θ = the Braggs diffraction angle, η = Lattice strain in the material.[30] Crystallite size, lattice strain, dislocation density, lattice planes, and d-spacing values are listed in Table 6.3.[31]

Table 6.3: Phase ID, 2θ, crystallite size, lattice strain, dislocation density, *hkl,* d-spacing of ZnO@Ag NPs as presented in XRD patterns analysis.

Phase	2θ (degree)	Full-width half maximum FWHM $[\beta]$	Crystallite size D (nm)	Lattice strain $\eta = \beta/tan\theta$	Dislocation density δ (nm^{-2})	hkl	d-spacing $d_{hkl} = \lambda/2sin\theta$
Ag	31.01	0.22	38.23	0.0136	0.0007	122	0.2881
ZnO	31.79	0.37	22.47	0.0225	0.0020	100	0.2813
ZnO	34.43	0.40	21.05	0.0222	0.0023	002	0.2602
ZnO	36.27	0.42	19.77	0.0225	0.0026	101	0.2475
Ag	38.14	0.53	15.90	0.0267	0.0040	111	0.2358
Ag	44.42	0.28	31.02	0.0118	0.0010	200	0.2038
ZnO	47.56	0.51	17.09	0.0201	0.0034	102	0.1910
Ag	55.16	0.28	32.31	0.0093	0.0010	142	0.1664
ZnO	56.63	0.49	18.45	0.0158	0.0029	110	0.1624
ZnO	62.90	0.59	15.78	0.0168	0.0040	103	0.1476
Ag	64.59	0.42	22.48	0.0115	0.0020	220	0.1442
ZnO	67.26	0.72	13.33	0.0188	0.0056	200	0.1391
ZnO	67.81	1.74	5.51	0.0451	0.0329	112	0.1381

6.3.5 TEM analysis

TEM analysis of ZnO@Ag NPs is shown in Figure6.5 (a-b), which points out the structure, morphology, particle size, and shape of NPs. The TEM images confirm the formation of the hybrid nanostructures with core@shell hetero-junctions that formed in spherical structure as Ag is surrounded throughout the ZnO surface and Ag nano-clusters anchored onto the ZnO reveal an average particle size of ZnO@Ag NPs are around 40 to 70 nm that shown on the histogram (Figure6.5 (c)). This nano core@shell is in the agglomerated form of spherical shape nanocrystals that cannot be discriminated against each other. The selected area diffraction patterns (SAED pattern) in Figure 6.5 (d) exhibit prominent diffraction ring patterns that were slightly diffuse, indicating that the texture was polycrystalline with small grain sizes associating to ZnO and Ag, consistent with results from the XRD pattern.
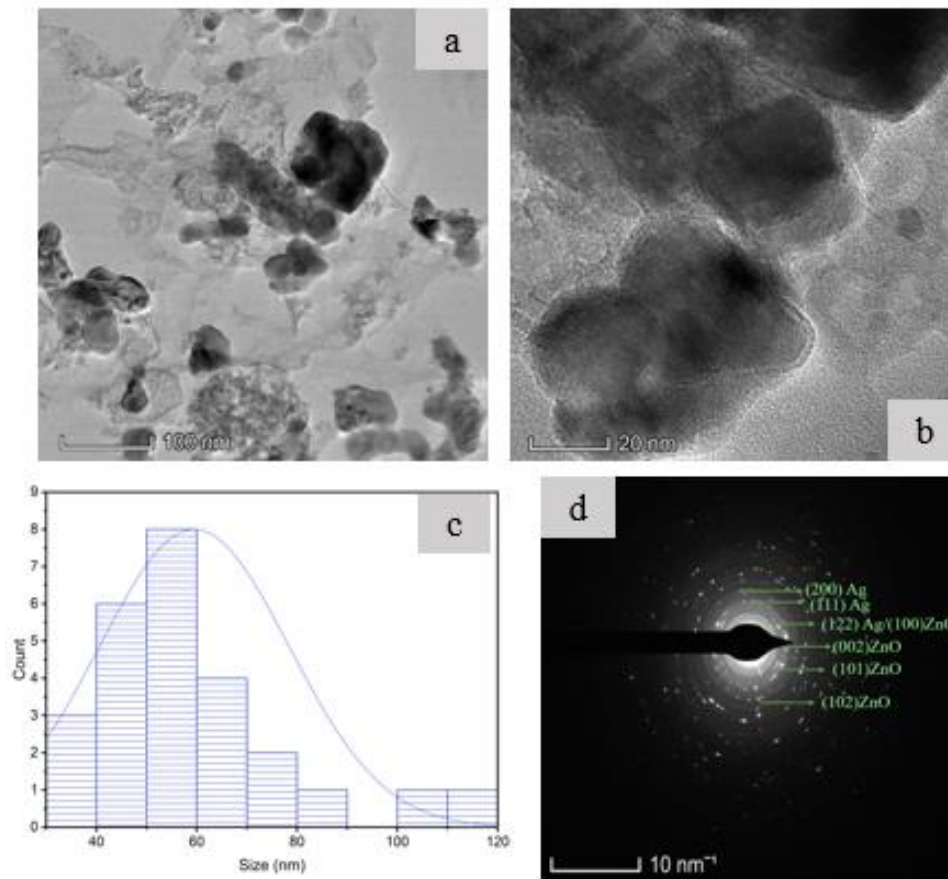
Figure 6.5: TEM images of (a, b) ZnO and ZnO@Ag NPs with different magnifications, (c) histogram, and (d) SAED pattern.

The diffraction rings present the mixed phase of ZnO and Ag as this unveils the ring-like diffraction pattern that coincides with the (122), (111), (200) lattice planes of Ag and (100), (002), (101) and (102) lattice planes of ZnO NPs. It is inspected that these absolute circle rings with spots are well coordinated with the XRD pattern of ZnO@Ag NPs, as that clarifies the profoundly crystalline nature.

6.3.6 SEM and EDX of coated fabrics

The SEM images showed the surface morphology of control and ZnO@Ag NPs coated fabrics in Figure 6.6 (a-d). Figure 6.6 (a) depicted control cotton fiber that exhibited a smooth, heterogeneous surface alongside a quality "twisted ribbon" with evident micro-fibrils without any contaminated particles.[32] However, the surface morphology is altered after coating with ZnO@Ag NPs that are shown at Figure 6.6 (b-d) with different magnifications where some spherical-shaped NPs can be detected on the surface of the coated fiber to reveal the attachment of NPs. It also explained that acrylic binder accomplishes the duty of the ''binding element'' of NPs with the fiber surface. The particle size of ZnO@Ag NPs is reported by the histogram (Figure 6.6 (e)) onto the coated cotton fabrics enlarges than TEM, as it may be because of some agglomerates of the NPs that formed throughout the coating process by padding due to lack of stirring during the impregnation process. Moreover, NPs are aggregated in a dispersion solution due to their low dimension.
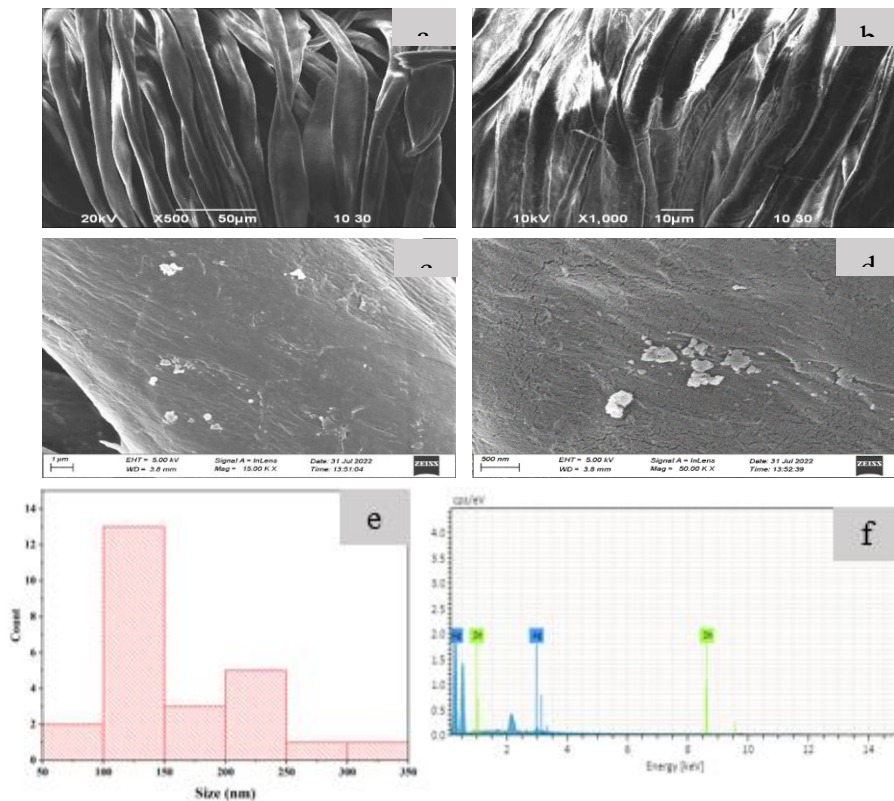
Figure 6.6: SEM images of (a) control cotton, (b-d) ZnO@Ag NPs coated cotton with different magnifications, (e) the histogram of particle size, (f) EDX spectrum of ZnO@Ag NPs coated cotton fabric.

The quality of the coated fabric depends on the homogeneous allotment of NPs on the fiber surface, and the quantity of NPs deposited on the fiber surface depends on the wettability and absorbing quality of the fabric.[33] The EDX spectra of coated cotton fabric were reported in Figure 6.6 (f) to express the identification of present elements onto the coated cotton fabric. This spectrum confirmed the presence of Zn and Ag on the surface of the coated fabric.

6.3.7 ATR-FTIR spectra of cotton fabrics

Both control and ZnO@Ag coated cotton fabrics were studied by FTIR-ATR analysis in transmittance mode and are expressed in Figure 6.7. All ATR-FTIR transmittance characteristics peaks are given in Table 6.4 There is a peak at 3383 cm^{-1} suggesting O-H

stretching vibration of H-bonded hydroxyl groups, a peak at 495 cm^{-1} suggesting Zn-O,[34] and 409 cm^{-1} indicating Ag-O.[35] After coating with ZnO NPs, the fabric's ATR-FTIR spectra saw minimal alteration. There were no chemical interactions between cotton cellulose and zinc oxide.
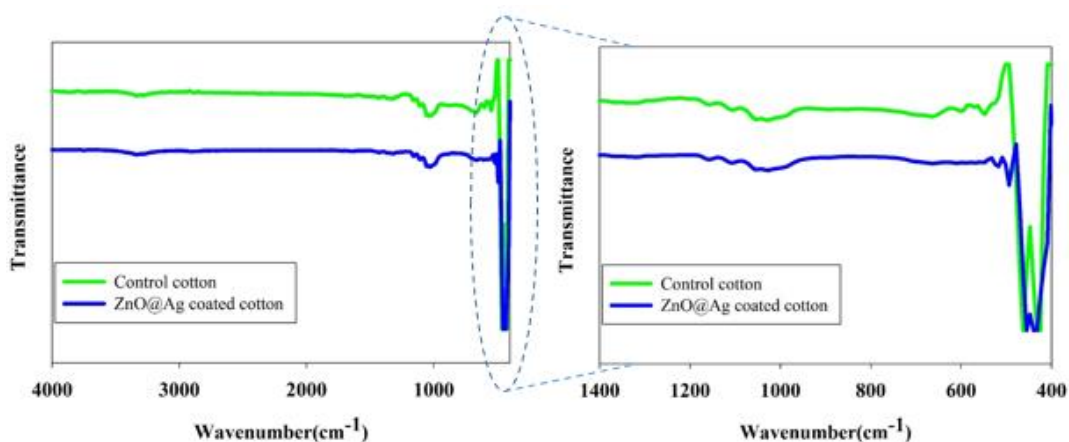
Figure 6.7: ATR-FTIR spectra of ZnO@Ag NPs control and coated fabrics.

Table 6.4: Assignment of ATR-FTIR transmittance characteristics peaks of control and ZnO@Ag NPs coated fabrics

Wavenumber (cm^{-1}) of control cotton fabric	Wavenumber (cm^{-1}) of ZnO@Ag NPs coated cotton fabric	Mode of vibration
3383	3383	O-H stretching vibration of H-bonded hydroxyl groups[35]
2916	2916	-CH$_2$ asymmetric stretching of long alkyl chain[35]
1433	1433	-CH wagging in plane bending[35]
1163, 1103	1163, 1103	Asymmetric bridge C-O-C[1]
1028	1028	C-O-C stretching,[35] Vibration of Ag+ ion of silver bonds[36]
660	660	C-H bending vibration[37]
---	495	Vibration of Zn-O[38]
---	409	Ag-O bonds[39]

6.3.8 Thermogravimetric analysis

Thermal characteristics of ZnO@Ag NPs coated cotton fabric are analyzed from room temperature to 500 °C temperature range to investigate the effect of performed treatment

on the cellulose pyrolysis process. TGA curves of control and coated cotton fabric with ZnO@Ag NPs are shown in Figure 6.8. Pyrolysis is a complex reaction in which various reactions such as endothermic, bond rupture, volatilization, and exothermic bond formation can coincide. The TGA thermogram shows the weight loss of fabrics in each pyrolysis stage.[40] The control cotton fabric's TGA thermogram indicates three significant weight loss steps. In the first step, the TGA curve is linear because of the initial pyrolysis stage, where the damage of celluloses is done primarily on the amorphous region of the polymer. Some physical properties of the fabric can be changed by showing gradual weight loss (4.5%) up to around 254 °C due to the removal of absorbed and adsorbed water. In the second step, a massive slope in curves is seen due to the significant weight loss of the sample as cellulose pyrolysis occurred in the crystalline region of the polymer. A gradual weight loss line shows up to 320 °C, and then drastic weight loss (around 83%) shows an endothermic peak up to 390 °C due to the formation of pyrolysis products like levoglucosan is produced.[41] In the third step, above 500 °C, the residual weight (8%) finally curves, which may be due only to char/ash matter. On the other hand, ZnO@Ag NPs coated cotton fabric shows the same pattern of curves except 320-380 °C and decomposition starts at 355 °C quicker than the control fabric though showing slightly more thermal stability than the control fabric due to the more char/ash formation (14%) because of ZnO@Ag NPs.
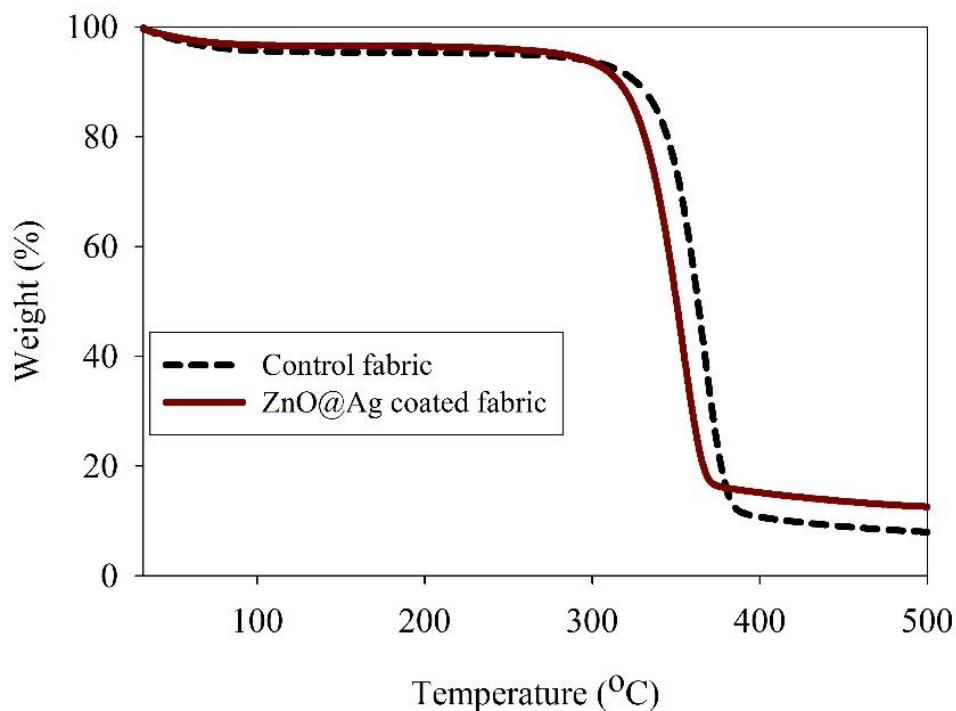
Figure 6.8: TGA analysis of control and coated cotton fabric with ZnO@Ag NPs.

6.3.9 Physical properties of coated fabric

All the examined physical and color fastness properties showed slight modifications shown in Table 6.5, indicating a slight increase in weight, and fabric density, whereas a decrease in bursting strength and air permeability due to the deposition of NPs on the fabric surface. An acrylic binder is used to immobilize NPs on the fiber surface, which justifies a decrease in bursting strength and coating in an aqueous solution. It also justifies the increase in density as the fabric becomes compacted by a water shrink. Moreover, a decrease in air permeability justifies due to the cross-linking of acrylic binding throughout the surface of the fabric. ZnO@Ag coated fabric showed good color fastness to washing, perspiration, and rubbing due to surface plasmon resonance of Ag NPs.

Table 6.5: Physical and fastness properties of control and coated cotton fabrics parameters.

Physical properties		Control fabric	Coated fabric	Standard
Weight (g/m^2)		147	149	ISO 12127:2003
Fabric density (number of yarns/10 cm)	Wales	161	163	ISO1049-2:2000
	Coarse	185	187	
Bursting strength (KPa)		180.5	155.8	ISO 13938-1:1999
Air permeability (cm^3 cm^{-2} s^{-1})		68.8	51.3	ISO 9237:1999
Colorfastness to wash		---	Color change: 4/5 Color staining:4/5	ISO 105-C06
Colorfastness to perspiration		---	Color change: 4/5 Color staining:4/5	ISO 105-E04
Colorfastness to rubbing		---	Dry rub:4/5 Wet rub: 4	ISO 105-X12

6.3.10 Color differences between control and coated fabrics

The ΔL^*, Δa^*, Δb^*, ΔC^*, and ΔH^* color coordinates of control and coated fabrics are presented in Table 6.6. A trend of reducing L^* values at different illuminants was seen. A drastic color-changing effect was observed both by visual and spectrophotometer within control and coated fabrics due to the surface plasmon resonance of Ag NPs.

Table 6.6: The color difference between control and coated fabrics.

Illuminants/Observer angle	CMC ΔE	ΔL^*	ΔC^*	ΔH^*	Δa^*	Δb^*
D65 10 Deg.	21.66	-49.58	11.46	-2.47	3.63	11.14
F11 10 Deg.	22.25	-48.96	13.04	-1.94	3.49	12.71
A 10 Deg.	22.61	-48.53	13.41	-1.74	5.56	12.32

6.3.11 **The antibacterial activity**

This study reveals that ZnO@Ag NPs coated fabric showed (Figure 6.9) potent antibacterial activity of maximum decrease (>99.9%) against *Staphylococcus aureus* or *S. aureus* (Gram-positive) and *Escherichia coli* or *E. coli* (Gram-negative) bacterial strains. Summarized data of related NPs for achieving antibacterial performances are listed in Table 6.7. The reduction (%) of surviving cells after disinfection of cotton with ZnO@Ag core-shell NPs is listed in Table 6.8. The antibacterial activity of ZnO@Ag NPs has demonstrated various mechanisms to achieve superior antibacterial action.

Table 6.7: Summarized data of related NPs for achieving antibacterial performances.

Types of NPs	Deposition process	Functionalized textile	Microbes used	Antimicrobial activity	Reference
Ag-ZnO nanoparticles hybrid	*In situ synthesis*	Woven cotton fabric	*S. aureus* and *E. coli*	Up to 99.99% reduction	[42]
Ag-ZnO nanocomposite	*In situ synthesis*	Cotton fibre	*S. aureus* and *E. coli*	>90.5%	[43]
Ag/ZnO nanocomposite	*In situ synthesis*	Cotton fabric	*S. aureus* and *E. coli*	100%	[6]
ZnO-Ag nanocomposite	*In situ synthesis*	Cotton fabric	*S. aureus* and *E. coli*	Inhibition zone: 0.5-5.5 mm	[44]
ZnO-Ag nanocomposite	Pad-dry-cure	Cotton fabric	*S. aureus* and *E. coli*	Inhibition zone: 1-11 mm	[45]
Ag:ZnO/chitosan nanocomposite	Pad-dry-cure	Cotton and cotton/polyester fabric	*E. coli* and *M. luteus*	Bacterial viability: 4-44%	[46]
ZnO@Ag NPs	Pad-dry-cure	Cotton fabric	*S. aureus* and *E. coli*	>99.9% reduction	Present work

Table 6.8: The reduction (%) of surviving cells after disinfection of cotton with ZnO@Ag core-shell NPs.

	Surviving cells (CFU/mL)		
Microorganism	**Control fabric**	**Coated fabric**	**Reduction (%)**
Staphylococcus aureus	9.99×10^5	0.90×10^2	99.99
Escherichia coli	1.11×10^5	0.22×10^2	99.98

Some leading mechanisms to cause cell death are enzyme inhibition by metal, cell membrane disruption, and the electrostatic attraction within the positive charge of Ag^+ and the negative
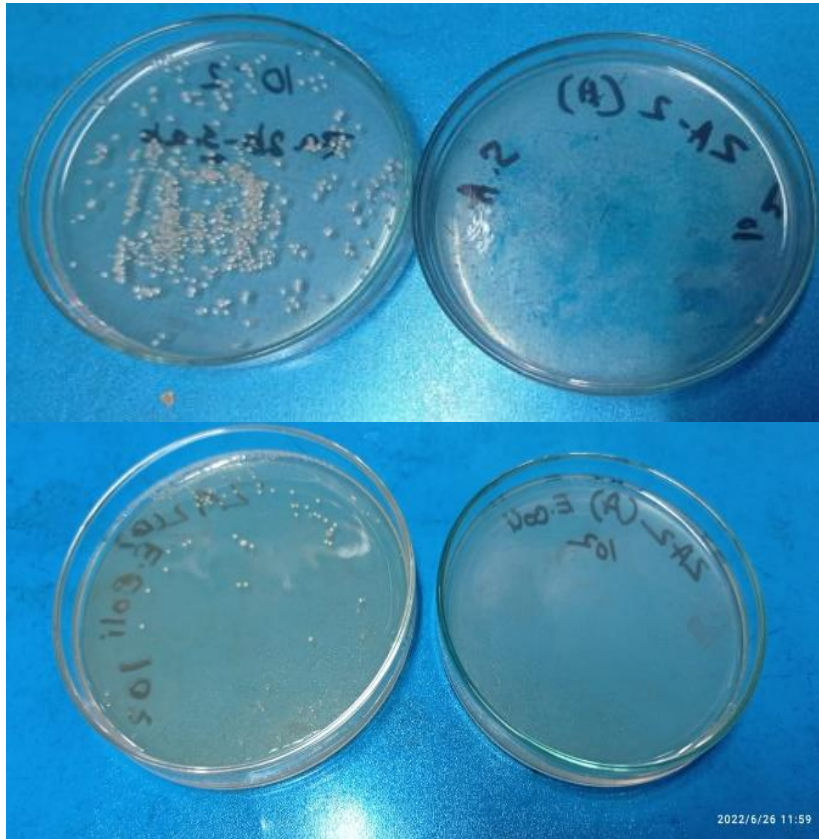
Figure 6.9: Antibacterial activity of ZnO@Ag core-shell NPs against *Staphylococcus aureus* or *S. aureus* (Gram-positive) and *Escherichia coli* or *E. coli* (Gram-negative) bacterial strains.

charge of the bacterial membrane as Ag+ can produce reactive oxygen species and natural antibiotic power.[47] Moreover, the nano size of ZnO@Ag NPs can show bactericidal activity by infusing with two steps; firstly, interacting with thiol group of the protein or sulfhydryl (-SH) groups and disbanding the protein by forming a stable S-metal complex structure, thus causing protein denaturation and extinction of bacterial cell.[30] Secondly, Ag^+ destabilized ATP (adenosine triphosphate) creation, condensed and destructed DNA replication by lacking hydrogen ion from protein that facilities accessible entrance of ZnO@Ag NPs within cells leading to apoptosis that prohibits the bacterial metabolism by damaging the cell membrane and finally causes microbes' death. The medium crystallite size of ZnO@Ag NPs found from the XRD results is around 5 to 38 nm, and its narrow band gap energy absorbs the energy from the visible light region, which also causes to improve the antibacterial efficiency.[48]

6.3.12 UV protection factor of ZnO@Ag NPs coated fabric

Solar UV radiation is composed of UV-A (400-315 nm), UV-B (315-290 nm), and UV-C (290-200 nm) radiation has a total of 3-5% of UV radiation that is hazardous to human health. These radiations are situated in natural terrestrial sunlight that can depend on the upper atmosphere's filtering capacity and local conditions like latitude, altitude, clouds, etc. However, the ozone layer filters UV-C and most UV-B radiation. Control cotton fabric is impotent to absorb UV radiation, which harms the human skin. UV protection fabric can protect human skin against UV radiation by increasing absorption and reflection and reducing transmittance in UV and visible regions. UV-protection properties of coated and control fabrics were measured according to equations (10-11), shown in Figure 6.10 and tabulated in Table 6.9.
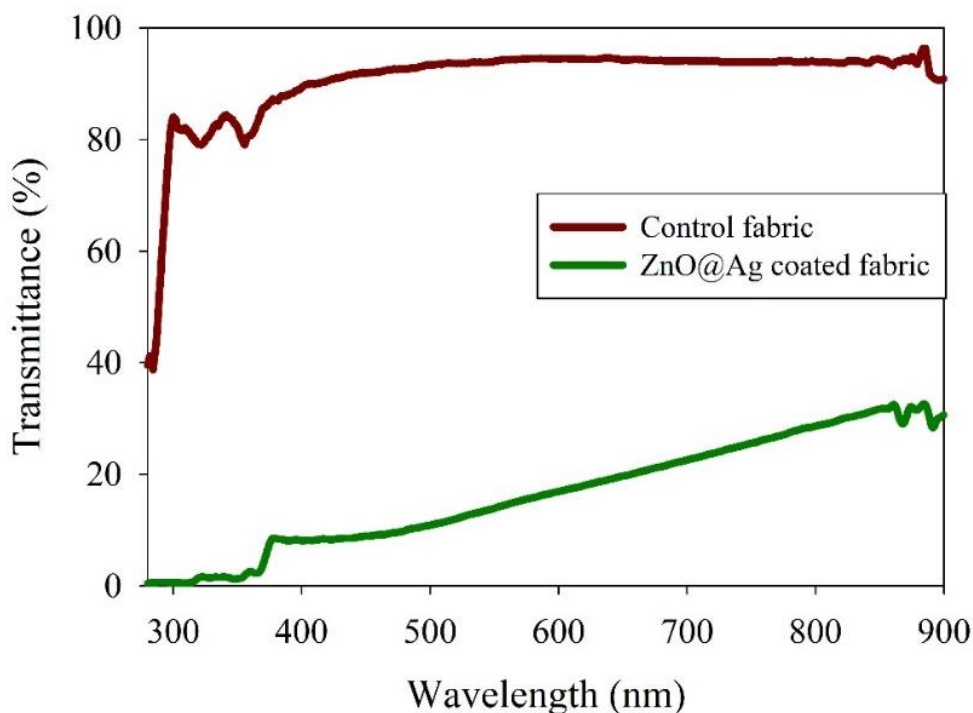
Figure 6.10: UV protection of control and ZnO@Ag NPs coated fabrics.

ZnO@Ag NPs coated fabric shows a UV protection factor (UPF) value of around 26.18. The sizes and morphology of NPs also influence these UV-blocking properties. Larger NPs in coating promote the dispersion of UV-blocking and decrease the total reflection of UV light due to the irregular and multiple reflections of UV light throughout the interface of NPs and fabric surface by significantly improving the absorption of the photon.[49] Summarized data of related NPs used for achieving UV protection performances are listed in Table 6.10.

Table 6.9: UPF (Eq. 10) and % UV transmission (Eq. 11) for control and coated fabrics against UV-A (315-400 nm) and UV-B (290-315 nm) radiation.

Sample	UPF	UV-A transmission (%)	UV-B transmission (%)
Control fabric	1.20	84.27	79.49
ZnO@Ag NPs coated fabric	26.18	4.51	1.42

Table 6.10: Summarized data of related NPs used for achieving UV protection performances.

NPs	Deposition process	Functionalized textile	UV protection factor	Reference
Ag–ZnO nanoparticles hybrid	*In situ synthesis*	Woven cotton fabric	>50	42
Ag/ZnO nanocomposite	*In situ synthesis*	Cotton fabric	>50	6
Ag-doped ZnO composite	Pad-dry-cure	Cotton fabric	>50	49
Ag/ZnO doping	Pad-dry-cure	Cotton fabric	9% transmittance of UV rays	50
ZnO@Ag core-shell	Pad-dry-cure	Cotton fabric	26.18	Present work

6.3.13 Self-cleaning properties

Curry masala contains different ingredients such as turmeric, cumin, coriander seed, black paper, cloves, red chilies, ginger, salt, garlic, mustard, etc. The curry stain is produced by mixing curry masala in hot water. However, this stain is generally because of the turmeric (Curcuma longa) stain on cotton due to the binding of the yellow pigments that are most of the curcumin and its derivatives with the cellulose of cotton. Curcumin is about 3-5% of total turmeric constituents and is also a yellow-colored substance consisting of two phenolic hydroxyl groups and two centrally located carbonyl groups that can exist in keto-enol tautomers in solution.[51] The mechanism behind the discoloration of the colored substances (high molecular weight organic compound) of curry stain by ZnO@Ag coated cotton under UV exposure means when the photon energy is higher than the band gap of ZnO@Ag NPs (2.13 eV), the electrons of ZnO@Ag will be excited and travel to the conduction band from the valence band thus resulting to the production of two kinds of oppositely charged carriers, i.e., hole (h^+) and electron (e^-). The electron (e^-) is converted to superoxide anion ($^\bullet O_2^-$) by oxygen, whereas the produced hole (h^+) is converted to hydroxyl radical ($^\bullet OH$) by the moisture (H_2O) present in the air. These superoxide anion and hydroxyl radicals are incredibly reactive particles responsible for redox reactions and the leading cause of organic materials' degradation (curry stain) into small molecules (CO_2 and H_2O) under UV irradiation of ZnO@Ag NPs.[52] The *K/S* values (absorption and

189

scattering coefficient; color strength) of control fabric unexposed and curry stain unexposed and curry stain exposed fabrics after 20 h irradiation under light source according to ISO 105 B02:2013 for self-cleaning efficiency were expressed in Figure 6.11. ZnO@Ag NPs coated fabric show super self-cleaning results as pretty near color strength (*K/S*) of the curry stain fabric with control fabric without stain means all stains are removed from the surface.
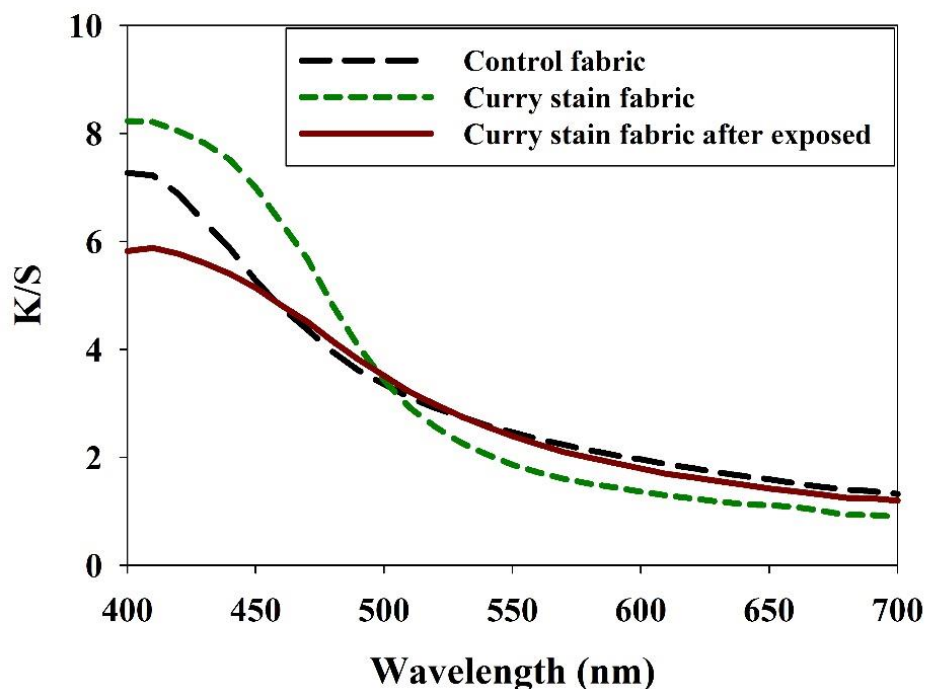
Figure 6.11: *K/S* values of control fabric, the curry stain fabric, and the curry stain fabric after exposure against 20 h irradiation.

6.4   Conclusions

The multifunctional fabric was prepared by depositing ZnO@Ag NPs onto cotton fabrics. ZnO@Ag NPs have been synthesized, characterized, and uniformly distributed on the fabric surface. This coated fabric shows good UV protection, exhibits synergistic and excellent antibacterial potency for gram-positive (*S. aureus*) and gram-negative (*E. coli*), and has outstanding self-cleaning properties attributed to the enormous interaction within semiconductor ZnO and metallic Ag. This high-value-added multifunctional fabric has a

wide range of practical applications and is in sync with developing future trends. This multifunctional fabric has promising applications in the textile industry.

References:

(1)   Capraru, O. A.; Lungu, B.; Virgolici, M.; Constantin, M.; Cutrubinis, M.; Chirila, L.; Cinteza, L. O.; Stanculescu, I. Gamma Irradiation and Ag and ZnO Nanoparticles Combined Treatment of Cotton Textile Materials. *Materials (Basel).* **2022**, *15* (8), 1–10. https://doi.org/10.3390/ma15082734.

(2)   Chen, W.; Feng, X.; Zhang, D.; Lu, F.; Wang, H.; Tan, J.; Xu, Q.; Liu, Y.; Cao, Z.; Su, X. In Situ Synthesis of TiO_2/NC on Cotton Fibers with Antibacterial Properties and Recyclable Photocatalytic Degradation of Dyes. *RSC Adv.* **2022**, *12* (31), 19974–19980. https://doi.org/10.1039/d2ra00992g.

(3)   Ivanuša, M.; Kumer, B.; Petrovčič, E.; Štular, D.; Zorc, M.; Jerman, I.; Gorjanc, M.; Tomšič, B.; Simončič, B. Eco-Friendly Approach to Produce Durable Multifunctional Cotton Fibres Using TiO_2, ZnO and Ag NPs. *Nanomaterials* **2022**, *12* (18). https://doi.org/10.3390/nano12183140.

(4)   Aladpoosh, R.; Montazer, M. Nano-Photo Active Cellulosic Fabric through in Situ Phytosynthesis of Star-like Ag/ZnO Nanocomposites: Investigation and Optimization of Attributes Associated with Photocatalytic Activity. *Carbohydr. Polym.* **2016**, *141*, 116–125. https://doi.org/10.1016/j.carbpol.2016.01.005.

(5)   Ibănescu, M.; Muşat, V.; Textor, T.; Badilita, V.; Mahltig, B. Photocatalytic and Antimicrobial Ag/ZnO Nanocomposites for Functionalization of Textile Fabrics. *J. Alloys Compd.* **2014**, *610*, 244–249. https://doi.org/10.1016/j.jallcom.2014.04.138.

(6)   Avazpour, S.; Karimi, L.; Zohoori, S. Simultaneous Coloration and Functional Finishing of Cotton Fabric Using Ag/ZnO Nanocomposite. *Color. Technol.* **2017**, *133* (5), 423–430. https://doi.org/10.1111/cote.12296.

(7)   Dinesh, V. P.; Biji, P.; Ashok, A.; Dhara, S. K.; Kamruddin, M.; Tyagi, A. K.; Raj, B. Plasmon-Mediated, Highly Enhanced Photocatalytic Degradation of Industrial Textile Dyes Using Hybrid ZnO@Ag Core-Shell Nanorods. *RSC Adv.* **2014**, *4* (103), 58930–58940. https://doi.org/10.1039/c4ra09405k.

(8)   Vivek, C.; Balraj, B.; Thangavel, S. Structural, Optical and Electrical Behavior of ZnO@Ag Core–Shell Nanocomposite Synthesized via Novel Plasmon-Green Mediated Approach. *J. Mater. Sci. Mater. Electron.* **2019**, *30* (12), 11220–11230. https://doi.org/10.1007/s10854-019-01467-x.

(9)   Wang, Y.; Zhu, S.; Chen, X.; Tang, Y.; Jiang, Y.; Peng, Z.; Wang, H. One-Step Template-Free Fabrication of Mesoporous ZnO/TiO_2 Hollow Microspheres with Enhanced Photocatalytic Activity. *Appl. Surf. Sci.* **2014**, *307*, 263–271. https://doi.org/10.1016/j.apsusc.2014.04.023.

(10)   Kumar, N. S.; Ganapathy, M.; Sharmila, S.; Shankar, M.; Vimalan, M.; Potheher, I. V. $ZnO/Ni(OH)_2$ Core-Shell Nanoparticles: Synthesis, Optical, Electrical and Photoacoustic Property Analysis. *J. Alloys Compd.* **2017**, *703*, 624-632. https://doi.org/10.1016/j.jallcom.2017.01.323.

(11)   Pietrzak, K.; Gutarowska, B.; Machnowski, W.; Mikołajczyk, U. Antimicrobial Properties of Silver Nanoparticles Misting on Cotton Fabrics. *Text. Res. J.* **2016**, *86* (8), 812–822. https://doi.org/10.1177/0040517515596933.

(12)   Campos Payá, J.; Díaz-García, P.; Montava, I.; Miró-Martínez, P.; Bonet, M. A New Development for Determining the Ultraviolet Protection Factor. *J. Ind. Text.* **2016**, *45* (6), 1571–1586. https://doi.org/10.1177/1528083714567238.

(13)   Awad, A.; Abou-Kandil, A. I.; Elsabbagh, I.; Elfass, M.; Gaafar, M.; Mwafy, E. Polymer Nanocomposites Part 1: Structural Characterization of Zinc Oxide Nanoparticles Synthesized via Novel Calcination Method. *J. Thermoplast. Compos. Mater.* **2015**, *28* (9), 1343–1358. https://doi.org/10.1177/0892705714551241.

(14)   Grifoni, D.; Bacci, L.; Zipoli, G.; Albanese, L.; Sabatini, F. The Role of Natural Dyes in the UV Protection of Fabrics Made of Vegetable Fibres. *Dye. Pigment.* **2011**, *91* (3), 279–285. https://doi.org/10.1016/j.dyepig.2011.04.006.

(15)   Gupta, K. K.; Jassal, M.; Agrawal, A. K. Functional Finishing of Cotton Using Titanium Dioxide and Zinc Oxide Nanoparticles. *Res. J Text. Appl.* **2007**, 11(3), 1560-6074. https://doi.org/10.1108/RJTA-11-03-2007-B001.

(16)   Xu, R. Progress in Nanoparticles Characterization: Sizing and Zeta Potential Measurement. *Particuology* **2008**, *6* (2), 112–115. https://doi.org/10.1016/j.partic.2007.12.002.

(17)   Mohamed, F.; Enaiet Allah, A.; Abu Al-Ola, K. A.; Shaban, M. Design and Characterization of a Novel Zno–Ag/Polypyrrole Core–Shell Nanocomposite for Water Bioremediation. *Nanomaterials* **2021**, *11* (7), 1688. https://doi.org/10.3390/nano11071688.

(18)   Sharma, V.; Anderson, D.; Dhawan, A. Zinc Oxide Nanoparticles Induce Oxidative DNA Damage and ROS-Triggered Mitochondria Mediated Apoptosis in Human Liver Cells (HepG2). *Apoptosis* **2012**, *17* (8), 852–870. https://doi.org/10.1007/s10495-012-0705-6.

(19) Akhtar, M. J.; Alhadlaq, H. A.; Alshamsan, A.; Majeed Khan, M. A.; Ahamed, M. Aluminum Doping Tunes Band Gap Energy Level as Well as Oxidative Stress-Mediated Cytotoxicity of ZnO Nanoparticles in MCF-7 Cells. *Sci. Rep.* **2015**, *5* (September), 1–16. https://doi.org/10.1038/srep13876.

(20) EL-Dafrawy, S. M.; Tarek, M.; Samra, S.; Hassan, S. M. Synthesis, Photocatalytic and Antidiabetic Properties of ZnO/PVA Nanoparticles. *Sci. Rep.* **2021**, *11* (1), 1–11. https://doi.org/10.1038/s41598-021-90846-8.

(21) Mostafa, A. M.; Mwafy, E. A. Synthesis of ZnO and Au@ZnO Core/Shell Nano-Catalysts by Pulsed Laser Ablation in Different Liquid Media. *J. Mater. Res. Technol.* **2020**, *9* (3), 3241–3248. https://doi.org/10.1016/j.jmrt.2020.01.071.

(22) Sharwani, A. A.; Narayanan, K. B.; Khan, M. E.; Han, S. S. Photocatalytic Degradation Activity of Goji Berry Extract Synthesized Silver-Loaded Mesoporous Zinc Oxide (Ag@ZnO) Nanocomposites under Simulated Solar Light Irradiation. *Sci. Rep.* **2022**, *12* (1), 1–18. https://doi.org/10.1038/s41598-022-14117-w.

(23) Jadhav, J.; Biswas, S. Structural and Electrical Properties of ZnO:Ag Core-Shell Nanoparticles Synthesized by a Polymer Precursor Method. *Ceram. Int.* **2016**, *42* (15), 16598–16610. https://doi.org/10.1016/j.ceramint.2016.07.081.

(24) Choudhary, M. K.; Kataria, J.; Bhardwaj, V. K.; Sharma, S. Green Biomimetic Preparation of Efficient Ag-ZnO Hetero-junctions with Excellent Photocatalytic Performance under Solar Light Irradiation: A Novel Biogenic-Deposition-Precipitation Approach. *Nanoscale Adv.* **2019**, *1* (3), 1035–1044. https://doi.org/10.1039/c8na00318a.

(25) Tauc, J.; Grigorovici, R.; Vancu, A. Optical Properties and Electronic Structure of Amorphous Germanium. *Phys. Stat. Sol.* (b). **1966**, *15*(2), 627–637. https://doi.org/10.1002/pssb.19660150224.

(26) Zhang, Q.; Xu, M.; You, B.; Zhang, Q.; Yuan, H.; Ostrikov, K. Oxygen Vacancy-Mediated ZnO Nanoparticle Photocatalyst for Degradation of Methylene Blue. *Appl. Sci.* **2018**, *8* (3), 1–12. https://doi.org/10.3390/app8030353.

(27) Ziashahabi, A.; Prato, M.; Dang, Z.; Poursalehi, R.; Naseri, N. The Effect of Silver Oxidation on the Photocatalytic Activity of Ag/ZnO Hybrid Plasmonic/Metal-Oxide Nanostructures under Visible Light and in the Dark. *Sci. Rep.* **2019**, *9* (1), 1–12. https://doi.org/10.1038/s41598-019-48075-7.

(28) Shahmoradi, Y.; Souri, D. Growth of Silver Nanoparticles within the Tellurovanadate Amorphous Matrix: Optical Band Gap and Band Tailing Properties, beside the Williamson-Hall Estimation of Crystallite Size and Lattice Strain. *Ceram. Int.* **2019**, *45* (6), 7857–7864. https://doi.org/10.1016/j.ceramint.2019.01.094.

(29) Król-Górniak, A.; Railean, V.; Pomastowski, P.; Płociński, T.; Gloc, M.; Dobrucka, R.; Kurzydłowski, K. J.; Buszewski, B. Comprehensive Study upon Physicochemical Properties of Bio-ZnO NCs. *Sci. Rep.* **2023**, *13* (1), 1–21. https://doi.org/10.1038/s41598-023-27564-w.

(30) Chauhan, A.; Verma, R.; Kumari, S.; Sharma, A.; Shandilya, P.; Li, X.; Batoo, K. M.; Imran, A.; Kulshrestha, S.; Kumar, R. Photocatalytic Dye Degradation and Antimicrobial Activities of Pure and Ag-Doped ZnO Using Cannabis Sativa Leaf Extract. *Sci. Rep.* **2020**, *10* (1), 1–16. https://doi.org/10.1038/s41598-020-64419-0.

(31) Zamiri, R.; Rebelo, A.; Zamiri, G.; Adnani, A.; Kuashal, A.; Belsley, M. S.; Ferreira, J. M. F. Far-Infrared Optical Constants of ZnO and ZnO/Ag Nanostructures. *RSC Adv.* **2014**, *4* (40), 20902–20908. https://doi.org/10.1039/c4ra01563k.

(32) El-Naggar, M. E.; Hassabo, A. G.; Mohamed, A. L.; Shaheen, T. I. Surface Modification of SiO2 Coated ZnO Nanoparticles for Multifunctional Cotton Fabrics. *J. Colloid Interface Sci.* **2017**, *498*, 413–422. https://doi.org/10.1016/j.jcis.2017.03.080.

(33) Gao, D.; Chen, C.; Ma, J.; Duan, X.; Zhang, J. Preparation, Characterization and Antibacterial Functionalization of Cotton Fabric Using Dimethyl Diallyl Ammonium Chloride-Allyl Glycidyl Ether-Methacrylic/Nano-ZnO Composite. *Chem. Eng. J.* **2014**, *258*, 85–92. https://doi.org/10.1016/j.cej.2014.07.072.

(34) Patil, A. H.; Jadhav, S. A.; More, V. B.; Sonawane, K. D.; Vhanbatte, S. H.; Kadole, P. V.; Patil, P. S. A New Method for Single Step Sonosynthesis and Incorporation of ZnO Nanoparticles in Cotton Fabrics for Imparting Antimicrobial Property. *Chem. Pap.* **2021**, *75* (3), 1247–1257. https://doi.org/10.1007/s11696-020-01358-0.

(35) Hasan, K. M. F.; Horváth, P. G.; Kóczán, Z.; Bak, M.; Alpár, T. Colorful and Facile in Situ Nanosilver Coating on Sisal/Cotton Interwoven Fabrics Mediated from European Larch Heartwood. *Sci. Rep.* **2021**, *11* (1), 1–13. https://doi.org/10.1038/s41598-021-01914-y.

(36) Tunc, I. The Effect of the Presence of Ag Nanoparticles on the Photocatalytic Degradation of Oxalic Acid Adsorbed on TiO_2 Nanoparticles Monitored by ATR-FTIR. *Mater. Chem. Phys.* **2014**, *144* (3), 444–450. https://doi.org/10.1016/j.matchemphys.2014.01.018.

(37) Ali, A.; Gul, A.; Mannan, A.; Zia, M. Efficient Metal Adsorption and Microbial Reduction from Rawal Lake Wastewater Using Metal Nanoparticle Coated Cotton. *Sci. Total Environ.* **2018**, *639*, 26–39. https://doi.org/10.1016/j.scitotenv.2018.05.133.

(38)   Shaban, M.; Mohamed, F.; Abdallah, S. Production and Characterization of Superhydrophobic and Antibacterial Coated Fabrics Utilizing ZnO Nanocatalyst. *Sci. Rep.* **2018**, *8* (1), 1–15. https://doi.org/10.1038/s41598-018-22324-7.

(39)   Al-Ariki, S.; Yahya, N. A. A.; Al-A'nsi, S. A.; Jumali, M. H. H.; Jannah, A. N.; Abd-Shukor, R. Synthesis and Comparative Study on the Structural and Optical Properties of ZnO Doped with Ni and Ag Nanopowders Fabricated by Sol Gel Technique. *Sci. Rep.* **2021**, *11* (1), 1–11. https://doi.org/10.1038/s41598-021-91439-1.

(40)   Perkins, R.; Drake, G. L.; Reeves, W. A. DTA and TGA Studies of Flame-Resistant Fabrics. *J. Appl. Polym. Sci.* **1966**, *10*, 1041–1066. https://doi.org/10.1002/app.1966.070100708.

(41)   Lessan, F.; Montazer, M.; Moghadam, M. B. Thermochimica Acta A Novel Durable Flame-Retardant Cotton Fabric Using Sodium Hypophosphite , Nano TiO$_2$ and Maleic Acid. *Thermochim. Acta* **2011**, *520* (1–2), 48–54. https://doi.org/10.1016/j.tca.2011.03.012.

(42)   Zhang, D.; Zhang, G.; Chen, L.; Liao, Y.; Chen, Y.; Lin, H. Multifunctional Finishing of Cotton Fabric Based on in Situ Fabrication of Polymer-Hybrid Nanoparticles. *J. Appl. Polym. Sci.* **2013**, *130* (5), 3778–3784. https://doi.org/10.1002/app.39634.

(43)   El-Nahhal, I. M.; Salem, J.; Anbar, R.; Kodeh, F. S.; Elmanama, A. Preparation and Antimicrobial Activity of ZnO-NPs Coated Cotton/Starch and Their Functionalized ZnO-Ag/Cotton and Zn(II) Curcumin/Cotton Materials. *Sci. Rep.* **2020**, *10* (1), 1–10. https://doi.org/10.1038/s41598-020-61306-6.

(44)   Barani, H. Surface Activation of Cotton Fiber by Seeding Silver Nanoparticles and in Situ Synthesizing ZnO Nanoparticles. *New J. Chem.* **2014**, *38* (9), 4365–4370. https://doi.org/10.1039/c4nj00547c.

(45)   da Silva, D. J.; Duran, A.; Cabral, A. D.; Fonseca, F. L. A.; Bueno, R. F.; Rosa, D. S. Questioning ZnO, Ag, and Ag/ZnO Nanoparticles as Antimicrobial Agents for Textiles: Do They Guarantee Total Protection against Bacteria and SARS-CoV-2? *J. Photochem. Photobiol. B Biol.* **2022**, *234* (January), 112538. https://doi.org/10.1016/j.jphotobiol.2022.112538.

(46)   Buşilə, M.; Muşat, V.; Textor, T.; Mahltig, B. Synthesis and Characterization of Antimicrobial Textile Finishing Based on Ag:ZnO Nanoparticles/Chitosan Biocomposites. *RSC Adv.* **2015**, *5* (28), 21562–21571. https://doi.org/10.1039/c4ra13918f.

(47) Panchal, P.; Paul, D. R.; Sharma, A.; Choudhary, P.; Meena, P.; Nehra, S. P. Biogenic Mediated Ag/ZnO Nanocomposites for Photocatalytic and Antibacterial Activities towards Disinfection of Water. *J. Colloid Interface Sci.* **2020**, *563*, 370–380. https://doi.org/10.1016/j.jcis.2019.12.079.

(48) Hosny, M.; Fawzy, M.; Eltaweil, A. S. Green Synthesis of Bimetallic Ag/ZnO@Biohar Nanocomposite for Photocatalytic Degradation of Tetracycline, Antibacterial and Antioxidant Activities. *Sci. Rep.* **2022**, *12* (1), 1–17. https://doi.org/10.1038/s41598-022-11014-0.

(49) Porrawatkul, P.; Pimsen, R.; Kuyyogsuy, A.; Teppaya, N.; Noypha, A.; Chanthai, S.; Nuengmatcha, P. Microwave-Assisted Synthesis of Ag/ZnO Nanoparticles Using Averrhoa Carambola Fruit Extract as the Reducing Agent and Their Application in Cotton Fabrics with Antibacterial and UV-Protection Properties. *RSC Adv.* **2022**, *12* (24), 15008–15019. https://doi.org/10.1039/d2ra01636b.

(50) Gao, D.; Liu, J.; Lyu, L.; Li, Y.; Ma, J.; Baig, W. Construct the Multifunction of Cotton Fabric by Synergism between Nano ZnO and Ag. *Fibers Polym.* **2020**, *21* (3), 505–512. https://doi.org/10.1007/s12221-020-9347-4.

(51) Priyadarsini, K. I. Journal of Photochemistry and Photobiology C : Photochemistry Reviews Photophysics , Photochemistry and Photobiology of Curcumin : Studies from Organic Solutions , Bio-Mimetics and Living Cells. **2009**, *10*, 81–95. https://doi.org/10.1016/j.jphotochemrev.2009.05.001.

(52) Qi, K.; Wang, X.; Xin, J. h. Photocatalytic Self-Cleaning Textiles Based on Nanocrystalline Titanium Dioxide. *Text. Res. J.* **2011**, *81* (1), 101–110. https://doi.org/10.1177/0040517510383618.

7. Synthesis and Application of TiO$_2$@ZnO Nanoparticles for Self-cleaning Cotton Fabrics

Abstract

The development of functional self-cleaning cotton fabric is a desirable and pressing issue for the sustainability of natural fibers. TiO$_2$@ZnO nanoparticles were synthesized using a wet chemical technique, while TiO$_2$ nanoparticles were synthesized using a sol-gel method. The particle size, optical, microstructure, and morphology of the TiO$_2$@ZnO nanoparticles were obtained by DLS, TIR spectroscopy, UV-vis spectroscopy, XRD, and TEM. The prepared TiO$_2$@ZnO NPs were coated onto cotton fabric using the pad-dry-cure technique. The morphology, and thermal properties of coated fabric were obtained by SEM) and thermogravimetry analysis, respectively. Coffee and curry stains were used as model dirt to examine self-cleaning properties. TiO$_2$@ZnO NPs-coated cotton fabric is observed to clean 80% coffee stain and 90% curry stain after 20 h of xenon UV light exposure.

Keywords
Self-cleaning textiles, titanium dioxide, zinc oxide, core@shell

7.1 Introduction

Functional finishes have gained much recognition due to consumers' interest in environmental preservation and achieving a secure, active, and enjoyable life over the past few decades.[1,2] Various materials with various properties can be incorporated into textiles by different treatments to produce functional textiles.[3] Cotton is not only a great natural fiber on earth, but it is also actively used in a variety of products, including clothing, and technical textiles, due to its exceptional qualities, including a high specific surface, effective moisture absorption, an absorbent structure, affordability, biodegradability, biocompatibility, and environmental friendliness. Self-cleaning functional cotton fabric promotes product value addition and intense academic and corporate interest due to its enormous consumer appeal.[4] Latest nanotechnology guide huge convenience in functional cotton by incorporating semiconductor-based metal oxide NPs onto cotton fibers as these NPs showed improved self-cleaning property by making reactive oxygen species by photo-

oxidation and photo reduction reaction with oxygen and water.[5] Moreover, core@shell NPs is a new field that greatly attracted the photocatalysis field due to its structure that possesses synergistic properties within the cores and shells based on their interactions.[6,7] These tailored properties of inorganic semiconductor-based core@shell have gained massive attention from academic, industrial, and technical applications.[8] TiO_2 is a popular semiconductor-based photocatalyst that is widely used to impart functional properties on textiles due to its facile manufacturing process, wide-bandgap, photocatalytic, phase-dependent optical properties, binding energy, good stability, electrical properties, cheap, and non-toxic nature.[9,10] High recombination rate of TiO_2 reduces its photocatalytic efficiency and lifetime. So combining with other semiconductors to produce heterostructure minimizes the recombination rate and provides a synergistic effect on photocatalytic efficiency. ZnO can be an excellent alternative to combine with TiO_2 to produce heterostructure semiconductor-based photocatalysts to upgrade photodegradation activity as ZnO possesses excellent characteristics like improved stability, direct bandgap, elevated electron mobility, and anisotropic growth as these properties also contribute to soaring on photocatalytic efficiency.[11] Semiconductor-based core@shell NPs have been widely studied due to their synergistic photocatalytic activity.[12] Attia et al.[13] applied TiO_2 and ZnO NPs on cotton/polyester blend and wool fabric by ultrasonication process and achieved excellent UV protection, antibacterial, and super hydrophobic functional fabric. Siwinska-Stefanska et al.[14] synthesized TiO_2-ZnO NPs by sol-gel process and evaluated their photocatalytic performance against three organic dyes.

This work aimed to synthesize TiO_2@ZnO NPs by wet chemical method with various curing temperatures, characterized by DLS, FT-IR, UV spectroscopy, XRD, and TEM and applied on cotton knit fabric by pad-dry-cure method. The morphological property of cotton fabric was evaluated by SEM equipped with EDX spectroscopy. Physical and thermal characteristics, whiteness, and self-cleaning properties of coated fabrics were also analyzed in detail.

7.2   Experimental

7.2.1   Materials

Titanium (IV) butoxide (Sigma- Aldrich), acetic acid and hydrochloric acid (RCI Labscan limited, Thailand), zinc nitrate hexahydrate (>98%, Merck), CTAB (>98%, Merck), NaBH$_4$ (>98%, ACROS organics, Belgium), binder of aqueous acrylate dispersion (Forbind OB 45, Fortune top Pte Ltd. New Taipei City, Taiwan) were used without further purification. Deionized water (conductivity: 0.055 µScm^{-1}), collected from the HPLC grade water purification system (BOECO), was used to prepare all solutions. Scoured and bleached 100% cotton knit fabric with a single jersey structure was used throughout all experiments.

7.2.2   Synthesis of TiO$_2$ NPs by sol-gel method

TiO$_2$ NPs were synthesized through a particular sol-gel process using titanium (IV) butoxide as a precursor material, and in synthesis, 0.2% HCl and 0.2% acetic acid were dissolved in 7 mL of deionized water followed by dropwise added 3 mL at 60 ℃ under stirring at 700 rpm for 48 h. The color of the solution changed to white, indicating the onset of the formation of TiO$_2$ NPs, and TiO$_2$ powder was extracted by adding a sufficient amount of 0.3% sodium carbonate aqueous solution until precipitation occurred, followed by centrifuged (Centrifuge Cencom II from J. P. Selecta, Spain) at 1000 rpm for 20 min to eliminate the liquid phase. The precipitates were then washed three times with deionized water and then dried overnight in an oven at 100 ℃ and ground into powder.[15]

7.2.3   Synthesis of TiO$_2$@ZnO NPs

To synthesize TiO$_2$@ZnO NPs, 0.7 mmol of TiO$_2$ NPs were dispersed in 50 mL deionized water by ultra-sonication for 30 min, followed by adding 0.09 mmol of CTAB under stirred at 300 rpm and then raised the temperature of the solution at 40 ℃ and then the temperature was slowly reduced to room temperature. Afterwards, a 25 mL aqueous solution of Zn(NO$_3$)$_2$·6H$_2$O was dropwise added, and leave the solution for one h. Then another 25 mL aqueous solution of 0.7 mmol of NaBH$_4$ was added to reduce ZnO NPs. The color of the solution changed from white to slightly off-white, indicating the onset of the formation of TiO$_2$@ZnO NPs. Then the solution was centrifuged and rinsed (3-4 times) with

deionized water before being cured overnight in a Muffle furnace (Nabertherm) oven at 400 °C, 500 °C, 600 °C. TiO$_2$@ZnO NPs cured at 400 °C denoted by TZ4, cured at 500 °C denoted by TZ5, and cured at 600 °C denoted by TZ6, throughout the study.[16]

7.2.4 Application of TiO$_2$@ZnO NPs coated cotton fabric

TiO$_2$@ZnO NPs were applied to 100% cotton knit fabrics by a pad-dry-cure method. At first, cotton fabric (20 cm×20 cm) was immersed into a 100 mL solution of 1% of TiO$_2$@ZnO NPs for 5 min under stirring to prevent precipitation of NPs and followed by padding. Afterward again padded by 1% binder in 100 mL distilled water. Padding is done by a standard laboratory machine with 2.5 m/min fabric speed and 2.8 kg/cm^2 padding pressure to maintain a pick-up% of about 70-75%. The pH value of the padding bath was maintained at around 6. The sample was dried at 80 °C for 5 min by an oven, and an SDL Mini-dryer steamer was used for curing at 140 °C for 2.5 min.

7.2.5 Material characterization

The average particle sizes and size distributions of the samples dispersed in water were measured using dynamic light scattering (DLS) measurements by a Malvern Zetasizer Nano ZS90 with a scattering angle of 90°. A He–Ne laser beam of 632.8 nm wavelength was used for the measurements. The average diameters were determined from cumulants mean of the intensity average of 50 runs using Stokes-Einstein equation, $d_H = k_B T/3\pi\eta D_{ef}$ where d_H was the hydrodynamic diameter, k_B was the Boltzmann constant, T was the temperature, η was the solvent viscosity, and D_{ef} was the diffusion coefficient. The reproducibility was checked from at least three measurements. The sample temperature was controlled automatically within ±0.01 K by a built-in Peltier device.

FTIR spectra were recorded by a Fourier transform spectrophotometer (Frontier, PerkinElmer) in transmittance mode for each KBr sample range between 400 and 4000 cm^{-1} at 4.0 cm^{-1} resolution.

The crystallographic and phase identification properties were determined by an X-ray diffractometer (Philips PW 1724) with an X-ray generator using XDC-700 Guinier-Hagg

focusing camera with monochromatized Cu Kα radiation (λ = 1.540598). According to Debye-Scherrer's equation $D = \frac{K\lambda}{\beta cos\theta}$, the crystallite diameters (D) were obtained from XRD peaks.

UV–vis absorption spectrum was recorded by a double-beam UV–vis spectrophotometer (UVD-3500, LABOMED, INC, USA), where cell length was 1 cm. Diffuse reflectance spectrum (DRS) was recorded using a double beam UV-vis spectrophotometer with an integrating sphere attachment DRA-CA-30I (Model: UV-1800, Shimadzu, Japan) to determine bandgap energy (E_g) of the solid NPs.

The surface morphology, structure, and attachment of ZnO on TiO_2 were studied with transmission electron microscopy (TEM), and the micrographs were attained by using the LEO system (model 912 AB) at 120kV for samples.

The morphological study used FESEM (ZEISS, Germany). The acceleration voltage of the electron gun was 20 kV with a probe current of 1.0 nA and magnifications ranging from 10,000 – 100,000. The images of samples were taken without sputtering and by mounting on the conducting carbon tape. The compositional study of the NPs is analyzed by EDX spectroscopy attached to the FESEM. Computer-adapted software (ImageJ 1.51k, java 1.60-24 (64 bit), USA) was used to measure average particle size in both the TEM and the FESEM images of NPs. Thermal properties were studied under a nitrogen atmosphere by a Hitachi instrument (TG/ DTA 7200) in the 30–550 °C temperature at a heating rate of 20 °C min^{-1}. The physical properties of the fabrics (weight, bursting strength, air permeability) were examined by ISO standards.

7.2.6 Color measurement and whiteness test

The colorimetric difference and whiteness within control and coated fabrics were determined by a spectrophotometer (Datacolor SF850, Datacolor International, USA) under D65 (average daylight), F11 (fluorescent lighting), A (tungsten-filament lighting) standard illuminants at a ten-observing angle with d/8 viewing geometry. The CIE *LCH* color coordinates (*L*, *C*, and *H*) where *L* represents white to black, *C* represents brighter duller, and *H* represents hue, whereas The CIE *Lab* color coordinates (*L*, *a* and *b*) where *L*

represents white to black, a and b represents redness–greenness and yellowness–blueness, respectively. The color difference (ΔE) between reference (control fabric) and sample (coated) fabrics was measured by the following equation(1-8):[17]

$$\Delta L = L_1 - L_2 \qquad (1)$$

$$\Delta a = a_1 - a_2 \qquad (2)$$

$$\Delta b = b_1 - b_2 \qquad (3)$$

$$\Delta C = C_1 - C_2 \qquad (4)$$

$$\Delta H = H_1 - H_2 \qquad (5)$$

$$C = \sqrt{\Delta a^2 + \Delta b^2} \qquad (6)$$

$$H = \tan^{-1} b/a \qquad (7)$$

Where, L_1, a_1, b_1, C_1, H_1 represents control fabric and L_2, a_2, b_2, C_2, H_2 represents coated fabric. The color difference, ΔE, provides the distance within the reference and coated fabric sample in the CIE computer color matching (CMC) color space and was calculated by the following equation (8):

$$\Delta ECMC = \Delta L \Delta C \Delta H \qquad (8)$$

Where ΔL, Δa, Δb, ΔC, and ΔH are the differences between control and coated fabrics. The whiteness of control and TiO_2@ZnO NPs coated cotton fabrics were measured according to ISO 105-J02:1997 (Textiles-Tests for color fastness-Instrumental assessment of relative whiteness). The whiteness indexes (W_{10}) for the samples were calculated by using equation (9):

$$W_{10} = Y_{10} + 800(0.3138 - x_{10}) + 1700(0.3310 - y_{10}) \qquad (9)$$

Where W_{10} is the whiteness value/index, Y_{10}, x_{10}, y_{10} are the chromaticity coordinates of the sample, and 0.3138 and 0.3310 are the x_{10}, y_{10} chromaticity coordinates for the perfect diffuser.[18]

7.2.7 Evaluation of the self-cleaning activity

The self-cleaning activity of control and coated fabrics was determined by the contrast of color strength of coffee and curry stains under UV irradiation. The coffee solution is made by dissolving 0.3 g 100% pure soluble coffee powder (*Nestle*) in 25 mL hot water, and curry paste is produced by adding 0.5 g 100% curry powder (*Radhuni*) in 10 mL hot water. Both coffee and curry stains were made by dropping one drop of coffee solution and one drop of curry paste respectively close on TiO_2@ZnO NPs coated fabric, allowed to spread and dried in the air, and then exposed to light irradiation. The irradiation of stained TiO_2@ZnO NPs coated fabric was carried out for 20 h in a Xenotest Alpha L.M. light exposure and weathering test instrument (air-cooled xenon arc lamp, Xenotest Alpha L.M., USA) by ISO 105 B02 test method. Half of each stain on the fabric was exposed to a Xenon arc lamp while the other half was unexposed with a steel frame to prevent irradiation. The exposed part of the stain was compared with the unexposed part for self-cleaning action. The self-cleaning action was quantified by comparing the color strength (*K/S*) between the exposed part and the unexposed part of the same stain. The reflectance of the stained fabric was measured by the spectrophotometer (Datacolor SF600, Datacolor International, USA). The reflectance (*R*) was used to calculate the color strength by the Kubelka-Munk equation (10).[19]

$$\frac{K}{S} = \frac{(1-R)^2}{2R} \qquad (10)$$

Here, *K/S* means color strength, and *K* and *S* are the absorptions and scattering coefficients. The *K/S* value of the unexposed part of the stain was taken as 100, and the relative reduction or stain degradation in the *K/S* value of the exposed part was calculated by using the below equation (11):[20]

$$\% \ Reduction \ in \frac{K}{S} \ value \ = \frac{\left(\frac{K}{S}\right)unexposed - \left(\frac{K}{S}\right)exposed}{\left(\frac{K}{S}\right)unexposed} \times 100 \qquad (11)$$

7.3   Results and Discussion

7.3.1   Dynamic light scattering analysis

In Figure 7.1, TiO$_2$ NPs show multiple sinusoidal peaks with tiny particles of 1 nm hydrodynamic diameter (d_H), moderate particles of 1 to 20 nm and particles of d_H about 50-220 nm reveal their existence, where, all TZ4, TZ5 and TZ6 expresses one broad sinusoidal peak of each start from 127 to 466 nm, 92 to 350 nm and 68 to 380 nm hydrodynamic diameter respectively. DLS expresses the particle size in solution form that can be swelled with time while measuring. [21,22] Furthermore, DLS analysis of all TZ4, TZ5, and TZ6 NPs justify the production of well-defined dimensions[23], and more miniature size of the NPs provides more self-cleaning activity due to higher surface area.[24]
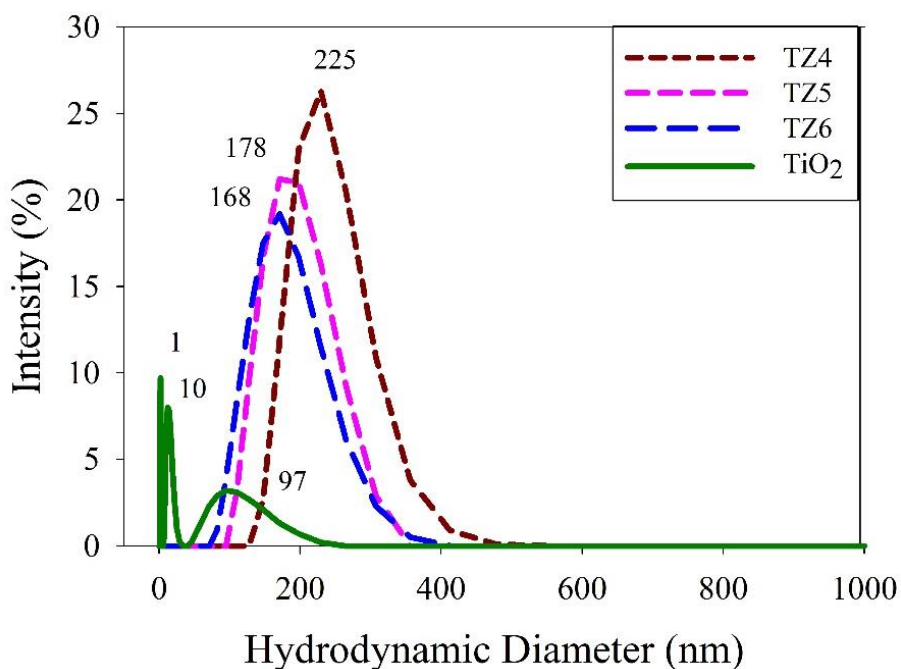
Figure 7.1.: The average hydrodynamic diameter of TiO$_2$, TZ4, TZ5, and TZ6 NPs.

7.3.2   FTIR spectroscopy

The FTIR spectra of TZ4, TZ5, and TZ6 NPs are shown in Figure 7.2 and the assignment of the characteristic peaks of TiO$_2$ NPs and TiO$_2$@ZnO NPs are tabulated at Table 7.1. In Figure 7.2, a peak around 465 cm^{-1} is associated with the bending vibration of Zn-O [25] and

a wide peak reported at around 551 cm^{-1} expressing Ti-O-Ti bond of TiO$_2$.[26,27] A broad and intense absorption peak at 3350 cm^{-1} corresponds to the stretching vibration of the O-H mode due to the O.H. groups of water.[28,29] The small peak at 1624 cm^{-1} is ascribed to the O-H bending mode, and 1383.2 cm^{-1} is attributed to the hydroxyl groups of moisture.[30] Zn-O-Zn bridging in 1056 cm^{-1} is found.[31]
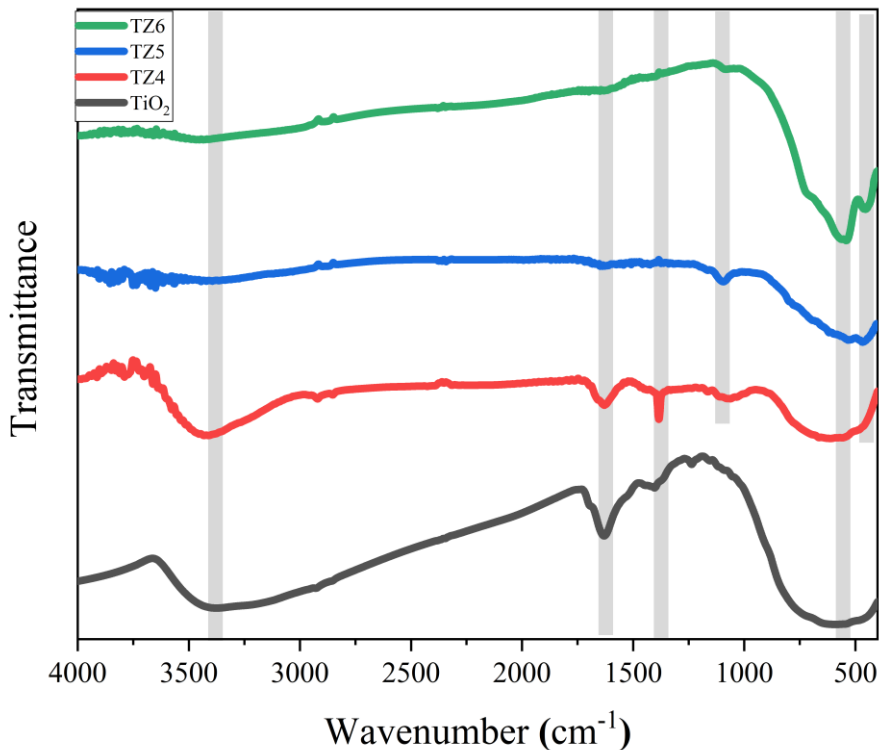
Figure 7.2.: FTIR spectra of TiO$_2$, TZ4, TZ5, and TZ6 NPs.

Table 7.1: The FTIR transmittance characteristic peaks of TiO_2 NPs and TiO_2@ZnO NPs

TiO₂ NPs	TiO₂@ZnO NPs	Assignment
-----------	465 cm^{-1}	Bending vibration of Zn-O[25]
580 cm^{-1}	551 cm^{-1}	Ti-O and Ti-O-Ti[26]
----------	1056 cm^{-1}	Zn-O-Zn bridging[32]
1389 cm^{-1}	1389 cm^{-1}	hydroxyl groups of moisture[30]
1624 cm^{-1}	1624 cm^{-1}	O.H. bond of vibration of the surface adsorbed of Ti-OH[33]
3350 cm^{-1}	3350 cm^{-1}	Surface O-H groups and absorbed water[28,29]

7.3.3 UV-vis absorption analysis

Figure 7.3 depicts UV-vis absorption spectra of pure TiO_2 and heterostructure TZ4, TZ5, and TZ6 NPs that reveal the optical absorption at 251 nm in the UV region resembles the electron migration to the conduction band from the valance band.[34] All TZ4, TZ5, and TZ6 NPs exhibit a red-shifted peak at 295 nm because of the solid interfacial electronic coupling and electron transfer process between TiO_2 and ZnO NPs in the Fermi levels.[35] The shifting of the light absorption edge of metal oxide NPs after shelling with other metal oxide was also reported in other studies.[36]
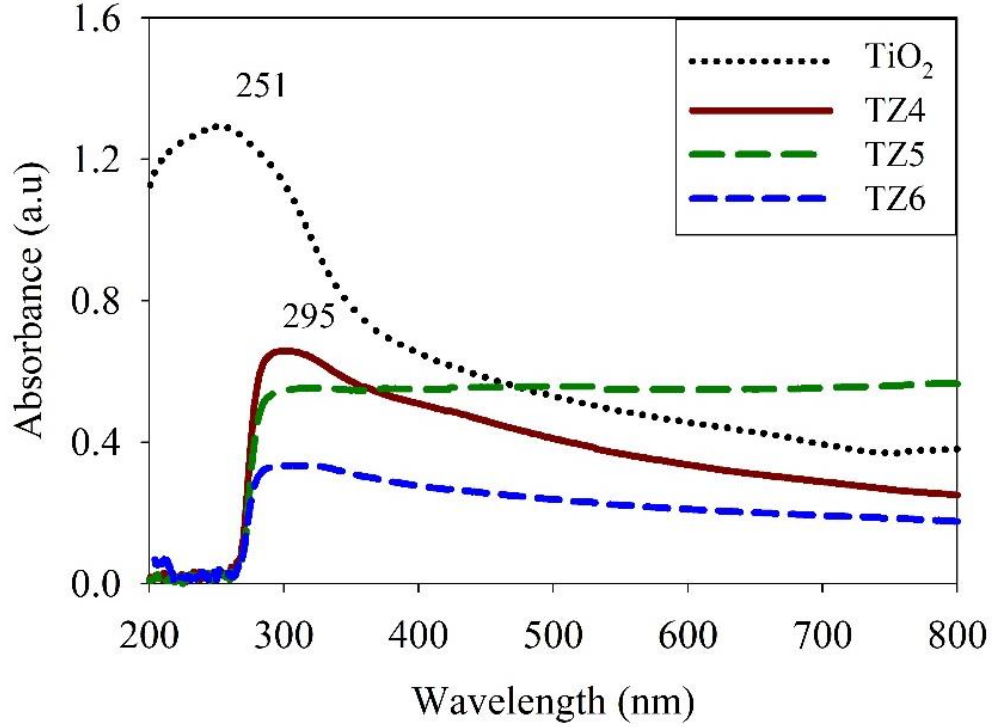
Figure 7.3.: UV-vis absorption spectra of aqueous solution of TiO_2, TZ4, TZ5, and TZ6 NPs.

7.3.4 Determination of optical band gap and the nature of optical charge carrier transitions

The optical bandgap of all TZ4, TZ5, and TZ6 NPs are reported by the derivation of the absorption spectrum fitting (DASF) method under the following equations (12-13):[37]

$$ln\left[\frac{f(R)}{\lambda}\right] + ln\,s = ln[B(hc)^{m-1}] + m\,ln(\frac{1}{\lambda} - \frac{1}{\lambda_g}) \qquad (12)$$

Now,

$$\frac{d\{ln\left[\frac{f(R)}{\lambda}\right]\}}{d(\frac{1}{\lambda})} = \frac{m}{\frac{1}{\lambda} - \frac{1}{\lambda_g}} \qquad (13)$$

As $f(R)$ is calculated by Kubelka–Munk method (equation 14) where R is the reflectance and $f(R)$ is proportional to the absorption coefficient (α).

$$f(R) = \frac{(1-R)^2}{2R} \qquad (14)$$

Where λ is the wavelength, c is the velocity of light, λ_g is the wavelength associated with the optical bandgap, B is a constant, and s is the scattering coefficient. $h\nu$ is the photon's energy and E_g is the bandgap energy of the sample. The optical bandgap of the samples is measured by the extrapolation of a linear portion in the plot of $dln[\alpha(\lambda)\lambda^{-1}]/d\lambda^{-1}$ against $h\nu$ extended in Figure 7.4a. The calculated E_g of TZ4, TZ5, and TZ6 are 3.19, 3.18, and 3.19, respectively, which are decreased from TiO_2 (3.2 eV).
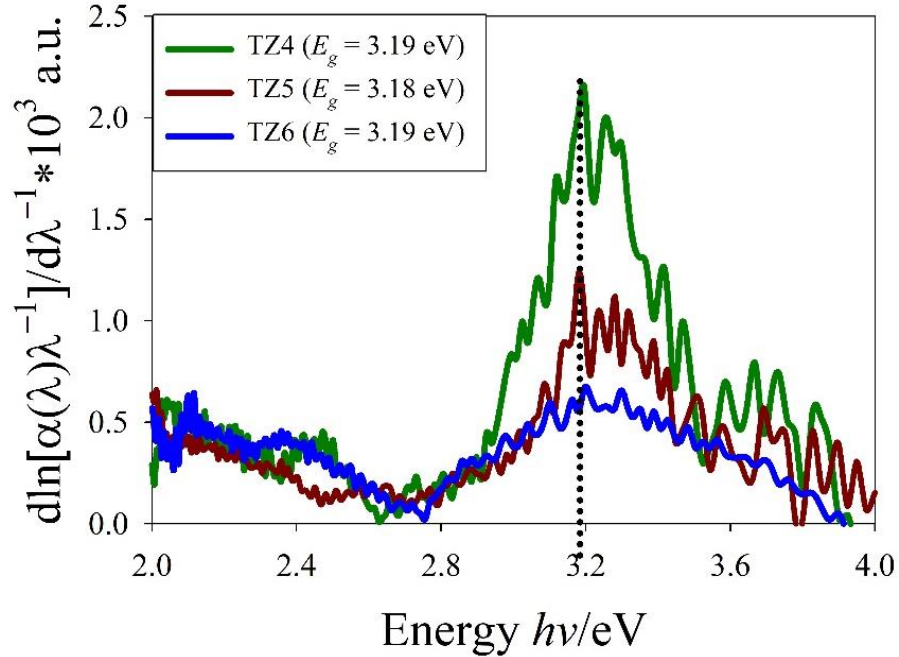
Figure 7.4a: DASF method calculated for bandgap by plotting of $dln[\alpha(\lambda)\lambda^{-1}]/d\,\lambda^{-1}$ versus hv.

The decrease of E_g after ZnO incorporation may suggest that ZnO has substituted TiO_2 in the lattice that, creates oxygen vacancies due to the valence difference between Ti^{4+} and Zn^{2+}. The created oxygen vacancies take a significant role in the narrowing of E_g since they act as trap centres that reduce the recombination rate of photo-generated charge carriers by capturing the electrons and broaden the absorbing range of light as both TiO_2 and ZnO are oxide semiconductors that have indirect bandgap associating a conduction band edge at -4.21 eV for TiO_2 whereas, ZnO has a conduction band edge at -4.19 eV.[38] Moreover, the Fermi level of ZnO is higher than the TiO_2 Fermi level allowing electrons to transfer

smoothly from ZnO NPs to TiO$_2$ NPs in the non-equilibrium state of the two systems. Furthermore, core TiO$_2$ states maybe interact with the shell ZnO state to create energy levels in the TiO$_2$ bandgap that reduce its optical band gap, thus improving the photocatalytic properties of ZnO.[39] The difference in bandgap values within TiO$_2$@ZnO and TiO$_2$ NPs depends on grain size, structural parameter, and carrier concentration. The corresponding coefficient (*m*) of the sample associated with an electronic transition and is calculated by the extrapolation of a linear portion in the plot of *ln[α(λ)λ^{-1}]* versus *ln[λ^{-1} – λ$_g$$^{-1}$]* extended in Figure 7.4b and found *m* = 1/2 identify the direct allowed transition.[40]

Figure 7.4b: DASF method calculated for corresponding coefficient (m) by plotting ln[α(λ)λ^{-1}] versus ln[λ^{-1} – λg^{-1}]. The inset is the reflectance spectra of TZ4, TZ5, and TZ6 NPs.

7.3.5 XRD analysis

Figure 7.5a-b expressed XRD analysis to determine the crystal structure, phase, and composition of TiO$_2$ and TZ4, TZ5, and TZ6 NPs. All the diffraction peaks of TiO$_2$ NPs can be indexed to anatase tetragonal structure (JCPDS no. 96-900-8217) with five sharp diffraction peaks (2θ) at 25.3°, 37.7°, 47.88°, 54.42° and 62.59° associated with the lattice

planes designated by Miller indices (101), (104), (200), (105) and (204). Good crystallization is also exhibited from sharp diffraction peaks, and these five diffraction peaks are present without any shift in $TiO_2@ZnO$ NPs, expressing that shelling by ZnO did not change the crystal structure of the TiO_2 domains. Moreover, $TiO_2@ZnO$ NPs showed additional peaks at 31.64°, 34.49°, 36.24°, and 56.61° belonging respectively to the (100), (002), (101), (142), and (110) planes of well indexed to wurtzite hexagonal structure of ZnO NPs and it was well coordinated with JCPDS, No. 891397. The average crystallite diameter D was calculated from Debye-Scherrer's equation (15):[41]

$$D = \frac{K\lambda}{\beta cos\theta} \qquad (15)$$

Figure 7.5: a) XRD patterns of TZ6 TZ5 TZ4 TiO_2, b) XRD patterns of TZ5 TZ4 TiO_2

Lattice strain was calculated by equation (16):

$$\eta = \frac{\beta}{tan\theta} \qquad (16)$$

The dislocation density (δ), which represents the number of defects in the crystal, was calculated by using the Williamson-Hall equation (17):

$$\delta = \frac{1}{D^2} \qquad (17)$$

The dislocation density is inversely proportional to D^2, and d-spacing was calculated by the following equation (18):

$$d_{hkl} = \frac{\lambda}{2sin\theta} \qquad (18)$$
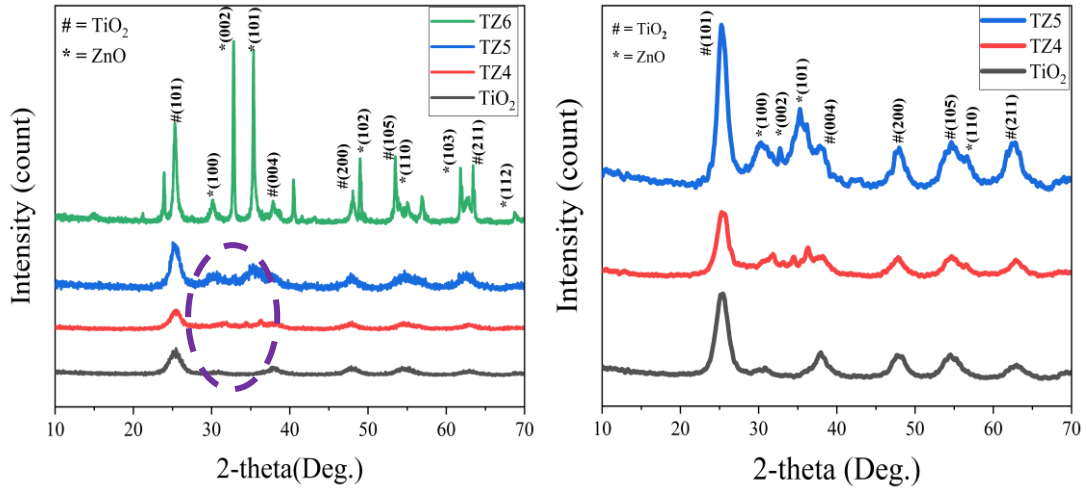
Where D is the crystallite size, $K = 0.9$, $\lambda =$ the wavelength of X-ray radiation (1.5406 Å), $\beta =$ the full-width half maximum of diffraction peak, $\theta =$ the Braggs diffraction angle, $\eta =$ Lattice strain in the material.[42] Crystallite size, lattice strain, dislocation density, lattice planes and d-spacing values are listed in Table 2.[43]

Table 7.2: Phase ID, 2θ, crystallite size, lattice strain, dislocation density, *hkl,* d-spacing of TiO_2@ZnO NPs as presented in XRD patterns analysis.

	Phase ID	2θ (degree)	B	D (nm)	$\eta = \beta/tan\theta$	δ (nm^{-2})	hkl	$d_{hkl} = \lambda/2sin\theta$
	TiO_2	25.40	1.71	4.77	0.1322	0.0439	101	0.3504
	ZnO	31.64	8.68	0.95	0.5346	1.1048	100	0.2826
	ZnO	34.49	0.40	20.92	0.0224	0.0023	002	0.2598
	ZnO	36.24	0.93	8.94	0.0498	0.0125	101	0.2477
TZ4	TiO_2	38.01	2.06	4.09	0.1041	0.0598	004	0.2366
	TiO_2	47.79	1.85	4.70	0.0728	0.0452	200	0.1902
	TiO_2	54.67	1.99	4.50	0.0671	0.0494	105	0.1677
	ZnO	56.61	1.20	7.52	0.0389	0.0177	110	0.1625
	TiO_2	62.94	2.00	4.67	0.0569	0.0459	211	0.1476
	TiO_2	25.36	1.46	5.58	0.1133	0.0321	101	0.3509
	ZnO	30.82	4.84	1.70	0.3065	0.3450	100	0.2899
	ZnO	33.35	0.06	138.22	0.0035	0.0001	002	0.2685
	ZnO	35.46	2.24	3.72	0.1223	0.0721	101	0.2529
TZ5	TiO_2	38.0	1.82	4.62	0.0923	0.0469	004	0.2366
	TiO_2	47.92	1.77	4.91	0.0695	0.0414	200	0.1895
	TiO_2	54.33	2.10	4.25	0.0714	0.0553	105	0.1687
	ZnO	56.68	2.60	3.47	0.0847	0.0832	110	0.1631
	TiO_2	62.57	2.49	3.73	0.0715	0.0717	211	0.1483
	TiO_2	25.34	0.52	15.76	0.0401	0.0040	101	0.3512
	ZnO	30.16	0.67	12.23	0.0436	0.0067	100	0.2961
	ZnO	32.82	0.21	39.67	0.0124	0.0006	002	0.2727
	ZnO	35.36	0.27	30.92	0.0148	0.0010	101	0.2536
TZ6	TiO_2	37.96	1.07	7.83	0.0544	0.0163	004	0.2368
	ZnO	48.07	0.57	15.13	0.0225	0.0044	200	0.1891
	TiO_2	49.01	0.26	33.25	0.0101	0.0009	102	0.1857
	TiO_2	54.37	2.17	4.11	0.0738	0.0592	105	0.1686
	ZnO	56.94	0.49	18.41	0.0158	0.0029	110	0.1616
	ZnO	62.28	1.46	6.36	0.0422	0.0247	103	0.1489

	TiO$_2$	63.47	0.30	31.65	0.0083	0.0010	211	0.1464
	ZnO	68.84	0.49	19.66	0.0125	0.0026	112	0.1363

7.3.6 TEM analysis

Figures 7.6 a-b, e-f, and i-j, expresses TEM analysis of TZ4, TZ5, and TZ6 NPs, respectively, with different magnifications that point out the structure, morphology, particle size, and shape of NPs whereas, TEM images confirm the formation of the hybrid hetero-junctions nanostructures with core@shell in spherical structure due to ZnO is surrounded throughout TiO$_2$ surface reveal an average particle size of TZ4 NPs are around 20 to 35 nm, TZ5 NPs are around 20 to 40 nm, and TZ6 NPs are around 30 to 40 nm that shown on histograms in Figures 7.6c, g, k respectively. These nano core@shells were in the agglomerated form of spherical shape nanocrystals that could not be easily separated from each other. The selected area diffraction patterns (SAED pattern) in Figure 7.6d, h, l show lightly diffuse sharp diffraction ring patterns indicating polycrystalline texture with small grain sizes associated with TiO$_2$ and ZnO that were consistent with XRD results.
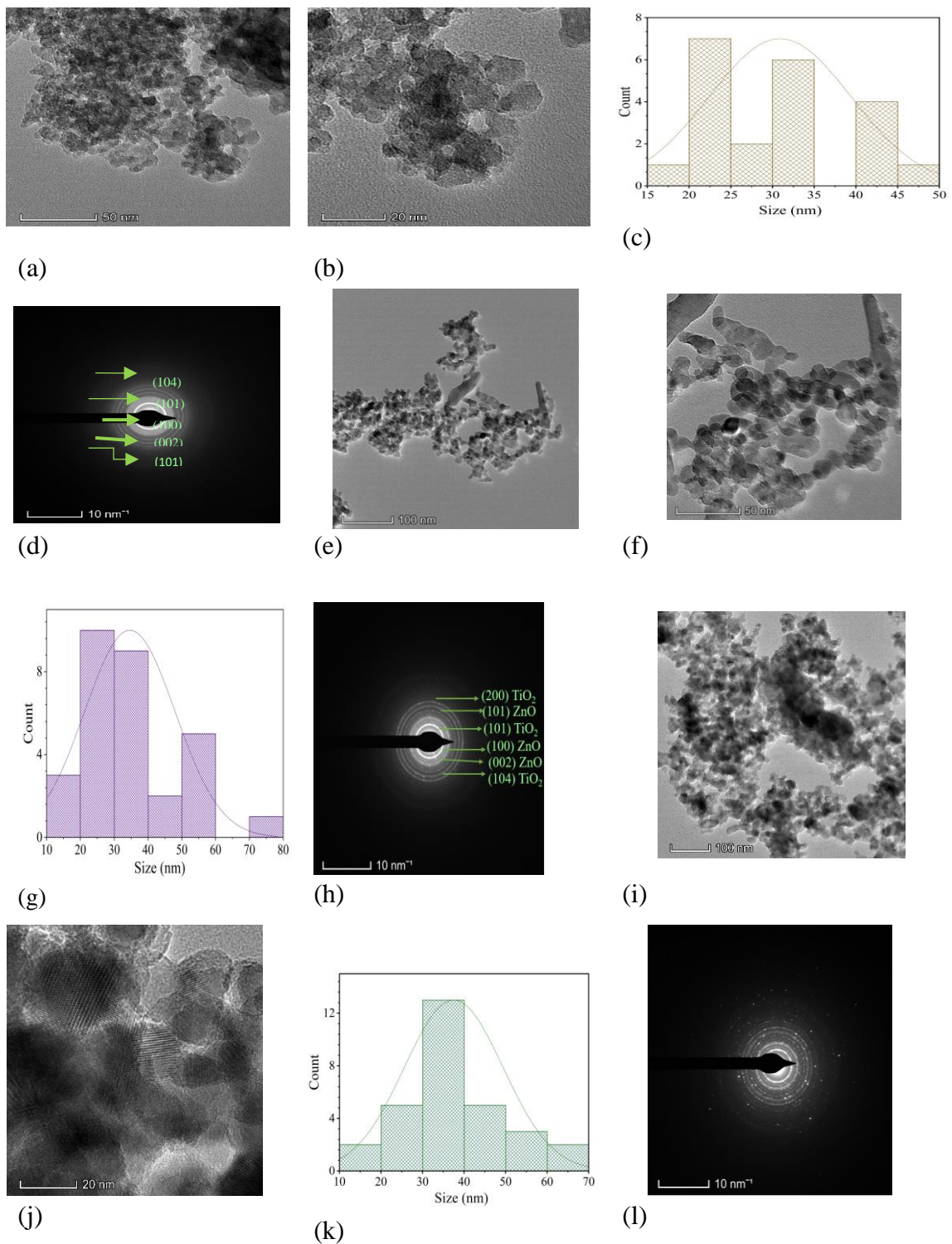
Figure 7.6 a-b. TEM images of TZ4 with different magnifications, c. histogram of TZ4 NPs and d. SAED pattern of TZ4 NPs, e-f. TEM images of TZ5 with different magnifications, g. histogram of TZ5 NPs and h. SAED pattern of TZ5 NPs, i-j. TEM images of TZ6

The diffraction rings present the mixed phase of TiO_2 and ZnO as these unveil the ring-like diffraction pattern that coincide with the (101), (104) lattice planes of TiO_2 and (100), (002) and (101) lattice planes of ZnO NPs and these absolute circle rings with spots are well coordinated with the XRD patterns of TZ4, TZ5, and TZ6 NPs as these explain greatly crystalline nature.

7.3.7   SEM and EDX of coated fabrics

Figure 7.7 reported SEM images that were used to analyze the surface morphology of control and TiO_2@ZnO NPs coated fabrics, and Figure 7.7a-b depicted control cotton fabric showing a very smooth heterogeneous surface of fibers alongside a quality "twisted ribbon" with evident micro-fibrils without any contaminated particles.[44] However, the surface morphology is altered after coating with TZ4, TZ5, and TZ6 NPs, as shown in Figure 7.7c-d, g-h, and k-l with different magnifications where some NPs can be detected on the surface of the coated fiber to reveal the attachment of NPs. It also explained that acrylic binder accomplishes the duty of the ''binding element'' of NPs with the fiber surface. The particle size of TZ4, TZ5, and TZ6 are reported by the histogram in Figure 7.7e, i, and m respectively onto the coated cotton fabrics enlarge than the particle size obtained from TEM shown in Table 3, as it may be because of some agglomerates of the NPs that formed throughout coating process by padding due to lack of stirring during the impregnation process. Moreover, NPs are aggregated in an aqueous solution due to their low dimension.

(a)

(b)

(c)

(d)

(e)

(f)

(g)

(h)

(i)

(j)

(k)

(l)

(m)

(n)
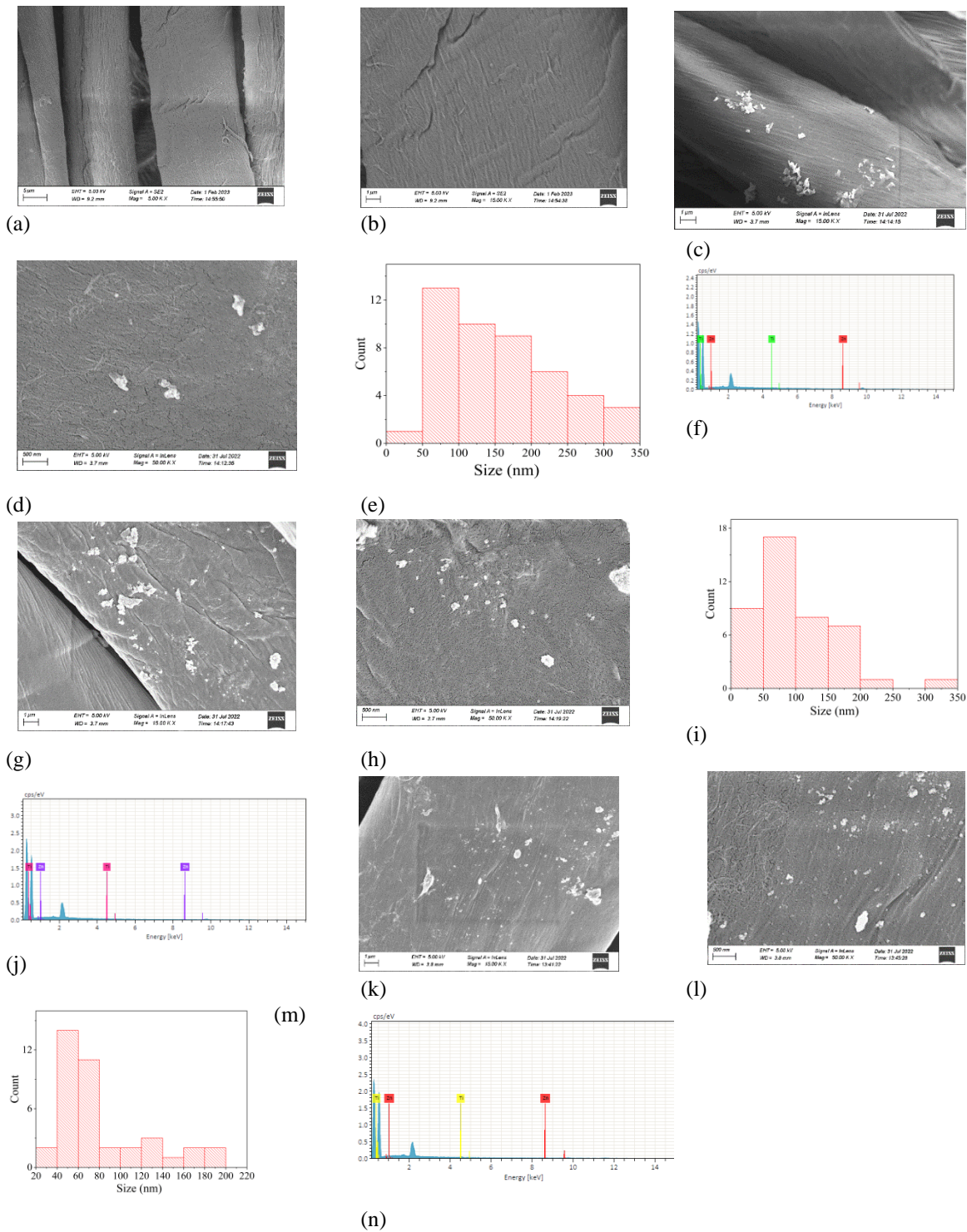
Figure 7.7: a-b SEM images of control cotton with different magnifications, c-d, g-h, k-l, TZ4, TZ5, and TZ6 NPs coated cotton fabric respectively with different magnifications, e, i, m, histogram of particle size of TZ4, TZ5 and TZ6 NPs respectively, whereas, f, j, n, EDX spectrum of TZ4, TZ5 and TZ6 NPs coated cotton fabric respectively.

The total quantity of NPs deposited on the fiber surface depends on the wettability and absorbing quality of the fabric, whereas the quality of the NPs coated fabric leans on the homogeneous attachment of NPs on the fiber surface.[45] The EDX spectra of confirmed the presence of Ti and Zn onto the surface of TZ4, TZ5, and TZ6 coated fabrics that were reported in Figure 7.6f, j, n as these express the identification of present elements onto the coated cotton fabric. Comparative analysis of particle sizes obtained from DLS, TEM, and SEM analysis are listed in Table 7.3.

Table 7.3: Comparative analysis of particle sizes obtained from DLS, TEM, and SEM analysis.

NPs	Particle size (nm)		
	DLS	TEM	SEM
TZ4	225 (125-477)	20-35 (15-50)	50-150 (10-350)
TZ5	178 (100-350)	20-40 (10-80)	50-100 (10-350)
TZ6	168 (62-390)	30-40 (10-70)	40-80 (20-200)

7.3.8 Thermogravimetric analysis

Thermal properties of TZ4, TZ5, and TZ6 NPs coated cotton fabric are evaluated range from room temperature to 550 ℃ temperature to analyze the effect of the coating process against the cellulose pyrolysis process. TGA curves of control and TZ4, TZ5, and TZ6 NPs coated cotton fabrics are shown in Figure 7.8. Pyrolysis is a complex reaction associated with endothermic bond rupture, volatilization, and exothermic bond formation that can be occurred at a time. The TGA thermogram shows the weight loss of fabrics in each pyrolysis stage, whereas control cotton fabric indicates three significant weight loss steps.[46] In the first step, the TGA curve is linear because of the initial pyrolysis stage, where the damage of celluloses is done primarily on the amorphous region of polymer. Some physical properties of the fabric can be changed by showing gradual weight loss (4.5%) up to around 254 ℃ due to the removal of absorbed and adsorbed water. In the second step, a massive slope in curves is seen due to the immense weight loss of the sample as cellulose pyrolysis occurred in the crystalline region of the polymer. A gradual weight loss line shows up to 320 ℃, and then drastic weight loss (around 83%) shows an endothermic peak up to 390 ℃ due to the formation of pyrolysis products like levoglucosan is produced.[20] In the third

step, above 500 ℃, finally curves the residual weight (8%), which may be due only to char/ash matter. On the other hand, all TZ4, TZ5, and TZ6 NPs coated cotton fabric shows the same pattern of curves except early and quicker decomposition than control fabric showing slightly low thermal stability than the control fabric due to exposure to high curing temperature in the coating process after impregnation and drying process as these may degrade some cellulose linkage.
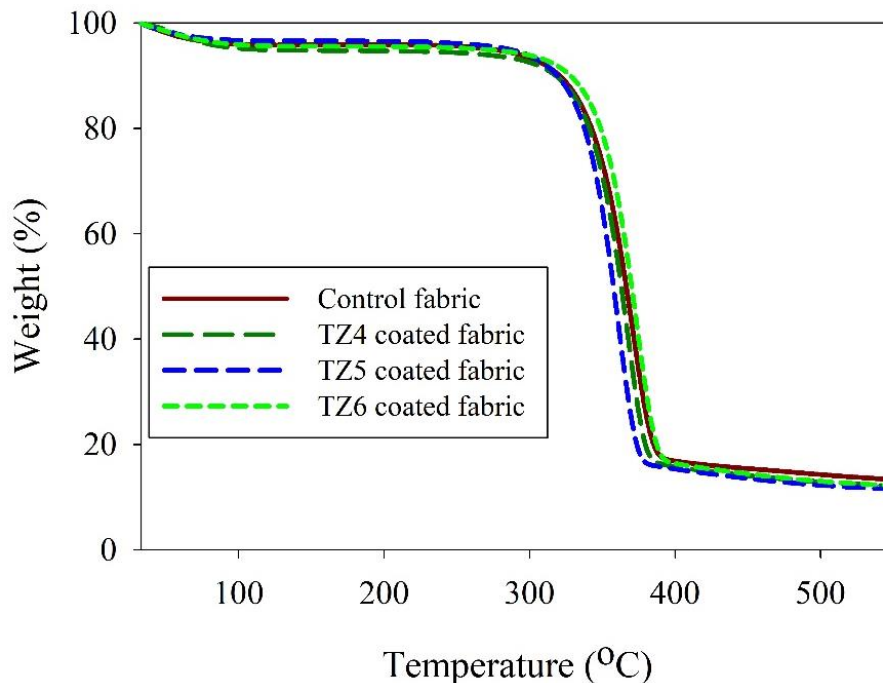
Figure 7.8. TGA analysis of control and coated cotton fabric with TZ4, TZ5, and TZ6 NPs.

7.3.9 Physical properties of coated fabric

Some physical properties such as weight, fabric density, bursting strength, and air permeability of TZ4, TZ5, and TZ6 coated fabrics are reported in Table 7.4, demonstrating minor gain in weight, fabric density due to fabric impregnated in an aqueous dispersion of NPs, facilitates some shrinkages in padding process whereas a decrease in bursting strength and air permeability due to the deposition of NPs on the fabric surface with acrylate binder to immobilization of NPs on fiber surface that justify a reduction in bursting strength and coating is done in aqueous solution, it also justifies the increase in density as in water fabric

become compact by shrinkage. Moreover, a decrease in air permeability justifies due to the cross-linking of acrylic binding throughout the surface of the fabric.

Table 7.4: Physical properties of control and coated cotton fabrics parameters

Physical properties		Control fabric	TZ4 coated fabric	TZ5 coated fabric	TZ6 coated fabric	Standard
Weight (g/m^2)		147	148	149	149	ISO 12127:2003
Fabric density (number of yarns/10 cm)	Wales	161	164	163	164	ISO1049-2:2000
	Coarse	185	187	188	188	
Bursting strength (KPa)		180.5	157.8	154.2	156.3	ISO 13938-1:1999
Air permeability (cm^3 cm^{-2} s^{-1})		68.8	51.3	52.1	50.7	ISO 9237:1999

7.3.10 **Color differences between control and coated fabrics**

The ΔL, Δa, Δb, ΔC, and ΔH color coordinates, whiteness and yellowness of control and TZ4, TZ5, and TZ6 coated fabrics are presented in Table 7.5. A slight trend of reduction of CMC ΔE and whiteness of all coated fabrics was seen due to higher curing temperatures that also justify increases in yellowness.

Table 7.5: Color difference, whiteness, and yellowness of control and coated fabrics

Sample	Illuminants/ Observer angle (10 Deg.)	CMC ΔE	ΔL	ΔC	ΔH	Δa	Δb	Whiteness (D65, 10 Deg.)		Yellowness (D65, 10 Deg.)
TZ4 coated fabric	D65	0.58	-0.86	0.44	-0.08	0.04	0.44	Control fabric	67.14	7.67
	F11	0.65	-0.84	0.52	-0.09	0.08	0.52	TZ4 coated fabric	62.97	8.58
	TL83	0.70	-0.83	0.59	-0.08	0.11	0.59	Delta CIE WI	-4.17	0.92
TZ5 coated fabric	D65	0.29	-0.33	0.23	0.03	-0.05	0.23	Control fabric	67.14	7.67
	F11	0.30	-0.33	0.25	-0.01	0.00	0.25	TZ5 coated fabric	65.28	8.07
	TL83	0.33	-0.33	0.29	-0.01	0.02	0.29	Delta CIE WI	-1.86	0.41
TZ6 coated fabric	D65	0.36	-0.45	0.29	0.03	-0.05	0.28	Control fabric	67.14	7.67
	F11	0.37	-0.46	0.31	-0.02	0.01	0.31	TZ6 coated fabric	64.72	8.18
	TL83	0.41	-0.45	0.35	-0.02	0.03	0.35	Delta CIE WI	-2.42	0.51

Standard CIE whiteness of control cotton is 67.14, whereas TZ4, TZ5, and TZ6 NPs coated cotton fabric is 62.97, 65.28, and 64.72, respectively, showing low reduction of whiteness for TZ5 coated fabric though whiteness is slightly reduced after coating, it is acceptable as these express good whiteness level.

7.3.11 **Self-cleaning properties**

The *K/S* values (absorption and scattering coefficient; color strength) of both the coffee and the curry stains on control and TZ4, TZ5, and TZ6 NPs coated fabrics after 20 h irradiation under light source according to ISO 105 B02:2013 for self-cleaning efficiency were expressed in Figures 7.9 and 7.10. Curry masala contains different ingredients such as turmeric, cumin, coriander seed, black paper, cloves, red chillies, ginger, salt, garlic, mustard, etc. The curry stain is produced by mixing curry masala in hot water though this stain is generally because of the turmeric (*Curcuma longa*) stain on cotton due to the binding of the yellow pigments that are most of the curcumin and its derivatives with the cellulose of cotton. Curcumin is about 3-5% of total turmeric constituents and is also a yellow-colored substance consisting of two phenolic hydroxyl groups and two centrally located carbonyl groups that can exist in keto-enol tautomers in solution.[47]
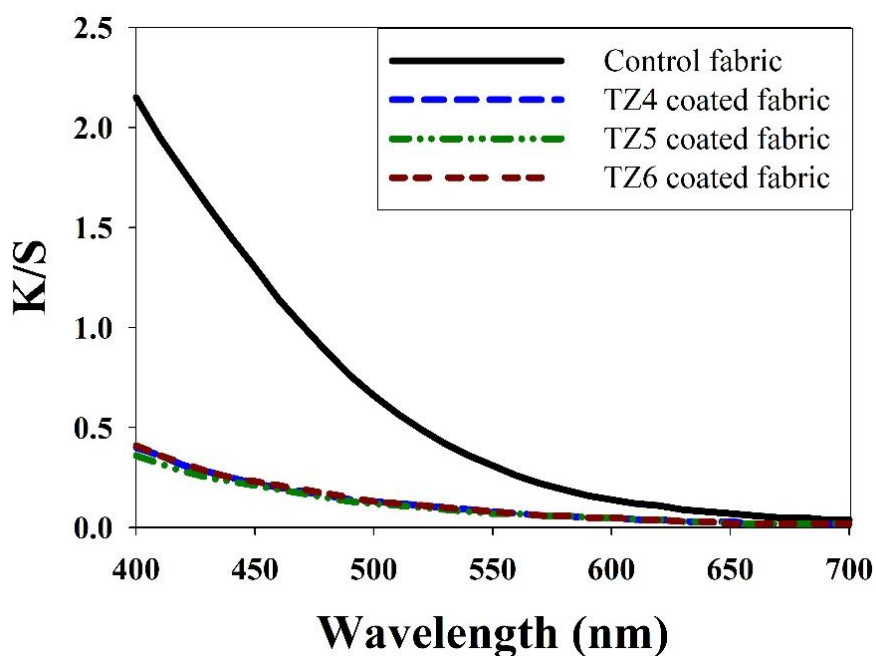
Figure 7.9: K/S values of the coffee stain of control and TZ4, TZ5, and TZ6 NPs coated fabrics after exposure against 20 h irradiation.
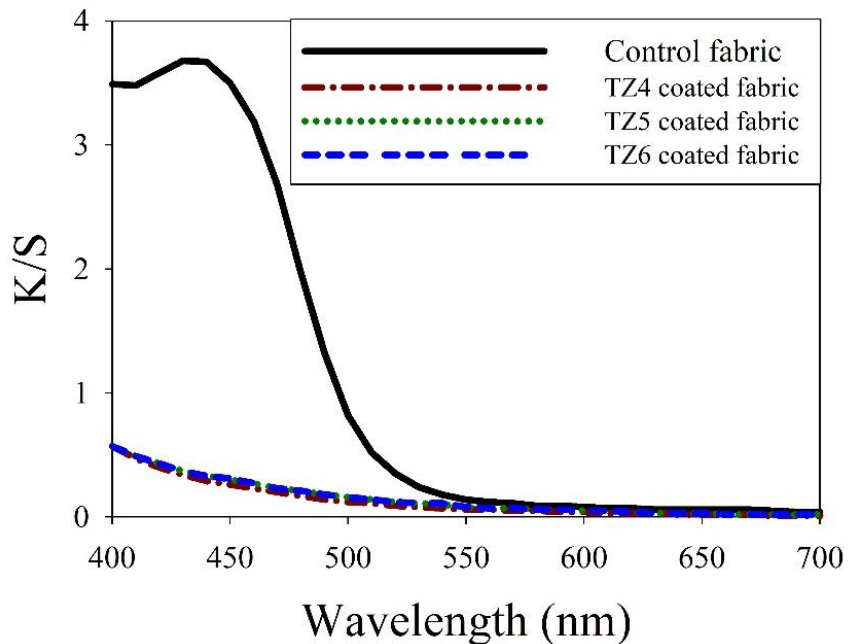
Figure 7.10: K/S values of the curry stain of control, TZ4, TZ5, and TZ6 NPs coated fabrics after exposure against 20 h irradiation.

The mechanism behind the discoloration of the colored substances (high molecular weight organic compound) of the curry stain by TZ4, TZ5, and TZ6 NPs coated cotton under UV exposure means when the photon energy is higher than the bandgap of respective NPs (3.19 eV, 3.2 eV, and 3.19 eV), the electrons of TZ4, TZ5, and TZ6 NPs will be excited and travel to the conduction band from the valence band thus resulting to the production of two kinds of oppositely charged carriers, i.e. hole (h^+) and electron (e^-). The electron (e^-) is converted to superoxide anion ($^\bullet O_2^-$) by oxygen, whereas the produced hole (h^+) is converted to hydroxyl radical ($^\bullet OH$) by the moisture (H_2O) present in the air. These superoxide anion and hydroxyl radicals are incredibly reactive particles that are responsible for redox reactions and mainly cause the degradation of organic materials (curry stain) into small molecules (CO_2 and H_2O) under UV irradiation of these NPs.[15] Summarized data of related NPs used to achieve self-cleaning performances are shown in Table 7.6.

Table 7.6: Summarized data of related NPs used to achieve self-cleaning performances.

Types of NPs	Deposition process	Functionalized textile	Light irradiation	The self-cleaning property	Ref.
TiO$_2$, ZnO	Electrospinning	Polyvinyl alcohol/TiO$_2$, Polyvinyl alcohol/ZnO nanofibers	Solar simulator (1000 W/m^2)	The dye degradation % is around 83%	48
TiO$_2$, ZnO	Pad-dry-cure	Cotton fabric	Sunlight	Reduction in K/S value (%) is up to 60% of coffee stain after 48 h exposure	19
ZnO	Pad-dry-cure	Polyester fabric	Sunlight	ΔE of direct green 6 dye stain after 7 days	49
ZnO	In-situ synthesis	Polyester woven fabric	UV light	Reduction in K/S value (%) is up to 90% after 24h of C.I. acid blue 9 stain	11
ZnO	Pad-dry-cure	Cotton fabric	Visible light	Visually satisfactory methylene blue color stain removed after 24 h	50
ZnO	*In-situ synthesis*	Cotton fabric	UV light	Visually satisfactory coffee stain removed after 17 h	51
ZnO	Electrospinning	nanofibers of co-polyester poly(1,4-cyclohexanedimethylene isosorbide terephthalate)	Solar simulator	Visually satisfactory methylene blue stain removed after 3 h	52
TiO$_2$	Pad-dry-cure	Cotton fabric	Sunlight	Reduction in K/S value (%) is up to 68% of coffee	53

				stain after 48 h exposure	
TiO$_2$	Pad-dry-cure	Woven fabric with 100% polyester, high-performance polyethylene: viscose blend, viscose: modacrylic blend	Visible light	Reduction in *K/S* value (%) is up to 54% for coffee stain after 24 h exposure	54
rGO-ZnO nanocomposite	*In-situ synthesis*	Cotton fabric	Sunlight	The self-cleaning degradation efficiency of up to 48% of organic dye and tea stain	55
TiO$_2$	Functionalized - grafted	Cotton fabric	UV light (Philips 200W/m^2)	M.B. Stain removal ΔE is satisfactory after 24 h exposure	56
TiO$_2$	Functionalized	Cotton fabric	UV light irradiation for 65 h	Visually satisfactory Oleic acid color stain removed after 65 h	57
TiO$_2$	Pad-dry-cure	Cotton fabric	Visible light	Reduction in *K/S* value (%) is up to 69% for coffee stain after 48 h exposure	58
Reactive blue 21+ TiO$_2$	Dip-pad-dry-cure	Cotton fabric	Visible light (45–95 mW cm^2)	Visually satisfactory removed	59
TiO$_2$	Dip-pad-dry-cure	Cotton fabric	UV light (1.2–1.3 mW cm^2)	Visually satisfactory removed coffee and wine stain	60
TiO$_2$-CNT	Dip-pad-dry-cure	Cotton and nylon fabric	Sunlight	Reduction in K/S value (%) is up to 36% for wine stain after 24 h exposure	61
TiO$_2$	Dip-pad-dry-cure	Cotton fabric	Xenon lamp	Reduction in *K/S* value (%) is up to 58% for the coffee stain and 76% for the curry stain after 20 h exposure.	Current

223

TZ4, TZ5, and TZ6 NPs coated fabrics show super self-cleaning results that shown in Table 7.7, as the percentage decrease in *K/S* value for the exposed sample of the coffee stain of TZ4, TZ5, and TZ6 coated fabrics are around 80 %, whereas the percentage decrease in *K/S* value for the exposed sample of curry stain of all coated fabrics are around 90 %.

Table 7.7: % of the decrease in K/S of TZ4, TZ5, and TZ6 NPs coated fabrics

Types of stain	NPs coated fabric	Unexposed Stain (K/S)	Exposed Stain (K/S)	% of the decrease in K/S
Coffee stain	TZ4	100	18.09	81.9 %
	TZ5	100	16.32	83.6 %
	TZ6	100	19.38	80.6 %
Curry stain	TZ4	100	9.22	90.7 %
	TZ5	100	10.27	89.7 %
	TZ6	100	9.20	90.8 %

7.4   Conclusions

Self-cleaning fabrics were prepared by depositing TZ4, TZ5, and TZ6 NPs onto cotton fabrics. TZ4, TZ5, and TZ6 NPs have been synthesized, characterized, and uniformly distributed on the surface of the fabrics, and these coated fabrics exhibit excellent self-cleaning properties attributed to the massive interaction within semiconductor-based TiO_2 and ZnO NPs. These high-value-added functional fabrics have a wide range of promising practical applications and are in sync with developing future trends in the textile industry.

References:

(1)   Andrade-Guel, M.; Cabello-Alvarado, C.; Bartolo-Pérez, P.; Medellin-Banda, D. I.; Ávila-Orta, C. A.; Cruz-Ortiz, B.; Espinosa-Muñoz, A.; Cadenas Pliego, G. Surface Modification of TiO_2/ZnO Nanoparticles by Organic Acids with Enhanced Methylene Blue and Rhodamine B Dye Adsorption Properties. *RSC Adv.* **2022**, *12* (44), 28494–28504. https://doi.org/10.1039/d2ra04961a.

(2)   Chen, W.; Feng, X.; Zhang, D.; Lu, F.; Wang, H.; Tan, J.; Xu, Q.; Liu, Y.; Cao, Z.; Su, X. In Situ Synthesis of TiO_2/NC on Cotton Fibers with Antibacterial Properties and Recyclable Photocatalytic Degradation of Dyes. *RSC Adv.* **2022**, *12* (31), 19974–19980. https://doi.org/10.1039/d2ra00992g.

(3)   Pham, T. T. H.; Vu, X. H.; Dien, N. D.; Trang, T. T.; Chi, T. T. K.; Phuong, P. H.; Nghia, N. T. Ag Nanoparticles on ZnO Nanoplates as a Hybrid SERS-Active Substrate for Trace Detection of Methylene Blue. *RSC Adv.* **2022**, *12* (13), 7850–7863. https://doi.org/10.1039/d2ra00620k.

(4)   Lam, S. M.; Lim, C. L.; Sin, J. C.; Zeng, H.; Lin, H.; Li, H. Facile Synthesis of MnO_2/ZnO Coated on Cotton Fabric for Boosted Antimicrobial, Self-Cleaning and Photocatalytic Activities under Sunlight. *Mater. Lett.* **2021**, *305* (September), 130818. https://doi.org/10.1016/j.matlet.2021.130818.

(5)   Nozari, B.; Montazer, M.; Mahmoudi Rad, M. Stable ZnO/SiO_2 Nano Coating on Polyester for Antibacterial, Self-Cleaning and Flame Retardant Applications. *Mater.   Chem.   Phys.*   **2021**,   *267*   (March),   124674. https://doi.org/10.1016/j.matchemphys.2021.124674.

(6)   Cai, J.; Cao, J.; Tao, H.; Li, R.; Huang, M. Three-Dimensional ZnO@TiO_2 Core-Shell Nanostructures Decorated with Plasmonic Au Nanoparticles for Promoting Photoelectrochemical Water Splitting. *Int. J. Hydrogen Energy* **2021**, *46* (73), 36201–36209. https://doi.org/10.1016/j.ijhydene.2021.08.140.

(7)   Behzadnia, A.; Montazer, M.; Rad, M. M. Simultaneous Sonosynthesis and Sonofabrication of N-Doped ZnO/TiO_2 Core-Shell Nanocomposite on Wool Fabric: Introducing Various Properties Specially Nano Photo Bleaching. *Ultrason.   Sonochem.*   **2015**,   *27*,   10–21. https://doi.org/10.1016/j.ultsonch.2015.04.017.

(8)   Vlazan, P.; Ursu, D. H.; Irina-Moisescu, C.; Miron, I.; Sfirloaga, P.; Rusu, E. Structural and Electrical Properties of TiO_2/ZnO Core-Shell Nanoparticles Synthesized by Hydrothermal Method. *Mater. Charact.* **2015**, *101*, 153–158. https://doi.org/10.1016/j.matchar.2015.01.017.

(9)   Katoueizadeh, E.; Zebarjad, S. M.; Janghorban, K. Investigation of Mechanical Characteristics of Functionalized Cotton Textiles by N-Doped TiO_2 Nanoparticles. *Mater. Chem. Phys.* **2018**, *218*, 239–245. https://doi.org/10.1016/j.matchemphys.2018.07.005.

(10)   Khandual, A.; Luximon, A.; Sachdeva, A.; Rout, N.; Sahoo, P. K. Enhancement of Functional Properties of Cotton by Conventional Dyeing with TiO_2 Nanoparticles. *Mater. Today Proc.* **2015**, *2* (4–5), 3674–3683. https://doi.org/10.1016/j.matpr.2015.07.128.

(11)   Ashraf, M.; Champagne, P.; Campagne, C.; Perwuelz, A.; Dumont, F.; Leriche, A. Study the Multi Self-Cleaning Characteristics of ZnO Nanorods Functionalized Polyester Fabric. *J. Ind. Text.* **2016**, *45* (6), 1440–1456. https://doi.org/10.1177/1528083714562086.

(12)   Thennakoon, C. A.; Rajapakshe, R. B. S. D.; Rajapakse, R. M. G.; Rajapakse, S. Anti-Stain and Durable Superhydrophobic/Antistatic Dual Functionality Surface for Fabric Materials Based on $F-ZnO/TiO_2$ Composite. *J. Sol-Gel Sci. Technol.* **2022**, *101* (3), 529–538. https://doi.org/10.1007/s10971-022-05734-y.

(13)   Attia, N. F.; Moussa, M.; Sheta, A. M. F.; Taha, R.; Gamal, H. Effect of Different Nanoparticles Based Coating on the Performance of Textile Properties. *Prog. Org. Coatings* **2017**, *104*, 72–80. https://doi.org/10.1016/j.porgcoat.2016.12.007.

(14)   Siwińska-Stefańska, K.; Kubiak, A.; Piasecki, A.; Goscianska, J.; Nowaczyk, G.; Jurga, S.; Jesionowski, T. TiO_2-ZnO Binary Oxide Systems: Comprehensive Characterization and Tests of Photocatalytic Activity. *Materials (Basel).* **2018**, *11* (5), 1–19. https://doi.org/10.3390/ma11050841.

(15)   Qi, K.; Wang, X.; Xin, J. h. Photocatalytic Self-Cleaning Textiles Based on Nanocrystalline Titanium Dioxide. *Text. Res. J.* **2011**, *81* (1), 101–110. https://doi.org/10.1177/0040517510383618.

(16)   Kumar, N. S.; Ganapathy, M.; Sharmila, S.; Shankar, M.; Vimalan, M.; Potheher, I. V. $ZnO/Ni(OH)_2$ Core-Shell Nanoparticles: Synthesis, Optical, Electrical and Photoacoustic Property Analysis. *J. Alloys Compd.* **2017**, 703, 624-632. https://doi.org/10.1016/j.jallcom.2017.01.323.

(17)   Aladpoosh, R.; Montazer, M. Nano-Photo Active Cellulosic Fabric through in Situ Phytosynthesis of Star-like Ag/ZnO Nanocomposites: Investigation and Optimization of Attributes Associated with Photocatalytic Activity. *Carbohydr. Polym.* **2016**, *141*, 116–125. https://doi.org/10.1016/j.carbpol.2016.01.005.

(18) Lessan, F.; Montazer, M.; Moghadam, M. B. A Novel Durable Flame-Retardant Cotton Fabric Using Sodium Hypophosphite, Nano TiO$_2$ and Maleic Acid. *Thermochim. Acta* **2011**, *520* (1–2), 48–54. https://doi.org/10.1016/j.tca.2011.03.012.

(19) Gupta, K. K.; Jassal, M.; Agrawal, A. K. Functional Finishing of Cotton Using Titanium Dioxide and Zinc Oxide Nanoparticles. *Res. J. Text. Appar.* **2007**, *11* (3), 1–10. https://doi.org/10.1108/RJTA-11-03-2007-B001.

(20) Lessan, F.; Montazer, M.; Moghadam, M. B. Thermochimica Acta A Novel Durable Flame-Retardant Cotton Fabric Using Sodium Hypophosphite , Nano TiO$_2$ and Maleic Acid. *Thermochim. Acta* **2011**, *520* (1–2), 48–54. https://doi.org/10.1016/j.tca.2011.03.012.

(21) Xu, R. Progress in Nanoparticles Characterization: Sizing and Zeta Potential Measurement. *Particuology* **2008**, *6* (2), 112–115. https://doi.org/10.1016/j.partic.2007.12.002.

(22) Domingos, R. F. ; B.; Ju-Nam, M. A. ; Reid, Y. ; Tufenkji, M. M. ; Lead, N. ; Leppard, J. R. ; Wilkinson, G. G. ;; J., K. Characterizing Manufactured Nanoparticles in the Environment: Multimethod Determination of Particle Sizes. *Env. Sci Technol* **2009**, *43*(19), 7277−7284. https://doi.org/10.1021/es900249m.

(23) Ashraf, M.; Champagne, P.; Perwuelz, A.; Campagne, C.; Leriche, A. Photocatalytic Solution Discoloration and Self-Cleaning by Polyester Fabric Functionalized with ZnO Nanorods. *J. Ind. Text.* **2015**, *44* (6), 884–898. https://doi.org/10.1177/1528083713519662.

(24) Paul, R.; Bautista, L.; de la Varga, M.; Botet, J. M.; Casals, E.; Puntes, V.; Marsal, F. Nano-Cotton Fabrics with High Ultraviolet Protection. *Text. Res. J.* **2010**, *80* (5), 454–462. https://doi.org/10.1177/0040517509342316.

(25) Niu, H.; Zhou, D.; Yang, X.; Li, X.; Wang, Q.; Qu, F. Towards Three-Dimensional Hierarchical ZnO Nanofiber@Ni(OH)$_2$ Nanoflake Core-Shell Heterostructures for High-Performance Asymmetric Supercapacitors. *J. Mater. Chem. A* **2015**, *3* (36), 18413–18421. https://doi.org/10.1039/c5ta04311e.

(26) Wang, Y. M.; Liu, S. W.; Xiu, Z.; Jiao, X. B.; Cui, X. P.; Pan, J. Preparation and Photocatalytic Properties of Silica Gel-Supported TiO$_2$. *Mater. Lett.* **2006**, *60* (7), 974–978. https://doi.org/10.1016/j.matlet.2005.10.061.

(27) Akhavan Sadr, F.; Montazer, M. In Situ Sonosynthesis of Nano TiO$_2$ on Cotton Fabric. *Ultrason. Sonochem.* **2014**, *21* (2), 681–691. https://doi.org/10.1016/j.ultsonch.2013.09.018.

(28) Perelshtein, I.; Applerot, G.; Perkas, N.; Wehrschetz-Sigl, E.; Hasmann, A.; Guebitz, G. M.; Gedanken, A. Antibacterial Properties of an in Situ Generated and Simultaneously Deposited Nanocrystalline ZnO on Fabrics. *ACS Appl. Mater. Interfaces* **2009**, *1* (2), 361–366. https://doi.org/10.1021/am8000743.

(29) Wang, L.; Ding, Y.; Shen, Y.; Cai, Z.; Zhang, H.; Xu, L. Study on Properties of Modified Nano-TiO_2 and Its Application on Antibacterial Finishing of Textiles. *J. Ind. Text.* **2014**, *44* (3), 351–372. https://doi.org/10.1177/1528083713487758.

(30) Tarigh, G. D.; Shemirani, F.; Maz'hari, N. S. Fabrication of a Reusable Magnetic Multi-Walled Carbon Nanotube-TiO_2 Nanocomposite by Electrostatic Adsorption: Enhanced Photodegradation of Malachite Green. *RSC Adv.* **2015**, *5* (44), 35070–35079. https://doi.org/10.1039/c4ra15593a.

(31) Zhang, D.; Chen, L.; Fang, di; Toh, G. W.; Yue, X.; Chen, Y.; Lin, H. In Situ Generation and Deposition of Nano-ZnO on Cotton Fabric by Hyperbranched Polymer for Its Functional Finishing. *Text. Res. J.* **2013**, *83* (15), 1625–1633. https://doi.org/10.1177/0040517512474362.

(32) Gharpure, S.; Yadwade, R.; Ankamwar, B. Non-Antimicrobial and Non-Anticancer Properties of ZnO Nanoparticles Biosynthesized Using Different Plant Parts of Bixa Orellana. *ACS Omega* **2022**, *7* (2), 1914–1933. https://doi.org/10.1021/acsomega.1c05324.

(33) Zhang, J.; Jin, X.; Yu, X.; Sang, Y.; Razzari, L.; Liu, H.; Claverie, J. An In Situ Polymerization-Encapsulation Approach to Prepare TiO_2–Graphite Carbon–Au Photocatalysts for Efficient Photocatalysis. *Part. Part. Syst. Charact.* **2018**, *35* (1), 1–6. https://doi.org/10.1002/ppsc.201700297.

(34) EL-Dafrawy, S. M.; Tarek, M.; Samra, S.; Hassan, S. M. Synthesis, Photocatalytic and Antidiabetic Properties of ZnO/PVA Nanoparticles. *Sci. Rep.* **2021**, *11* (1), 1–11. https://doi.org/10.1038/s41598-021-90846-8.

(35) Vivek, C.; Balraj, B.; Thangavel, S. Structural, Optical and Electrical Behavior of ZnO@Ag Core–Shell Nanocomposite Synthesized via Novel Plasmon-Green Mediated Approach. *J. Mater. Sci. Mater. Electron.* **2019**, *30* (12), 11220–11230. https://doi.org/10.1007/s10854-019-01467-x.

(36) Mostafa, A. M.; Mwafy, E. A. Synthesis of ZnO and Au@ZnO Core/Shell Nano-Catalysts by Pulsed Laser Ablation in Different Liquid Media. *J. Mater. Res. Technol.* **2020**, *9* (3), 3241–3248. https://doi.org/10.1016/j.jmrt.2020.01.071.

(37) Tauc, J.; Grigorovici, R.; Vancu, A. Optical Properties and Electronic Structure of Amorphous Germanium. *Phys. Stat. Sol. (b).* **1966**, *15*, 627-637. https://doi.org/10.1002/pssb.19660150224.

(38) Zhang, Q.; Xu, M.; You, B.; Zhang, Q.; Yuan, H.; Ostrikov, K. Oxygen Vacancy-Mediated ZnO Nanoparticle Photocatalyst for Degradation of Methylene Blue. *Appl. Sci.* **2018**, *8* (3), 1–12. https://doi.org/10.3390/app8030353.

(39) Ziashahabi, A.; Prato, M.; Dang, Z.; Poursalehi, R.; Naseri, N. The Effect of Silver Oxidation on the Photocatalytic Activity of Ag/ZnO Hybrid Plasmonic/Metal-Oxide Nanostructures under Visible Light and in the Dark. *Sci. Rep.* **2019**, *9* (1), 1–12. https://doi.org/10.1038/s41598-019-48075-7.

(40) Shahmoradi, Y.; Souri, D. Growth of Silver Nanoparticles within the Tellurovanadate Amorphous Matrix: Optical Band Gap and Band Tailing Properties, beside the Williamson-Hall Estimation of Crystallite Size and Lattice Strain. *Ceram. Int.* **2019**, *45* (6), 7857–7864. https://doi.org/10.1016/j.ceramint.2019.01.094.

(41) Król-Górniak, A.; Railean, V.; Pomastowski, P.; Płociński, T.; Gloc, M.; Dobrucka, R.; Kurzydłowski, K. J.; Buszewski, B. Comprehensive Study upon Physicochemical Properties of Bio-ZnO NCs. *Sci. Rep.* **2023**, *13* (1), 1–21. https://doi.org/10.1038/s41598-023-27564-w.

(42) Chauhan, A.; Verma, R.; Kumari, S.; Sharma, A.; Shandilya, P.; Li, X.; Batoo, K. M.; Imran, A.; Kulshrestha, S.; Kumar, R. Photocatalytic Dye Degradation and Antimicrobial Activities of Pure and Ag-Doped ZnO Using Cannabis Sativa Leaf Extract. *Sci. Rep.* **2020**, *10* (1), 1–16. https://doi.org/10.1038/s41598-020-64419-0.

(43) Zamiri, R.; Rebelo, A.; Zamiri, G.; Adnani, A.; Kuashal, A.; Belsley, M. S.; Ferreira, J. M. F. Far-Infrared Optical Constants of ZnO and ZnO/Ag Nanostructures. *RSC Adv.* **2014**, *4* (40), 20902–20908. https://doi.org/10.1039/c4ra01563k.

(44) El-Naggar, M. E.; Hassabo, A. G.; Mohamed, A. L.; Shaheen, T. I. Surface Modification of SiO_2 Coated ZnO Nanoparticles for Multifunctional Cotton Fabrics. *J. Colloid Interface Sci.* **2017**, *498*, 413–422. https://doi.org/10.1016/j.jcis.2017.03.080.

(45) Gao, D.; Chen, C.; Ma, J.; Duan, X.; Zhang, J. Preparation, Characterization and Antibacterial Functionalization of Cotton Fabric Using Dimethyl Diallyl Ammonium Chloride-Allyl Glycidyl Ether-Methacrylic/Nano-ZnO Composite. *Chem. Eng. J.* **2014**, *258*, 85–92. https://doi.org/10.1016/j.cej.2014.07.072.

(46) Perkins, R.; Drake, G. L.; Reeves, W. A. DTA and TGA Studies of Flame-Resistant Fabrics. *J. Appl. Polym. Sci.* **1966**, *10*(7), 1041–1066. https://doi.org/10.1002/app.1966.070100708.

(47)   Priyadarsini, K. I. Journal of Photochemistry and Photobiology C : Photochemistry Reviews Photophysics , Photochemistry and Photobiology of Curcumin : Studies from Organic Solutions , *Bio-Mimetics and Living Cells*. **2009**, *10*, 81–95. https://doi.org/10.1016/j.jphotochemrev.2009.05.001.

(48)   Khan, M. Q.; Kharaghani, D.; Ullah, S.; Waqas, M.; Abbasi, A. M. R.; Saito, Y.; Zhu, C.; Kim, I. S. Self-Cleaning Properties of Electrospun PVA/TiO$_2$ and PVA/ZnO Nanofibers Composites. *Nanomaterials* **2018**, *8* (9), 644. https://doi.org/10.3390/nano8090644.

(49)   Mohammadi, M.; Karimi, L.; Mirjalili, M. Simultaneous Synthesis of Nano ZnO and Surface Modification of Polyester Fabric. *Fibers Polym.* **2016**, *17* (9), 1371–1377. https://doi.org/10.1007/s12221-016-6497-5.

(50)   Zhu, C.; Shi, J.; Xu, S.; Ishimori, M.; Sui, J.; Morikawa, H. Design and Characterization of Self-Cleaning Cotton Fabrics Exploiting Zinc Oxide Nanoparticle-Triggered Photocatalytic Degradation. *Cellulose* **2017**, *24* (6), 2657–2667. https://doi.org/10.1007/s10570-017-1289-7.

(51)   Tran Thi, V. H.; Lee, B. K. Development of Multifunctional Self-Cleaning and UV Blocking Cotton Fabric with Modification of Photoactive ZnO Coating via Microwave Method. *J. Photochem. Photobiol. A Chem.* **2017**, *338*, 13–22. https://doi.org/10.1016/j.jphotochem.2017.01.020.

(52)   Khan, M. Q.; Lee, H.; Koo, J. M.; Khatri, Z.; Sui, J.; Im, S. S.; Zhu, C.; Kim, I. S. Self-Cleaning Effect of Electrospun Poly (1,4-Cyclohexanedimethylene Isosorbide Terephthalate) Nanofibers Embedded with Zinc Oxide Nanoparticles. *Text. Res. J.* **2018**, *88* (21), 2493–2498. https://doi.org/10.1177/0040517517723026.

(53)   Sundaresan, K.; Sivakumar, A.; Vigneswaran, C.; Ramachandran, T. Influence of Nano Titanium Dioxide Finish, Prepared by Sol-Gel Technique, on the Ultraviolet Protection, Antimicrobial, and Self-Cleaning Characteristics of Cotton Fabrics. *J. Ind. Text.* **2012**, *41* (3), 259–277. https://doi.org/10.1177/1528083711414962.

(54)   Abbas, M.; Iftikhar, H.; Malik, M. H.; Nazir, A. Surface Coatings of TiO$_2$ Nanoparticles onto the Designed Fabrics for Enhanced Self-Cleaning Properties. *Coatings* **2018**, *8* (1), 35. https://doi.org/10.3390/coatings8010035.

(55)   Kumbhakar, P.; Pramanik, A.; Biswas, S.; Kole, A. K.; Sarkar, R.; Kumbhakar, P. In-Situ Synthesis of RGO-ZnO Nanocomposite for Demonstration of Sunlight Driven Enhanced Photocatalytic and Self-Cleaning of Organic Dyes and Tea Stains of Cotton Fabrics. *J. Hazard. Mater.* **2018**, *360*, 193–203. https://doi.org/10.1016/j.jhazmat.2018.07.103.

(56)   Wijesena, R. N.; Tissera, N. D.; Perera, R.; Nalin De Silva, K. M.; Amaratunga, G. A. J. Slightly Carbomethylated Cotton Supported TiO2 Nanoparticles as Self-Cleaning Fabrics. *J. Mol. Catal. A Chem.* **2015**, *398*, 107–114. https://doi.org/10.1016/j.molcata.2014.11.012.

(57)   Yu, M.; Wang, Z.; Liu, H.; Xie, S.; Wu, J.; Jiang, H.; Zhang, J.; Li, L.; Li, J. Laundering Durability of Photocatalyzed Self-Cleaning Cotton Fabric with TiO_2 Nanoparticles Covalently Immobilized. *ACS Appl. Mater. Interfaces* **2013**, *5* (9), 3697–3703. https://doi.org/10.1021/am400304s.

(58)   Dr.B.Senthil kumar, A. P. Self-Cleaning Finish on Cotton Textile Using Sol-Gel Derived TiO_2 Nano Finish\n. *IOSR J. Polym. Text. Eng.* **2015**, *2* (1), 01–05. https://doi.org/10.9790/019X-0210105.

(59)   Ahmad, I.; Kan, C. W.; Yao, Z. Photoactive Cotton Fabric for UV Protection and Self-Cleaning. *RSC Adv.* **2019**, *9* (32), 18106–18114. https://doi.org/10.1039/c9ra02023c.

(60)   Qi, K.; Daoud, W. A.; Xin, J. H.; Mak, C. L.; Tang, W.; Cheung, W. P. Self-Cleaning Cotton. *J. Mater. Chem.* **2006**, *16* (47), 4567–4574. https://doi.org/10.1039/b610861j.

(61)   Lee, H. J.; Kim, J.; Park, C. H. Fabrication of Self-Cleaning Textiles by TiO_2-Carbon Nanotube Treatment. *Text. Res. J.* **2014**, *84* (3), 267–278. https://doi.org/10.1177/0040517513494258.

8. General Conclusions and Prospect

8.1   General Conclusions

TiO_2, ZnO, and Ag nanoparticles were successfully synthesized and characterized. The prepared NPs could be successfully applied on cotton fabric using pad-dry-cure technique and homogeneous coatings of NPs on cotton fabric could be obtained. The TiO_2 and ZnO nanoparticles-coated fabric showed excellent photocatalytic activity and outstanding self-cleaning properties. TiO_2 nanoparticles-coated cotton textile could remove 58% of coffee stains and 76% of curry stains whereas ZnO nanoparticles-coated cotton textiles removed 67% coffee stain and 82% curry stain after 20 h of xenon UV light exposure. The cotton fabric coated with Ag nanoparticles have great multifunctional characteristics like UV-protection, self-cleaning capability, and antibacterial activity. It has the capability to reduce more than 98% for *Staphylococcus aureus* and around 99.9% for *Escherichia coli* bacteria and shows a ultraviolet protection factor, UPF of 26.01.

To impose multifunctionality in a single material, core@shell nanoparticles were prepared and cotton fabric with fabricated with the nanoparticles to achieve multifunctional textiles. Core@shell nanoparticles like TiO_2@Ag, ZnO@Ag, and TiO_2@ZnO could be successfully synthesized and applied to the control cotton fabric. Both the TiO_2@Ag- and ZnO@Ag-coated fabric have multifunctional properties coming from both the semiconductor core and metallic shell. Semiconducting core provides the potential for self-cleaning capability whereas the metallic shell provides the UU protection and antimicrobial properties. Both the TiO_2@Ag coated fabric and ZnO@Ag coated fabric could reduce more than 99.9% for *Staphylococcus aureus* and around 99.9% for *Escherichia coli* bacteria which is higher than the normal Ag nanoparticles due to the synergistic effect. The UPF values for TiO_2@Ag- and ZnO@Ag-coated fabric are 28.40 and 26.14 respectively which also increased from the single nanoparticles. The self-cleaning properties also increased for the core@shell nanoparticles- coated fabric which shows a potential route to gain increasing multifunctional characteristics on the textiles.

TiO$_2$@ZnO core@shell nanoparticles could also be prepared and applied on the control cotton fabric to get better self-cleaning property. The synergistic effect of the both semiconducting nanoparticles provides more effective self-cleaning route. Whereas TiO$_2$ and ZnO-coated fabric could reduce coffee stain maximum 68% and curry stain up to 82%, the TiO$_2$@ZnO coated cotton fabric reduced 83.6% coffee stain and 90.8% curry stain.

Application of core@shell NPs on the surface of fabric exhibited a great potential to get multifunctional properties in the textiles. Not only the multifunctional properties of the both core and shell were exhibited by the core@shell NPs but also their synergistic effect played an important role for enhancement of the corresponding properties.

8.2   Prospects

Metallic and metal oxide nanoparticles have a great prospect for preparation of multifunctional textiles. The versatile properties of these nanoparticles provide numerous options to produce task specific fabrics. Metal oxide nanoparticles such as TiO$_2$ and ZnO nanoparticles are good semiconductors having a band gap in the UV region. So, irradiation of the fabric functionalized with these nanoparticles provides a photocatalyst on the surface of fabric which forms electron-hole pair and further generates reactive oxygen species that can break down organic compounds even the organic dyes and dusts. These characteristics of these metal oxide nanoparticles make them susceptible for application in self-cleaning textiles as well as potential photocatalysts.

One the other hand, metallic nanoparticles have also properties like UV protection, electrical conductivity, antibacterial and antimicrobial capacity, etc. So, Application of metal nanoparticles on any fabric also provides an opportunity to impose these excellent properties in normal fabrics. Ag nanoparticles are especially effective for UV protection and antibacterial activity. Nanoparticles like Ag forms ions of corresponding metals which are capable to form reactive oxygen species that can damage cellular wall of bacteria and damage the bacterial cell. So, imposing these types of nanoparticles provides an efficient means to impose functionality onto fabric surface.

Whereas a single constituent nanoparticle can provide specific one or two functional properties, two or different types of nanoparticles give an opportunity to impose more functionality in the textiles. The preparation of core@shell nanoparticles using two different materials, one is inside the core and another in on the outside shell of this single nanoparticle. Multifunctional characteristics comes from both core and shell inside the single nanoparticles. Application of such core@shell type nanoparticles on simple textiles makes them may render them smart with a range of functionalities. Besides, a synergistic effect also plays an important role on increasing the magnitude of the related functional properties. Smart textiles may thus be developed by exploiting the concept.

The multifunctional fabrics with high value-added features have a diverse range of practical applications and are aligned with the emerging trends of the future. This versatile multifunctional textile possesses considerable potential for utilization in the textile sector in the future.